IMPACT OF MAGNETIC FIELD ON PERISTALTIC TRANSPORT OF NANO-COUPLED STRESS FLUID IN AN INCLINED POROUS TUBE

M.P. Molimol[1,2], K. Maruthi Prasad[1]*, N. Subadra[2]

[1]*Department of Mathematics, School of Science, GITAM (Deemed to be University), Hyderabad, Telangana state, India -502329*
[2]*Department of Mathematics, Geethanjali College of Engineering and Technology,*
Medchal Dist., Hyderabad, Telangana state, India -501301
*Corresponding Author e-mail: mkaranam@gitam.edu

This study provides a theoretical investigation of peristaltic transport of couple-stress nanofluid under the influence of a magnetic field in an inclined porous tube. With low Reynolds number, long wavelength approximations, appropriate analytical methods are employed to investigate the fluid's velocity, frictional force, time-averaged flux, nanoparticle phenomena, pressure drop, and temperature profile. The effects of various physical parameters, including the thermophoresis parameter, Brownian motion parameter, local nanoparticle Grashof number, and local temperature Grashof number, on frictional force and pressure drop characteristics are investigated. Graphs are used to illustrate expressions for pressure drop, velocity, nanoparticle phenomena, temperature profile, and frictional force.
Keywords: *Thermophoresis parameter; Peristalsis; Brownian motion parameter; Nanoparticles; Magnetic field; Couple stress fluid; Porous medium*
PACS: 47.15.-x, 47.63.-b, 47.50.-d

Nomenclature

a^*	'Tube Radius'	C'	'Nanoparticle Concentration'
b^*	'Amplitude'	D_B^{*}	'Brownian diffusion coefficient'
c_1	'Wave Speed'	$D_{T'}^{*}$	'Thermophoretic diffusion coefficient'
λ^*	'Wave Length'	C_0'	'Nanoparticle Concentration as $r^* \to h$'
$\emptyset$	'Inclination Angle'	T_0'	'Ambient Temperature as $r^* \to h$'
T_{ij}^A and T_{ij}	'Antisymmetric Tensor and Symmetric Tensor'	θ^*	'Temperature'
$w_i{}^*$	'Velocity Vector	σ^*	'Concentration'
M_{ij}	'Couple-stress Tensor'	N_t^*	'Thermophoresis parameter'
μ_{ij}	'Deviatoric part of M_{ij}'	N_b^*	'Brownian motion parameter'
$\omega_{ij}{}^*$	'Vorticity Vector'	G_r^*	'Local temperature Grashof number'
d_{ij}	'Symmetric part of Velocity Gradient'	B_r^*	'Local nanoparticle Grashof number'
η and $\bar{\alpha}$	'Couple-stress Fluid Parameters'	r^*	'Radial Coordinate'
p	'Pressure'	z	'Axial Coordinate'
$\rho^*{}_f$	'Fluid Density'	w^*	'Axial Velocity'
$\rho^*{}_p$	'Density of Particle'	k	'Porosity'
F	'Body Force'	δ_1	'Electrical Conductivity'
C	'Volumetric thermal expansion coefficient'	B_0	'Uniform Magnetic Field'
d/dt	'Material derivative'	M^*	'Hartmann Number'

INTRODUCTION

Peristaltic pumping is the gradual contraction of a tube along its length. The cross-sectional area subsequently changes. Peristalsis naturally takes place in various tubular organs within the human body. Peristaltic motion has been used in several industrial applications, such as the transport of sterile and hygienic fluids, blood pumps for the heart and lungs, and the handling of chemically aggressive fluids. Researchers have studied the peristaltic transport of both non-Newtonian and Newtonian fluids under a wide range of conditions, recognizing its significance.

[1] conducted detailed research on Magnetohydrodynamic flow of nano-coupled stress fluid in the tapered, non-uniform passage within a porous medium, considering velocity slip and convective boundaries. Their model integrates key physical influences such as nanoparticle dynamics (Brownian motion and thermophoresis), magnetic fields, and porous resistance. Numerical results reveal that stronger magnetic fields reduce axial velocity but improve heat transfer. The wall-slip and permeable medium significantly affect the flow and thermal behaviour. [2] explained the combined impact of magnetic field and heat transfer on peristaltic transport of couple-stress fluid through an inclined tube. Their model accounts for body forces, low Reynolds number, and long wavelength approximation due to inclination, along with temperature-dependent source terms. The results reveal that flow characteristics, including temperature gradients, pressure rise, and velocity profiles, are significantly affected by the interplay between magnetic damping, couple stress effects, and inclination angle.

[3-4] explained the theoretical study of the peristaltic flow of couple stress fluid, including mass and heat transfer effects. This study assumes a low Reynolds number, long wavelength approximation, which allows analytical solutions. Key aspects investigated are velocity distribution, time-averaged flux, frictional force, mechanical efficiency, pressure-drop, nanoparticle behaviour, coefficients of heat and mass transport, and temperature profile. The influence of several physical parameters, such as Brownian motion, the couple stress fluid parameter, thermophoresis, nanoparticle, and temperature Grashof numbers, is thoroughly examined. and further it was studied with nanoparticles in an inclined tube by [5].

Researchers typically use the couple-stress fluid model because it is more mathematically simpler than other models. Blood, lubricants with electro-rheological suspensions, synthetic fluids, and high polymer-based additives exhibit couple-stress and rotation, unlike Newtonian fluids. The couple stress fluid model provides a better representation for these fluids. [6] Stokes developed couple-stress fluids in 1966. [7] developed a stress model of blood flow in the microcirculation. [8] conducted a study on peristaltic transport of couple-stress fluid, focusing on its relevance to hemodynamic applications. [9] explored how the boundary layer affects peristaltic flow of couple stress fluid. [10] demonstrated the hydromagnetic influence on inclined peristaltic flow of couple stress fluid.

Nanotechnology has significant impact on industry due to the distinctive physiochemical characteristics of nanoscale materials. Common base fluids used in nanofluid applications include oil, ethylene glycol, and water. Nanofluids are widely utilized in heat transfer processes, including those in fuel cells, microelectronics, hybrid engines, and pharmaceutical manufacturing. There is extensive literature available on nano fluids and their uses. [11] was the first to research nanofluids and further it was studied in an inclined tube by [12]. [13] carried out research concerning pool boiling behaviour of nanofluids in horizontally oriented narrow tubes. [14] studied peristaltic motion of third order nanofluids under mixed convection in the presence of an inclined magnetic field. [15-17] investigated the peristaltic flow of nanoparticle-laden micropolar fluid, taking into account heat and mass transfer effects in an inclined tube. Many ducts in the physiological system are inclined with the axis, rather than being horizontal. [18] explored the effect of slip conditions on the peristaltic transport of power-law fluid through the inclined tube.

In the previous literature, the researchers studied (i) peristaltic transport of Newtonian or micropolar fluids with MHD, (ii) peristaltic transport of a couple-stress fluid with MHD, but without nanoparticles, porous medium. In this work, we considered couple-stress fluid with nanoparticles in an inclined tube under the influence of MHD through porous medium. This comprehensive model is especially important for advanced applications such as biomedical engineering (magnetic targeting of drug carriers in porous tissues and blood flow under external magnetic fields), thermal management of electronics (cooling microchips using nanofluids in porous heat sinks with MHD flow control), and industrial processes (peristaltic pumping of complex fluids in chemical reactors with porous linings).

With all of the aforementioned in mind, the peristaltic flow of couple stress nanofluid within inclined tube was examined under the assumptions of low Reynolds number and long wavelength. Homotopy perturbation method (HPM) was employed to solve the coupled equations governing temperature profile and nanoparticle phenomena. Analytical solutions for nanoparticle phenomena, velocity, temperature profile, frictional force, and pressure drop were developed. Impact of various conditions on these flow parameters has been represented using graphs.

MATHEMATICAL FORMULATION

Peristaltic flow of an incompressible couple-stress nanofluid having a uniform cross-sectional radius a_1 in an inclined tube. A sinusoidal wave travels along the tube border with amplitude b^*, wavelength λ^*, speed c_1, and inclined tube angle is $\emptyset$.
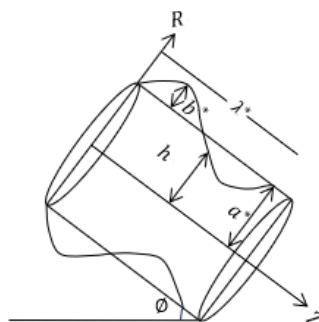

Figure 1. Geometry of the problem

Consider the cylindrical polar coordinate system (R, θ^*, Z) then the geometry of the wall surface is

$$R = H(z, t^*) = b^* Sin \frac{2\pi}{\lambda^*}(Z - c_1 t^*) + a^* \tag{1}$$

In a fixed coordinate frame, the governing equations of an incompressible couple-stress fluid containing nanoparticles, neglecting body couples or body moments, are expressed as follows

$$T_{ji.j} = \rho^* \frac{dw_i^*}{dt^*} \tag{2}$$

$$e_{ijk}^* T_{jk}^A + M_{ji.j} = 0 \tag{3}$$

$$l_{ij} = -p\delta_{ij}^* + 2\mu_{ij}d_{ij} \tag{4}$$

$$\mu_{ij} = 4\eta\omega_{j.i}^* + 4\eta'\omega_{ij}^* \tag{5}$$

$$(\rho^* c)_f \frac{dT'}{dt^*} = k\nabla^2 T' + (\rho^* c)_p \left[D_B^* \nabla C'.\nabla T' + \frac{D_{T'}^*}{T_0'}\nabla T'.\nabla T' \right] \tag{6}$$

$$\frac{dC'}{dt^*} = D_B^* \nabla^2 C' + \left[\frac{D_{T'}^*}{T_0'} \right]\nabla^2 T' \tag{7}$$

By applying the transformation

$$r^* = R, z = Z - c_1 t^*, \theta^* = \theta^*, u^* = U, w^* = W - c_1$$

Transforming from a stationary to a moving reference frame, we get

$$\frac{\partial u^{*'}}{dr^{*'}} + \frac{u^{*'}}{r^{*'}} + \frac{\partial w^{*'}}{\partial z'} = 0 \tag{8}$$

$$\mu\nabla^2 \left[1 - \frac{1}{\bar{\alpha}^2}\nabla^2 \right] w^{*'} = \frac{dp'}{dz'} + \rho^* g\beta^*(T' - T_0') + \rho^* g\beta^*(C' - C_0') + \frac{sin\emptyset}{F} + \delta_1 B_0^2 w^{*'} + \frac{\mu}{k}w^{*'} \tag{9}$$

$$\left[u^{*'}\frac{\partial T'}{\partial r^{*'}} + w^{*'}\frac{\partial T'}{\partial z'} \right] = \beta^* \left[\frac{\partial^2 T'}{\partial r^{*'2}} + \frac{1}{r^{*'}}\frac{\partial T'}{\partial r^{*'}} + \frac{\partial^2 T'}{\partial z'^2} \right] + \tau \left\{ D_B^* \left[\frac{\partial C'}{\partial r^{*'}}\frac{\partial T'}{\partial r^{*'}} + \frac{\partial C'}{\partial z'}\frac{\partial T'}{\partial z'} \right] + \frac{D_{T'}^*}{T_0'} \left[\left(\frac{\partial T'}{\partial r^{*'}} \right)^2 + \left(\frac{\partial T'}{\partial z'} \right)^2 \right] \right\} \tag{10}$$

$$\left[u^{*'}\frac{\partial C'}{\partial r^{*'}} + w^{*'}\frac{\partial C'}{\partial z'} \right] = D_B^* \left[\frac{\partial^2 C'}{\partial r^{*'2}} + \frac{1}{r^{*'}}\frac{\partial C'}{\partial r^{*'}} + \frac{\partial^2 C'}{\partial z'^2} \right] + \frac{D_{T'}^*}{T_0'} \left[\frac{\partial^2 T'}{\partial r^{*'2}} + \frac{1}{r^{*'}}\frac{\partial T'}{\partial r^{*'}} + \frac{\partial^2 T'}{\partial z'^2} \right] \tag{11}$$

with $\nabla^2 = \frac{1}{r^*}\frac{\partial}{\partial r^*}\left(r^*\frac{\partial}{\partial r^*} \right)$

where $\tau = \frac{(\rho^* C)_p}{(\rho^* C)_f}$ and $F = \frac{1}{\rho^* g}$

The dimensionless quantities:

$$r^* = \frac{r^{*'}}{a^*}, h' = \frac{h}{a^*}, z = \frac{z'}{\lambda^*}, w^* = \frac{w^{*'}}{c_1}, p = \frac{a^{*2}p'}{\lambda^* c_1\mu}, t^* = \frac{c_1 t^{*'}}{\lambda^*}, u^* = \frac{\lambda u^{*'}}{a^* c_1}, \theta^* = \frac{T' - T_0'}{T_0'},$$

$$R_e = \frac{2\rho^* c_1 a^*}{\mu}, \ \beta^* = \frac{k_1}{(\rho^* C)_f}, N_b^* = \frac{(\rho^* C)_p D_B^* C_0'}{(\rho^* C)_f}, N_t^* = \frac{(\rho^* C)_p D_{T'}^* T_0'}{(\rho^* C)_f \beta^*}, \sigma^* = \frac{C' - C_0'}{C_0'},$$

$$\bar{\alpha} = a^* \emptyset = \sqrt{\frac{\mu}{\eta}}a^*, \ k = \frac{k}{a^{*2}}, M^* = \frac{\delta_1 B_0^2 a^{*2}}{\mu}, G_r^* = \frac{g\beta^* a^{*3} T_0'}{\gamma^2}, B_r^* = \frac{g\beta^* a^{*3} C_0'}{\gamma^2}$$

Here G_r^* and B_r^* are the temperature and nanoparticle Grashof numbers, respectively. They quantify the ratio of buoyancy forces to the viscous forces in the flow. A larger B_r^* signifies a stronger influence of free convection induced by nanoparticle concentration differences.

Substituting the dimensionless quantities into equations (8) to (11), and taking long wavelength and low Reynolds number approximations while omitting the initial terms, we get

$$\frac{\partial p}{\partial r} = 0 \tag{12}$$

$$\frac{1}{r^*}\frac{\partial}{\partial r^*}\left(r^*\frac{\partial}{\partial r^*}\left(1 - \frac{1}{\bar{\alpha}^2}\nabla^2 \right)w^* \right) = \frac{dp}{dz} + G_r^*\theta^* + B_r^*\sigma^* + \frac{sin\emptyset}{F} + \left(\frac{\mu}{k} + M^* \right)w^* \tag{13}$$

$$0 = \frac{1}{r^*}\frac{\partial}{\partial r^*}\left(r^*\frac{\partial\theta^*}{\partial r^*} \right) + N_b^*\frac{\partial\sigma^*}{\partial r^*}\frac{\partial\theta^*}{\partial r^*} + N_t^*\left(\frac{\partial\theta^*}{\partial r^*} \right)^2 \tag{14}$$

$$0 = \frac{1}{r^*}\frac{\partial}{\partial r^*}\left(r^*\frac{\partial\sigma^*}{\partial r^*} \right) + \frac{N_t^*}{N_b^*}\left(\frac{1}{r^*}\frac{\partial}{\partial r^*}\left(r^*\frac{\partial\theta^*}{\partial r^*} \right) \right) \tag{15}$$

Dimensionless boundary conditions are

$$\frac{\partial w^*}{\partial r^*} = 0, \frac{\partial\sigma^*}{\partial r^*} = 0, \frac{\partial\theta^*}{\partial r^*} = 0 \text{ at } r^* = 0 \tag{16}$$

$$w^* = 0, \sigma^* = 0, \theta^* = 0 \text{ at } r^* = h(z) = 1 + \epsilon sin2\pi z \tag{17}$$

$$\frac{\partial^2 w^*}{\partial r^{*2}} - \frac{\bar{\eta}}{r^*}\frac{\partial w^*}{\partial r^*} = 0 \text{ at } r^* = h(z) = 1 + \epsilon sin2\pi z \tag{18}$$

$$\frac{\partial^2 w^*}{\partial r^{*2}} - \frac{\bar{\eta}}{r^*}\frac{\partial w^*}{\partial r^*} \text{ is finite at } r^* = 0 \tag{19}$$

Here $\epsilon^* = \frac{b^*}{a^*}$ and $\eta' = \frac{\bar{\eta}}{\eta}$

SOLUTION OF THE PROBLEM

HPM: It combines the perturbation and homotopy methods. This methodology is more suitable than the other classic perturbation approaches.

The homotopy formulations for (14) and (15) are (He, J. H. (1999))

$$H(\varsigma, \theta^*) = (1 - \varsigma)[L(\theta^*) - L(\theta_{10}^*)] + \varsigma\left[N_b^*\left(\frac{\partial\sigma^*}{\partial r^*}\right)\left(\frac{\partial\theta^*}{\partial r^*}\right) + N_t^*\left(\frac{\partial\theta^*}{\partial r^*}\right)^2\right] \tag{20}$$

$$H(\varsigma, \sigma^*) = (1 - \varsigma)[L(\sigma^*) - L(\sigma_{10}^*)] + \varsigma\left[\frac{N_t^*}{N_b^*}\left(\frac{1}{r^*}\frac{\partial}{\partial r^*}\left(r^*\frac{\partial\theta^*}{\partial r^*}\right)\right)\right] \tag{21}$$

Let the linear operator be $L = \frac{1}{r^*}\frac{\partial}{\partial r^*}\left(r^*\frac{\partial}{\partial r^*}\right)$ and

$$\theta_{10}^*(r^*, z) = \left(\frac{r^{*2} - h^2}{4}\right), \sigma_{10}^*(r^*, z) = -\left(\frac{r^{*2} - h^2}{4}\right) \text{ are initial guesses} \tag{22}$$

Define

$$\theta^*(r^*, z) = \theta_0^* + \varsigma\theta_1^* + \varsigma^2\theta_2^* + - - - - - - \tag{23}$$

$$\sigma^*(r^*, z) = \sigma_0^* + \varsigma\sigma_1^* + \varsigma^2\sigma_2^* + - - - - - - \tag{24}$$

Expressions for nanoparticle concentration and temperature profile are obtained for $\varsigma = 1$ as

$$\sigma^* = -\frac{N_t^*}{N_b^*}(N_b^* - N_t^*)\left(\frac{r^{*4} - h^4}{64}\right) \tag{25}$$

$$\theta^* = N_b^*(N_b^* - N_t^*)\left(\frac{r^{*6} - h^6}{1152}\right) - 2N_t^*(N_b^* - N_t^*)\left(\frac{r^{*6} - h^6}{1152}\right) + (2N_t^* - N_b^*)\left(\frac{r^{*4} - h^4}{64}\right) \tag{26}$$

Substituting (25) and (26) in equation (13), we get

$$\frac{1}{r^*}\frac{\partial}{\partial r^*}\left(r^*\frac{\partial}{\partial r^*}\left(1 - \frac{1}{\bar{\alpha}^2}\nabla^2\right)w^*\right) = \frac{dp}{dz} + \frac{sin\phi}{F} + G_r^*\left[N_b^*(N_b^* - N_t^*)\left(\frac{r^{*6} - h^6}{1152}\right) - 2N_t^*(N_b^* - N_t^*)\left(\frac{r^{*6} - h^6}{1152}\right) + \right.$$
$$\left.(2N_t^* - N_b^*)\left(\frac{r^{*4} - h^4}{64}\right)\right] + B_r^*\left(-\frac{N_t^*}{N_b^*}(N_b^* - N_t^*)\left(\frac{r^{*4} - h^4}{64}\right)\right) + \left(\frac{\mu}{k} + M^*\right)w^* \tag{27}$$

On solving equation (27) using the boundary conditions, we get

$$w^* = \frac{1}{\left[1 - \bar{\alpha}^2\left(\frac{r^{*2}}{4} - \left(\frac{\mu}{k} + M^*\right)\frac{r^4}{64}\right)\right]}\bar{\alpha}^2\left\{\left(\frac{dp}{dz} + \frac{sin\emptyset}{F}\right)\left(-\frac{r^{*4}}{64} + \frac{h^2r^{*2}}{16} - \frac{3h^4}{64}\right) - G_r^*\left[N_b^*(N_b^* - N_t^*)\left(\frac{r^{*10}}{7372800} - \frac{h^6r^{*4}}{73728} + \frac{5h^8r^{*2}}{98304} - \right.\right.\right.$$
$$\left.\frac{23h^{10}}{614400}\right) - N_t^*(N_b^* - N_t^*)\left(\frac{r^{*10}}{3686400} - \frac{h^6r^{*4}}{36864} + \frac{5h^8r^{*2}}{50752} - 0.00000716628h^{10}\right) + (2N_t^* - N_b^*)\left(\frac{r^{*8}}{147456} - \frac{h^4r^{*4}}{4096} + \frac{h^6r^{*2}}{1152} - \right.$$
$$\left.\left.\frac{31h^8}{49152}\right)\right] - B_r^*\left[-\frac{N_t^*}{N_b^*}(N_b^* - N_t^*)\left(\frac{r^{*8}}{147456} - \frac{h^4r^{*4}}{4096} + \frac{h^6r^{*2}}{1152} - \frac{31h^8}{49152}\right)\right]\right\} \tag{28}$$

Dimensionless flux is

$$q^* = \int_0^h 2r^*w^*dr^* \tag{29}$$

Substituting w^* from (28) in (29) and solving, we get

$$q^* = \bar{\alpha}^2 \left\{ \left(\frac{dp}{dz} + \frac{sin\emptyset}{F} \right) \left[-\frac{h^6}{48} + \bar{\alpha}^2 \left(-\frac{5h^8}{3072} - \left(\frac{\mu}{k} + M^* \right) \left(\frac{-h^{10}}{20480} \right) \right) \right] - G_r^* \left[N_b^* (N_b^* - N_t^*) \left(-\frac{73h^{12}}{4423680} + \right. \right. \right.$$

$$\bar{\alpha}^2 \left(-0.000001283676h^{14} - \left(\frac{\mu}{k} + M^* \right) (-0.00000003841188h^{16}) \right) \right) - N_t^* (N_b^* - N_t^*) \left(0.0000330958h^{12} + \right.$$

$$\bar{\alpha}^2 \left(0.0000056283h^{14} - \left(\frac{\mu}{k} + M^* \right) (0.00000377848h^{16}) \right) \right) + (2N_t^* - N_b^*) \left(-\frac{17h^{10}}{61440} + \bar{\alpha}^2 \left(-\frac{19h^{12}}{884736} - \right. \right.$$

$$\left(\frac{\mu}{k} + M^* \right) (-0.00000064184h^{14}) \right) \right] - B_r^* \left[-\frac{N_t^*}{N_b^*} (N_b^* - N_t^*) \left(-\frac{17h^{10}}{61440} + \bar{\alpha}^2 \left(-\frac{19h^{12}}{884736} - \left(\frac{\mu}{k} + \right. \right. \right.$$

$$M^* \right) (-0.00000064184h^{14}) \right) \right] \right\} \tag{30}$$

From equation (30), the expression for $\frac{dp}{dz}$ is

$$\frac{dp}{dz} = -\frac{1}{A_1} q^* + \frac{B_1}{A_1} \tag{31}$$

Where $A_1 = \bar{\alpha}^2 \left[-\frac{h^6}{48} + \bar{\alpha}^2 \left(-\frac{5h^8}{3072} + \left(\frac{\mu}{k} + M^* \right) \frac{h^{10}}{20480} \right) \right]$
and

$$B_1 = \bar{\alpha}^2 \left\{ \frac{sin\emptyset}{F} \left[-\frac{h^6}{48} + \bar{\alpha}^2 \left(-\frac{5h^8}{3072} + \left(\frac{\mu}{k} + M^* \right) \left(\frac{h^{10}}{20480} \right) \right) \right] - G_r^* \left[N_b^* (N_b^* - N_t^*) \left(-\frac{73h^{12}}{4423680} + \right. \right. \right.$$

$$\bar{\alpha}^2 \left(-0.00000128h^{14} + \left(\frac{\mu}{k} + M^* \right) (0.0000000384h^{16}) \right) \right) - N_t^* (N_b^* - N_t^*) \left(0.000033h^{12} + \right.$$

$$\bar{\alpha}^2 \left(0.0000056h^{14} - \left(\frac{\mu}{k} + M^* \right) (0.00000378h^{16}) \right) \right) + (2N_t^* - N_b^*) \left(-\frac{17h^{10}}{61440} + \bar{\alpha}^2 \left(-\frac{19h^{12}}{884736} + \left(\frac{\mu}{k} + \right. \right. \right.$$

$$M^* \right) (0.00000064184h^{14}) \right) \right) \right] - B_r^* \left[-\frac{N_t^*}{N_b^*} (N_b^* - N_t^*) \left(-\frac{17h^{10}}{61440} + \bar{\alpha}^2 \left(-\frac{19h^{12}}{884736} + \left(\frac{\mu}{k} + \right. \right. \right.$$

$$M^* \right) (0.00000064184h^{14}) \right) \right] \right\}$$

Pressure drop over the wavelength is

$$\Delta p_\lambda^* = -\int_0^1 \frac{dp}{dz} dz \tag{32}$$

By substituting $\frac{dp}{dz}$ from (31) in (32), we get

$$\Delta p_\lambda^* = q^* S_1 + S_2 \tag{33}$$

$$\text{Here } S_1 = -\int_0^1 \frac{1}{A_1} dz \tag{34}$$

and

$$S_2 = \int_0^1 \frac{B_1}{A_1} dz \tag{35}$$

Time-averaged flux is

$$Q^* = 1 + \frac{\epsilon^{*2}}{2} + q^* \tag{36}$$

By substituting (33) in (36), time-averaged flux is

$$Q^* = 1 + \frac{\epsilon^{*2}}{2} + \frac{\Delta p_\lambda^*}{S_1} - \frac{S_2}{S_1} \tag{37}$$

The dimensionless frictional force is given as

$$F^* = \int_0^1 h^2 \left(-\frac{dp}{dz}\right) dz \qquad (38)$$

Mechanical efficiency is defined as $E^* = \dfrac{\text{useful pumping power}}{\text{total work done per wavelength}}$

$$E^* = \frac{\Delta p_\lambda{}^* Q^*}{\frac{3b^{*2}}{8}\Delta p_\lambda{}^* + \int_0^1 \int_0^1 \frac{dp}{dz}\{b^* sin2\pi(z-t^*) - b^{*2} sin^4\pi(z-t^*) dz dt^*\}} \qquad (39)$$

Maximum flow rate is

$$Q_0{}^* = 1 + \frac{\epsilon^{*2}}{2} + \frac{\int_0^1 \frac{B_1}{A_1} dz}{\int_0^1 \frac{1}{A_1} dz} \qquad (40)$$

The reflux limit is

$$Q^* < 1 + \frac{\epsilon^{*2}}{2} + \frac{\int_0^1 \frac{B_1}{A_1} dz}{\int_0^1 \frac{1}{A_1} dz} \qquad (41)$$

Graphical Illustrations

Semi analytical approaches are used to obtain expressions of concentration, temperature, reflux limit, mechanical efficiency, frictional force, pressure drop, velocity, and time-averaged flux. Figures in the following subsections display graphical findings of relevant parameters for σ^*, θ^*, E^*, $\Delta p_\lambda{}^*$, F^* and reflux limit by using Mathematica.

Pressure drop

Figure (2) illustrates variation of absolute value of pressure drop for different values of $G_r{}^*$, $B_r{}^*$, $N_b{}^*$, μ, $N_t{}^*$, M^*, k^* compared to time-averaged flux (Q^*). Figures 2(a)-2(g) shows that rise in porosity (k), and Brownian motion parameter ($N_b{}^*$) results in an undesirable reaction in pressure drop ($\Delta p_\lambda{}^*$), whereas $\Delta p_\lambda{}^*$ rises with larger magnitudes of magnetic parameter (M^*), nanoparticle Grashof number ($B_r{}^*$), thermophoresis parameter ($N_t{}^*$), temperature Grashof number ($G_r{}^*$), and dynamic viscosity (μ).
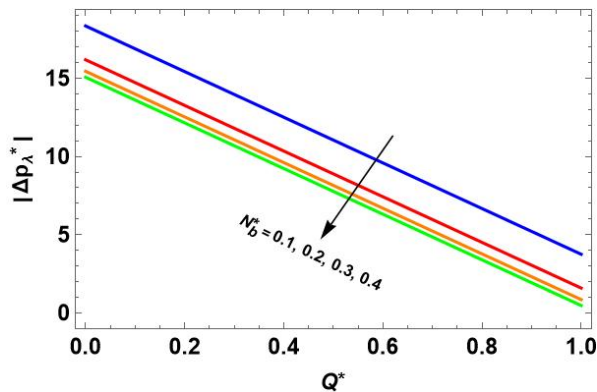

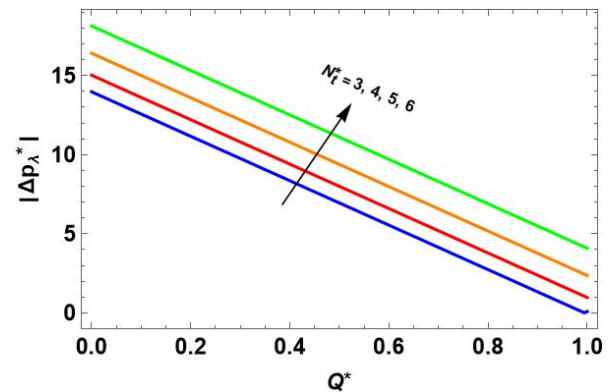**Figure 2(a).** Variations in Pressure drop for $N_b{}^*$
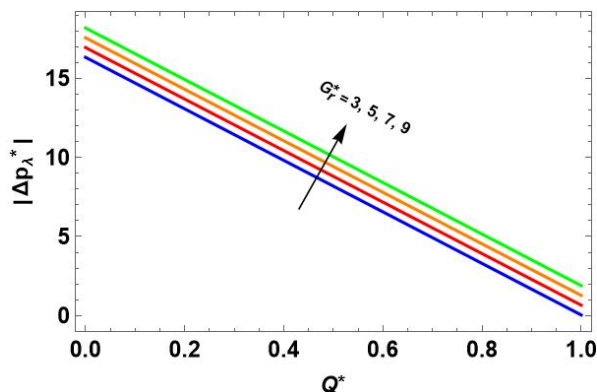

Figure 2(b). Variations in Pressure drop for $N_t{}^*$

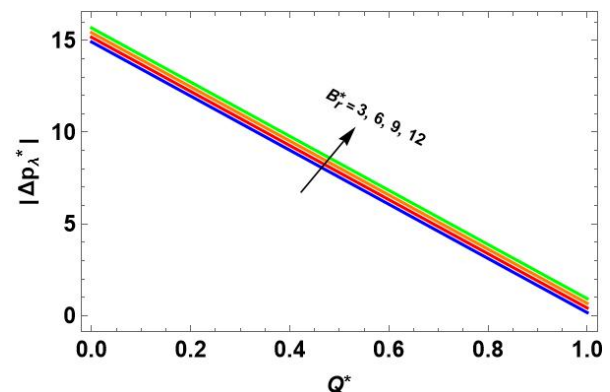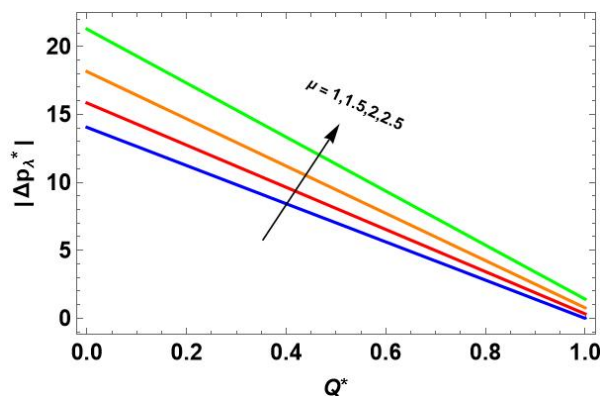**Figure 2(c).** Variations in Pressure drop for $G_r{}^*$

Figure 2(d). Variations in Pressure drop for $B_r{}^*$

Figure 2(e). Variations in Pressure drop for μ

Figure 2(f). Variations in Pressure drop for M^*

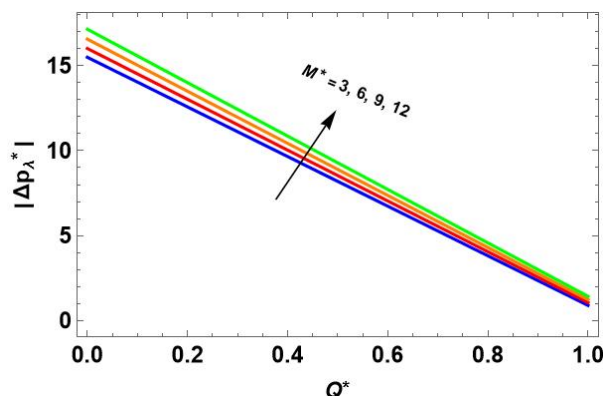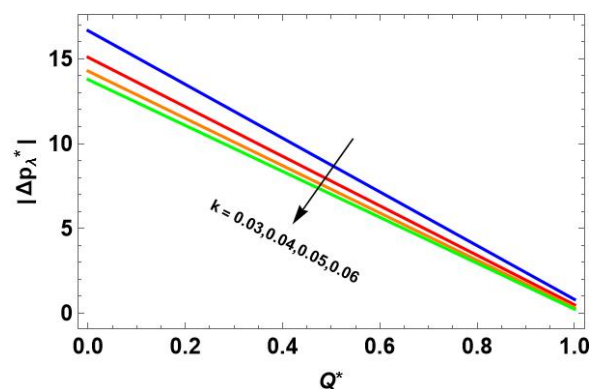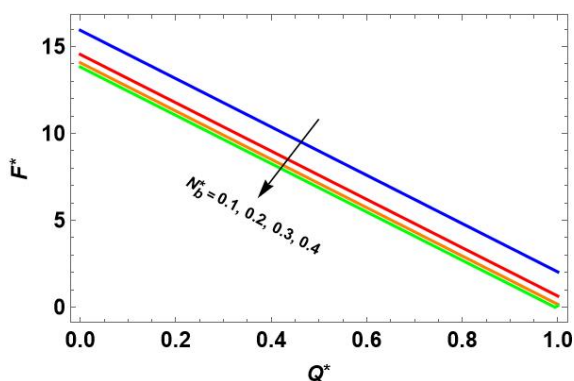**Figure 2**(g). Variations in Pressure drop for k

Frictional Force

Figure 3(a)-3(g) shows how various parameters affect the frictional force (F^*). F^* upsurges with rise in thermophoresis (N_t^*), temperature Grashof number (G_r^*), nanoparticle Grashof number (B_r^*), dynamic viscosity (μ), magnetic parameter (M^*) but decreases with rise in porosity (k), and Brownian motion (N_b^*).

Figure 3(a). Variations in Frictional force F^* against N_b^*
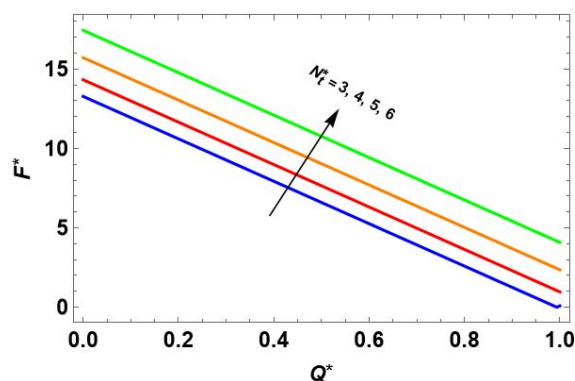
Figure 3(b). Variations in Frictional force F^* against N_t^*
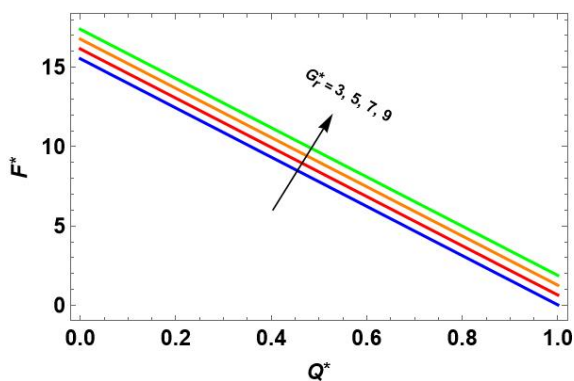
Figure 3 (c) Variations in Frictional force F^* against G_r^*
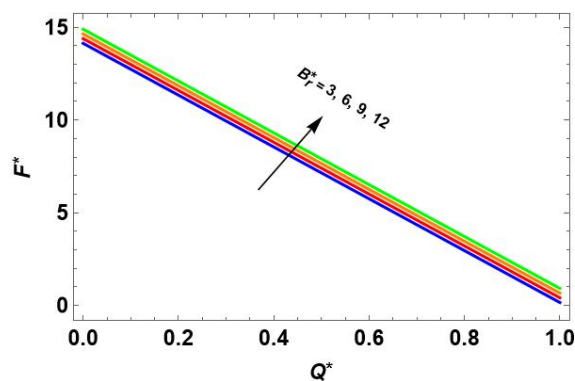
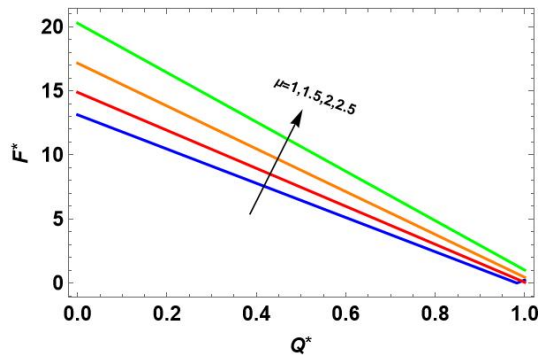**Figure 3** (d) Variations in Frictional force F^* against B_r^*

Figure 3(e). Variations in Frictional force F^* against μ
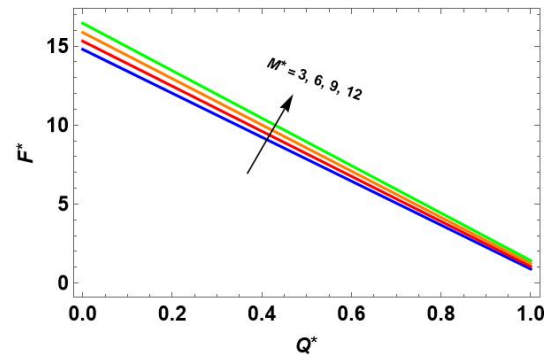
Figure 3(f). Variations in Frictional force F^* against M^*
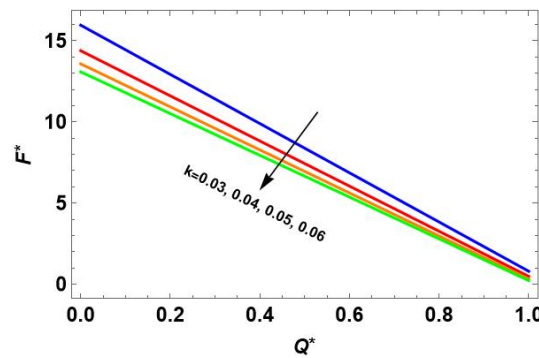
Figure 3(g). Variations in Frictional force F^* against k

Temperature Profile

Figure (4) illustrates the variations of temperature (θ^*) for thermophoresis (N_t^*) and Brownian motion (N_b^*). Decrease in N_t^* and N_b^* causes a rise in temperature, which signifies the enhanced thermal diffusion resulting from intensified nanoparticle motion, which acts to homogenize the temperature field.

Figure 4(a). Effect of N_b^* on Temperature

Figure 4(b). Effect of N_t^* on Temperature

Nanoparticle Phenomena

Figure (5) shows that increasing the Brownian motion (N_b^*) improves concentration, but increasing thermophoretic parameter (N_t^*) decreases concentration significantly.

Figure 5(a) Nanoparticle phenomenon against N_b^*
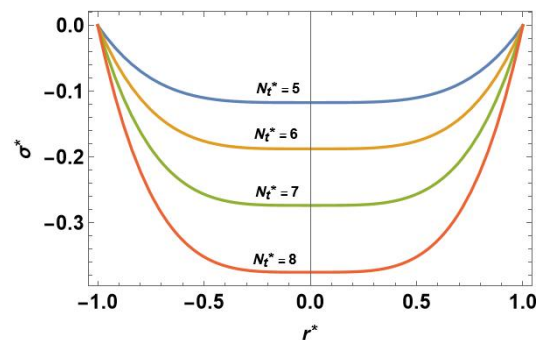
Figure 5(b) Nanoparticle phenomenon against N_t^*
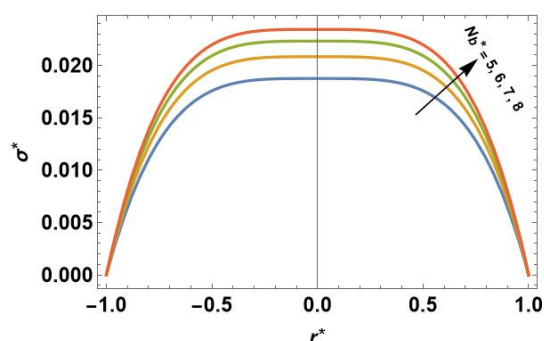
Figure 5(a) Nanoparticle phenomenon against $N_b{}^*$
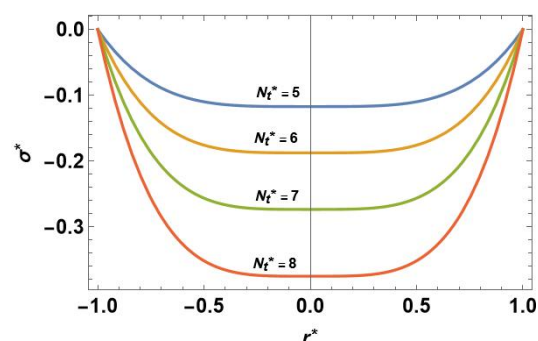
Figure 5(b) Nanoparticle phenomenon against $N_t{}^*$

Mechanical Efficiency

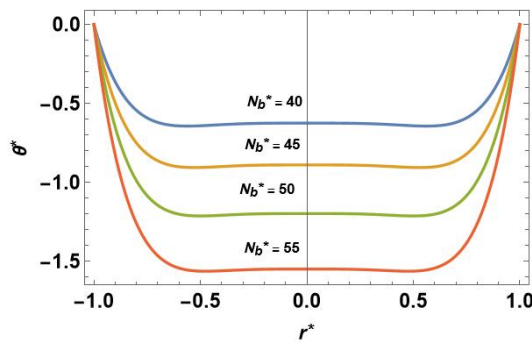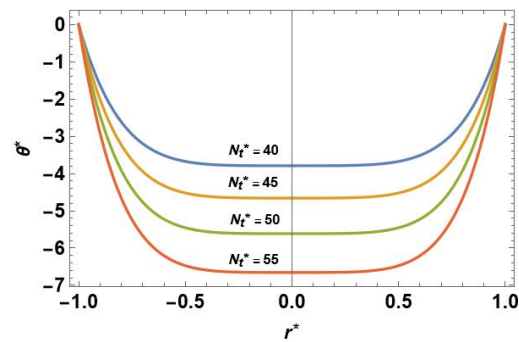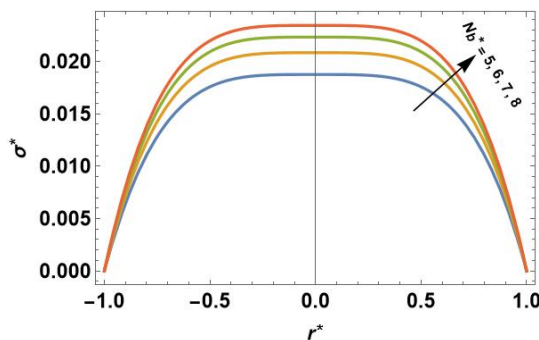Figure (6 and 6.1), Variations in Mechanical efficiency E^* are illustrated for different values of $\mu, N_b{}^*, k, N_t{}^*, G_r{}^*, M^*, B_r{}^*$ compared to amplitude (b^*) and the ratio of averaged flow rate and maximum flow rate $(Q^*/Q_0{}^*)$. Figures 6(a)-6(g), shows that rise in porosity k, nanoparticle Grashof number $B_r{}^*$, and Brownian motion N_b^* results in an undesirable reaction in Mechanical efficiency(E^*) whereas E^* rises with larger magnitudes of magnetic parameter (M^*), temperature Grashof number $(G_r{}^*)$, dynamic viscosity (μ), and thermophoresis parameter $(N_t{}^*)$. Figures 6.1(a)-(g), show that E^* upsurges with rise in nanoparticle Grashof number $B_r{}^*$, porosity k, and Brownian motion N_b^* whereas E^* reduces with increase in dynamic viscosity (μ), temperature Grashof number $G_r{}^*$, thermophoresis parameter $(N_t{}^*)$, and magnetic parameter (M^*).
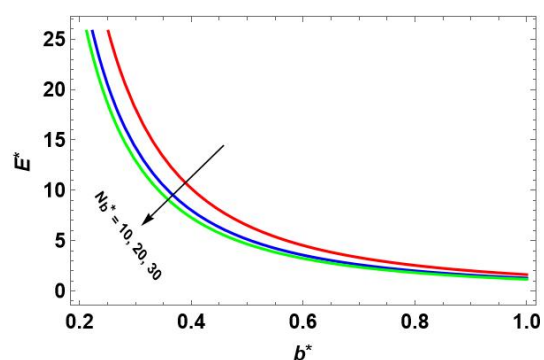
Figure 6(a). Mechanical Efficiency vs amplitude for different $N_b{}^*$
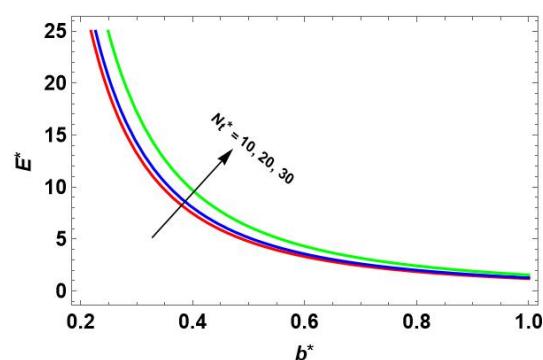
Figure 6(b). Mechanical Efficiency vs amplitude for different $N_t{}^*$
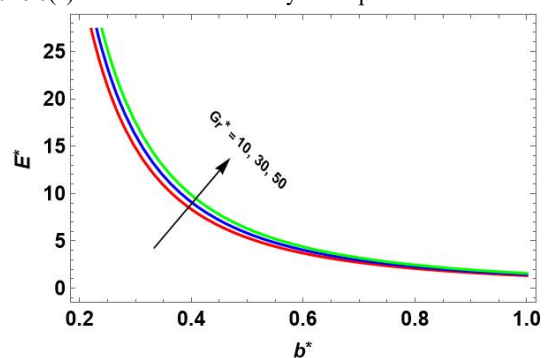
Figure 6(c). Mechanical Efficiency vs amplitude for different $G_r{}^*$
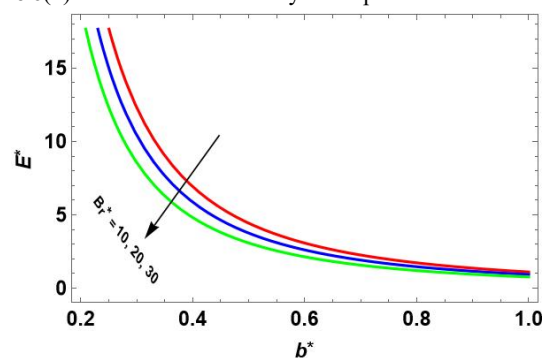
Figure 6(d). Mechanical Efficiency vs amplitude for different $B_r{}^*$
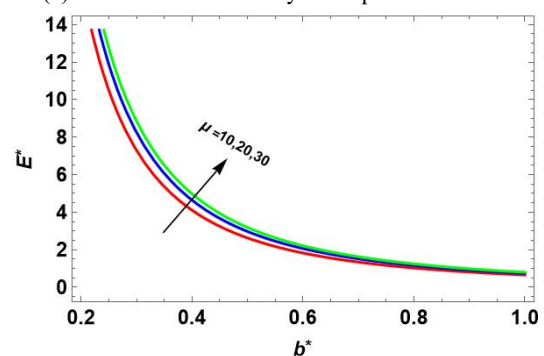
Figure 6(e). Mechanical Efficiency vs amplitude for different μ
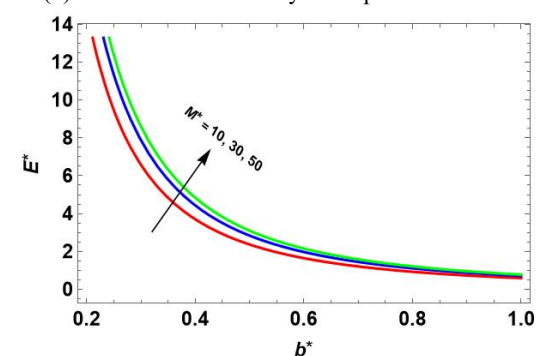
Figure 6(f). Mechanical Efficiency vs amplitude for different M^*
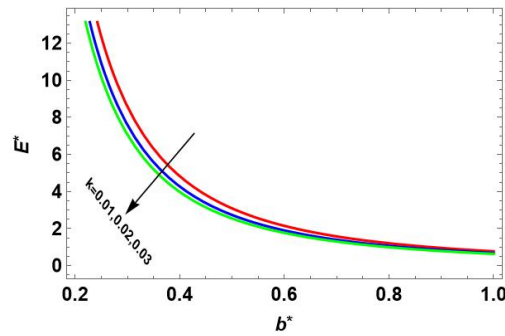
Figure 6(g). Mechanical Efficiency vs amplitude for different k
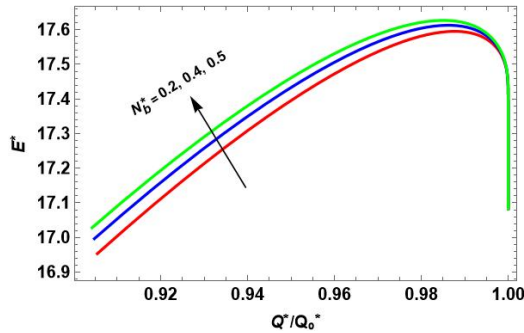
Figure 6.1(a). Mechanical Efficiency vs Q^*/Q_0^* for different N_b^*
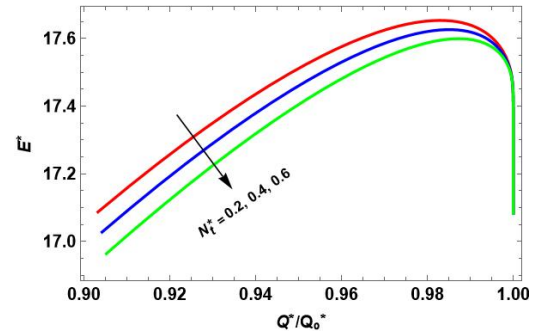
Figure 6.1(b). Mechanical Efficiency vs Q^*/Q_0^* for different N_t^*
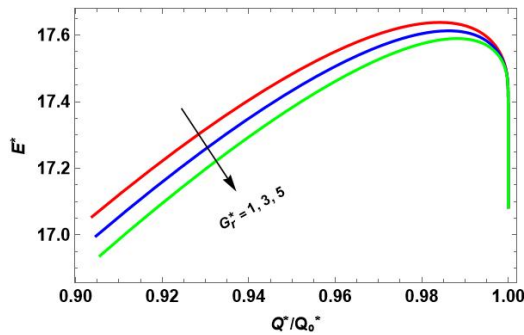
Figure 6.1(c). Mechanical Efficiency vs Q^*/Q_0^* for different G_r^*
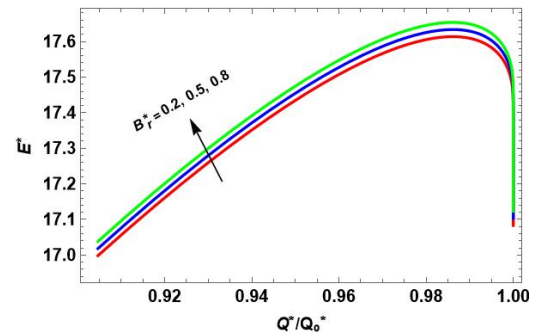
Figure 6.1(d). Mechanical Efficiency vs Q^*/Q_0^* for different B_r^*
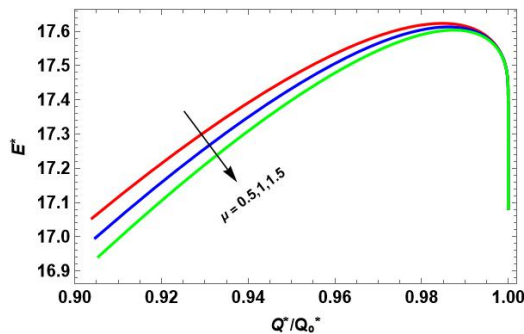
Figure 6.1(e). Mechanical Efficiency vs Q^*/Q_0^* for different μ
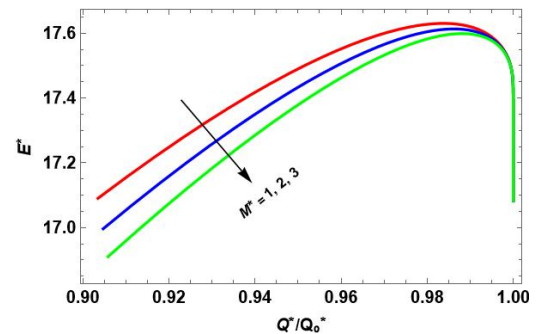
Figure 6.1(f). Mechanical Efficiency vs Q^*/Q_0^* for different M^*
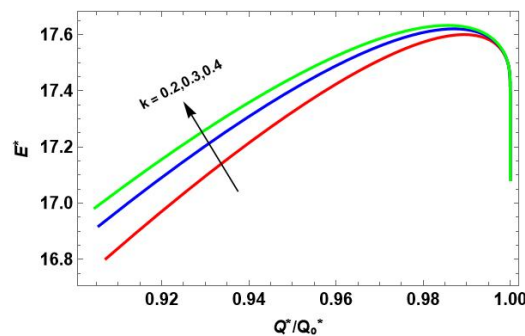
Figure 6.1(g). Mechanical Efficiency vs Q^*/Q_0^* for different k

Reflux Limit

Figure 7(a)-7(g) show that, with increase in nanoparticle Grashof number B_r^*, porosity k, temperature Grashof number G_r^*, and thermophoresis N_t^* results in a significant increase in reflux flow rate whereas higher values of magnetic parameter M^*, Brownian motion N_b^* and dynamic viscosity μ results in a reduction in reflux flow rate.
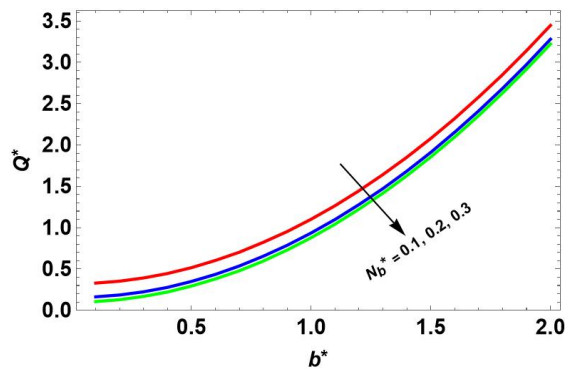
Figure 7(a). Reflux limit against N_b^*
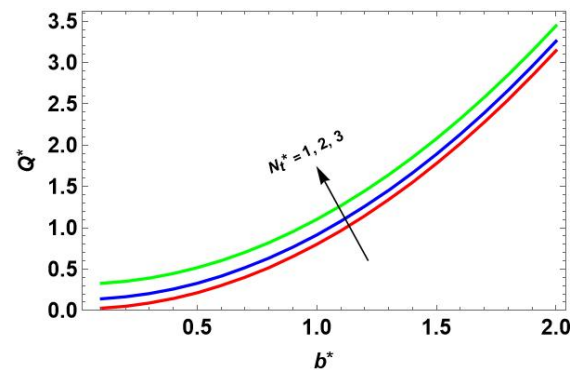
Figure 7(b). Reflux limit against N_t^*
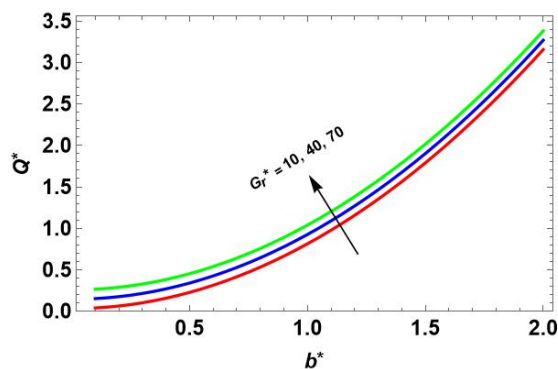
Figure 7(c). Reflux limit against G_r^*
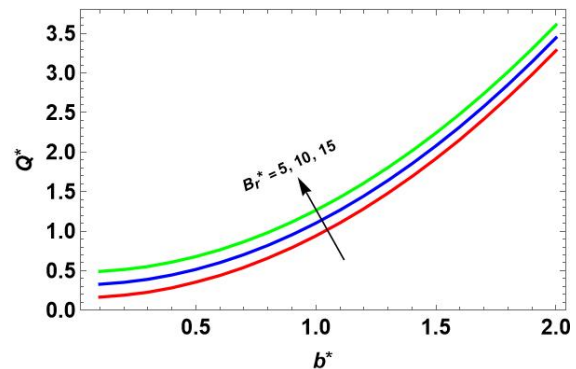
Figure 7(d). Reflux limit against B_r^*
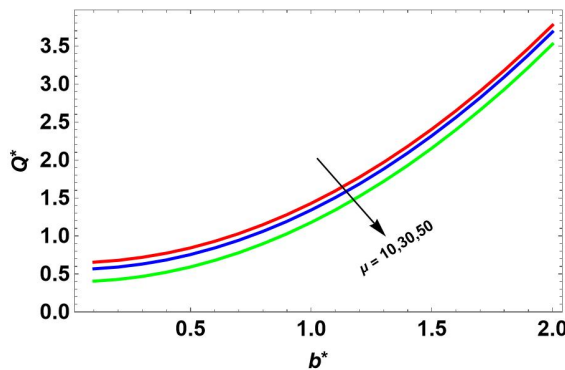
Figure 7(e). Reflux limit against μ
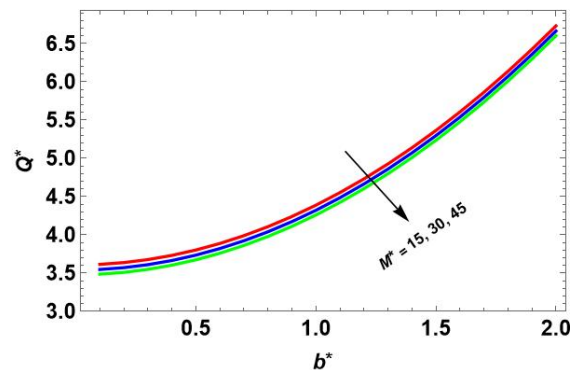
Figure 7(f). Reflux limit against M^*
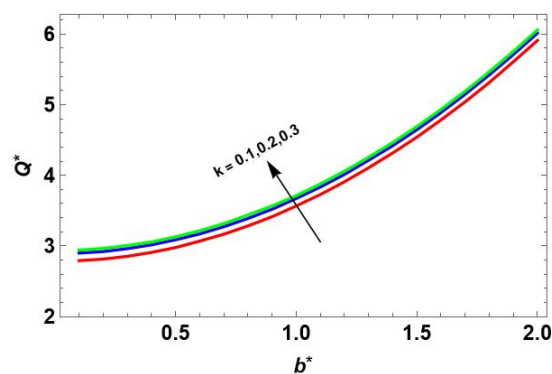
Figure 7(g). Reflux limit against k

Comparing the result with previous study

Magnetohydrodynamic effects on the peristaltic flow of couple stress fluid in an inclined tube with endoscope (previous study)	**Impact of Magnetic field on peristaltic transport of Nano-coupled stress fluid in an inclined porous tube (present study)**
Variations in Pressure drop for M	Variations in Pressure drop for M^*
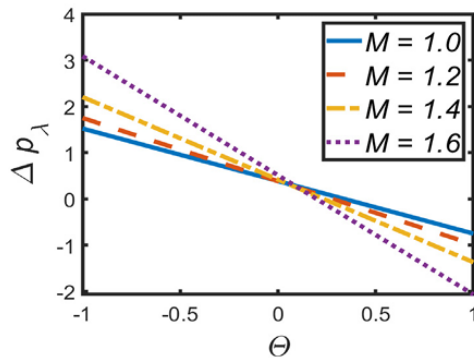
CONCLUSIONS

Governing equations for an incompressible nano-coupled stress fluid passing through a circular tube under the influence of magnetic field in porous medium are modeled and used to simulate fluid flow in the tube. The study under consideration is crucial from a rheological standpoint, and it has applications in various scientific fields, including fluid flow simulation. This research focuses on how nanoparticle Grashof number (B_r^*), porous medium (k^*), magnetic parameter (M^*), and temperature Grashof number (G_r^*) affect net flow rate. The key conclusions of the present research are:

- Thermophoresis (N_t^*) and Brownian motion (N_b^*) decreases as temperature upsurges.

- Increase in Brownian motion parameter N_b^*, increases concentration whereas it reduces with rise in thermophoresis N_t^*.

- Decrease in porous medium parameter (k^*) and Brownian motion (N_b^*) increases pressure-drop, but increasing thermophoresis (N_t^*) and magnetic parameter (M^*) significantly increases pressure drop.

- Frictional force (F^*) upsurges as magnetic parameter (M^*) and thermophoretic parameter (N_t^*) increases, whereas F^* reduces with rise in porous medium parameter (k^*) and Brownian motion (N_b^*).

- An elevation in the thermophoresis parameter N_t^*, nanoparticle Grashof number B_r^*, porosity k, and temperature Grashof number G_r^* substantially augments the reflux flow rate which promote fluid movement by enhancing thermal convection, reducing viscous drag, and allowing freer passage through the porous medium. Elevated values of μ, M^*, and N_b^* leads to decrease in reflux limit.

- An increase in B_r^*, N_b^*, and k leads to decrease in mechanical efficiency. This behavior suggests that enhanced nanoparticle diffusion, elevated viscous dissipation, and increased permeability introduce greater resistance and energy loss within the system. Conversely, higher values of the temperature Grashof number (G_r^*), thermophoresis parameter (N_t^*), dynamic viscosity (μ), and magnetic parameter (M^*) are associated with an improvement in mechanical efficiency. These parameters appear to promote more stable and directed fluid motion, potentially due to stronger thermal gradients, buoyancy effects, and controlled stress fields that enhance flow alignment.

- Interestingly, mechanical efficiency E^* expressed exclusively in terms of the flow rate ratio (Q^*/Q_0^*) reveals an opposite trend in certain cases i.e., increasing N_b^*, B_r^*, and k results in enhanced mechanical efficiency and in contrast, larger values of N_t^*, G_r^*, μ and M^* lead to a decrease in mechanical efficiency under the same flow conditions. This indicates that, depending on the operating regime, excessive thermophoretic effects, strong magnetic field interactions may suppress efficient energy transport within the system. Changing porosity or nanoparticle Grashof number can change time-averaged flow by affecting buoyancy-driven convection and also change frictional dissipation by adjusting viscosity. If the modification increases flux more than dissipation then E^* increases otherwise it reduces.

- When $N_b^* = 0, N_t^* = 0, M^* = 0, k = 0$, the velocity or pressure relations can be reduced to long wavelength solution. Increasing the MHD parameter (M^*) reduces reflux and stabilizes pumping. Moderate levels of the thermophoresis parameter (N_t^*) implies good nanoparticle distribution while preventing excessive energy loss. The inclination angle can be optimized to reduce reflux in biomedical devices or systems.

ORCID

M.P. Molimol, https://orcid.org/0000-0001-5343-9138; **K. Maruthi Prasad,** https://orcid.org/0000-0002-9010-6452;
N. Subadra, https://orcid.org/0000-0001-8901-1870

REFERENCES

[1] P. Deepalakshmi, G. Shankar, E.P. Siva, D. Tripathi, and O. Anwar Beg, "MHD Analysis of Couple Stress Nanofluid through a Tapered Non-Uniform Channel with Porous Media and Slip-Convective Boundary Effects", International Journal of Thermofluids, **27**, 101208 (2025). https://doi.org/10.1016/j.ijft.2025.101208

[2] M.M. Ahmed, I.M. Eldesoky, Ahmed G. Nasr, Ramzy M. Abumandour, and Sara I. Abdelsalam, "The profound effect of heat transfer on magnetic peristaltic flow of a couple stress fluid in an inclined annular tube", Modern Physica Letter B, **38**(25), No. 25, 2450233 (2024). https://doi.org/10.1142/S0217984924502336

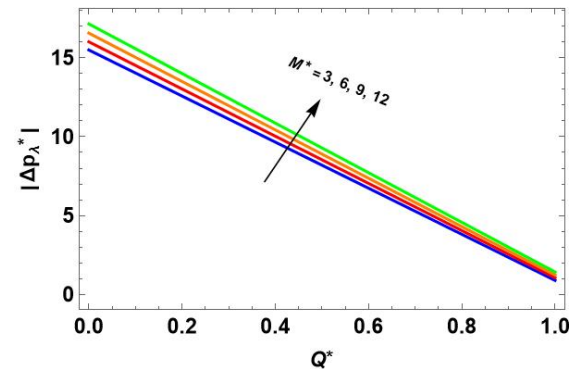[3] M. Devakar, K. Ramesh, and K. Vajravelu, "Magnetohydrodynamic effects on the peristaltic flow of couple stress fluid in an inclined tube with endoscope", Journal of Computational Mathematics and Data Science, **2**, 2772-4158 (2022). https://doi.org/10.1016/j.jcmds.2022.100025

[4] A.H. Shapiro, M.Y. Jaffrin, and S.L. Weinberg, "Peristaltic pumping with long wavelengths at low Reynolds number", Journal of Fluid Mechanics, **37**(04), 799–825 (1969). https://doi.org/10.1017/s0022112069000899

[5] K.M. Prasad, N. Subadra, and U.S. Mahabaleshwar, "Peristaltic Transport of a Couple-Stress Fluid with Nanoparticles in an Inclined Tube", International Journal of Engineering Trends and Technology (IJETT), **48**(7), 354-362 (2017). https://doi.org/10.14445/22315381/IJETT-V48P262

[6] V.K. Stokes, "Couple stresses in fluids", Physics of Fluids, **9**(9), 1709–1715 (1966). https://doi.org/10.1063/1.1761925

[7] D. Pal, N. Rudraiah, and R. Devanathan, "A couple stress model of blood flow in the microcirculation", Bulletin of Mathematical Biology, **50**(4), 329–344 (1988). https://doi.org/10.1007/BF02459703

[8] S. Maiti, and J. Misra, "Peristaltic transport of a couple stress fluid: some applications to hemodynamics", Journal of Mechanics in Medicine and Biology, **12**(03), 1250048 (2012). https://doi.org/10.1142/S0219519411004733

[9] K.M. Prasad, and G. Radhakrishnamacharya, "Effect of Peripheral Layer on Peristaltic Transport of a Couple Stress Fluid", International Journal of Fluid Mechanics Research, **36**(6), 573–583 (2009). https://doi.org/10.1615/InterJFluidMechRes.v36.i6.80

[10] G.C. Shit, and M. Roy, "Hydromagnetic effect on inclined peristaltic flow of a couple stress fluid", Alexandria Engineering Journal, **53**(4), 949–958 (2014). https://doi.org/10.1016/j.aej.2014.07.007

[11] S.U.S. Choi, and J.A. Eastman, "Enhancing thermal conductivity of fluids with nanoparticles", in: *ASME FED, Proceedings of the ASME International Mechanical Engineering Congress and Exposition*, (San Francisco, CA, 1995).

[12] K.M. Prasad, N. Subadra, and M. Srinivas, "Peristaltic Transport of a Nanofluid in an Inclined Tube", American Journal of Computational and Applied Mathematics, **5**(4), 117–128 (2015). https://doi.org/10.5923/j.ajcam.20150504.04
S.K. Das, N. Putra, and W. Roetzel, "Pool boiling of nano-fluids on horizontal narrow tubes", International Journal of Multiphase Flow, **29**(8), 1237-1247 (2003). https://doi.org/10.1016/S0301-9322(03)00105-8

[13] S. Noreen, "Mixed Convection Peristaltic Flow of Third Order Nanofluid with an Induced Magnetic Field", PLoS ONE, **8**(11), e78770 (2013). https://doi.org/10.1371/journal.pone.0078770

[14] K.M. Prasad, N. Subadra, and M. Srinivas "Study of Peristaltic Motion of Nano Particles of a Micropolar Fluid with Heat and Mass Transfer Effect in an Inclined Tube", in: *International conference on computational heat and mass transfer (ICCHMT) - 2015*, **127**, 694–702 (2015). https://doi.org/10.1016/j.proeng.2015.11.368

[15] N.S. Akbar, and S. Nadeem, "Peristaltic flow of a micropolar fluid with nanoparticles in small intestine", Applied Nanoscience, **3**(6), 461-468 (2013). https://doi.org/10.1007/s13204-012-0160-2

[16] D. Srinivasacharya, M. Mishra, and A.R. Rao, "Peristaltic pumping of a micropolar fluid in a tube" Acta Mechanica, **161**(3-4), 165–178 (2003). https://doi.org/10.1007/s00707-002-0993-y

[17] A.E.H.A.El. Naby, and I.El. Shamy, "Slip effects on peristaltic transport of power-law fluid through an inclined tube", Applied Mathematical Sciences, **1**(60), 2967–2980 (2007).

[18] K. Maruthi Prasad, and G. Radhakrishnamacharya, "Flow of Herschel–Bulkley fluid through an inclined tube of non-uniform cross-section with multiple stenoses", Archives of Mechanics, **60**(2), 161–172 (2008).

ВПЛИВ МАГНІТНОГО ПОЛЯ НА ПЕРИСТАЛЬТИЧНИЙ ТРАНСПОРТ НАНОРІДИНИ З НАПРУЖЕННЯМИ У ПОХИЛІЙ ПОРИСТІЙ ТРУБЦІ
М.П. Молімол[1,2], К. Маруті Прасад[1], Н. Субадра[2]
[1]*Кафедра математики, школа природничих наук, GITAM (Вважається університетом), Хайдерабад, Телангана, Індія -502329*
[2]*Кафедра математики, інженерно-технологічний коледж Гітанджалі, Район Медчал, Хайдерабад, Телангана, Індія -501301*

Це дослідження пропонує теоретичне дослідження перистальтичного транспорту нанорідини з напруженнями під впливом магнітного поля в похилій пористій трубці. З низьким числом Рейнольдса, наближеннями довгих хвиль, використовуються відповідні аналітичні методи для дослідження швидкості рідини, сили тертя, усередненого за часом потоку, явищ наночастинок, перепаду тиску та профілю температури. Досліджено вплив різних фізичних параметрів, включаючи параметр термофорезу, параметр броунівського руху, локальне число Грасгофа для наночастинок та локальне число Грасгофа для температури, на характеристики сили тертя та перепаду тиску. Графіки використовуються для ілюстрації виразів для перепаду тиску, швидкості, явищ, пов'язаних з наночастинками, температурного профілю та сили тертя.
Ключові слова: *параметр термофорезу; перистальтика; параметр броунівського руху; наночастинки; магнітне поле; рідина з парним напруженням; пористе середовище*

PHOTOLUMINESCENCE AND MAGNETIC ENHANCEMENT IN ZnSe QUANTUM DOTS VIA CONTROLLED COBALT DOPING

Thi Diem Bui[1]*, Quang-Liem Nguyen[2], Van Cuong Nguyen[1], Trong Tang Nguyen[1], Huu Phuc Dang[3]*

[1]Faculty of Chemical Engineering, Industrial University of Ho Chi Minh City, Ho Chi Minh City, Vietnam
[2]Institute of Materials Science, Vietnam Academy of Science and Technology, Hanoi, Vietnam
[3]Faculty of Fundamental Science, Industrial University of Ho Chi Minh City, Ho Chi Minh City, Vietnam
*Corresponding Author E-mail: buithidiem@iuh.edu.vn, danghuuphuc@iuh.edu.vn

Co^{2+} ion-doped ZnSe semiconductor quantum dots (QDs) were synthesized in aqueous solution using starch as a surface stabilizer to ensure nanoparticle dispersion. Structural and compositional analyses using X-ray diffraction (XRD) and energy-dispersive X-ray spectroscopy (EDX) confirmed the successful incorporation of Co^{2+} ions into the ZnSe matrix. XRD and UV-visible absorption spectroscopy were used to determine the crystalline structure, lattice parameters, and particle sizes of Co-doped ZnSe QDs. The optical properties were analyzed using absorption and fluorescence spectroscopy, revealing a blue shift in the absorption peak with increasing Co concentration due to quantum confinement effects and changes in particle size. Photoluminescence (PL) analysis revealed dual emission peaks, corresponding to band-to-band recombination and Co-related defect states, with maximum luminescence efficiency observed at the 9% Co doping level. Beyond this concentration, the quenching effects attributed to the Co-Co interactions reduced the fluorescence intensity. Magnetic hysteresis measurements demonstrated that the Co-doped ZnSe QDs exhibited room-temperature ferromagnetism, with saturation magnetization increasing with co-doping concentrations of up to 12%. The ferromagnetic properties were ascribed to the exchange interactions between the Co^{2+} ions and the ZnSe matrix.

Keywords: *ZnSe:Co; Starch surface stabilizer; Cobalt doped; Magnetic properties; Photoluminescence*
PACS: 78.67.Hc, 78.55.-m, 75.50.Pp, 81.05.Dz

1. INTRODUCTION

Scientists have focused their research on semiconductor nanoparticles in recent decades because of their distinct features compared to bulk semiconductors [1, 2, 3, 4]. Scientists have focused their study on the fabrication process and physical and chemical properties of group II-VI semiconductor nanoparticles, which are direct bandgap semiconductors with high quantum efficiency and are suitable for lighting and energy conversion applications [2, 4]. ZnSe quantum dots (QDs) are among the most non-toxic and chemically stable II-VI semiconductors. ZnSe is an n-type, direct bandgap semiconductor with a band gap of ~2.75 eV in bulk material, a Bohr radius of ~ 3.8 nm, and a large exciton binding energy of ~ 21 meV [5]. ZnSe QDs have gained attention as promising nanotechnology materials in recent years. Owing to their significant optical and electrical characteristics [6–8], ZnSe QDs have a wide range of potential applications including light-emitting devices, solar cells, chemical sensors, biomedicine, photocatalysis, and energy storage [9–11].

ZnSe is an effective substrate for doping various contaminants. Transition metals are frequently doped with QDs to produce novel materials with electrical, magnetic, and optical characteristics [13, 14]. QDs doped with metal ions exhibit novel, intriguing, and exceptional features compared to those of undoped semiconductor nanoparticles. Metal-doped quantum dots (QDs) have a wide range of potential applications. This is because the emission of impurity ions frequently results in greater thermal and optical stabilities in many distinct substrates [14]. Quantum dots doped with additional metal ions such as Cr, Fe, Co, Ni, V, Cu, or Mn, contributed to reducing structural defects and improving existing device technologies such as spin-LEDs and magnetic memory. Furthermore, these materials frequently exhibit significantly longer fluorescence lifetimes than undoped semiconductors [15–17]. Despite these advantages, significant questions remain regarding the fabrication method and the material's physical properties. These issues stem from the fact that the fabrication method for doped semiconductor nanostructures is highly complex, making it challenging to obtain good optical and electromagnetic properties within the same material.

In this study, Co^{2+} ions were doped into ZnSe QDs to generate various electronic states in the bandgap, thereby enhancing and broadening the emission band. Furthermore, Co^{2+} ions are highly magnetic substances that improve the magnetic characteristics of materials. The impact of Co^{2+} ions on the structural, optical, and magnetic characteristics of ZnSe QDs was explored.

2. EXPERIENCE
2.1 Materials

Zinc acetate dihydrate ($Zn(CH_3COO)_2 \cdot 2H_2O$), cobalt acetate tetrahydrate ($Co(CH_3COO)_2 \cdot 4H_2O$), sodium hydrogen selenide (NaHSe), starch (as a stabilizer), ammonium hydroxide (NH_4OH), and deionized water were used as starting materials for the synthesis of ZnSe:Co quantum dots (QDs). All reagents were of analytical grade and used without further purification.

2.2 Synthesis ZnSe: Co-Starch *QDs*

Co^{2+}-doped ZnSe quantum dots (QDs) were synthesized using an aqueous chemical precipitation method with starch as a stabilizing agent to prevent nanoparticle aggregation. A 250 mL round-bottom flask was used to mix 15 mL of Zn^{2+} solution with varying volumes of Co^{2+} solution (corresponding to different doping concentrations). To enhance dispersion and control particle growth, 50 mL of 0.1N starch solution and 90 mL of deionized water were added, and the mixture was stirred for 15 minutes to ensure homogeneity. The pH of the solution was carefully adjusted to 10 using 2M NH_4OH, as this pH level was optimized to stabilize metal precursors, prevent $Zn(OH)_2$ precipitation, and reduce defect-related recombination centers. The reaction temperature gradually increased to 70°C, which was identified as the optimal temperature for controlled nucleation and growth of ZnSe:Co QDs. Lower temperatures (<50°C) resulted in incomplete nucleation and polydisperse QDs, whereas higher temperatures (>80°C) led to rapid particle growth, diminishing quantum confinement effects. Once the system stabilized at 70°C, the NaHSe solution was added dropwise, initiating QD formation. The reaction was maintained for 3 hours, as this duration allowed for adequate crystal growth while preserving nanoscale properties. Shorter reaction times (<1 hour) led to defect-rich, underdeveloped QDs with weak fluorescence, while longer reaction times (>5 hours) caused excessive particle aggregation, reducing the quantum confinement effect. Upon completion, the synthesized ZnSe:Co QDs were collected via centrifugation at 10,000 rpm for 15 minutes, followed by multiple washing steps with deionized water and ethanol to remove unreacted precursors and byproducts. The purified QDs were then dried at 60°C under a vacuum for further characterization.
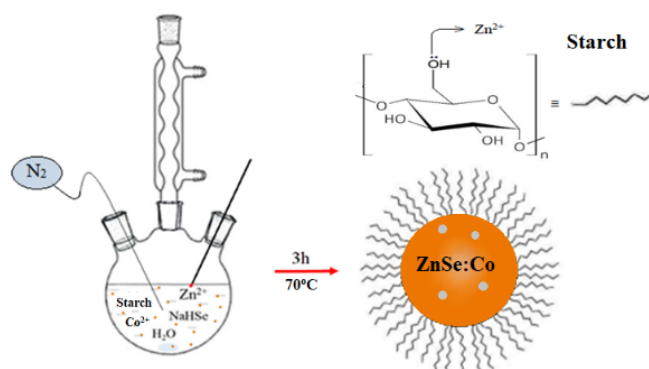
Scheme 1. Synthesis of ZnSe:Co Starch

2.3 Characteristics of ZnSe:Co Starch QDs

Using spectroscopic techniques, the structural, optical, and compositional properties of ZnSe:Co Starch quantum dots were comprehensively analyzed. The crystallographic structure and phase purity of the samples were analyzed using an X-ray diffractometer (XRD) (Bruker D8 Advance, Cu Kα radiation, λ = 0.15406 nm, 40 kV, 40 mA, scan range 20°-80°). The elemental composition and doping efficiency of Co^{2+} in ZnSe QDs were examined using EDX analysis (Oxford Instruments, model X-MaxN, 20 kV accelerating voltage, SEM mode). The optical bandgap and quantum confinement effects were studied using a Shimadzu UV-2600 spectrophotometer (range: 200–800 nm, scan speed: 200 nm/min, quartz cuvette, 1 cm path length). Emission characteristics and defect-related transitions were analyzed using a Fluorescence Spectrometer (Horiba FluoroMax-4, excitation wavelength: 325 nm, emission range: 350–750 nm, slit width: 2 nm). Surface functional groups and interaction between ZnSe QDs and starch stabilizer were identified using FTIR spectroscopy (Bruker Vertex 70, range: 4000–500 cm^{-1}, resolution: 4 cm^{-1}, ATR mode). The oxidation states and chemical environment of Zn, Se, and Co were determined using XPS (Thermo Fisher ESCALAB 250Xi, monochromatic Al Kα source, 1486.6 eV, pass energy: 20 eV for high-resolution scans). Morphology, particle size distribution, and crystallinity were examined using STEM (JEOL JEM-2100F, accelerating voltage: 200 kV, bright-field and dark-field imaging modes). SAED patterns were recorded to confirm the phase purity of the ZnSe:Co QDs. The magnetic properties were analyzed using a Vibrating Sample Magnetometer (VSM, Lakeshore 7404, temperature: 300 K, applied field: ±1.5 T) to measure hysteresis loops and saturation magnetization (M_s).

3.   RESULTS AND DISCUSSION

Figure 1a shows the X-ray diffraction (XRD) patterns of the undoped and Co-doped ZnSe QDs with varying concentrations. Figure 1a shows that all samples exhibit diffraction peaks at 2θ angles of approximately 25.69°, 27.12°, 27.09°, 37.96°, 45.58°, 49.51°, 53.78°, 60.58°, and 69.58°, corresponding to the lattice planes (100), (002), (101), (102), (110), (103), (112), (202), and (203), respectively, corresponding to the hexagonal wurtzite ZnSe structure. The XRD patterns of the obtained samples match those of ZnSe (JCPDS# 15-0105). Notably, no additional peaks corresponding to Co metal or secondary Co-based phases were observed, indicating successful Co incorporation into the ZnSe lattice.

To further examine the crystalline and phase purity, SAED analysis was performed (Figure 1b). The SAED pattern displays a series of concentric diffraction rings, characteristic of nanocrystalline materials. These diffraction rings correspond to the expected lattice planes of wurtzite ZnSe [19, 20], further validating the XRD results. It is important to note that individual ZnSe:Co QDs are single-crystalline, but since multiple QDs are illuminated within the electron

diffraction aperture, the ensemble produces a polycrystalline-like diffraction pattern. This observation does not indicate that the QDs themselves are polycrystalline but rather reflects the diffraction contributions from multiple nanoscale crystallites within the selected area. The combination of XRD and SAED confirms that the ZnSe:Co QDs maintain high crystallinity and phase purity, with Co^{2+} incorporation inducing minimal structural distortion.
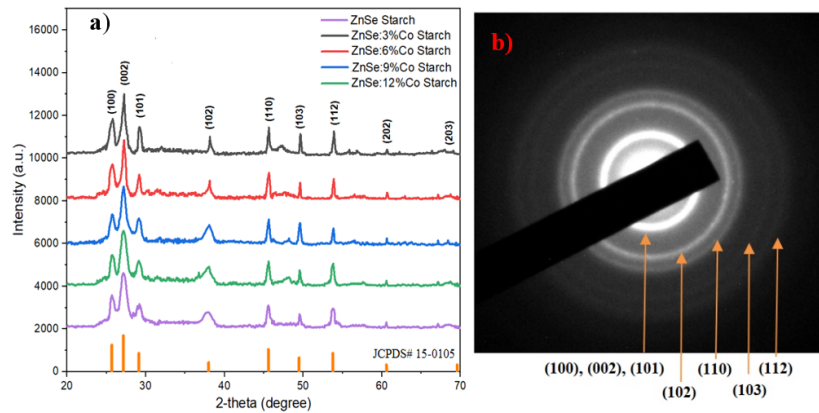
Figure 1. a) The XRD results of ZnSe:Co Starch at 70 °C with various Co^{2+}/Zn^{2+} ratios and b) SEAD of ZnSe:9%Co Starch
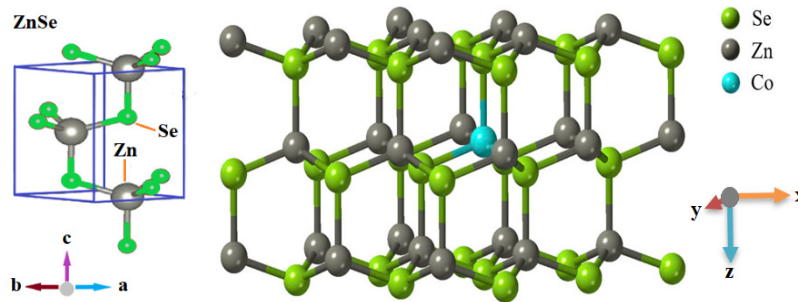
Figure 2. Illustrations of the unit cell and crystal structure of ZnSe.Co.

The ZnSe:Co unit cells and crystal structures are shown in Figure 2. The unit cell of hexagonal ZnSe (Figure 2) and Co-doped ZnSe crystal structure (Figure 2) are best illustrated using the VESTA visualization tool using experimentally determined parameters, which are also shown in Table 1. Equations (1) – (3) [21, 22] were used to compute the lattice parameters a, c, and the cell volume, which are listed in Table 1.

$$d_{hkl} = \frac{K\lambda}{\beta Cos\theta} \tag{1}$$

where d is the average crystallite size, β is the full width at half maximum (FWHM) of the peaks, λ is the well-known X-ray wavelength (0.15406 nm), K is a constant assumed to be 0.9, θ is the angle of Bragg diffraction, and the Miller index of the crystal plane is (hkl).

Using the XRD pattern and Equation (2), the lattice parameters a and c of the hexagonal structure were computed and are listed in Table 1.

$$\frac{1}{d_{hkl}^2} = \frac{4}{3}\left(\frac{h^2 + hk^2 + k^2}{a^2}\right) + \frac{l^2}{c^2} \tag{2}$$

Lattice constants a and c were computed for the (100) and (002) planes, respectively. The volume (V) of the unit cell of the hexagonal system was computed using Equation (3):

$$V = \frac{\sqrt{3}}{2}c.a^2 \tag{3}$$

Table 1. Concentration-dependent average semiconductor nanocrystal size, lattice properties, and unit cell volume

Sample Name	d (nm)	a (Å)	c (Å)	c/a (Å)	Volume, V (Å³)
ZnSe-Starch	7.22	3.995	6.557	1.641	90.61
ZnSe:3%Co Starch	6.72	3.992	6.552	1.641	90.41
ZnSe:6%Co Starch	6.33	3.987	6.547	1.642	90.14
ZnSe:9%Co Starch	5.02	3.984	6.545	1.643	89.97
ZnSe:12%Co Starch	4.90	3.986	6.542	1.641	90.00

The parameters that were determined are listed in Table 1. The addition of Co to the ZnSe lattice alters the lattice parameters a and c of the ZnSe.Co QDs. As the concentration of Co increased, the lattice parameters a, c, c/a, and the cell

volume decreased. The results revealed a decrease in the lattice constants (a and c) with increasing Co doping concentration, attributed to the substitution of Zn^{2+} ions (ionic radius: 0.74 Å) with smaller Co^{2+} ions (ionic radius: 0.72 Å). These findings establish a direct relationship between doping concentration and structural modifications in ZnSe QDs, providing valuable insights for tuning their physical properties for specific applications. In addition, the c/a ratio remained consistent with the ideal wurtzite structure, confirming the structural integrity of the ZnSe lattice despite the doping.
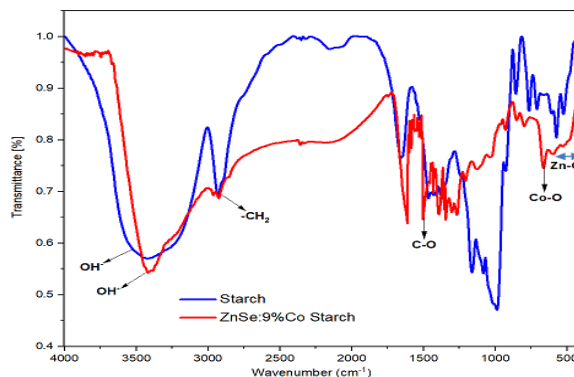
Figure 3. FT-IR spectra of Starch and ZnSe.9%Co Starch QDs

The FT-IR spectra of the starch paste and ZnSe.9%Co Starch sample (Figure 3). This figure shows that the vibration peaks of -OH, C-C, -CH$_2$, and -CO of starch paste still exist, proving that a bond has been formed on the surface between ZnSe crystals and starch paste, and the starch paste was bonded with QDs particles. This increases its capacity to diffuse in water, making it more suitable for biological applications because it is compatible with biological cells [22]. Figure 3 shows that the vibration peaks corresponding to the wavenumber 3405 cm^{-1} are characteristic vibrations of the -O-H bond of starch [25, 26]. The width of the vibration peak is attributed to the formation of hydrogen bonds [25], and the peak at 1650 cm^{-1} is characteristic of the -O-H bond of water adsorbed on the material surface [26]. The 1156 cm^{-1} peak corresponds to the C-O bond of the C-O-H group. The peak at 2895 cm^{-1} corresponds to the asymmetric C-H bond [25]. The peaks that correspond to the wavenumbers at 1020 cm^{-1} and 1417 cm^{-1} are indicative of the C-O bond of the C-O-C and C-C groups in the anhydrous glucose ring, respectively [27,28]. The vibrational peak at 992 cm^{-1} corresponds to the α 1-4 glycosidic (C-O-O) vibration. The Zn-O absorption band at 400 to 600 cm^{-1} is attributed to Zn-O [29–32]. The peak at 671,2 cm^{-1} corresponded to stretching vibrational modes of Co-O in ZnSe.9%Co Starch QDs [33]. The C-C bond was identified by the vibrational peak at 757 cm^{-1}, which corresponds to the wavenumber [25]. Therefore, the -OH, C-C, -CH$_2$, and -CO vibration peaks of the starch paste were still present at the same time, indicating the development of a link between the ZnSe crystals and the starch paste on the surface. This makes them more friendly to biological cells, improves their dispersion in water, and aids beneficial biological applications [22].
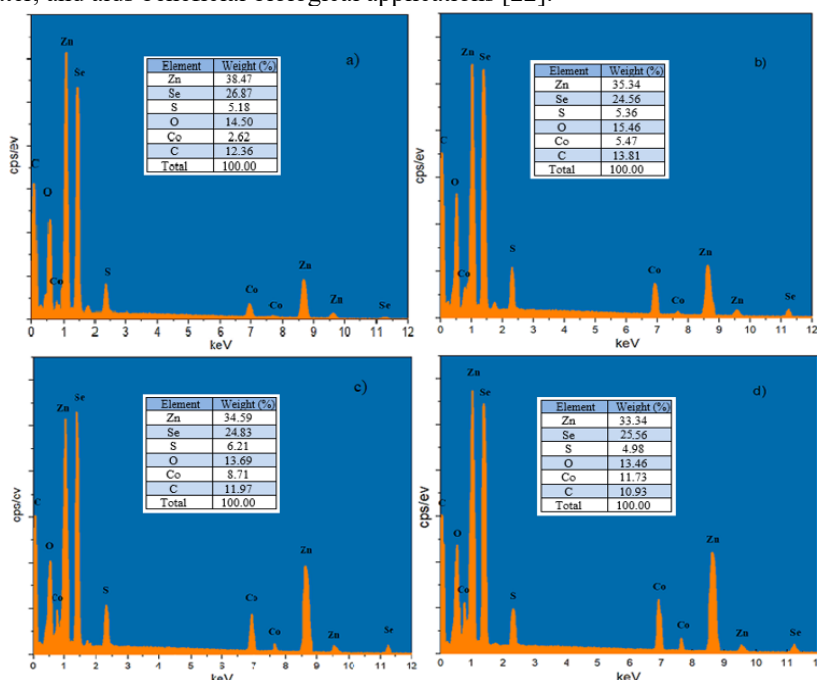
Figure 4. EDX spectra of Co-doped ZnSe QDs with various Co^{2+}/Zn^{2+} ratio:
(a) ZnSe:3%Co Starch, (b) ZnSe:6%Co Starch, (c) ZnSe:9%Co Starch, (d) ZnSe:12%Co Starch

EDX spectroscopy was employed to validate the elemental composition of ZnSe:Co QDs (Figure 4). The spectra (Figure 4a, b, c, d) revealed the presence of Zn, Se, and Co, along with carbon and oxygen from the starch stabilizer. As the Co doping concentration increased, the proportion of Co ions incorporated into the ZnSe matrix correspondingly increased. However, the measured Co/Zn ratio was slightly lower than the theoretical value, suggesting partial loss of Co ions during the synthesis and washing processes. The consistent absence of unexpected elements confirmed the high purity of the synthesized QDs. In addition, an even distribution of elements within the samples was observed, further supporting the successful integration of Co ions into the ZnSe lattice.

Figure 5 shows the energy-dispersive X-ray spectrum (EDS) of ZnSe:Co Starch obtained using scanning transmission electron microscopy (STEM). Zn and Se atoms were found throughout the particles. The presence of Co, O, and C in ZnSe:Co Starch has also been established.
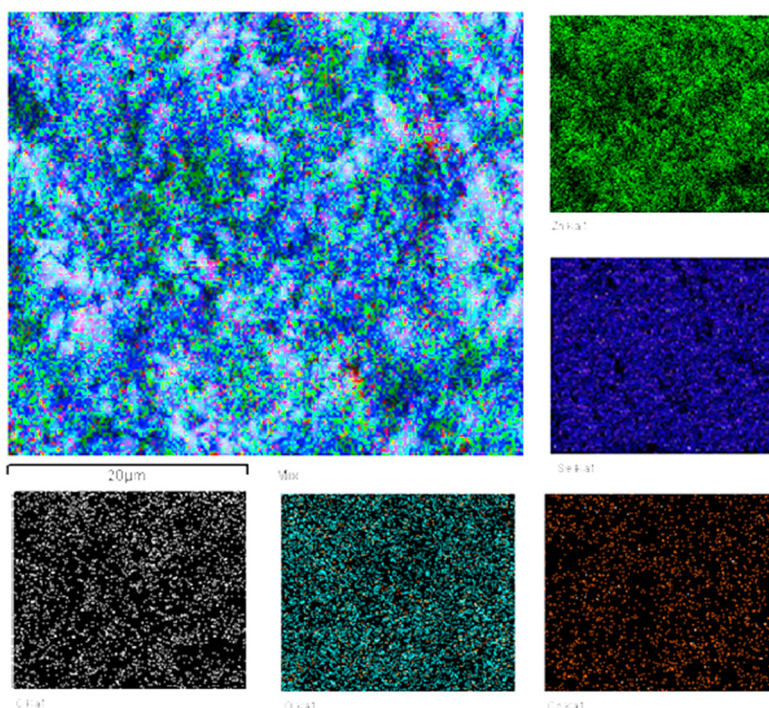
Figure 5. EDS-STEM image of the ZnSe:9%Co Starch particles
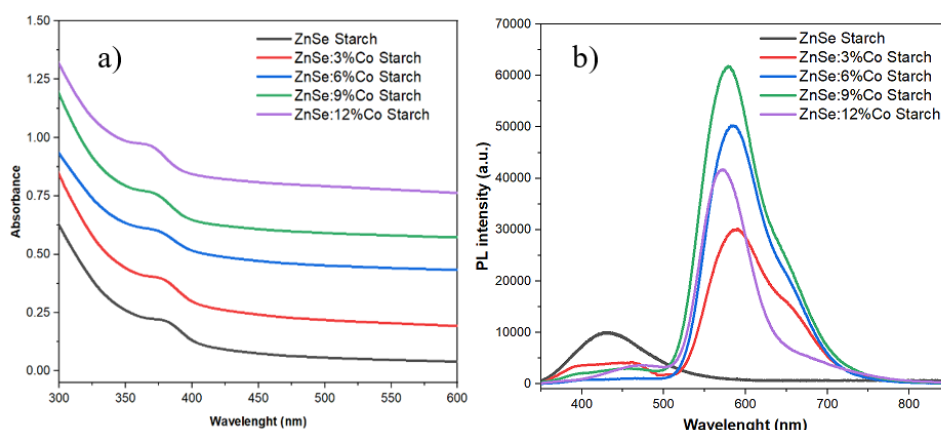
Figure 6. a) Uv-Vis spectrum and b) photoluminescence of ZnSe Starch, ZnSe:
Co Starch (3, 6, 9 and 12%) QDs synthesized at 70°C, pH 10

Figure 6a shows the absorption spectrum of ZnSe:Co Starch QDs. The UV-visible absorption spectra of the ZnSe:Co QDs displayed distinct blue shifts in the excitonic absorption peak with increasing Co^{2+} doping concentration. The initial absorption peak of the undoped ZnSe QDs was observed at 387 nm, corresponding to an energy of 3.16 eV. This energy is significantly higher than that of the bulk ZnSe bandgap (2.75 eV) owing to quantum confinement effects. As the Co doping concentration increased from 3% to 12%, the absorption peak shifted to shorter wavelengths, indicating a decrease in the particle size. This blue shift and reduction in size are consistent with the substitution of Zn^{2+} ions by smaller Co^{2+} ions, which affects the lattice structure and enhances quantum confinement [34,35]. The photoluminescence spectra of the ZnSe:Co QDs (Figure 6b) exhibited two distinct emission peaks: a high-energy peak at approximately 435 nm and a

broad, long-wavelength peak around 579 nm. The high-energy peak corresponds to band-to-band recombination in ZnSe, whereas the broader emission at 579 nm is attributed to defect states and Co-related transitions within the doped lattice. The intensity of the PL emission strongly depended on the Co doping concentration. At lower doping levels (3%), the intensity of the Co-related emission peak is relatively weak, indicating fewer Co-related defect states. As the doping concentration increased to 6% and 9%, the intensity of the long-wavelength emission peak increased significantly, reaching a maximum of 9%. This enhancement is attributed to the increased number of Co^{2+} ions substituting Zn^{2+} ions in the lattice, creating more Co-related defect centers that act as luminescent centers.

However, when the Co doping concentration exceeded 9%, the intensity of the Co-related emission decreased. This quenching effect is likely due to Co-Co interactions, which lead to the formation of nonradiative recombination pathways, reducing the overall fluorescence efficiency. In addition, spin-spin coupling between Co^{2+} ions at higher concentrations may further suppress luminescence. These observations highlight the delicate balance between the doping concentration and optical properties. An optimal doping concentration of 9% achieved the highest luminescence efficiency, making it the most suitable for applications requiring strong emission properties. The results confirm that Co^{2+} doping significantly influences the optical characteristics of ZnSe QDs by modulating the defect states and luminescence behavior of the material.

The presence of Co^{2+} ions in the crystal field of ZnSe resulted in distinct energy levels in the bandgap. Under the effect of the crystal field and spin-orbit interactions, the energy levels are divided into distinct sub-energy levels [36]. This result once again proves that Co^{2+} ions enter the ZnSe matrix and replace the Zn ions. The energy-level diagram of the Co-doped ZnSe QDs is depicted in Scheme 2.
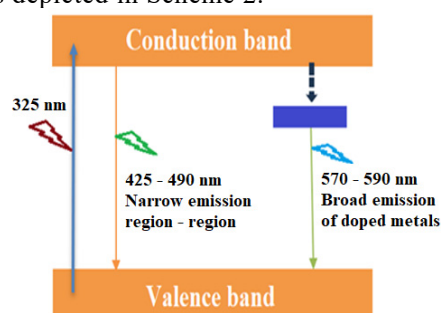
Scheme 2. Energy band diagram and emission mechanisms of Co-doped ZnSe QDs
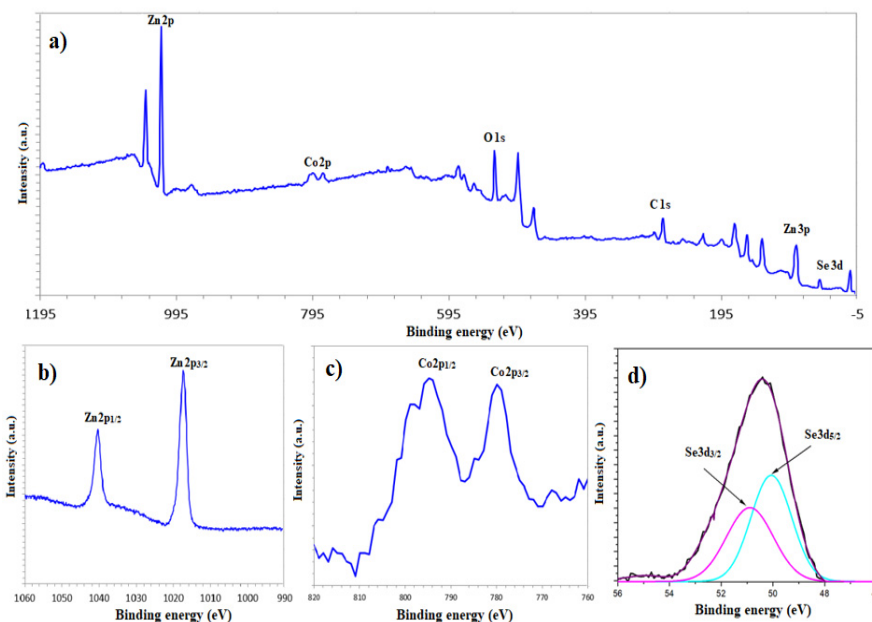
Figure 7. XPS spectrum of ZnSe.9%Co-starch, (b) Zn 2p peak, (c) Co 2p peak, and (d) Se3d peak.

XPS analysis (Figure 7) was employed to determine the elemental composition and chemical states of the ZnSe:Co QDs. The survey spectrum confirms the presence of Zn, Se, Co, O, and C in the doped QDs. High-resolution spectra (Figure 7a) provide further insight into the chemical environment of the elements. The Zn 2p peaks (Figure 7b) were observed at binding energies of 1021.6 eV (Zn $2p_{3/2}$) and 1044.8 eV (Zn $2p_{1/2}$), consistent with Zn in the +2-oxidation state [37–39]. The peak at 527.3 eV corresponds to the binding energy of O 1s. For Co, the Co $2p_{3/2}$ and Co $2p_{1/2}$ peaks (Figure 7c) were observed at 780.1 eV and 795.8 eV, respectively, indicating the presence of Co in the +2 oxidation state [38,39]. Additionally, satellite peaks in the Co 2p region confirmed the high-spin state of the Co^{2+} ions. The Se 3d peaks in Figure 7d can be separated into two overlapping peaks, Se $3d_{5/2}$ and Se $3d_{3/2}$, at binding energies of 50.2 eV and

51.5 eV, respectively, reflecting Se 3d in Zn-Se. The XPS results strongly support the successful doping of Co^{2+} ions into the ZnSe lattice and their interactions with the crystal matrix. These findings align with the structural and optical analyses, reinforcing the multifunctional nature of ZnSe:Co QDs.
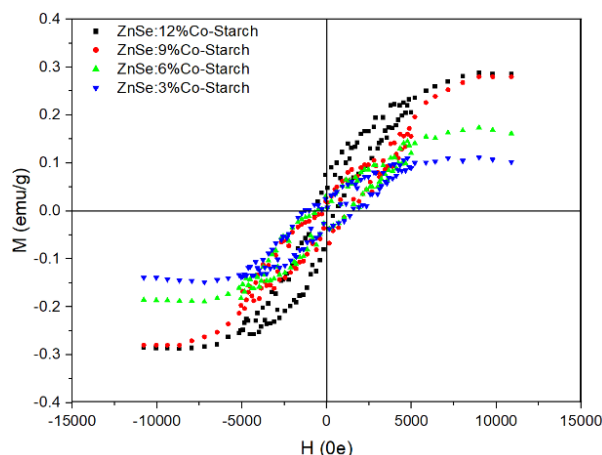
Figure 8. Hysteresis curves of ZnSe.3%Co Starch, ZnSe:6%Co Starch, ZnSe:9%Co Starch, and ZnSe:12%Co Starch QDs

The magnetic properties of the ZnSe:Co QDs were investigated using magnetic hysteresis measurements, which revealed clear evidence of ferromagnetic behavior at room temperature (Figure 8). The saturation magnetization ("Ms") of the Co-doped ZnSe QDs increased with Co^{2+} doping concentration, reaching a maximum value at 12% Co^{2+} doping. Specifically, the Ms values recorded were 0.112, 0.174, 0.280, and 0.288 emu/g for samples with Co^{2+} doping concentrations of 3%, 6%, 9%, and 12%, respectively. The magnetic properties of the Co-doped ZnSe QDs can be explained by the exchange interaction between the Co^{2+} ions and the substrate lattice. The half-filled 3D shell of Co^{2+} can contribute to sp3 bonding and substitute for Zn ions, resulting in local spin in the dilute magnetic semiconductors of the $A_{II}B_{VI}$ group [42]. Co^{2+} in the $A_{II}B_{VI}$ group semiconductor compounds is divalent, resulting in a high-spin configuration d^5.

At lower doping levels, the interaction between the Co^{2+} ions was relatively weak, resulting in moderate magnetization. As the Co^{2+} concentration increased, stronger exchange interactions occurred, which enhanced the overall magnetic moment. However, at higher doping levels, such as 12%, saturation of Ms was observed, indicating a potential limit for the effective incorporation of Co^{2+} ions into the ZnSe lattice. Beyond this concentration, Co clustering or the formation of secondary phases may contribute to changes in magnetic behavior, limiting further increases in magnetization. This demonstrates that Co doping imparts ferromagnetic properties to ZnSe QDs and enables the precise tuning of their magnetic characteristics by controlling the Co^{2+} concentration. The combination of optical and magnetic properties makes Co-doped ZnSe QDs promising candidates for application in spintronics, magnetic memory devices, and multifunctional nanomaterials.

4. CONCLUSIONS

Co-doped ZnSe QDs with molar ratios of Co^{2+}/Zn^{2+} ranging from 3-12% were produced with a wurtzite structure and a size of 5-7 nm. Co-doping of the ZnSe matrix did not modify the matrix structure but diminished the crystal lattice constant and grain size as the Co^{2+} concentration increased. As the Co^{2+} concentration rises, more Co^{2+} ions with a smaller radius (0.72 Å) are substituted for Zn^{2+} ions with a larger radius (0.74 Å) in ZnSe, which results in a decrease in the lattice constant. As the Co concentration rises from 3-12%, the absorption and fluorescence maxima from to 4-16 nm likewise shifted blue owing to the shrinkage of the ZnSe: Co QDs. The PL spectra of the Co-doped ZnSe QDs showed two peaks at short wavelengths (approximately 435 nm) and long wavelengths (approximately 579 nm), corresponding to Co^{2+} concentrations ranging from 3-12%, whereas the emission intensity at short wavelengths decreased and increased. This phenomenon can be explained by the fact that as the concentration of Co^{2+} increased, so did the substitution of Co^{2+} by Zn^{2+}. Co-doped ZnSe QDs are ferromagnetic. The saturation magnetization values of the Co-doped ZnSe QDs at concentrations of 3, 6, 9, and 12% were 0.112, 0.174, 0.280, and 0.288 emu/g, respectively. The magnetism of Co-doped ZnSe QDs is induced by an exchange contact between Co^{2+} ions and the matrix or by Co cluster formation.

Authors' Contributions: Thi-Diem Bui: Methodology, Validation, Project administration. **Van Cuong Nguyen**: Investigation, **Trong Tang Nguyen:** Resources. **Phuc Huu Dang**: Writing, review, and editing. **Quang-Liem Nguyen:** Writing - review & editing,
Availability of data and material Not applicable.
    Declarations
        Ethical Approval Not applicable.
        Consent to Participate Not applicable.
        Consent for Publication: Not applicable.
        Competing Interest: The authors have no competing interest to declare

ORCID

◎**Thi Diem Bui,** https://orcid.org/0000-0003-3668-1496; ◎**Quang-Liem Nguyen,** https://orcid.org/0000-0003-1804-5031
◎**Trong Tang Nguyen,** https://orcid.org/0000-0002-3706-1048; ◎**Huu Phuc Dang,** https://orcid.org/0000-0002-8982-0421

REFERENCES

[1]   S.B. Singh, M.V. Limaye, S.K. Date, *et al*. "Iron substitution in CdSe nanoparticles: Magnetic and optical properties," Phys. Rev. B, **80**(23), 235421 (2009). https://doi.org/10.1103/physrevb.80.235421

[2]   H.T. Van, N.D. Vinh, N.X. Ca, *et al*. "Effects of ligand and chemical affinity of S and Se precursors on the shape, structure and optical properties of ternary CdS1−xSex alloy nanocrystals," Mater Lett. **264**, 127387 (2020). https://doi.org/10.1016/j.matlet.2020.127387

[3]   N.X. Ca, H.T. Van, P.V. Do, *et al*. "Influence of precursor ratio and dopant concentration on the structure and optical properties of Cu-doped ZnCdSe-alloyed quantum dots," RSC Adv. **10**(43), 25618–25628 (2020). https://doi.org/10.1039/d0ra04257a

[4]   S. Das, and K.C. Mandal, "Optical downconversion in rare earth (Tb3+ and Yb3+) doped CdS nanocrystals," Mater Lett. **66**(1), 46–49 (2012). https://doi.org/10.1016/j.matlet.2011.08.034

[5]   K. Senthilkumar, T. Kalaivani, S. Kanagesan, *et al*. "Synthesis and characterization studies of ZnSe quantum dots," Journal of Materials Science: Materials in Electronics, **23**(11), 2048–2052 (2012). https://doi.org/10.1007/s10854-012-0701-1

[6]   U.B. Memon, U. Chatterjee, M.N. Gandhi, *et al*. "Synthesis of ZnSe Quantum Dots with Stoichiometric Ratio Difference and Study of its Optoelectronic Property," Procedia Materials Science, **5**, 1027–1033 (2014). https://doi.org/10.1016/j.mspro.2014.07.393

[7]   F. Baum, M.F. da Silva, G. Linden, *et al*. "Growth dynamics of zinc selenide quantum dots: the role of oleic acid concentration and synthesis temperature on driving optical properties," Journal of Nanoparticle Research, **21**(2), 42 (2019). https://doi.org/10.1007/s11051-019-4485-6

[8]   N.R. Vempuluru, H. Kwon, R. Parnapalle, *et al*. "ZnS/ZnSe heterojunction photocatalyst for augmented hydrogen production: Experimental and theoretical insights," Int. J. Hydrogen Energy, 51, 524–539 (2024). https://doi.org/10.1016/j.ijhydene.2023.08.249

[9]   S. Lin, J. Li, C. Pu, *et al*. "Surface and intrinsic contributions to extinction properties of ZnSe quantum dots," Nano Res. **13**(3), 824–831 (2020). https://doi.org/10.1007/s12274-020-2703-2

[10] T. Zahra, M.M. Alanazi, S.D. Alahmari, *et al*. "Hydrothermally synthesized ZnSe@FeSe nanocomposite: A promising candidate for energy storage devices," Int. J. Hydrogen Energy, **59**, 97–106 (2024). https://doi.org/10.1016/j.ijhydene.2024.01.293

[11] M. El-Assar, T.E. Taha, F.E.A. El-Samie, *et al*. "ZnSe-based highly-sensitive SPR biosensor for detection of different cancer cells and urine glucose levels," Opt. Quantum Electron. **55**, 76 (2023). https://doi.org/10.1007/s11082-022-04326-y

[12] N.T. Hien, P.M. Tan, H.T. Van, *et al*. "Photoluminescence properties of Cu-doped CdTeSe alloyed quantum dots versus laser excitation power and temperature," J. Lumin. **218**, 116838 (2020). https://doi.org/10.1016/j.jlumin.2019.116838

[13] N.X. Ca, N.T. Hien, P.N. Loan, *et al*. "Optical and Ferromagnetic Properties of Ni-Doped CdTeSe Quantum Dots," J. Electron. Mater. **48**(4), 2593–2599 (2019). https://doi.org/10.1007/s11664-019-07017-9

[14] N.A. Hamizi, F. Aplop, H.Y. Haw, *et al*. "Tunable optical properties of Mn-doped CdSe quantum dots synthesized via inverse micelle technique," Opt. Mater. Express, **6**(9), 2915 (2016). https://doi.org/10.1364/ome.6.002915

[15] H.T. Van, N.D. Vinh, P.M. Tan, *et al*. "Synthesis and optical properties of tunable dual emission copper doped CdTe1-xSex alloy nanocrystals," Opt. Mater. (Amst). **97**, 109392 (2019). https://doi.org/10.1016/j.optmat.2019.109392

[16] A. Ganguly, and S.S. Nath, "Mn-doped CdS quantum dots as sensitizers in solar cells," Materials Science and Engineering: B, **255**, 114532 (2020). https://doi.org/10.1016/j.mseb.2020.114532

[17] F. Ibraheem, M.A. Mahdy, E.A. Mahmoud, *et al*. "Tuning Paramagnetic effect of Co-Doped CdS diluted magnetic semiconductor quantum dots," J. Alloys Compd. **834**, 155196 (2020). https://doi.org/10.1016/j.jallcom.2020.155196

[18] S. Xiong, B. Xi, C. Wang, *et al*. "Solution-Phase Synthesis and High Photocatalytic Activity of Wurtzite ZnSe Ultrathin Nanobelts: A General Route to 1D Semiconductor Nanostructured Materials." Chemistry – A European Journal, **13**(28), 7926-7932 (2007). https://doi.org/10.1002/chem.200700334

[19] T. Gupta, and R.P. Chauhan, "Structural, morphological, and electrical properties of ZnSe nanostructures: Effects of Zn precursors," Surfaces and Interfaces, **25**, 101196 (2021). https://doi.org/10.1016/j.surfin.2021.101196

[20] R.K. Yadav, and P. Chauhan, "Estimation of lattice strain in Mn-doped ZnO nanoparticles and its effect on structural and optical properties," Indian Journal of Pure & Applied Physics, **57**, 881-890 (2019). https://nopr.niscair.res.in/bitstream/123456789/52775/1/IJPAP%2057%2812%29%20881-890.pdf

[21] R. Khalid, A.N. Alhazaa, and M.A.M. Khan, "Synthesis, characterization and properties of Mn-doped ZnO nanoparticles," Applied Physics A, **124**(8), 536 (2018). https://doi.org/10.1007/s00339-018-1934-5

[22] M.T. Yaraki, M. Tayebi, M. Ahmadieh, *et al*. "Synthesis and optical properties of cysteamine-capped ZnS quantum dots for aflatoxin quantification," J. Alloys Compd. **690**, 749–758 (2017). https://doi.org/10.1016/j.jallcom.2016.08.158

[23] F. Iselau, T.P. Xuan, A. Matic, *et al*. "Competitive adsorption of amylopectin and amylose on cationic nanoparticles: a study on the aggregation mechanism," Soft Matter. **12**(14), 3388–3397 (2016). https://doi.org/10.1039/c6sm00165c

[24] O.S. Oluwafemi, and O.O. Adeyemi, "One-pot room temperature synthesis of biopolymer-capped ZnSe nanoparticles," Mater. Lett. **64**(21), 2310–2313 (2010). https://doi.org/10.1016/j.matlet.2010.07.021

[25] K. Senthilkumar, T. Kalaivani, S. Kanagesan, *et al*. "Low temperature method for synthesis of starch-capped ZnSe nanoparticles and its characterization studies," J. Appl. Phys. 112(11), (2012). https://doi.org/10.1063/1.4767924

[26] M. Grabolle, M. Spieles, V. Lesnyak, *et al*. "Determination of the Fluorescence Quantum Yield of Quantum Dots: Suitable Procedures and Achievable Uncertainties," Anal. Chem. **81**(15), 6285–6294 (2009). https://doi.org/10.1021/ac900308v

[27] N. Soltani, E. Saion, W.M.M. Yunus, *et al*. "Enhancement of visible light photocatalytic activity of ZnS and CdS nanoparticles based on organic and inorganic coating," Appl. Surf. Sci. **290**, 440–447 (2014). https://doi.org/10.1016/j.apsusc.2013.11.104

[28] I. Elhamdi, H. Souissi, O. Taktak, *et al*. "Experimental and modeling study of ZnO:Ni nanoparticles for near-infrared light emitting diodes," RSC Adv. **12**(21), 13074–13086 (2022). https://doi.org/10.1039/d2ra00452f

[29] A. Sahai, and N. Goswami, "Structural and vibrational properties of ZnO nanoparticles synthesized by the chemical precipitation method," Physica E: Low Dimens. Syst. Nanostruct. **58**, 130–137 (2014). https://doi.org/10.1016/j.physe.2013.12.009

[30] R. Yuvakkumar, J. Suresh, B. Saravanakumar, *et al*. "Rambutan peels promoted biomimetic synthesis of bioinspired zinc oxide nanochains for biomedical applications," Spectrochim Acta A: Mol. Biomol. Spectrosc. **137**, 250–258 (2015). https://doi.org/10.1016/j.saa.2014.08.022

[31] R.F. Silva, and M.E.D. Zaniquelli, "Morphology of nanometric size particulate aluminium-doped zinc oxide films," Colloids Surf. A: Physicochem. Eng. Asp. **198–200**, 551–558 (2002). https://doi.org/10.1016/s0927-7757(01)00959-1

[32] K.M. Gendo, R.F. Bogale, and G. Kenasa, "Green Synthesis, Characterization, and Evaluation of Photocatalytic and Antibacterial Activities of Co₃O₄–ZnO Nanocomposites Using *Calpurnia aurea* Leaf Extract," ACS Omega, **9**(26), 28354–28371 (2024). https://doi.org/10.1021/acsomega.4c01595

[33] L. Liu, L. Yang, Y. Pu, *et al*. "Optical properties of water-soluble Co2+:ZnS semiconductor nanocrystals synthesized by a hydrothermal process," Mater. Lett. **66**(1), 121–124 (2012). https://doi.org/10.1016/j.matlet.2011.08.025

[34] S. Sambasivam, D.P. Joseph, J.G. Lin, *et al*. "Doping induced magnetism in Co–ZnS nanoparticles," J. Solid State Chem. **182**(10), 2598–2601 (2009). https://doi.org/10.1016/j.jssc.2009.07.015

[35] G. Murugadoss, B. Rajamannan, and V. Ramasamy, "Synthesis and Photoluminescence Study Of PVA-Capped ZnS:Mn2+ Nanoparticles, Dig. J. Nanomater. Biostruct. **991**(1–3), 202-206 (2010). https://doi.org/10.1016/j.molstruc.2011.02.026

[36] F. Qiao, R. Kang, Q. Liang, *et al*. "Tunability in the Optical and Electronic Properties of ZnSe Microspheres via Ag and Mn Doping," ACS Omega, 4(7), 12271–12277 (2019). https://doi.org/10.1021/acsomega.9b01539

[37] G.M. Lohar, H.D. Dhaygude, R.A. Patil, *et al*. "Studies of properties of Fe2+ doped ZnSe nano-needles for photoelectrochemical cell application," Journal of Materials Science: Materials in Electronics. **26**(11), 8904–8914 (2015). https://doi.org/10.1007/s10854-015-3572-4

[38] C. Li, H. Zhang, and C. Cheng, "CdS/CdSe co-sensitized 3D SnO ₂ /TiO ₂ sea urchin-like nanotube arrays as an efficient photoanode for photoelectrochemical hydrogen generation," RSC Adv. **6**(44), 37407–37411 (2016). https://doi.org/10.1039/c6ra02176j

[39] S. Laureti, E. Agostinelli, G. Scavia, *et al*. "Effect of oxygen partial pressure on PLD cobalt oxide films," Appl. Surf. Sci. **254**(16), 5111–5115 (2008). https://doi.org/10.1016/j.apsusc.2008.02.055

[40] X. Su, L. Wang, J. Chen, *et al*. "Role of cobalt in ZnO∶Co thin films," J. Phys. D Appl. Phys. **44**(26), 265002 (2011). https://doi.org/10.1088/0022-3727/44/26/265002

[41] N.F. Djaja, D.A. Montja, and R. Saleh, "The Effect of Co Incorporation into ZnO Nanoparticles. Advances in Materials Physics and Chemistry," **03**(01), 33–41 (2013). https://doi.org/10.4236/ampc.2013.31006

ФОТОЛЮМІНЕСЦЕНЦІЯ ТА МАГНІТНЕ ПІДСИЛЕННЯ В КВАНТОВИХ ТОЧКАХ ZnSe ЧЕРЕЗ КЕРОВАНЕ ЛЕГУВАННЯ КОБАЛЬТОМ

Тхі Дьєм Буй[1], Куанг-Лієм Нгуєн[2], Ван Куонг Нгуєн[1], Тронг Танг Нгуєн[1], Хуу Фук Данг[3]
[1]Факультет хімічної інженерії, Індустріальний університет Хошиміна, Хошимін, В'єтнам
[2]Інститут матеріалознавства, В'єтнамська академія наук і технологій, Ханой, В'єтнам
[3]Факультет фундаментальних наук, Індустріальний університет Хошиміна, Хошимін, В'єтнам

Квантові точки (КТ) напівпровідників ZnSe, леговані іонами Co²⁺, були синтезовані у водному розчині з використанням крохмалю як поверхневого стабілізатора для забезпечення дисперсії наночастинок. Структурний та композиційний аналізи з використанням рентгенівської дифракції (XRD) та енергодисперсійної рентгенівської спектроскопії (EDX) підтвердили успішне включення іонів Co2+ у матрицю ZnSe. Для визначення кристалічної структури, параметрів решітки та розмірів частинок квантових точок ZnSe, легованих Co, були використані рентгенівська дифракція та УФ-видима абсорбційна спектроскопія. Оптичні властивості були проаналізовані за допомогою абсорбційної та флуоресцентної спектроскопії, яка виявила зсув піку поглинання до синього кольору зі збільшенням концентрації Co через ефекти квантового обмеження та зміни розміру частинок. Аналіз фотолюмінесценції (PL) виявив подвійні піки випромінювання, що відповідають міжзонній рекомбінації та дефектним станам, пов'язаним з Co, з максимальною ефективністю люмінесценції, що спостерігається при рівні легування 9% Co. Поза цією концентрацією ефекти гасіння, пов'язані з взаємодіями Co-Co, зменшували інтенсивність флуоресценції. Вимірювання магнітного гістерезису показали, що квантові точки ZnSe, леговані Co, демонструють феромагнетизм при кімнатній температурі, при цьому намагніченість насичення зростає з концентрацією легування до 12%. Феромагнітні властивості були приписані обмінним взаємодіям між іонами Co²⁺ та матрицею ZnSe.

Ключові слова: *ZnSe:Co; поверхневий стабілізатор крохмалю; легування кобальтом; магнітні властивості; фотолюмінесценція*

SYNTHESIS OF CdTe QUANTUM DOTS VIA THE MOLECULAR PRECURSOR METHOD AND INVESTIGATION OF THEIR OPTICAL PROPERTIES

Karimberdi E. Onarkulov, **Adkhamjon I. Zokirov***

Fergana State University, Fergana, Uzbekistan
*Corresponding Author e-mail: a.zokirov3001@gmail.com

Cadmium telluride (CdTe) quantum dots (QDs) were synthesizedwere synthesized via a molecular precursor (hot-injection) method and their optical properties were investigated. A cadmium oleate precursor in octadecene/oleic acid was heated to 180 °C under an inert atmosphere, and a trioctylphosphine–tellurium (TOP-Te) solution was swiftly injected to initiate nucleation. By varying the growth time, the QD size was tuned, giving emission colors from green to red. The nanocrystals were characterized by UV–visible absorption and photoluminescence (PL) spectroscopy, which revealed a clear red shift in the optical spectra with increasing particle size. The QDs exhibited size-dependent optical properties consistent with quantum confinement, with the first excitonic absorption peak shifting from approximately 520 nm to 700 nm as the diameter increased. All samples showed high luminescence, with photoluminescence quantum yield (PLQY) values ranging from 60% to 90%. This colloidal synthesis at relatively low temperatures produced colloidally stable QDs with tunable band gaps. These results demonstrate a straightforward route to tailor QD optical properties by controlling the reaction time and provide insights into the growth kinetics and defect states in CdTe QDs.and provide insights into the growth kinetics and defect states in CdTe QDs.

Keywords: *Quantum dot; Cadmium telluride; Molecular precursor; Hot injection; Quantum confinement; Photoluminescence; Absorption; Nanocrystal; Colloidal synthesis; Semiconductor*
PACS: 78.67.Hc, 78.55.Et, 78.30.Fs, 81.07.Ta, 81.16.Be

INTRODUCTION

Quantum dots (QDs) are semiconductor nanocrystals with unique optoelectronic properties that strongly depend on their size [1]. By tuning the particle size, one can tune the absorption and photoluminescence (PL) spectra of QDs – a manifestation of quantum confinement effects [2,3,4]. This size-dependent band gap enables a spectrum of applications in solid-state lighting, display technology, solar cells, and biomedicine [5,6]. Indeed, QDs have been utilized as fluorescent probes in bioimaging, as color converters in LED displays, and as sensitizers in photovoltaic devices, among others [2,3]. The significance of QDs in science and technology was underscored by the awarding of the 2023 Nobel Prize in Chemistry to Ekimov, Brus, and Bawendi for the discovery and synthesis of quantum dots [1]. This achievement highlighted decades of development in colloidal QD synthesis that have led to readily available nanomaterials with high-quality optical properties [9,10].

Colloidal CdTe QDs, in particular, are of great interest as they can emit across the visible spectrum into the near-infrared and have favorable band-gap energies for optoelectronic applications [12,13]. Two of the most common approaches to synthesize CdTe and other II–VI QDs are (1) organometallic (hot-injection) methods in high-boiling organic solvents and (2) aqueous methods with thiol stabilizers [14,15,16]. In a typical organometallic route, a cadmium precursor (e.g., cadmium oleate) in a nonpolar solvent is rapidly injected with a molecular chalcogen source at high temperature, causing burst nucleation followed by nanocrystal growth. This method, introduced in the early 1990s by Murray, Norris and Bawendi, produces nearly monodisperse QDs with excellent crystallinity and optical quality [17]. In contrast, aqueous colloidal synthesis uses water-soluble precursors (e.g., Cd^{2+} salts with NaHTe or TeO_3^{2-} reduced by $NaBH_4$) along with stabilizing thiol ligands such as 3-mercaptopropionic acid (MPA) to obtain QDs at relatively low temperatures (typically 80–100°C) [18]. Both approaches can yield highly luminescent CdTe QDs; however, organometallic methods often produce better size uniformity and higher quantum yields, whereas aqueous methods yield water-dispersible QDs that are more suited for biological applications [19].

The term "molecular precursor method" generally refers to the organometallic hot-injection technique, where a molecular tellurium source (e.g., trioctylphosphine telluride, TOP-Te) is injected into a hot cadmium-containing solution [9]. In this work, we employ the molecular precursor (hot-injection) method to synthesize CdTe QDs at 180 °C, a relatively moderate temperature compared with classical CdSe/CdS syntheses (>300 °C). Our approach emphasizes simplicity and rapid synthesis, allowing us to obtain highly luminescent CdTe QDs within minutes. The emission color can be tuned from green to red by adjusting the reaction time. While similar hot-injection strategies for CdTe have been reported (including the use of single-molecule precursors, such as cadmium diphenylditelluride, in coordinating solvents) [9,20], this study focuses on a straightforward TOP-Te injection into a cadmium oleate solution. We also compare our results with alternative recent techniques; for instance, microwave-assisted aqueous syntheses have achieved tunable emission of thioglycolic acid (TGA)-capped CdTe QDs by varying reaction time and conditions [21]. In this paper, we detail the synthesis of CdTe

QDs via the molecular precursor method, characterize their size-dependent optical properties, and discuss the quantum confinement effects observed.

METHODS

Cadmium oxide (CdO, 99.99%), oleic acid (OA, technical grade, 90%), 1-octadecene (ODE, 90%), and trioctylphosphine (TOP, 90%) were used as received. Tellurium powder (99.999%) was used. All synthesis manipulations were carried out under an inert atmosphere (argon) using standard air-free techniques to prevent oxide formation.

Preparation of precursors: Cadmium oleate, the Cd precursor, was prepared in situ by heating CdO with excess oleic acid in ODE. In a three-neck round-bottom flask, CdO (13 mg, ~0.10 mmol), OA (~0.6 mL, 1.9 mmol), and ODE (10 mL) were combined. The mixture was heated to 120°C under vacuum for 30 min to remove moisture and dissolved gases, then purged with argon. The temperature was then raised to 180 °C, at which point the CdO had completely reacted with OA to form cadmium oleate (yielding a clear solution). Separately, a TOP-Te precursor solution was prepared by reacting Te powder with TOP. Approximately 13 mg of Te (0.10 mmol) was added to 1 mL of TOP in a small flask and heated (under Ar) to ~200 °C until the Te dissolved, yielding a clear amber-colored TOP-Te solution.

Synthesis of CdTe QDs: Once the cadmium oleate solution reached 180 °C, the TOP-Te solution (1 mL) was swiftly injected into the hot Cd-oleate/ODE solution, marking time zero for QD nucleation. The reaction mixture was vigorously stirred and maintained at 180 °C for the duration of nanocrystal growth. Aliquots were withdrawn at specific reaction times (3, 7, 9, and 16 min) to obtain CdTe QD samples. Growth was quenched by rapidly cooling each aliquot to room temperature (e.g., by an ice-water bath). No additional shell was added; the native oleate ligand matrix was relied upon to passivate and stabilize the QD surfaces. The following simplified reaction equations summarize the precursor formation and QD nucleation steps:

$$CdO + 2OA \xrightarrow{180°C} Cd(OA)_2 + H_2O, \tag{1}$$

$$Te(s) + TOP \xrightarrow{200°C} TOP - Te \ (solution), \tag{2}$$
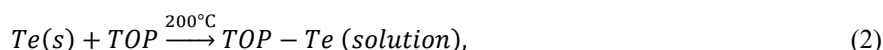
In the above, OA represents oleic acid and TOP-Te denotes trioctylphosphine telluride (a molecular Te complex in solution). Upon injection of TOP-Te into the hot Cd(OA)_2/ODE solution (Equation 2), CdTe nuclei form and then grow as the reaction progresses. During growth, the solution's color visibly changes: initially nearly colorless immediately after nucleation, then pale yellow, orange, and finally dark red as the nanocrystals enlarge – indicating a progressive shift of the absorption edge to longer wavelengths.

After the desired reaction time, the QDs were isolated by a standard purification procedure. Specifically, an aliquot was removed from the hot reaction mixture and mixed with anhydrous ethanol (to induce precipitation of the QDs and remove excess ligands/byproducts), then centrifuged to collect the QD precipitate. The precipitated QDs were redispersed in a nonpolar solvent (hexane or toluene). This precipitation/redispersion wash was repeated twice to yield clean, stable colloidal CdTe QDs capped with oleic acid. All samples were stored in sealed vials under inert gas (argon) in the dark. The molar concentration of each QD dispersion was estimated via the Beer–Lambert law at the first excitonic absorption maximum, c = A/(εl), with $l = 1.00 \ cm$. The size-dependent molar extinction coefficient ε for CdTe QDs was taken from literature; we used the empirical CdTe relation $\varepsilon = 10043D^{2.12} \ (M^{-1} \ cm^{-1})$, where D is the TEM/optically estimated diameter in nm.

Characterization: UV–Vis absorption spectra were collected on a double-beam spectrophotometer with hexane as both solvent and reference. Photoluminescence (PL) spectra were recorded on a fluorescence spectrometer ($\lambda_{exc} = 350 \ nm$; 1 cm quartz cuvettes; room temperature) and are reported without detector-response correction, as our analysis focuses on peak positions and qualitative line shapes. The absorbance and PL intensity scales were verified with a calibrated tungsten lamp and a silicon photodiode, respectively.

PL quantum yields (PLQY) were determined by the relative method using quinine sulfate in 0.1 M H_2SO_4 (literature $\Phi \approx 54\%$) as the standard. The standard and QD dispersions were prepared to have matched absorbance at 350 nm (A ≈ 0.05–0.10) and were measured under identical integration settings. For each sample, PLQY was obtained from the slope of integrated emission vs. absorbance, averaged over three independently prepared dispersions. All optical measurements (absorbance, PL, PLQY) were acquired in triplicate and are reported as mean ± standard deviation.

Colloidal dispersions were also inspected visually under ambient light and 365 nm UV to assess emission color and any qualitative signs of precipitation. Transmission electron microscopy (TEM) and X-ray diffraction (XRD) were used to determine particle size, morphology, and crystal structure. For TEM, a drop of the hexane dispersion was cast onto a carbon-coated copper grid, dried under ambient conditions, and imaged at 200 kV. For XRD, purified QDs were drop-cast onto glass to form a thin film and measured on a powder diffractometer with Cu Kα radiation (λ = 1.5406 Å) over 2θ = 20°–60°; peak positions were compared with reference CdTe patterns to confirm phase identity and estimate crystallite size.

RESULTS

Optical appearance and qualitative emission: Figure 1 is a schematic illustration of the CdTe QD synthesis via the molecular precursor method. After injection and during growth (0–16 min), the solution color evolves from nearly

colorless (immediately after nucleation) to yellow, orange, and finally red, corresponding to increasing QD size and a red-shifting band gap. This color change is apparent in the actual QD samples. Figure 2a shows photographs of vials containing CdTe QD dispersions (in hexane) under normal ambient light for four different reaction durations (from left to right: 3 min, 7 min, 9 min, 16 min). The solution color deepens with longer synthesis time: the 3 min sample is nearly colorless with only a faint yellow tint, while the 16 min sample is visibly reddish-brown. This progression indicates the growth of larger CdTe nanoparticles, since larger QDs have narrower band gaps and thus absorb more lower-energy (visible) light, imparting a stronger color to the solution. Figure 2b presents the same set of samples under ultraviolet illumination (365 nm). A striking rainbow of fluorescence is observed: the shortest reaction (smallest QDs) emits green light, and as the QD size increases, the emission color shifts through yellow and orange to red for the largest QDs. All samples show bright, saturated fluorescence, confirming efficient surface passivation by the oleic acid ligands. The emission colors correspond roughly to the expected PL peak wavelengths for CdTe QDs of these sizes (approximately 520–540 nm for the green-emitting smallest dots, 580–600 nm for medium-sized QDs emitting yellow-orange, and ~640–680 nm for the red-emitting largest dots). These qualitative observations already suggest successful tuning of QD size via reaction time, consistent with quantum confinement theory [18].
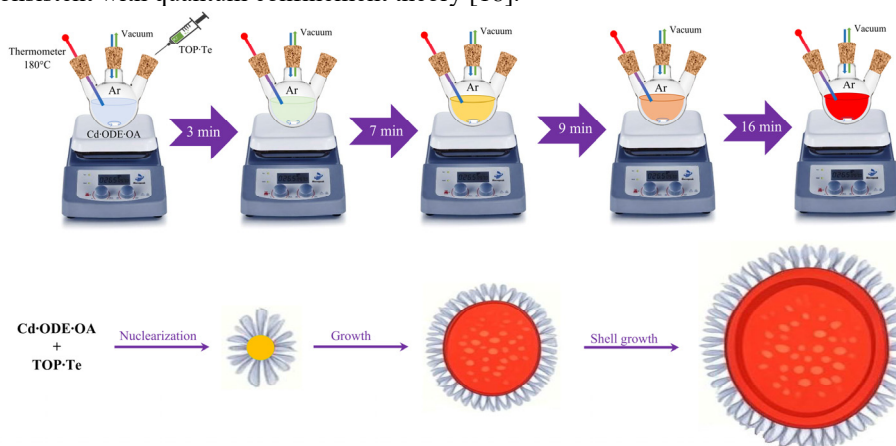
Figure 1. Schematic illustration of the CdTe QD synthesis via the molecular precursor method

a	b

Figure 2. Photographs of CdTe QD samples at various reaction times, showing (a) solution color under ambient light and (b) photoluminescence under 365 nm UV light

UV–Vis absorption spectra: Figure 3 shows the UV–Vis absorption spectra of the CdTe QD samples (dispersed in hexane) for the four different growth times.
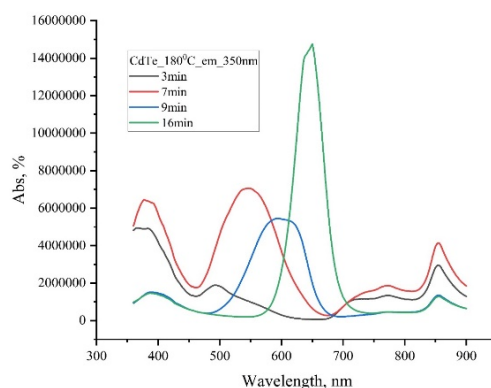
Figure 3. UV–Vis absorption spectra of CdTe QDs (in hexane) grown at 180 °C with different reaction times (black: 3 min; red: 7 min; blue: 9 min; green: 16 min)

All spectra exhibit a distinct first excitonic absorption peak, a hallmark of quantum-confined semiconductor nanocrystals. For the 3 min sample (black curve), the first absorption peak appears around 500–520 nm (in the blue-green

region). With increasing growth time, this peak systematically shifts to longer wavelength: approximately 560 nm for the 7 min sample (red curve), ~620 nm for the 9 min sample (blue curve), and ~700 nm for the 16 min sample (green curve). Concomitantly, the absorption edge (onset of strong absorption) moves from roughly 550 nm (3 min sample) to about 800 nm (16 min sample). This pronounced red-shift of the absorption features clearly indicates an increase in particle size over the reaction interval. Longer reaction times allow the initially formed CdTe nuclei to grow larger, resulting in reduced quantum confinement and thus a smaller effective band gap. The observed absorption peak positions are in good agreement with literature values for CdTe QDs in the ~2–5 nm size range. For instance, the 16 min sample's first exciton peak at ~700 nm is consistent with QDs about 4–5 nm in diameter, whereas the 3 min sample's peak near 500 nm corresponds to very small nanocrystals of around ~2 nm diameter. These size estimates are supported by the qualitative PL colors in Figure 2b and by empirical sizing formulas reported in previous studies [18].

Photoluminescence spectra: Photoluminescence spectra of the same four CdTe QD samples are shown in Figure 4. Under 350 nm UV excitation, the emission maxima exhibit a parallel red-shift with increasing reaction time, mirroring the absorption trend in Figure 3. Specifically, the PL peak moves from ~525 nm for the 3 min QDs to ~580 nm (7 min), ~630 nm (9 min), and ~650–670 nm for the 16 min QDs. Each spectrum consists of a single prominent emission band; we did not observe any secondary long-wavelength emission bands (within the detection limit), indicating an absence of significant trap-state luminescence. The PL full-width at half-maximum (FWHM) for all samples is on the order of 30–50 nm, which is relatively narrow. Such narrow emission peaks suggest a fairly uniform QD size distribution (narrow size polydispersity) and good crystallinity. The Stokes shift (the difference between the absorption peak and PL peak) remains modest (~20–30 nm for these samples), which further indicates effective surface passivation with minimal defect-related Stokes losses. The qualitative brightness observed under UV illumination (Figure 2b) is reflected in the PL spectra intensity; all samples were highly emissive. We note that although we did not perform time-resolved PL measurements, the absence of any low-energy (red/NIR) trap emission in steady-state PL implies that radiative recombination is primarily via band-edge exciton decay. A detailed study of recombination lifetimes (e.g., via time-resolved PL) would be valuable future work to confirm this and to quantify carrier dynamics in these QDs.
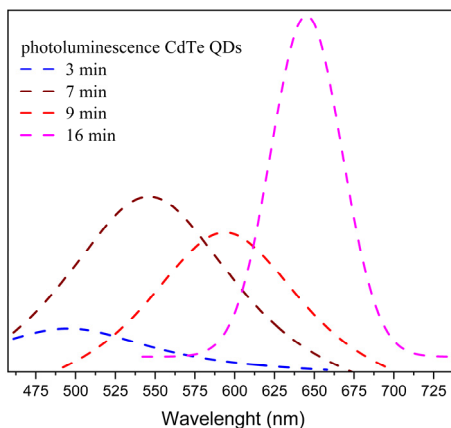
Figure 4. Photoluminescence (PL) spectra of CdTe QDs grown at 180 °C for 3, 7, 9, and 16 min. All samples were measured in hexane at room temperature (excitation: 350 nm).

Photoluminescence quantum yield: In addition to qualitative brightness, we quantitatively evaluated the photoluminescence efficiency of the QDs. PL quantum yield (PLQY) values for all samples, measured relative to a quinine sulfate standard, are summarized in Table 1.

Table 1. Photoluminescence characteristics of CdTe QDs as a function of reaction time.

| Growth time	λ_{em} (nm)	Diameter (nm)	Absorbance A	ε (M⁻¹·cm⁻¹)	Concentration (µM)	PL FWHM (nm)	Stokes shift (nm)	PLQY (%)
3 min	525	2.0	0.045	43.656	1.03	47	25	88.9 ± 2.5
7 min	580	3.5	0.051	142.984	0.36	50	20	63.9 ± 3.1
9 min	630	4.0	0.061	189.771	0.32	53	30	61.9 ± 4.0
16 min	670	5.0	0.043	304.565	0.14	54	20	64.0 ± 3.7

The 3 min CdTe QDs exhibited the highest PLQY, around ~89%. The intermediate-sized QDs (7 min and 9 min samples) showed slightly lower PLQYs (~64% and ~62%, respectively), and the largest QDs (16 min) had a PLQY of ~64%. All samples thus have moderately high quantum yields (exceeding 60%), even without any core/shell structure. The trend of decreasing PLQY with increasing QD size could be due to a greater likelihood of crystalline imperfections or surface defects in the larger nanocrystals, or reabsorption effects in samples with more red-shifted emission. Conversely, the smallest QDs may have fewer nonradiative surface recombination centers relative to their volume, thanks to the strong binding of oleate ligands. Regardless of the exact mechanism, these QY values indicate that the CdTe cores synthesized by this method are of good optical quality. We anticipate that adding an epitaxial shell (e.g., ZnS) around

these cores would further enhance the PLQY and stability, as has been observed in core-shell QD systems; however, this is beyond the scope of the present work.

We quantified the QD number concentration from the UV–Vis spectra using the Beer–Lambert law at the first excitonic peak and a size-dependent extinction coefficient for CdTe QDs. The diameters used in $\varepsilon(D)$ were taken from TEM (and cross-checked against the excitonic peak positions). Table 1 summarizes the results for the 3-, 7-, 9-, and 16-minute samples.

These values ($\approx$0.14–1.03 μM) are typical for colloidal QD dispersions prepared in nonpolar solvents and are sufficiently dilute to minimize inner-filter and reabsorption artifacts during optical measurements.

Growth and reproducibility: Nucleation began almost immediately upon TOP-Te injection, as evidenced by an instantaneous color change to pale yellow. Thereafter, the absorption edge and PL maximum red-shifted progressively with time as the nanocrystals grew. By ~16 min, growth slowed markedly, consistent with precursor depletion and the onset of Ostwald ripening. No secondary nucleation was detected after the initial burst, in line with the classical LaMer mechanism for achieving narrow size distributions. All samples were time-stamped aliquots from a single batch, and their consistent optical trends confirm reproducible, well-controlled growth.

Our results align well with other reports on CdTe QD growth. For example, da Costa et al. (2024) monitored CdTe QD formation in situ. They found that emission peaks shifted from ~550 nm to ~655 nm as reaction time or temperature increased, corresponding to QD diameters growing from ~2 nm (green-emitting) to ~4 nm (red-emitting). This is in excellent agreement with the size progression achieved in our study. Such consistency confirms that the molecular precursor (TOP-Te) method effectively produces CdTe QDs whose size can be tuned predictably by reaction time, similar to the control achieved by adjusting temperature or precursor ratios in other synthesis methods [18].
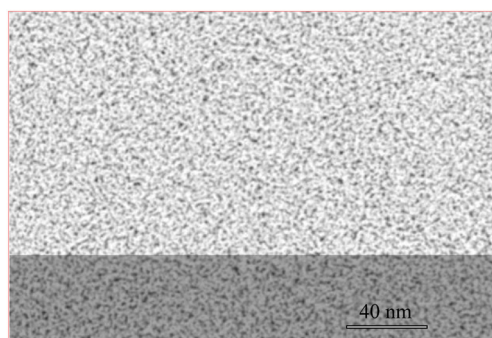
Figure 5. TEM image of the synthesized CdTe QDs (representative sample) showing nearly spherical nanocrystals with an average diameter of ~4 nm (scale bar: 40 nm)
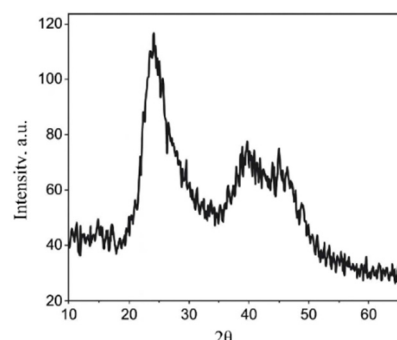
Figure 6. XRD pattern of a purified CdTe QD sample, confirming the crystalline zinc-blende CdTe structure

The above results demonstrate a clear correlation between reaction time, particle size, and optical properties for CdTe QDs synthesized by the molecular precursor (hot-injection) method. Short reaction times yield small QDs that absorb and emit in the blue-green region, whereas longer times produce progressively larger QDs with red-shifted spectra. This behavior is a direct consequence of quantum confinement: smaller nanocrystals confine charge carriers in a tighter volume, raising their kinetic energy and thus increasing the energy of optical transitions [1]. As the CdTe QDs grow, the confinement energy decreases, leading to lower band-gap energies and emission at longer wavelengths (approaching the bulk CdTe band edge of ~820 nm). Our experimental data (Figures 2–4) vividly illustrate this tunability, which is one of the defining advantages of colloidal QDs.

It is worth noting some practical benefits of the synthetic approach we used. The reaction is rapid – within a few minutes, a spectrum of sizes (and colors) can be obtained – and it occurs at 180 °C, which is a relatively low temperature compared to many classic organometallic syntheses of II–VI QDs (often $\geq$300 °C for CdSe or CdS). A lower synthesis temperature simplifies the experimental setup and can reduce unwanted side reactions or precursor degradation. In our case, the moderate temperature was sufficient because TOP-Te is a highly reactive Te source that readily reacts with cadmium oleate even at 180 °C. This is in contrast to some older methods, where, for example, elemental Te would have to be injected into a 300°C solvent, or where cadmium precursors, such as $CdCl_2$, had to be reduced in situ with $NaBH_4$ in an aqueous solution [18]. By using pre-formed Cd–oleate and a molecular Te precursor (TOP-Te), we bypassed the need for an external reducing agent and leveraged the reactivity of organometallic precursors to achieve CdTe formation under milder conditions.

Another advantage of our approach is the monodispersity observed in the QD samples. The relatively narrow absorption peaks (Figure 3) and the vivid, narrow emission bands (Figure 4 and visually in Figure 2b) indicate a uniform QD size distribution for each sample. This can be attributed to the classic hot-injection mechanism, promotes a burst of nucleation followed by focused growth on existing seeds, rather than continuous nucleation. Our observation that no new nucleation occurred after the initial stage (with aliquots taken at later times yielding larger QDs but no significant second population of small QDs) supports the notion of effective Ostwald ripening and growth on seed crystals only [9]. In practice, this means one can simply stop the reaction at a desired time to obtain QDs of a target emission wavelength – a convenient way to tune QD color by controlling reaction duration.

We also briefly compare our results with the aqueous route for CdTe QD synthesis. While not the focus of this study, it is known that aqueous-synthesized CdTe QDs (typically using thiol ligands like MPA) generally require longer reaction times (on the order of hours) to achieve similar emission wavelengths, and often the size distribution is broader than that of hot-injection QDs [1]. However, a key benefit of aqueous QDs is that they are directly obtained as water-soluble colloids. In contrast, the oleic-acid-capped QDs we produced are hydrophobic (soluble only in nonpolar organic solvents). We did not perform a ligand exchange to water in this work, but we acknowledge its importance. In fact, recent studies have shown that microwave-assisted aqueous synthesis can produce CdTe QDs with controlled emission by varying parameters [21], offering a complementary, more environmentally benign approach. Exploring ligand exchange or direct aqueous synthesis for our QDs is an important future direction to extend their applicability.

The optical quality of our CdTe QDs suggests good surface passivation by the oleate ligands. We did not observe any secondary (trap-related) emission peak in PL, and the PL intensity remained stable (with no significant drop) over at least several weeks when the samples were stored under inert conditions in the dark. This implies that as-synthesized QDs have relatively few surface trap states initially, and that the oleic acid capping provides a degree of protection against immediate oxidation or photodegradation. However, we did not carry out comprehensive long-term stability tests or deliberate oxidation/photobleaching experiments. It is likely that exposure to air, moisture, or prolonged UV excitation would eventually lead to oxidation of the QD surface (e.g., forming CdO or TeO_2) and a corresponding decline in optical quality, as is known for many II–VI QDs without additional protective shells. In future work, systematic stability studies (such as monitoring PL intensity and peak position over time under various storage conditions, and performing photobleaching assays under continuous illumination) should be conducted to quantify the long-term colloidal and photostability of these CdTe QDs. Additionally, further improvements in stability and quantum yield could be achieved by overcoating the CdTe cores with a wider-bandgap shell. For example, growing a CdTe/ZnS core–shell structure (as conceptually depicted in Figure 1 after the core formation step) can dramatically enhance the QD's resistance to oxidation and increase QY by confining excitons away from surface defects. Although shell growth was outside the scope of this study, core/shell CdTe QDs are well known to exhibit superior stability and brightness [13].

Theoretical interpretation. The size-dependent spectral shifts we observe are consistent with the effective mass approximation (EMA) for semiconductor nanocrystals. The Brus equation provides a quantitative estimate of the first-exciton energy as a function of radius, capturing quantum-confinement effects. Using literature parameters for CdTe (electron effective mass $\approx 0.096\ m_0$, hole effective mass $\approx 0.60\ m_0$, and the bulk dielectric constant) [18], a 3 nm QD is expected to have a first-exciton energy near 2.4 eV (≈ 515 nm), while a 5 nm QD is expected near 1.9 eV (≈ 653 nm). These estimates agree with the absorption peaks of our smallest and largest samples. More sophisticated models could include surface strain, ligand-field effects, and dielectric screening (which can induce slight red shifts), but the EMA captures the dominant trends in our data.

Overall, our findings confirm that the molecular precursor (hot-injection) method is a powerful technique for producing high-quality CdTe QDs with controllable size. The combination of a rapid injection and proper ligand capping yields nanocrystals whose optical properties can be finely tuned, which is crucial for optimizing QDs for specific applications. In the next section, we summarize the conclusions and also outline some remaining challenges and future directions.

CONCLUSIONS

In summary, we have successfully synthesized CdTe quantum dots using a molecular precursor (TOP-Te) hot-injection method and investigated their optical properties as a function of particle size. By adjusting the growth time from 3 min to 16 min at 180 °C, we obtained a series of QD samples with tunable emission across the visible spectrum (from green to red). UV–Vis and PL spectroscopy confirmed a pronounced red-shift in absorption and emission peaks with increasing QD size, in agreement with quantum confinement theory. The CdTe QDs exhibit narrow excitonic absorption peaks and bright, size-dependent photoluminescence with high quantum yields (up to ~90%), indicating good crystalline quality and effective surface passivation by oleate ligands. These experimental observations were consistent with theoretical expectations (as estimated by the Brus equation) and with literature reports, validating the effectiveness of the relatively mild hot-injection synthesis approach for CdTe.

Direct structural and morphological characterization supported these findings: XRD confirmed the cubic CdTe phase and nanocrystal domain size, and TEM provided direct visualization of particle sizes (~3–5 nm) and their distribution, consistent with optical estimates. A logical next step is time-resolved PL to probe recombination dynamics and to test explicitly for trap-state contributions via exciton lifetimes. We also plan extended stability studies—exposure to air, light, and elevated temperature over longer periods—to assess long-term colloidal stability and resistance to photobleaching. The results will guide strategies such as core–shell encapsulation and optimized ligand treatments to enhance robustness. Finally, translating these QDs into aqueous media is important for specific uses; although we did not pursue ligand exchange here, future work should explore replacing oleate with hydrophilic ligands (or other phase-transfer methods) to yield water-dispersible CdTe QDs. Such surface modifications, together with protective shells, will broaden the applicability of these materials in optoelectronics, biology, and beyond.

ORCID
Karimberdi E. Onarkulov, https://orcid.org/0000-0002-8916-978X; **Adkhamjon I. Zokirov**, https://orcid.org/0000-0003-1651-1115

REFERENCES

[1] K.D. Wegner, and U. Resch-Genger, "The 2023 Nobel Prize in Chemistry: Quantum dots. Analytical and Bioanalytical Chemistry," **416**(14), 3283–3293 (2024). https://doi.org/10.1007/s00216-024-05225-9

[2] W. Li, "Quantum Dots for Biological Imaging," in: *Molecular Imaging. Advanced Topics in Science and Technology in China*, (Springer, Berlin, Heidelberg, 2023), pp. 501–511. https://doi.org/10.1007/978-3-642-34303-2_14

[3] Z. Ren, and J. Zhang, "Applications of fluorescent biosensors based on quantum dots," Highlights in Science, Engineering and Technology, **3**(1), 93-100 (2022). https://doi.org/10.54097/hset.v3i.697

[4] N. Ilaiyaraja, S.J. Fathima, and F. Khanum, "Quantum dots: A novel fluorescent probe for bioimaging and drug delivery applications," in: *Inorganic Frameworks as Smart Nanomedicines*, (William Andrew Publishing, 2018), pp. 529–563. https://doi.org/10.1016/B978-0-12-813661-4.00012-2

[5] E. Fresta, V. Fernández-Luna, P.B. Coto, and R.D. Costa, "Merging biology and solid-state lighting: Recent advances in light-emitting diodes based on biological materials," Advanced Functional Materials, **28**(24), 1707011 (2018). https://doi.org/10.1002/adfm.201707011

[6] J. Chen, H. Ding, and X. Sheng, "Advanced manufacturing of microscale light-emitting diodes and their use in displays and biomedicine," Journal of Information Display, **25**(1), 1–12 (2023). https://doi.org/10.1080/15980316.2023.2248403

[7] M. Green, "The origin and evolution of molecular precursors for quantum dot synthesis," Materials Advances, **5**(18), 7130–7139 (2024). https://doi.org/10.1039/d4ma00352g

[8] Y. Kwon, J. Oh, E.J. Lee, S.H. Lee, A. Agnes, G. Bang, J. Kim, *et al*., "Evolution from unimolecular to colloidal-quantum-dot-like character in chlorine- or zinc-incorporated InP magic-size clusters," Nature Communications, **11**(1), 3127 (2020). https://doi.org/10.1038/s41467-020-16855-9

[9] E. Lee, Y. Kwon, A. Agnes, Y. Ryu, and S. Kim, "Multiple roles of magic-sized clusters in quantum dot synthesis," Journal of Physical Chemistry C, Phys. Chem. C, **128**(4), 1809–1818 (2024). https://doi.org/10.1021/acs.jpcc.3c07189

[10] Y. Wang, B. Si, S. Lu, X. Ma, E. Liu, J. Fan, X. Li, and X. Hu, "Effective improvement in optical properties of colloidal CdTe@ZnS quantum dots synthesized from aqueous solution," Nanotechnology, **27**(36), 365707 (2016). https://doi.org/10.1088/0957-4484/27/36/365707

[11] H.H. Kim, J.-S. Park, I.K. Han, S.O. Won, C. Park, D.K. Hwang, and W.K. Choi, "Emissive CdTe/ZnO/GO quasi-core–shell–shell hybrid quantum dots for white light-emitting diodes," Nanoscale, **8**(47), 19737–19743 (2016). https://doi.org/10.1039/C6NR06314D

[12] X. Zhang, Y. Li, Y. Pan, and Q. Zhao, "Synthesis of water-soluble CdTe quantum dots and its influencing factors," Journal of Functional Materials, **43**(5), 667–670 (2012). https://doi.org/10.3969/j.issn.1004-1656.2012.05.002

[13] X.L. Liao, N. Yang, L.X. Xie, X.C. Yang, and X.P. Yang, "Synthesis and characterization of CdTe quantum dots capped by N-acetyl-L-cysteine," Applied Mechanics and Materials, **275–277**, 1956–1959 (2013). https://doi.org/10.4028/www.scientific.net/AMM.275-277.1956

[14] B. Zhou, F. Yang, X. Zhang, W. Cheng, W. Luo, L. Wang, and W. Jiang, "One-pot aqueous phase synthesis of CdTe and CdTe/ZnS core/shell quantum dots," Journal of Nanoscience and Nanotechnology, **16**(6), 5755–5760 (2016). https://doi.org/10.1166/jnn.2016.11764

[15] C.B. Murray, D.J. Norris, and M.G. Bawendi, "Synthesis and characterization of nearly monodisperse CdE (E = S, Se, Te) semiconductor nanocrystallites," Journal of the American Chemical Society, **115**(19), 8706–8715 (1993). https://doi.org/10.1021/ja00072a025

[16] P.F.G.M. da Costa, L.G. Merízio, N. Wolff, H. Terraschke, and A.S.S. de Camargo, "Real-time monitoring of CdTe quantum dots growth in aqueous solution," Scientific Reports, **14**(1), 1160 (2024). https://doi.org/10.1038/s41598-024-57810-8

[17] Y. Shi, Z. Ma, N. Cui, Y. Liu, X. Hou, W. Du, and L. Liu, "In situ preparation of fluorescent CdTe quantum dots with small thiols and hyperbranched polymers as co-stabilizers," Nanoscale Research Letters, **9**(1), 121 (2014). https://doi.org/10.1186/1556-276X-9-121

[18] M.P. Campos, and J.S. Owen, "Synthesis and surface chemistry of cadmium carboxylate-passivated CdTe nanocrystals from cadmium bis(phenyltellurolate)," Chemistry of Materials, **28**(1), 227–233 (2016). https://doi.org/10.1021/acs.chemmater.5b03914

[19] L. Ding, Z. Peng, W. Sun, T. Liu, Z. Chen, M. Gauthier, and F. Liang, "Microwave synthesis of CdTe/TGA quantum dots and their thermodynamic interaction with bovine serum albumin," Journal of Wuhan University of Technology–Materials Science Edition, **31**(6), 1408–1414 (2016). https://doi.org/10.1007/s11595-016-1546-x

СИНТЕЗ КВАНТОВИХ ТОЧОК CdTe МЕТОДОЮ МОЛЕКУЛЯРНИХ ПОПЕРЕДНИКІВ ТА ДОСЛІДЖЕННЯ ЇХ ОПТИЧНИХ ВЛАСТИВОСТЕЙ

Карімберді Е. Онаркулов, Адхамджон І. Зокіров
Ферганський державний університет, Фергана, Узбекистан

Квантові точки (КТ) телуриду кадмію (CdTe) були синтезовані методом молекулярного прекурсора (гарячої інжекції) та досліджені їхні оптичні властивості. Прекурсор олеату кадмію в октадецені/олеїновій кислоті нагрівали до 180°C в інертній атмосфері, а розчин триоктилфосфіну-телурію (TOP-Te) швидко вводили для ініціювання нуклеації. Змінюючи час росту (3-16 хв), розмір КТ налаштовували, створюючи кольори випромінювання від зеленого до червоного. Нанокристали були охарактеризовані за допомогою УФ-Vis абсорбційної та фотолюмінесцентної (ФЛ) спектроскопії, яка показала чітке червоне зміщення оптичних спектрів зі збільшенням розміру частинок. Квантові точки CdTe демонструють оптичні властивості, що залежать від розміру, що узгоджуються з квантовим обмеженням, причому перший екситонний пік поглинання зміщується від ~520 нм до ~700 нм зі збільшенням діаметра. Всі зразки були високолюмінесцентними, зі значеннями квантового виходу фотолюмінесценції (PLQY) в діапазоні 60–90%. Цей простий синтез при відносно низькій температурі дає колоїдно стабільні квантові точки CdTe з настроюваними забороненими зонами. Результати демонструють простий шлях до налаштування оптичних властивостей квантових точок шляхом контролю часу реакції та дають уявлення про кінетику росту та квантово-розмірні ефекти в квантових точках CdTe.

Ключові слова: *квантова точка; телурид кадмію; молекулярний прекурсор; гаряча інжекція; квантове обмеження; фотолюмінесценція; поглинання; нанокристал; колоїдний синтез; напівпровідник*

EFFECT OF NICKEL DIFFUSION ON TRAP STATES AND INTERFACE QUALITY IN POLYCRYSTALLINE SILICON STRUCTURES

Kanatbay A. Ismailov[1], Nurulla F. Zikrillaev[2], Zoir T. Kenzhaev[1],
Sherzod Z. Ollamberganov[1], Bayrambay K. Ismaylov[1], Alloberdi K. Saparov[1]

[1]Karakalpak State University, Nukus, 230112 Uzbekistan
[2]Tashkent State Technical University, University St., 2; Tashkent 100095, Uzbekistan
*Corresponding Author E-mail: osherzod12121212@gmail.com; E- mail: ismaylovb81@gmail.com
Received July 3, 2025; revised September 13, 2025; accepted September 19, 2025

This work presents a comprehensive Deep-Level Transient Spectroscopy (DLTS) investigation into the influence of nickel (Ni) diffusion on the defect landscape and electronic properties of polycrystalline silicon (poly-Si) structures. The study aims to clarify how Ni incorporation modifies electrically active traps, alters charge carrier dynamics, and affects interface quality in Schottky diodes formed on poly-Si substrates. Two types of samples—undoped and Ni-diffused—were prepared via controlled thermal processing at 1000 °C, followed by surface passivation and gold/aluminum metallization to form Au/Poly-Si/Al Schottky diodes. DLTS measurements over the temperature range 20–300 K revealed distinct differences in the deep-level trap behavior of the two sample types. In undoped samples, only weak and broad trap signals were observed, primarily associated with intrinsic grain boundary defects and residual impurities. In contrast, Ni-diffused samples exhibited sharp, intense DLTS peaks, with a dominant trap level observed between 200 and 220 K. The corresponding activation energy was estimated to be approximately 0.492 eV, and the capture cross-section was in the range of 10^{-14}–10^{-13} cm². These parameters indicate the formation of nickel-related complex defects, such as Ni–V or Ni–O clusters, primarily located at grain boundaries. C–V profiling further confirmed the influence of Ni incorporation, showing reduced capacitance, a smoother transition in the depletion region, and improved interface uniformity, suggesting partial passivation of native and boundary-related traps. The Ni-diffused sample displayed a smoother capacitance–voltage transition, reduced junction capacitance, and improved interface uniformity, suggesting partial passivation of native defects. Complementary G_p–V measurements showed a significant decrease in parallel conductance for Ni-doped structures, indicating a reduction in interface trap density and recombination centers. These results suggest a dual role of nickel - both as a source of deep-level traps and as a passivating agent, depending on local atomic environment and thermal treatment conditions. Surface morphology analysis using Scanning Electron Microscopy (SEM) and Energy-Dispersive X-ray Spectroscopy (EDX) confirmed the formation of Ni-rich precipitates, particularly at grain boundaries. The spatial correlation between Ni and oxygen suggests the formation of Ni–O-based complexes, which likely contribute to the electrical passivation effects observed in DLTS and G_p–V data. Overall, this study demonstrates that controlled Ni diffusion offers a promising approach for defect engineering in polycrystalline semiconductors. By selectively introducing and passivating defect states, Ni doping can enhance the electronic quality and thermal stability of poly-Si, thereby improving its suitability for high-efficiency solar cells, radiation detectors, and other advanced electronic and optoelectronic devices.
Keywords: *Polycrystalline silicon; Nickel clusters; DLTS; Deep-level defects; Schottky diode; Impurity diffusion*
PACS: PACS: 72.20.Jv, 73.61.Cw, 73.40.Ns, 85.30.De.

INTRODUCTION

The advancement of low-cost, large-area silicon-based technologies increasingly depends on effective control of crystalline defects and impurity behavior in polycrystalline silicon (poly-Si). Compared to monocrystalline silicon, poly-Si exhibits a higher density of grain boundaries and intrinsic structural imperfections, which serve as non-radiative recombination centers and negatively impact device performance [1-3].

Among external impurity elements, transition metals such as nickel (Ni) play a dual role in silicon matrices. On one hand, they can passivate intrinsic traps under certain conditions; on the other hand, they may form deep-level trap complexes that deteriorate carrier lifetimes. Notably, nickel's high diffusivity in silicon and its tendency to agglomerate at grain boundaries create favorable conditions for cluster formation, which are often responsible for distinct electronic activity detectable through electrical techniques [4-8]. Deep-Level Transient Spectroscopy (DLTS) is a powerful method for studying electrically active defects. By analyzing the transient capacitance response of Schottky diodes to thermal stimuli, DLTS can determine key trap-state parameters, such as activation energy and capture cross-section. While many studies have examined metal-induced defects in monocrystalline silicon, there is a lack of detailed analysis of Ni-related defect clusters in polycrystalline matrices [9, 10]. This work addresses this gap by exploring the electronic impact of nickel diffusion in polycrystalline silicon using DLTS and Schottky barrier analysis. By establishing clear differences in trap profiles between doped and undoped samples, we provide insights into the defect formation mechanisms and their potential for material optimization.

METHODS

To investigate the electrical activity and microstructural effects of nickel-induced deep-level defects in polycrystalline silicon (poly-Si), a multi-step sample preparation and characterization methodology was employed.

Commercially available polycrystalline silicon wafers with a resistivity of 10^2–10^3 $\Omega\cdot$cm were selected and cut into 5×10 mm² squares using a diamond saw to ensure minimal edge damage and compatibility with standard measurement setups.

Each sample underwent an extensive surface preparation procedure to ensure high measurement accuracy. Mechanical polishing was conducted in stages, starting with coarse SiC papers and progressing to alumina (Al_2O_3) suspensions with particle sizes decreasing from 3 μm to 0.05 μm to produce a smooth, mirror-like surface. After mechanical treatment, samples were ultrasonically cleaned in acetone, isopropanol, and deionized water [10]. A standard RCA cleaning procedure was applied to remove residual organic and metallic contaminants. To eliminate the native oxide layer and activate the surface, a 5% HF solution etch was performed for 30 seconds. The samples were then immediately transferred to the deposition chamber to prevent reoxidation. A thin nickel layer (~50 nm) was deposited on one side of the samples using thermal vacuum evaporation under a base pressure of 5×10^{-4} Torr. The deposition thickness was monitored using a quartz crystal microbalance. Subsequently, the samples were annealed in a nitrogen ambient at 1000°C for 30 minutes in a quartz tube furnace. This thermal treatment enabled the diffusion of nickel atoms into the grain boundaries and defect-rich regions of the poly-Si matrix. The samples were gradually cooled to minimize thermal shock [11]. Post-diffusion, any remaining surface nickel was removed using a chemical etchant composed of nitric acid (HNO_3), acetic acid (CH_3COOH), and hydrofluoric acid (HF) in a volumetric ratio of 5:3:2 for 15 seconds. This step ensured a clean and uniform surface before device fabrication. Schottky diodes were fabricated by depositing circular gold contacts (1 mm in diameter) via thermal evaporation onto the nickel-diffused surface using a shadow mask. The rear side of each sample was coated with aluminum to form an ohmic contact. The devices were annealed at 200°C in a nitrogen atmosphere for 10 minutes to enhance the metal-semiconductor interface properties.

To investigate the microstructural effects of nickel diffusion, surface morphology analysis was performed using Scanning Electron Microscopy (SEM). A Zeiss AURIGA FIB-SEM system was used to acquire high-resolution images of the nickel-diffused silicon surfaces. SEM analysis enabled the direct visualization of surface features such as grain boundaries, diffusion-induced surface texture changes, and possible clustering effects [12]. Images were obtained in both secondary electron (SE) and backscattered electron (BSE) modes to enhance contrast between silicon and nickel-rich regions. These microstructural observations were used to correlate the electrical activity observed in DLTS measurements with the physical manifestation of defect sites and clusters on the polycrystalline surface.

Deep-Level Transient Spectroscopy (DLTS) measurements were conducted over a temperature range of 20–300 K using a stepwise heating protocol. The Schottky diodes were reverse-biased at –5 V, and filling pulses of –2 V amplitude with 1 ms duration were applied. The transient capacitance signal was recorded at multiple rate windows (80 s^{-1}, 200 s^{-1}, 400 s^{-1}, 800 s^{-1}) to resolve traps with different emission time constants. The resulting DLTS spectra were analyzed to extract the activation energy, capture cross-section, and defect concentration corresponding to nickel-related trap states [13-17].

EXPERIMENTAL RESULTS

In this experimental section, we investigate the impact of nickel diffusion into polycrystalline silicon by comparing DLTS and C–V measurements. The measurements were performed on both undoped and Ni-diffused samples using various rate windows (80, 200, 400, and 800 s^{-1}) for DLTS and a voltage sweep from -2 to -5 V for C–V profiling. The goal is to determine the deep-level trap behavior, concentration, and how nickel incorporation affects the electrical quality of the material.

a   b
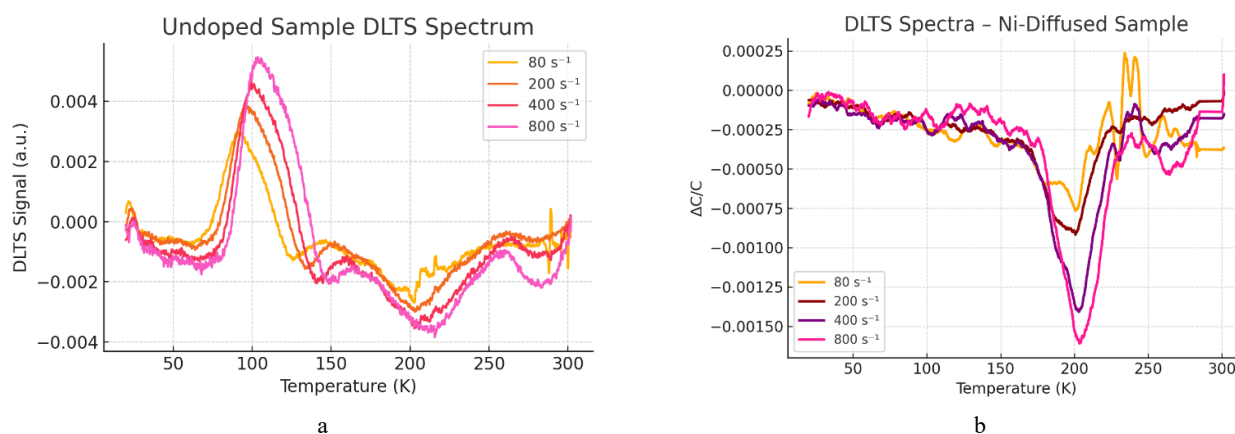
Figure 1. DLTS spectra of polycrystalline silicon samples at different rate windows
(a) undoped sample; (b) sample with Ni-diffused

Undoped sample (Fig. 1a) showing relatively low signal amplitude and broad trap responses across the temperature range, indicating the presence of intrinsic grain boundary and bulk defects; A pronounced peak appears around 110 K, indicating the presence of shallow-level traps likely associated with intrinsic point defects such as

oxygen or carbon complexes. The DLTS signal amplitude increases with rate window, confirming thermally activated emission characteristics. Ni-diffused sample (Fig. 1b) with sharper and deeper peaks, especially between 180–250 K, corresponding to the formation of Ni-related deep-level traps such as Ni–V and Ni–Si complexes. The enhanced signal intensity and shift in peak position reflect changes in trap energy levels and charge emission rates induced by nickel diffusion.

Figures 2a and b illustrate the Arrhenius plots obtained for the undoped and Ni-diffused polycrystalline silicon samples.

a   b
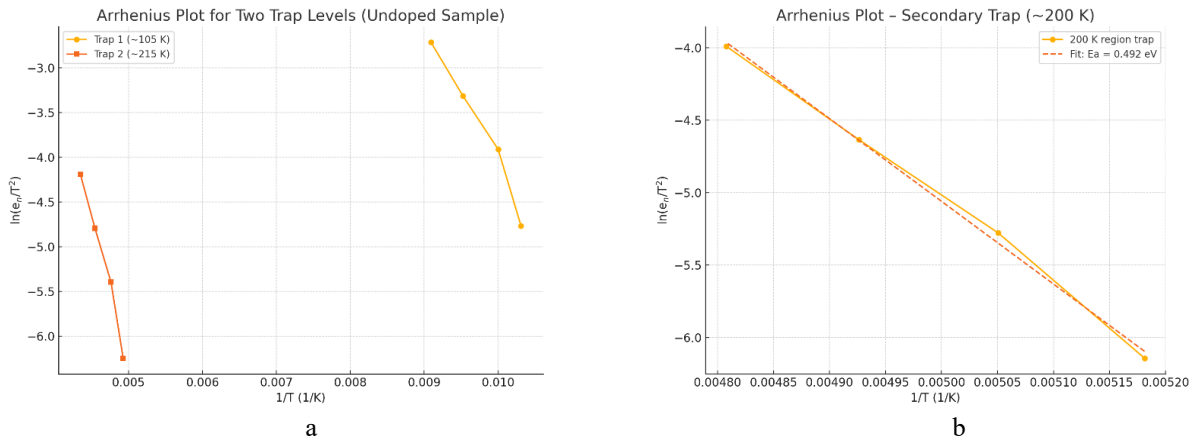
Figure 2. Arrhenius plots for trap level analysis in polycrystalline silicon samples derived from DLTS measurements

The emission rate data were extracted from DLTS spectra over various rate windows and plotted as $\ln(e_n/T^2)$ versus $1/T$ to determine the activation energies of the observed deep-level traps. In the undoped sample (Figure 2a), two distinct trap levels were identified at approximately 105 K and 215 K, corresponding to activation energies of $E_a \approx 0.141$ eV and $E_a \approx 0.275$ eV, respectively. In contrast, the Ni-diffused sample (Figure 2b) showed a dominant single trap around ~200 K, with a significantly higher activation energy of $E_a \approx 0.492$ eV. This increase in energy suggests the formation of new, deeper traps, possibly associated with Ni-related complexes or defect passivation mechanisms.

These findings confirm that Ni diffusion leads to the emergence of deeper trap levels and potentially alters the defect structure of the polycrystalline silicon matrix. [18-19].

c   d
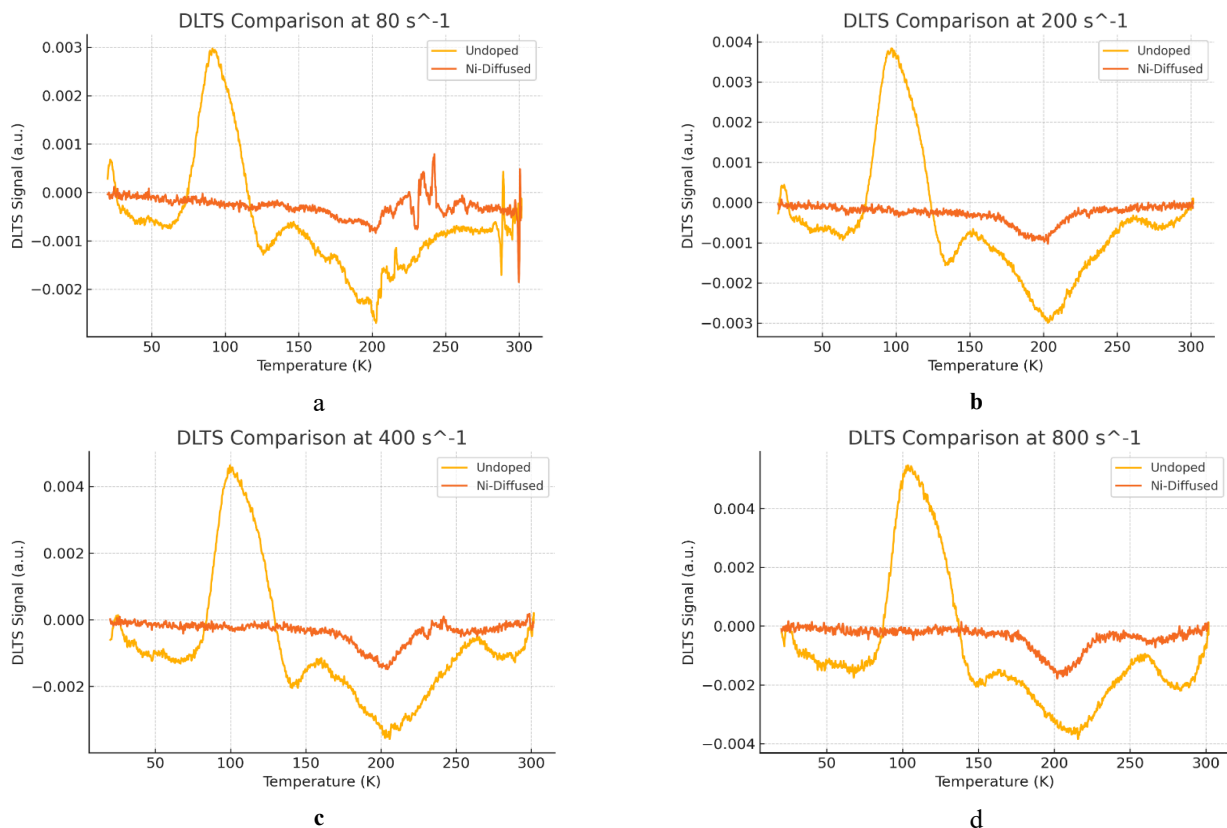
Figure 3. Comparison of DLTS spectra of undoped and Ni-diffused polycrystalline silicon samples at various rate windows
(a) 80 s^{-1}, (b) 200 s^{-1}, (c) 400 s^{-1}, and (d) 800 s^{-1}

In all measurements, the Ni-diffused sample shows significantly deeper and sharper DLTS signals, with multiple peak formations compared to the undoped sample (Fig. 3.). This indicates increased trap concentration and enhanced recombination activity due to the formation of Ni-related deep levels. The undoped sample exhibits broader and shallower responses, consistent with intrinsic grain boundary and bulk defects. The variation in signal intensity and peak position with increasing rate window reflects differences in emission rates and activation energies of the traps.

a   b
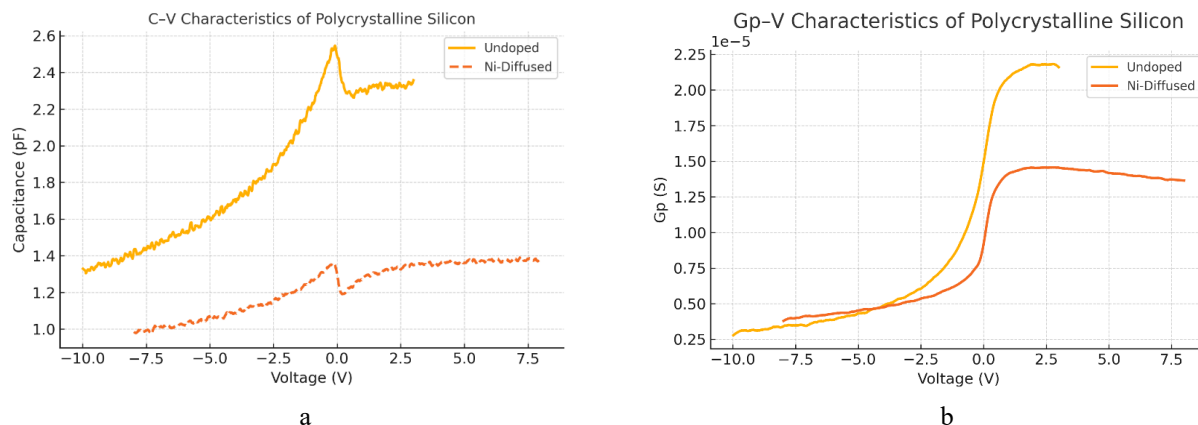
Figure 4. a) Capacitance–Voltage (C–V) characteristics of undoped and Ni-diffused polycrystalline silicon samples.
b) Gp–V characteristics of undoped and Ni-diffused polycrystalline silicon samples.

The undoped sample (Figure 4a) exhibits higher capacitance values and a sharper transition in the depletion region, which may be attributed to a lower defect density and more abrupt junction interface. In contrast, the Ni-diffused sample shows a reduced capacitance with a smoother voltage response, indicating an increased trap concentration and possible passivation of grain boundaries. The shift in capacitance behavior reflects the changes in dopant distribution and interface quality resulting from nickel diffusion. The Ni-diffused sample (Figure 4b) shows a reduced parallel conductance across the voltage range, indicating effective passivation of interface and grain boundary states. In contrast, the undoped sample exhibits higher Gp values, especially in the depletion region, which suggests a greater density of interface traps and enhanced recombination activity. The suppression of Gp in the doped structure confirms that nickel incorporation reduces the density of electrically active defects and improves the junction quality.
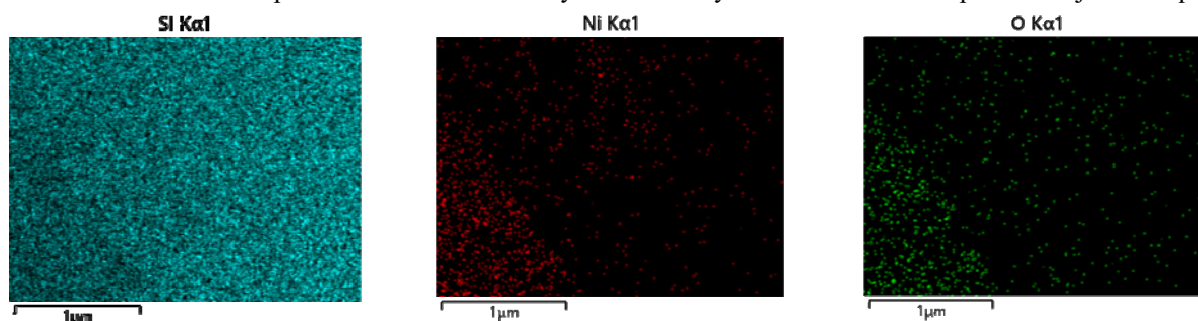
Figure 5. SEM image and EDX elemental maps of the Ni-diffused polycrystalline silicon sample

The Figure 5 left panel shows the surface morphology, while the middle and right panels illustrate the spatial distribution of Ni (red) and O (green), respectively. The overlapping regions of Ni and O signals confirm the formation of Ni–O-based precipitates. These precipitates are believed to contribute to the passivation of electrically active traps, as evidenced by the reduced DLTS signal amplitude, the suppressed $G_p – V$ peak, and the stabilized C–V profile in the Ni-diffused sample.

DISCUSSION

Based on the experimental results obtained through DLTS and C–V profiling, it is evident that the introduction of nickel atoms into polycrystalline silicon significantly modifies the defect landscape and electrical activity within the material. One of the most notable findings is the formation of a pronounced deep-level trap centered at approximately 115 K in Ni-diffused samples, which is absent in undoped specimens. This suggests the creation of specific Ni-related defect complexes, potentially involving interactions at grain boundaries where structural imperfections act as diffusion pathways and clustering sites.

The improved interface characteristics observed in C–V measurements indicate that nickel atoms not only create new trap centers but may also participate in passivating native defects. This dual nature of nickel, acting both as a defect generator and a passivating agent, aligns with previous studies on transition metal doping in silicon-based materials. The smoother capacitance-voltage curves and lower trap density in the Ni-diffused samples support the hypothesis that

nickel can be harnessed to tailor the electronic properties of poly-Si, particularly by forming stable Ni–Si complexes or precipitates that neutralize recombination-active centers [20-24].

Parallel conductance–voltage (G_p–V) measurements further confirmed the presence and partial passivation of interface and grain boundary traps. Compared to undoped samples, the Ni-diffused structures exhibited reduced G_p values across the depletion region, suggesting a lower density of electrically active recombination centers. This suppression is attributed to the interaction of nickel with native defects, likely forming electrically inert Ni–O or Ni–Si complexes.

Additionally, the temperature-dependent suppression of DLTS peak amplitudes across multiple rate windows implies that the trap states in Ni-diffused samples exhibit reduced thermal activity, which can enhance the thermal stability and long-term reliability of devices built on such materials. This behavior is crucial for high-performance applications such as radiation detectors and solar cells operating under fluctuating thermal conditions.

Overall, the findings suggest that controlled nickel diffusion presents a promising avenue for defect engineering in polycrystalline semiconductors, offering a balance between defect introduction and passivation that could be strategically exploited to improve material performance in advanced electronic and optoelectronic systems.

Scanning Electron Microscopy (SEM) images revealed noticeable changes in surface morphology of the Ni-diffused polycrystalline silicon samples. Grain boundary regions became more distinct and slightly rougher, indicating nickel segregation and possible clustering at these structural imperfections. The formation of Ni-rich precipitates observed in SEM supports the electrical activity identified in DLTS measurements.

CONCLUSIONS

This study demonstrated that controlled nickel diffusion improves the electronic quality of polycrystalline silicon by partially passivating grain-boundary-related defects. Capacitance-voltage (C-V) and parallel conductance (Gp-V) measurements revealed a reduced interface trap density and improved junction characteristics. DLTS analysis revealed a significant deep-level trap in the Ni-diffused sample at around 220 K, absent in the undoped structure, indicating the formation of nickel-related defect complexes. SEM and EDX analyses confirmed nickel accumulation and Ni–O clustering at grain boundaries, which are likely responsible for the observed defect passivation. These findings emphasize the dual role of nickel in modifying and stabilizing polycrystalline silicon, offering promising prospects for advanced silicon-based electronic and optoelectronic devices.

ORCID

Kanatbay A. Ismailov, https://orcid.org/0000-0003-2867-0826; **Nurulla F. Zikrillaev,** https://orcid.org/0000-0002-6696-5265; **Zoir T. Kenzhaev,** https://orcid.org/0000-0002-5335-0405; **Sherzod Z. Ollamberganov,** https://orcid.org/0009-0007-2915-9321; **Bayrambay K. Ismaylov,** https://orcid.org/0000-0002-5880-4568; **Alloberdi K. Saparov,** https://orcid.org/0009-0002-3049-5668

REFERENCES

[1] H.P. Hjalmarson, *et al*., Physical Review Letters, **44**(13), 810 (1980). https://doi.org/10.1103/PhysRevLett.44.810

[2] Z. Li, and X. Zang, Journal of Materials Science: Materials in Electronics, **28**(24), 19147 (2017).

[3] Yu.N. Barabanenkov, *et al*., Physics of the Solid State, **54**(6), 1205 (2012). (in Russian)

[4] Z.T. Kenzhaev, Kh.M. Iliev, V.B. Odzhaev, G.Kh. Mavlonov, V.S. Prosolovich, E.Zh. Kosbergenov, B.K. Ismaylov, *et al*., Surface Engineering and Applied Electrochemistry, **60**(6), 851 (2024).

[5] B.K. Ismaylov, N.F. Zikrillayev, Z.T. Kenzhaev, and K.A. Ismailov, Physical Sciences and Technology, **10**(1), 13 (2023). https://doi.org/10.26577/phst.2023.v10.i1.02

[6] Z.T. Kenzhaev, N.F. Zikrillaev, K.S. Ayupov, K.A. Ismailov, S.V. Koveshnikov, and T.B. Ismailov, Surface Engineering and Applied Electrochemistry, **59**(6), 858 (2023).

[7] B.K. Ismaylov, N.F. Zikrillayev, K.A. Ismailov, and Z.T. Kenzhaev, Quantum Electronics & Optoelectronics, **27**(3), 294 (2024). https://doi.org/10.15407/spqeo27.03.294

[8] N. Zikrillayev, Z. Kenzhaev, U. Kurbanova, B. Aliyev, and T. Ismailov, E3s Web of Conferences, **434**, 01036 (2023).

[9] K.A. Ismailov, Z.T. Kenzhaev, S.V. Koveshnikov, E.Zh. Kosbergenov, and B.K. Ismaylov, Physics of the Solid State, **64**(3), 154 (2022). https://doi.org/10.1134/S1063783422040011

[10] Y. Shao, J. Li, D. Yang, and J. Lu, Solar Energy Materials and Solar Cells, **145**, 44 (2016). https://doi.org/10.1016/j.solmat.2015.08.015

[11] Yu.N. Barabanenkov, *et al*., Physics of the Solid State, **54**(6), 1205 (2012).

[12] C.W. Byun, A.M. Reddy, S.W. Son, and S.K. Joo, Electronic Materials Letters, **8**(4), 369 (2012). https://doi.org/10.1007/s13391-012-2112-0

[13] Y. Shao, J. Li, D. Yang, and J. Lu, Solar Energy Materials and Solar Cells, **145**, 44 (2016). https://doi.org/10.1016/j.solmat.2015.08.015

[14] I. Bayrambay, I. Kanatbay, K. Khayratdin, S. Gulbadan, AIP Conference Proceedings, **2552**, 060015 (2022). https://doi.org/10.1063/5.0129486

[15] S. Solmi, M. Bersani, A. Parisini, and G. Ottaviani, Journal of Applied Physics, **94**(8), 4950 (2003). https://doi.org/10.1063/1.1610458

[16] Z.T. Kenzhaev, Kh.M. Iliev, K.A. Ismailov, G.Kh. Mavlonov, S.V. Koveshnikov, B.K. Ismaylov, and S.B. Isamov, Physical Sciences and Technology, **11**(1), 13 (2024). https://doi.org/10.26577/phst2024v11i1a2

[17] K.A. Ismailov, N.F. Zikrillaev, B.K. Ismaylov, Kh. Kamalov, S.B. Isamov, and Z.T. Kenzhaev, J. Nano- Electron. Phys. **16**(5), 05022 (2024). https://doi.org/10.21272/jnep.16(5).05022

[18] J. Lee, H. Park, J. Kim, and Y. Cho, Scientific Reports, **9**, 2354 (2019). https://doi.org/10.1038/s41598-019-39503-9

[19] D.V. Lang, Journal of Applied Physics, **45**(7), 3023 (1974). https://doi.org/10.1063/1.1663719

[20] A.R. Peaker, V.P. Markevich, and J. Coutinho, Journal of Physics D: Applied Physics, **47**(37), 374001 (2014). https://doi.org/10.1088/0022-3727/47/37/374001

[21] D. M. Esbergenov, and S. S. Nasriddinov, Russian Physics Journal, **65**(9), (2022). (in Russian)

[22] B.G. Svensson, and A. Hallén, Journal of Applied Physics, **74**(10), 6521 (1993). https://doi.org/10.1063/1.355052

[23] M. Shiraishi, J.-U. Sachse, H. Lemke, and J. Weber, Materials Science and Engineering B, **58**(1–3), 130 (1999). https://doi.org/10.1016/S0921-5107(98)01052-8

[24] M.K. Bakhadyrkhanov, B.K. Ismaylov, S.A. Tachilin, K.A. Ismailov, and N.F. Zikrillaev, Semiconductor Physics, Quantum Electronics & Optoelectronics, **23**(4), 361 (2020). https://doi.org/10.15407/spqeo23.04.361

ВПЛИВ ДИФУЗІЇ НІКЕЛЮ НА СТАН ПАСТОК ТА ЯКІСТЬ ІНТЕРФЕЙСУ В СТРУКТУРАХ ПОЛІКРИСТАЛІЧНОГО КРЕМНІЮ

Канатбай А. Ісмаїлов[1], Нурулла Ф. Зікріллаєв[2], Зоір Т. Кенжаєв[1], Шерзод З. Олламберганов[1], Байрамбай К. Ісмайлов[1], Аллоберді К. Сапаров[1]

[1]*Каракалпакський державний університет, Нукус, 230112 Узбекистан*

[2]*Ташкентський державний технічний університет, 100095, м. Ташкент, вул. Університетська, 2, Узбекистан*

Ця робота представляє комплексне дослідження глибокорівневої перехідної спектроскопії (DLTS) впливу дифузії нікелю (Ni) на ландшафт дефектів та електронні властивості структур полікристалічного кремнію (poli-Si). Мета дослідження - з'ясувати, як включення Ni модифікує електрично активні пастки, змінює динаміку носіїв заряду та впливає на якість інтерфейсу в діодах Шоткі, сформованих на полі-Si підкладках. Два типи зразків - нелеговані та дифузовані Ni - були отримані шляхом контрольованої термічної обробки при 1000°С, з подальшою пасивацією поверхні та металізацією золотом/алюмінієм для формування діодів Шоткі Au/Poly-Si/Al. Вимірювання DLTS, проведені в діапазоні температур 20–300 K, виявили суттєві відмінності в поведінці глибокорівневих пасток двох типів зразків. У нелегованих зразках спостерігалися лише слабкі та широкі сигнали пасток, в основному пов'язані з власними дефектами на межах зерен та залишковими домішками. На противагу цьому, зразки з дифузією Ni демонстрували різкі та інтенсивні піки DLTS, з домінуючим рівнем пасток, що спостерігався приблизно в межах 200–220 K. Відповідна енергія активації оцінювалася приблизно в 0,492 eB, а поперечний переріз захоплення знаходився в діапазоні 10^{-14}–10^{-13} см². Ці параметри вказують на утворення комплексних дефектів, пов'язаних з нікелем, таких як кластери Ni–V або Ni–O, розташовані переважно на межах зерен. C–V профілювання додатково підтвердило вплив включення Ni, показавши зниження ємності, більш плавний перехід в області виснаження та покращену однорідність інтерфейсу, що свідчить про часткову пасивацію власних та пов'язаних з межами пасток. Зразок з дифузією Ni демонстрував більш плавний перехід ємність-напруга, зниження ємності переходу та покращену однорідність інтерфейсу, що свідчить про часткову пасивацію власних дефектів. Додаткові вимірювання Gp–V показали значне зниження паралельної провідності для структур, легованих Ni, що вказує на зменшення щільності пасток на інтерфейсі та центрів рекомбінації. Ці результати вказують на подвійну роль нікелю — як джерела глибоких пасток, так і пасивуючого агента, залежно від локального атомного середовища та умов термічної обробки. Аналіз морфології поверхні за допомогою скануючої електронної мікроскопії (SEM) та енергодисперсійної рентгенівської спектроскопії (EDX) підтвердив утворення багатих на Ni преципітатів, особливо на межах зерен. Просторова кореляція між Ni та киснем свідчить про утворення комплексів на основі Ni–O, які, ймовірно, сприяють ефектам електричної пасивації, що спостерігаються в даних DLTS та Gp–V. Загалом, це дослідження демонструє, що контрольована дифузія Ni пропонує перспективний підхід до дефектної інженерії в полікристалічних напівпровідниках. Шляхом вибіркового введення та пасивації дефектних станів, легування Ni може покращити електронну якість та термічну стабільність полікремнію, тим самим покращуючи його придатність для високоефективних сонячних елементів, детекторів випромінювання та інших передових електронних та оптоелектронних пристроїв.

Ключові слова: *полікристалічний кремній; нікелеві кластери; DLTS; глибокі дефекти; діод Шоткі; дифузія домішок*

MORPHOLOGY AND ELECTRICAL PROPERTIES OF ITO FILMS OBTAINED ON SILICON SUBSTRATES BY CVD METHOD

A.S. Saidov[1], Sh.N. Usmonov[1], M.U. Khajiev[1,3], A. Kutlimratov[1], T.T. Ishniyazov[1], N.B. Ismatov[2], A.A. Ganiev[3], S.M. Khajieva[4], Kh.N. Juraev[1]*, M. Tagaev[5], D.Sh. Saidov[6], T.A Khudaybergenov[6]

[1]*Physical-Technical Institute of Uzbekistan Academy of Sciences, Chingiz Aytmatov Str. 2B, Tashkent 100084, Uzbekistan*
[2]*Institute of Nuclear Physics of the Academy of Sciences of the Republic of Uzbekistan, Khuroson 1str., Tashkent 100214, Uzbekistan*
[3]*Tashkent State Technical University, University Str. 2, Tashkent 100095, Uzbekistan*
[4]*Tashkent University of Information Technologies, Amir Temur Str., 108, Tashkent 100200, Uzbekistan*
[5]*Karakalpak State University named after Berdak, Nukus 230112, Uzbekistan*
[6]*Urgench Ranch University of Technology, Uzbekistan*
Corresponding Author e-mail: knjuraev@uzsci.net
Received July 7, 2025; revised October 6, 2025; accepted October 14, 2025

ITO films were obtained on silicon substrates using an improved chemical vapor deposition (CVD) method in a quasi-enclosed volume at normal atmospheric pressure, without using a carrier gas. The resulting films had a thickness of 2.8–3.0 microns and a fairly low sheet resistance. Using an SPM 9700HT type scanning probe microscope, the surfaces of 500×500 nm ITO film samples were examined, and the results are presented in the form of two-dimensional (2D) and three-dimensional (3D) images. The electrophysical properties of the grown films were studied by the Hall method and it was shown that the films have an n-type conductivity, a mobility of $\mu \approx 2.5$ cm^2/(V×s) and a concentration of charge carriers n $\approx 1.35 \times 10^{20}$ cm^{-3} and a sheet resistance of $\rho \approx 1.85 \times 10^{-5}$ Ω·sq^{-1} (ohms per square). It is shown that our modified method of chemical vapor deposition makes it possible to obtain ITO films with good characteristics acceptable for use in optoelectronics and photovoltaics devices as a transparent contact layer.
Keywords: *Indium tin oxide; CVD method; Concentration and mobility of carriers; Sheet resistance*
PACS: 68.55.Jk, 73.61.Le, 81.15.Gh, 73.40.Qv, 68.37.Hk

1. INTRODUCTION

ITO (Indy Tin Oxide) thin films attract a lot of attention due to their optical transparency and low resistivity [1, 2]. They are widely used in various optoelectronic devices as transparent electrical contacts or electrodes [3, 4]. For example, they are used in LEDs [5-7], flat-panel displays [8], thin-film solar cells (SC) [9-14], and various sensors [15]. Optoelectronics typically uses transparent conductive thin-film ITO electrodes with a ratio of In$_2$O$_3$:SnO$_2$ = 9:1 (90 wt.% In and 10 wt.% Sn) [16, 17]. They are also used as an anti-reflective wide-band "window" in SC due to their high refractive index (n = 1.97-2.06) and relatively low sheet resistance ($\leq 10^{-2}$–10^{-3} Ω·sq^{-1}). At the same time, ITO contact layers with high charge-carrier mobility and low sheet resistance <10 Ω·sq^{-1} with optical transparency ($\geq$80%) in the visible and near-infrared (IR) ranges make it possible to ensure high efficiency of SC [9-14]. However, due to the growing technological demand for transparent conductive contacts for flat-panel displays with a larger area, as well as for SC and LED structures, new materials with higher electrical and optical properties are required [8, 16], as well as relatively affordable and easy-to-manage technologies for their production [15]. Although ITO films are transparent in the visible range (380-780 nm), their transmission coefficients are low in the near-infrared (IR) range (950-1800 nm). This leads to a decrease in the efficiency of SC in the long-wavelength range of the solar radiation spectrum [9-14]. Therefore, all this requires improving the transparency of ITO films in the near-infrared range to increase the efficiency of SC, as well as the development of relatively inexpensive technological methods for producing ITO films.

To improve transparency while maintaining good electrical conductivity of ITO films, researchers use various methods. Methods for obtaining oxide films with high mobility of charge carriers are presented in [14], and the mechanisms underlying high mobility in oxide films are discussed. Another interesting way to improve the electrical conductivity of oxide films while maintaining their transparency is to create multilayer structures in the form of dielectric/metal/dielectric (ITO/metal/ITO) [6, 17, 18]. Because multilayer films reduce the reflection of light from metal and, due to a sufficiently thin (not strongly affecting transparency) metal layer, provide high electrical conductivity of films [17-19]. In the message [20], polycrystalline ITO films with good optoelectronic characteristics and a homogeneous surface were obtained by chemical deposition from the gas phase (CVD) followed by annealing at a temperature of 550°C in a nitrogen (N$_2$) atmosphere. The use of the CVD process for the synthesis of ITO, as described in this paper, may become an alternative to the method of magnetron deposition of ITO films, which are quite suitable for use in various optoelectronic devices.

2. MATERIALS AND METHODS

There are various methods to obtaining ITO films; for example, in [16, 21, 22] ITO films were obtained by high-frequency reactive sputtering with simultaneous ion treatment. Some researchers prefer to use the sol-gel method to obtain In_2O_3 and SnO_2 films [23, 24]. However, in some cases, the CVD method (chemical vapor deposition) is used to obtain high-purity and high–quality films [25]. In the CVD method, reagents are fed directly to the surface of the substrate, where the vaporized molecules of the substances that make up In_2O_3 and SnO_2 thermally decompose and react to synthesize ITO layers consisting of a mixture of In_2O_3 and SnO_2 on the surface of the substrate. In this case, the decomposition of the reagents occurs at temperatures above 120-140 °C and the ITO deposition process is carried out in air, since the deposition product is an oxide, and the oxygen environment does not interfere with the synthesis of ITO oxide material.

In this paper, to facilitate the control of the ratio of the components of the film composition, we modified the method of chemical vapor deposition (CVD) in such a way that the deposition of ITO layers is carried out under quasi-closed volume conditions, i.e., under atmospheric air and pressure conditions [26]. In short, in this method, the deposition process does not occur in a carrier gas stream but in a quasi-enclosed volume at normal atmospheric pressure, which makes it possible to create a large partial pressure of the components close to the saturation pressure of their vapors for a given temperature [20]. This, on the one hand, makes it possible to increase the growth rate, and on the other hand, to reduce the loss of reagents and increase the percentage of raw materials used. The film growth rate in this method is almost 10 times higher than with conventional technology. Figure 1 shows a block diagram of an upgraded ITO film production facility on various substrates at different temperatures of the evaporator and substrate.

ITO films were deposited on silicon substrates by decomposing vapors of alcohol solutions of indium and tin chlorides in the temperature range of 120-140 °C (evaporator temperature) and at substrate temperatures of ~240-250°C. The technological modes were set by controlling the temperature of the substrate, the evaporators to which solutions of indium and tin chlorides are supplied, as well as the ratio of the solution components and the rate of solution supply. The precursors were alcoholic solutions of indium chloride ($InCl_3$) and tin chloride ($SnCl_2$), which we prepared by separately heating metallic indium (In-99.99) and tin (Sn-99.99) in dilute (1:1) hydrochloric acid (HCl-extra pure). During the deposition of ITO films in our upgraded CVD method, the precursor solution is fed to an evaporator heated to 120-140°C, where indium and tin chlorides evaporate from the evaporator, decompose, and to form indium and tin oxides (In_2O_3 and SnO_2) under the influence of temperature. Which then, continuing to move in the direction of evaporation, are directed towards the substrate, and deposited on it. The properties of ITO films obtained by this method depend mainly on the temperatures of the substrate, and the evaporator.
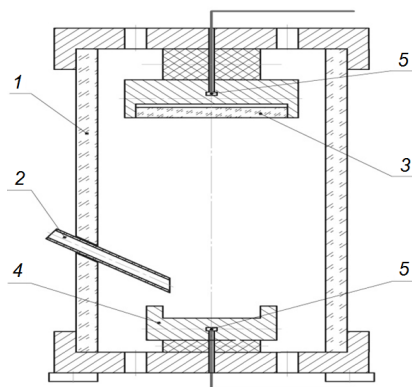
Fig. 1. Block diagram of a CVD reactor for deposition of ITO films on various substrates at different substrate and evaporator temperatures, as well as in different ratios of the In_2O_3:SnO_2 film composition: 1-quartz reactor; 2-tube for supplying reagent solution to the evaporator; 3-substrate; 4-evaporator; 5-thermocouples for controlling the temperature of the substrate and evaporator

3. RESULTS AND DISCUSSIONS

ITO thin films used in many optoelectronic devices are typically less than one micrometer thick. The thicknesses of the ITO films obtained by us, measured on a microinterferometer MII-4 microscope, were 2.8-3.0 μm. We previously demonstrated in [27, 28] that ITO films obtained by the above-described method exhibited a polycrystalline structure with a specific texture. Therefore, we do not present the results of the X-ray diffraction analysis of the obtained ITO layers here.

Studying of the sample surface $0.9In_2O_3$:$0.1SnO_2$ was performed on a scanning probe microscope of the SPM 9700HT type. The measurement was carried out in contact mode, and, for this purpose, a sample area measuring 500×500 nm was selected. Results of the study of the sample surface $0.9In_2O_3$:$0.1SnO_2$ in the form of two-dimensional (2D) and three-dimensional (3D) images are shown in Figs. 2 and 3.

Fig. 2 shows that the film is almost uniform with a small texture (Fig. 3). The sharp peaks of the crystals indicate the nanocrystalline structure of the film. As can be seen from Fig. 3, the heights of the texture peaks are approximately 20-40 nm, but there are also a small number of peaks exceeding 50-60 nm.

Electrophysical parameters of ITO films ($0.9In_2O_3:0.1SnO_2$) were measured by the Hall method (HMS-7000). The results showed that the grown ITO layers have an n-type conductivity with a sheet resistance of $\rho \approx 1.85 \times 10^{-5}$ $\Omega \cdot sq^{-1}$ and a mobility of $\mu \approx 2.5$ $cm^2/(V \times s)$ at a charge carrier concentration of $n \approx 1.35 \times 10^{20}$ cm^{-3}.
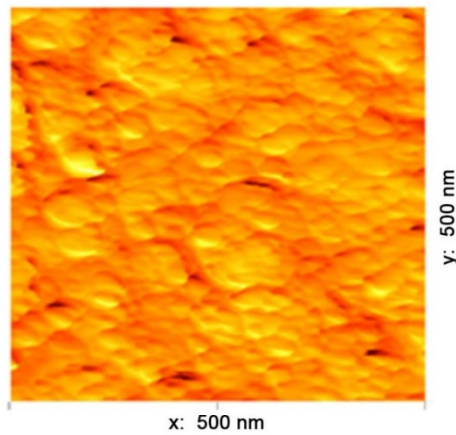
Figure 2. Two-dimensional (2D) image (500×500 nm) of the $0.9In_2O_3:0.1SnO_2$ sample surface, captured using SEM
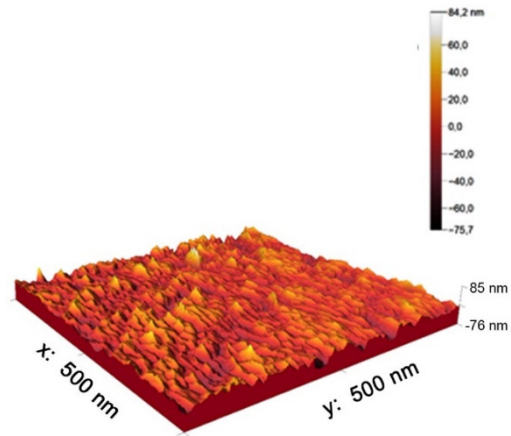
Figure 3. Three-dimensional (3D) image (500×500 nm) of the $0.9In_2O_3:0.1SnO_2$ sample surface, captured using SEM

The temperature dependencies of the concentration (Fig. 4) and mobility (Fig. 5) of charge carriers, as well as the sheet resistance (Fig. 6) of the ITO film obtained at a substrate temperature of 240°C (optimal, determined experimentally), were studied. It can be seen from Fig. 4 that the concentration of charge carriers depends nonmonotonically on temperature and varies almost twice in the temperature range from 300 to 420 K, which in turn leads to a decrease in resistivity by nearly a factor of two (Fig. 6).
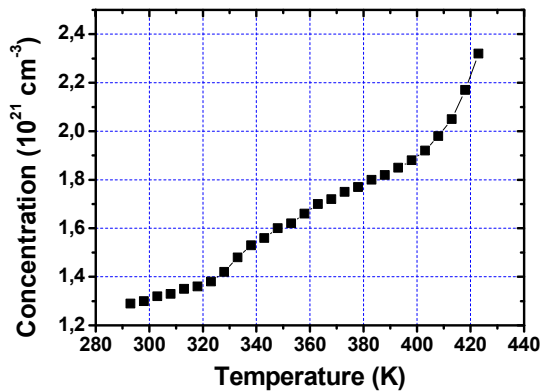
Figure 4. Temperature dependence of the charge carrier concentration in an *n*-ITO ($0.9In_2O_3$):$0.1SnO_2$) film grown on a polycrystalline *p*-Si substrate. (The sample was grown at a substrate temperature of 240°C)
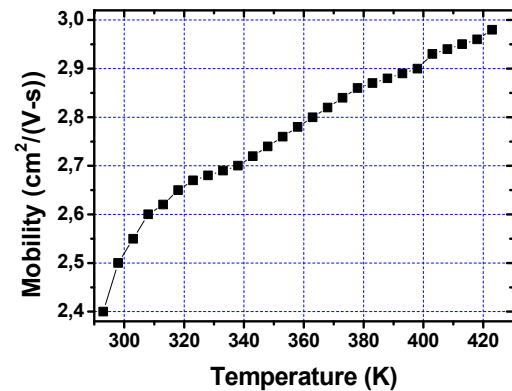
Figure 5. Temperature dependence of the mobility of charge carriers of the *n*-ITO film ($0.9In_2O_3:0.1SnO_2$) grown on a polycrystalline *p*-Si substrate. (The sample was grown at a substrate temperature of 240 °C)
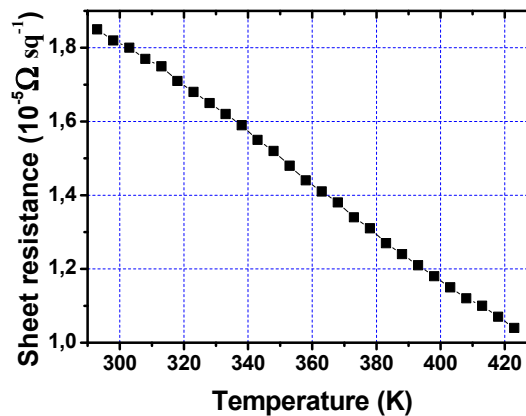
Figure 6. Temperature dependence of the sheet resistance of the *n*-ITO film ($0.9In_2O_3:0.1SnO_2$) grown on a polycrystalline *p*-Si substrate (The sample was grown at a substrate temperature of 240°C)

This indicates that the film exhibits semiconductor properties, as confirmed by studies of the temperature dependence of charge-carrier mobility (Fig. 5). As shown in Fig. 5, the mobility of charge carriers increases non-monotonically with temperature.

In some papers, to improve optical characteristics, specifically to enhance transparency, film oxidation was employed, which the authors considered a diffusion process. In the pre-oxidation experiments conducted in these studies, the film did not have time to oxidize in 30 seconds at a temperature of 550°C and below. The authors of [29] claim that it is possible to achieve film transparency at lower temperatures (200-220°C), but this requires longer annealing times (>60 min). This was also confirmed by the results we obtained, as well as the findings of other studies that varied widely in their annealing regimes. For example, during low-temperature annealing for up to 1000 min at 125-165°C [30] and 30-60 min at 200-300°C [31].

4. CONCLUSIONS

Using the modified CVD method, ITO films with a thickness of ~3.0 μm were obtained on *p*-type silicon substrates, and their structural and electrical properties were investigated. The resulting layers exhibit n-type conductivity and a nanocrystalline structure, with a specific electrical resistance of 1.85×10^{-3} sq^{-1}, making them suitable for use as transparent conductive contact layers in solar cells and LED structures.

The studies conducted in this work have demonstrated that our modified CVD method can produce ITO films at relatively low substrate temperatures (240-250°C), with thicknesses of several micrometers and good properties under normal atmospheric pressure and quasi-enclosed volume conditions. We hope these preliminary results will provide valuable insights and support future research on the synthesis of high-quality ITO films. The composition, structure, and properties of such coatings can be adjusted by varying the evaporator and substrate temperatures, as well as through additional post-application treatments.

ORCID

Amin S. Saidov, https://orcid.org/0000-0002-9124-6430; **Shukrullo N. Usmonov,** https://orcid.org/0000-0001-7683-0017
Mardonbek U. Khajiev, https://orcid.org/0000-0003-0007-8484; **Aleksandr Kutlimratov,** https://orcid.org/0000-0001-6390-7812
Tolmas T. Ishniyazov, https://orcid.org/0000-0001-8518-626X; **Normamat B. Ismatov,** https://orcid.org/0000-0001-5736-3281
Abduvoxid Ganiev, https://orcid.org/0000-0003-1879-1931; **Sevinch M. Khajieva,** https://orcid.org/0009-0005-0614-6638
Khimmatali N. Juraev, https://orcid.org/0000-0001-8963-3848; **Marat Tagaev,** https://orcid.org/0000-0002-1833-8339
Dilmurod Sh. Saidov, https://orcid.org/0009-0001-8269-7782; **Timur A. Khudaybergenov,** https://orcid.org/0000-0002-5958-582X

REFERENCES

[1] G.S. Belo, B.J.P. da Silva, E.A. de Vasconcelos, W.M. de Azevedo, and Jr. E.F. da Silva , "A simplified reactive thermal evaporation method for indium tin oxide electrodes," Appl. Surf. Sci. **255**, 755 (2008.). https://doi.org/10.1016/j.apsusc.2008.07.020

[2] Yu.S. Zhidik, and P.E. Troyan, "Processing technique of reception of electroconducting ITO films of a high optical transparency with low value of per-unit-area resistance," Proceedings of TUSUR University, **26**(2), 169 (2012). https://journal.tusur.ru/en/archive/2-2-2012

[3] X. Guo, X. Liu, F. Lin, H. Li, Y. Fan, and N. Zhang, "Highly Conductive Transparent Organic Electrodes with Multilayer Structures for Rigid and Flexible Optoelectronics," Sci. Rep. **5**, 10569 (2015). https://doi.org/10.1038/srep10569

[4] T. Neubert, F. Neumann, K. Schiffmann, P. Willich, and A. Hangleiter, "Investigations on oxygen diffusion in annealing processes of non-stoichiometric amorphous indium tin oxide thin films," Thin Solid Films, **513**, 319 (2006). https://doi.org/10.1016/j.tsf.2006.02.007

[5] L.K. Markov, I.P. Smirnova, A.S. Pavlyuchenko, E.M. Arakcheeva, and M.M. Kulagina, "Reflecting p-contact based on thin ITO films for AlGaInN flip-chip LEDs," Semicond. **43**, 1521 (2009). https://doi.org/10.1134/S1063782609110219.

[6] A.K. Isiyaku, A.H. Ali, and N. Nayan, "Structural Optical and Electrical Properties of a Transparent Conductive ITO/Al–Ag/ITO Multilayer Contact," Beilstein J. Nanotechnol. **11**, 695 (2020). https://doi.org/10.3762/bjnano.11.57

[7] J. Lewis, S. Grego, B. Chalamala, E. Vick, and D. Temple, "Highly flexible transparent electrodes for organic lightemitting diode-based displays," Appl. Phys. Lett. **85**(16), 3450 (2004). http://apl.aip.org/resource/1/applab/v85/i16/p3450_s1

[8] U. Betz, M.K. Olsson, J. Marthy, J. Escola, and F. Atamny, "Thin films engineering of indium tin oxide: Large area flat panel displays application," Surf. Coat. Technol. **200**, 5751 (2006). https://doi.org/10.1016/j.surfcoat.2005.08.144

[9] K. Dasgupta, S. Bose, A. Mondal, S. Jana, and U. Gangopadhyay, "Fabrication and Mathematical Modelling of a ITO-Al$_2$O$_3$-Si SIS Solar Cell," Silicon, **14**, 11963 (2022). https://doi.org/10.1007/s12633-022-01910-5

[10] W-H. Park, and J. Kim, "Transparent and conductive multi-functional window layer for thin-emitter Si solar cells," Mat. Express, **6**(5), 451–455 (2016). https://doi.org/10.1166/mex.2016.1331

[11] Z. Yu, I. Perera, T. Daeneke, S. Makuta, Y. Tachibana, J.J. Jasieniak, A. Mishra, *et al*., "Indium tin oxide as a semiconductor material in efficient p-type dye-sensitized solar cells," NPG Asia Mater, **8**, e305 (2016). https://doi.org/10.1038/am.2016.89

[12] B. Parida, H.Y. Ji, G.H. Lim, and S. Park, and K. Kim, "Enhanced photocurrent of Si solar cell with the inclusion of a transparent indium tin oxide thin film," J. Renew. Sustain. Energy, **6**(5), 053120 (2014). https://doi.org/10.1063/1.4897656

[13] K. Ryu, Y-J. Lee, M. Ju, H. Choi, B. Kim, J. Lee, W. Oh, *et al*., "Optimal Indium Tin Oxide Layer as Anti Reflection Coating for Crystalline Silicon Solar Cell with Shallow Emitter," Thin Solid Films, **521**, 50 (2012). https://doi.org/10.1016/j.tsf.2012.03.073

[14] S. Calnan, and A.N. Tiwari. "High mobility transparent conducting oxides for thin film solar cells," Thin Solid Films, **518**, 1839-1849 (2010). https://doi.org/10.1016/j.tsf.2009.09.044

[15] N. Vieira, E. Fernandes, A.A.A. De Queiroz, and F.E.G. Guimarães, "Indium tin oxide synthesized by a low cost route as SEGFET pH Sensor," Mater. Res. **16**(5), 1156 (2013). https://doi.org/10.1590/S1516-14392013005000101

[16] A.K. Isiyaku, A.H. Ali, S.G. Abdu, M. Tahan, N.A. Raship, A.S. Bakri, and N. Nayan, "Characterization and Optimization of Transparent and Conductive ITO Films Deposited on n and p-types Silicon Substrates," Phys. Memoir. J. Theor. Appl. Phys. **2**(1), 15 (2020).

[17] D. Shcherbinin, V. Rybin, S. Rudyi, A. Dubavik, S. Cherevkov, Y. Rozhdestvensky, and A. Ivanov, "Charged Hybrid Microstructures in Transparent Thin-Film ITO Traps: Localization and Optical Control," Surfaces, **2023**, 6 133–144. https://doi.org/10.3390/surfaces6020010

[18] M.N. Rezaie, N. Manavizadeh, E.M.N. Abadi, E. Nadimi, and F.A. Boroumand, "Comparison study of transparent RF-sputtered ITO/AZO and ITO/ZnO bilayers for near UV-OLED applications," Appl. Surf. Sci. **392**, 549 (2017). https://doi.org/10.1016/j.apsusc.2016.09.080

[19] I. Crupi, S. Boscarino, G. Torrisi, G. Scapellato, S. Mirabella, G. Piccitto, F. Simone, and A. Terrasi, "Laser irradiation of ZnO:Al/Ag/ZnO:Al multilayers for electrical isolation in thin film photovoltaics," Nanoscale Res. Lett. **8**, 392 (2013). https://doi.org/10.1186/1556-276X-8-392

[20] M.G. Jeffrey, and W.Sh. David, "Deposition of indium tin oxide by atmospheric pressure chemical vapour deposition," Thin Solid Films, **520**, 4110 (2012). http://dx.doi.org/10.1016/j.tsf .2011.04.191

[21] L.P. Amosova, and M.V. Isaev, "Deposition of transparent indium tin oxide electrodes by magnetron sputtering of a metallic target on a cold substrate," Tech. Phys. **59**, 1545 (2014). https://doi.org/10.1134/S1063784214100053

[22] P.N. Krylov, R.M. Zakirova, and V. FedotovaI, "Optical properties of ITO films obtained by high-frequency magnetron sputtering with accompanying ion treatment," Semicond. **47**, 1412 (2013). https://doi.org/10.1134/S1063782613100175

[23] S. Ray, P.S. Gupta, and G. Singh, "Electrical and optical properties of sol-gel prepared Pd-doped SnO_2 thin films: Effect of multiple layers and its use as room temperature methane gas sensor," J. Ovonic Res. **6**(1), 23 (2010).

[24] E. Manea, E. Budianu, M. Purica, C. Podaru, A. Popescu, I. Cernica, F. Babarada, and C.C. Parvulescu, "SnO_2 Thin Films Prepared by Sol Gel Method for "Honeycomb" Textured Silicon Solar Cells," ROMJIST. **10**(1), 25 (2007).

[25] I.G. Atabaev, M.U. Hajiev, and V.A. Pak, "Growth of ITO Films by Modified Chemical Vapor Deposition Method," Inter. J. Thin Films Sci. Techn. **5**(1), 13 (2016). http://dx.doi.org/10.18576/ijtfst/050102

[26] A. Kutlimratov, M.A. Zufarov, R.R. Kabulov, and M.U. Xajiyev, "Structial, Electrophysical, and Optical Properties of ITO Films Produced by the Modified CVD Method," Appl. Solar Energy, **58**(4), 497 (2022). https://doi.org/10.3103/S0003701X22040107

[27] I.G. Atabaev, M.U. Hajiev, V.A. Pak, S.B. Zakirova, and Kh.N. Juraev, "Growth of transparent electrical conducting films of indium and tin oxides by chemical vapor deposition," Appl. Sol. Energy, **52**, 118–121 (2016). https://doi.org/10.3103/S0003701X16020079

[28] T. Neubert, F. Neumann, K. Schiffmann, P. Willich, and A. Hangleiter, "Investigations on oxygen diffusion in annealing processes of non-stoichiometric amorphous indium tin oxide thin films," Thin Solid Films, **513**, 319 (2006). https://doi.org/10.1016/j.tsf.2006.02.007

[29] R.M. Zakirova, "Development of a method for modifying the properties of ITO films by ion-beam treatment during reactive RF magnetron sputtering," D. Sci. Thesis Udmurt State University 2013.

[30] D.C. Paine, T. Whitson, D. Janiac, R. Beresford, C.O. Yang, and B. Lewis, "A study of low temperature crystallization of amorphous thin film indium-tin-oxide," J. Appl. Phys. **85**, 8445 (1999). https://doi.org/10.1063/1.370695

МОРФОЛОГІЯ ТА ЕЛЕКТРИЧНІ ВЛАСТИВОСТІ ПЛІВОК ITO, ОТРИМАНИХ НА КРЕМНІЄВИХ ПІДЛОЖКАХ МЕТОДОМ CVD

А.С. Саідов[1], Ш.Н. Усмонов[1], М.У. Хаджиєв[1,3], А. Кутлімратов[1], Т.Т. Ішніязов[1], Н.Б. Ісматов[2], А.А. Ганієв[3], С.М. Хаджієва[4], Х.Н. Джураєв[1], М. Тагаєв[5], Д.Ш. Саідов[6], Т.А Худайбергенов[6]

[1]Фізико-технічний інститут Академії наук Узбекистану, вул. Чингіза Айтматова 2В, Ташкент 100084, Узбекистан
[2]Інститут ядерної фізики Академії наук Республіки Узбекистан, вул. Хуросон 1, Ташкент 100214, Узбекистан
[3]Ташкентський державний технічний університет, вул. 2, Ташкент 100095, Узбекистан
[4]Ташкентський університет інформаційних технологій, вул. Аміра Темура, 108, Ташкент 100200, Узбекистан
[5]Каракалпакський державний університет імені Бердака, Нукус 230112, Узбекистан
[6]Ургенчський ранчовий технологічний університет, Узбекистан

Плівки ITO були отримані на кремнієвих підкладках за допомогою вдосконаленого методу хімічного осадження з парової фази (CVD) у квазізамкненому об'ємі за нормального атмосферного тиску без використання газу-носія. Отримані плівки мали товщину 2,8–3,0 мікрона та досить низький шаровий опір. За допомогою скануючого зондового мікроскопа типу SPM 9700HT були досліджені поверхні зразків плівок ITO розміром 500×500 нм, а результати представлені у вигляді двовимірних (2D) та тривимірних (3D) зображень. Електрофізичні властивості вирощених плівок досліджували методом Холла, і було показано, що плівки мають n-тип провідності, рухливість $\mu \approx 2,5$ см²/(В×с) та концентрацію носіїв заряду $n \approx 1,35 \times 10^{20}$ см⁻³, а також шаровий опір $\mu \approx 1,85 \times 10^{-5}$ Ом на квадрат. Показано, що наш модифікований метод хімічного осадження з парової фази дозволяє отримувати плівки ITO з хорошими характеристиками, прийнятними для використання в оптоелектроніці та фотоелектричних пристроях як прозорий контактний шар.

Ключові слова: *оксид індію-олова; метод CVD; концентрація та рухливість носіїв; шаровий опір*

PHYSICAL PRINCIPLES OF PHOTOCURRENT GENERATION IN A SILICON-BASED PHOTODIODE STRUCTURE WITH A SCHOTTKY BARRIER

Feruza A. Giyasova[1], Akhmad Z. Rakhmatov[2], Khayot N. Bakhronov[3], Murodjon A. Yuldoshev[4]*,
Farkhod A. Giyasov[1], Abdurauf N. Olimov[5], Nosirbek A. Sattarov[1]

[1]Kimyo International University in Tashkent, Uzbekistan
[2]JSC Photon, Tashkent, Uzbekistan
[3]Tashkent University of Information Technologies named after Muhammad al-Khwarizmi, Uzbekistan
[4]Turan International University, Namangan, Uzbekistan
[5]Institute of Ion-Plasma and Laser Technologies, Uzbekistan Academy of Sciences, 33, Durmon Yuli St., 100125, Tashkent, Uzbekistan
Corresponding Author e-mail: murod.yuldoshev1993@gmail.com
Received September 11, 2025; revised October 17, 2025; accepted October 29, 2025

Homojunction structures of the type Ag–nSi–n$^+$Si–(In+Sn) with perfect single-crystal (111) orientation and a high-resistivity compensated layer at the n$^+$Si/n-Si interface were obtained using the liquid-phase epitaxy method. The results of investigating photogeneration processes and current transport mechanisms in the silicon Schottky-barrier photodiode structure are presented. A two-barrier model of the structure was developed, according to which current transport has a multifactorial nature and is governed by the combined contributions of thermionic emission, tunneling, and generation–recombination processes. Furthermore, it was established that the photosensitivity of the studied structure covers a photon energy range of 0.387÷1.016 eV, shifted toward the long-wavelength region. The formation of a near-surface high-resistivity layer contributes to an increased response and enables photosensitivity values of up to 0.338 A/W. It was found that reducing the barrier capacitance to 8÷10 pF broadens the frequency range and enhances the speed of response. The Ag–nSi–n$^+$Si–(In+Sn) structures are promising for use in photodiodes of optoelectronic devices operating in the visible and infrared spectral regions.
Keywords: *Structure; Homojunction; Characteristic; Index; Mechanism; Capacity; Barrier; Photogeneration; Photosensitivity; Photocurrent; Intensity; Photodiode*
PACS: 64.70.kg, 73.40.Kp, 68.37.Hk

INTRODUCTION

At the current stage of information technology development, there is a need to create photodetectors with low noise levels, high stability, linear photoelectric characteristics, and minimal inertia [1–3]. The use of semiconductor structures in optoelectronic systems is driven by their inertial properties and the dependence of the photocurrent on both the applied voltage and the intensity of optical radiation [4]. Since optoelectronic systems operate at high frequencies, it is necessary to minimize signal delay in the photodetectors employed. Schottky-barrier diode structures are the most suitable for this purpose, as they offer the potential to reduce inertia by lowering capacitance [5].

For example, structures with two rectifying barriers [6] exhibit reduced capacitance compared to similar single-junction structures [7,8] and demonstrate superior performance under high-frequency operating conditions.

According to preliminary data [9], adding a second rectifying barrier to a potential-barrier structure helps to reduce its capacitance. However, the implementation of such a structure requires careful optimization of the base region parameters and precise control over the technology used to form the Schottky barriers. In addition, it is necessary to improve the noise characteristics, which depend not only on the magnitude of the reverse current but also on the operating mode of the device. From this standpoint, photodetectors operating in photovoltaic mode are of particular interest. Photovoltaic detectors belong to this class of semiconductor devices. Yet, they face a significant challenge: the surface layer of the p–n junction absorbs short-wavelength radiation, while long-wavelength radiation often passes through the junction without being absorbed.

These limitations can be overcome by creating multilayer heterojunction structures [10,11] with an extended spectral absorption range. Such structures are fabricated using molecular epitaxy, though certain technological constraints exist [12,13]. Noise reduction can be achieved by operating photodetectors in photovoltaic mode and by lowering the reverse dark currents. Additionally, the issue of inertia must be addressed. One of the most effective ways to overcome these issues is the development of advanced silicon-based Schottky-barrier photodetectors, which eliminate charge accumulation. The choice of silicon is justified by its extensive study and the well-established fabrication processes available for it. However, novel methods employed in gallium arsenide structures with metal–semiconductor junctions have not yet been applied to silicon systems. At the same time, further research is required to evaluate the potential outcomes.

It is known that in the early 1990s, research began on the physical and technological aspects of fabricating metal–semiconductor barrier structures based on silicon [14,15]. Photodetector structures were fabricated on bulk silicon, and

in some cases on epitaxial layers. Their spectral range depended on the material of the base region, with the maximum photocurrent observed near the intrinsic absorption wavelength ($0.9 \div 1.0$ μm) [16].

In conventional Schottky-barrier structures [17], the reverse currents exceed those typical of p–n junctions, which necessitates higher signal levels for their proper operation. To improve the photoelectric characteristics of silicon structures with double-sided barriers and to study the possible mechanisms of photosensitivity and their relationship to the parameters of the base region (such as thickness and carrier concentration), comprehensive physical and technological investigations are required. This includes developing new physical principles for the operation of such structures, which are promising for optoelectronic systems. This task remains relevant, as the challenge of creating low-noise photodetectors for optoelectronics has not yet been fully resolved.

At present, researchers are focused on the tasks of receiving and processing laser and optical radiation, paying particular attention to the development of suitable photodetectors [18]. Intensive efforts are being made to develop methods for creating photodetectors for the ultraviolet and infrared spectral ranges, where optical losses in fibers are minimal [19–21].

Elemental and binary semiconductors have begun to be used for their fabrication, where variation of the composition and thickness of the base region makes it possible to achieve photosensitivity over a wide spectral range ($0.3 \div 1.8$ μm) [22]. In particular, Schottky-barrier photodetectors based on silicon have been developed, in which charge carrier transport occurs primarily via thermionic emission [23,24]. It should be noted that the minimum detectable signal level turned out to be higher than in similar p–n junction structures. This is explained by the high saturation current (I_s) values resulting from the relatively low potential barrier height (φ). Functionally, Schottky-barrier and p–n junction structures are interchangeable. They are widely used for alternating-current rectification, as well as in mixer diodes, Zener diodes, pulse diodes, and parametric diodes [25–28]. Recently, new metal–thin dielectric–semiconductor (MIS) structures have emerged, providing semiconductor devices with a range of new functional properties [29].

In this regard, the present article examines the physical principles related to photogeneration processes in Schottky-barrier structures, which characterize the electronic phenomena occurring in the space-charge region of the potential barrier in the Ag–nSi–n$^+$Si–(In+Sn) photodiode structure. The structure under investigation is a complex multilayer metal–semiconductor–metal system, considered promising for use in photodiodes and sensor elements.

EXPERIMENTAL SAMPLES AND MEASUREMENT METHODS

The studies were performed using Ag-nSi-n$^+$Si-(In+Sn) homojunction photodiode structures formed on the basis of a heavily doped KEF-7.8 silicon substrate. The substrates were silicon wafers with a crystallographic orientation of (111), 25 mm in diameter and about 380 μm thick. The material was characterized by a carrier concentration of $N_n=2.3\times10$ cm^{-3} and a resistivity of 7.8 Ohm cm. The wafers were made of single-crystal silicon provided by JSC Photon. The base region was a high-resistance silicon layer ($\rho \approx 4.2\times10^6$ Ω·cm) 36 μm thick, characterized by n-type conductivity at a carrier concentration of $N_n=1.1\times10^9$ см$^{-3}$.

The initial preparation of the silicon substrates consisted of grinding followed by double-sided polishing using ASM-1.5 diamond paste. Before applying the metal coatings, the silicon wafers were treated in a polishing etchant containing HF, HNO$_3$, and CH$_3$COOH in a 1:8:1 ratio. Afterward, they were thoroughly rinsed in deionized water and dried.

Next, an active n$^+$Si region was formed on the surface of the substrate -an epitaxial layer grown by liquid-phase epitaxy with a thickness of 36 μm. To reduce dark currents, the structures were annealed in a hydrogen flow at 310°C for 30 minutes.

As a contact layer, a silver (Ag) film was deposited on the surface of the active n-Si region, forming a potential barrier. The deposition was carried out in vacuum ($\sim10^{-7}$ Torr) at 386°C from a silver source (mass 34 mg), resulting in a film thickness of 95 Å. On the back side of the structure, an ohmic contact was obtained by vacuum deposition of an (In+Sn) alloy (mass 53 mg) at 212 °C, with a thickness of 125 Å. The film thicknesses were measured using a Linnik MII-4 microinterferometer.

The resulting Ag-nSi-n$^+$Si-(In+Sn) homojunction structure was then scribed into discrete samples with an area of 5-9 mm². Structurally, the device is a semiconductor photodiode fabricated on a heavily doped substrate, as shown in Fig. 1.

Figure 1. Geometric cross-section of the single-base photodiode structure Ag-nSi-n$^+$Si-(In+Sn)

The current–voltage characteristics (I–V curves) of the Ag-nSi-n$^+$Si-(In+Sn) photodiode structure were recorded according to the standard circuit described in [30], in both forward and reverse bias, over a wide range of current and voltage values at room temperature (293 K). The operating voltage was supplied by B5-48 and B5-50 power supplies with a step of 0.05 V. Voltage and current were measured using universal voltmeters V7-21A and V7-35. The minimum measurable current was 2 nA, and the relative measurement error was 0.2÷0.4%.

The capacitance–voltage characteristics (C–V curves) of the structure were recorded over a wide frequency range from 50 Hz to 10 kHz. The study showed that in the frequency ranges f ≤ 100 Hz and f≥1 kHz, the C–V characteristics exhibit different features and capacitance values. Therefore, the primary focus of the investigation was on frequencies around 100 Hz and 8.3 kHz. The C–V characteristics of the studied homostructures were measured for capacitance values in the range C=1.0÷70 pF using the standard setup described in [30].

The illuminated current–voltage characteristics of the structure were measured under reverse current direction at room temperature (T=293 K) under illumination in the range E=0÷160 lx. Illumination of the structures was provided by a special incandescent lamp SIRSh 6-100 with power W=100 W, which is equivalent in its parameters to a standard white light reference lamp. It should be noted that one lumen of electromagnetic radiation in the visible spectral region corresponds to a power of 9.1·10⁻³ W.

RESULTS AND DISCUSSION

The morphology of the Ag-nSi-n$^+$Si-(In+Sn) homostructure samples on silicon substrates was studied using a scanning electron microscope SEM EVO MA 10 (Carl Zeiss, Germany) and is shown in Fig. 2. For elemental composition analysis, an energy-dispersive X-ray spectrometer EDX (Oxford Instruments) – Aztec Energy Advanced X-act SDD – was used. During the measurements, an accelerating voltage of 15 kV was applied to the filament, with a working distance of 8.5 mm from the sample surface. Scanning was carried out from one side of the investigated homostructure.

a   b
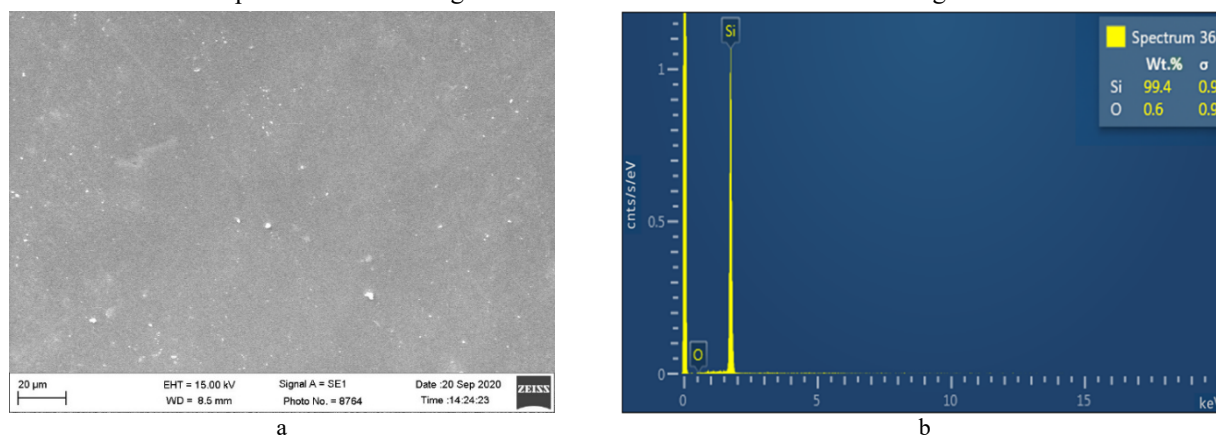
Figure 2. SEM images of the surface (a) and elemental analysis (b) of the Ag-nSi-n$^+$Si-(In+Sn) homostructure based on n-type monocrystalline silicon

The data obtained using the scanning electron microscope (SEM) and presented in Fig. 2 indicate a dominant silicon content in the sample, which is confirmed by the high intensity of its main peak. The weak oxygen (O) peak suggests the possible presence of oxide compounds or surface contaminants formed during the growth or storage of the structure. According to the quantitative analysis, the mass fraction of silicon is 99.4%, while that of oxygen is 0.6%.

As is well known, such m-n-n$^+$-m structures are often used to study transient effects and rectification characteristics. The I–V characteristics of the Ag-nSi-n$^+$Si-(In+Sn) structure under forward and reverse bias, shown in linear (a) and semilogarithmic (b) scales, are presented in Fig. 3, in accordance with the equivalent circuit shown in Fig. 4.

a   b
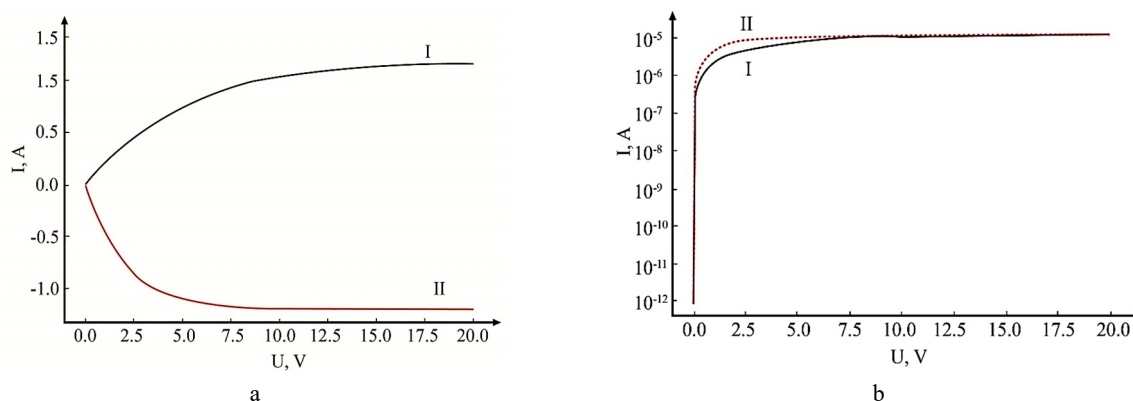
Figure 3. Current–voltage characteristics of the Ag-nSi-n$^+$Si-(In+Sn) structure in linear scale (a) and semilogarithmic scale (b) under different biasing modes: I – (-) Ag-nSi-n$^+$Si-(In+Sn) (+), II – (+) Ag-nSi-n$^+$Si-(In+Sn) (-)
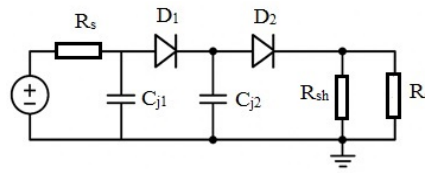
Figure 4. Two-barrier equivalent circuit of the Ag-nSi-n⁺Si-(In+Sn) structure

Within the framework of the two-barrier approximation, the equivalent circuit of the structure can be represented as a series connection of two diodes (Fig. 4), which makes it possible to accurately describe the experimental current–voltage characteristics [31, 32]. This model includes the following elements:

- two oppositely connected diodes (D_1 and D_2) corresponding to the barriers $\varphi_{\beta1}$ and $\varphi_{\beta2}$: D_1 describes the Schottky barrier at the Ag–nSi contact, characterized by barrier height $\varphi_{\beta1}$, series resistance R_s, saturation current I_{s1}, and junction capacitance C_{j1}; D_2 corresponds to the n–n⁺Si junction, with similar parameters: $\varphi_{\beta2}$, I_{s2}, and C_{j2}; series resistance R_s, taking into account ohmic losses in the volume of the semiconductor and contacts, expressed as,

$$R_s = R_{\text{contact}} + R_{\text{volumetric layer}} + R_{\text{substrates}};\qquad(1)$$

- parallel resistance R_{sh}, simulating leakage currents through defective channels and the periphery of the structure;
- barrier capacitances C_{j1} and C_{j2}, which determine the capacitive properties of the depleted regions.
- R_c is the resistance at the metal-semiconductor boundaries (Ag-nSi and (In+Sn)-n⁺Si), caused by imperfect contacts and barrier effects, affecting the real current-voltage characteristic and photosensitivity of the structure.

The proposed two-barrier equivalent circuit is versatile, allowing a consistent interpretation of the experimental characteristics over a wide voltage range: from the low-voltage regime, where generation–recombination processes dominate, to the high-voltage region, where thermionic emission and tunneling through localized states become the determining mechanisms.

According to the equivalent circuit (Fig. 4), when the polarity of the applied voltage changes, the base is blocked alternately on one side or the other, which determines the current flowing through the structure [33]. The observed difference in the current values confirms that the Schottky barrier at the Ag-nSi contact and the isotypic n-n⁺ junction (nSi-n⁺Si with an (In+Sn) contact) have different electrical characteristics due to differences in the work function of the metals and the conditions for the formation of interphase boundaries. Under forward and reverse biases, the current is determined by a combination of charge carrier transport mechanisms, including thermionic emission through the Schottky barrier, tunneling current through the depletion layer, and recombination-generation processes in the space charge region [34]. An important factor is the change in the width of the depletion layer, which decreases under forward bias and expands under reverse bias, which directly affects the probability of tunneling and the effective barrier height. In addition, in real structures [33, 36], a significant role is played by localized states in the forbidden band of silicon, arising due to lattice defects and impurity centers. These states participate in recombination-generation processes and can significantly modify the shape of the I-V characteristic, especially in the region of low voltages. From the analysis of the I-V characteristic, it is evident that the dependence of the current on the voltage is approximated by a power function of the form $I \propto U^\gamma$ [37], with two characteristic sections being distinguished. In the forward bias region, the first section corresponds to the exponent $\gamma \approx 0.28$, which indicates a significant contribution of the tunneling mechanism through a narrow depletion layer. With a further increase in voltage, the exponent increases to $\gamma \approx 1.42$, which indicates a transition to the diffusion and thermionic transport mechanisms, consistent with a decrease in the effective barrier height [37]. The combined analysis of the current-voltage characteristics indicates the multifactorial nature of current transport, where the interaction of the barrier height plays a decisive role. The dynamics of the depletion layer width and localized states in the forbidden zone allow for a deeper interpretation of the conductivity mechanisms in the structure under study.

In the locking mode, the value of the power-law exponent in the initial section is ~1.15, which corresponds to an almost linear dependence of the current on the voltage $I \propto U^{\sim1}$. This mode is interpreted as a manifestation of thermionic injection with insignificant nonlinearity and the absence of significant current limitation from the side of the barrier contact. In the next section, an increase in the power-law exponent to a value of about 2.84 is observed, which indicates a change in the dominant conductivity mechanism and the involvement of a volume-limited current with the participation of traps. It should be noted that in both cases, in the second characteristic measurement interval, the values of the power-law exponent approach 0.5. With forward bias, this indicates the impossibility of describing the structure behavior within the framework of the classical diode exponent; the current is formed due to defective conductivity channels. In the reverse bias mode, this indicator reflects the predominance of tunneling processes through the potential barrier, involving distributed localized states in the band gap associated with surface generation.

As follows from the equivalent circuit (Fig. 4), when a common external voltage $U_{general}^{(+)Ag-nSi-n+Si-(In+Sn)(-)}$ is applied to the structure, a total current will flow:

$$U_{general}^{(+)Ag-nSi-n+Si-(In+Sn)(-)} = U_{straight}^{(+)Ag-nSi} = U_{arr}^{n+Si-(In+Sn)}\qquad(2)$$

However, the total voltage consists of the sum of the voltages dropped at each junction:

$$U_{general}^{(+)Ag-nSi-n+Si-(In+Sn)(-)} = U_{1straight}^{(+)Ag-nSi} + U_2^{nSi-n+Si} + U_{3arr}^{n+Si-(In+Sn)} \tag{3}$$

The potential barrier height for the Ag-nSi transition is 0.65 eV, and for the isotypic nSi-n⁺Si transition it is 0.197 eV. Using data on the carrier concentration and the effective density of states in the conduction band of silicon ($N_c \approx 2 \times 10^{18}$ cm^{-3}), the position of the Fermi level was calculated using the formula [37]:

$$Å_F = E_C - \frac{kT}{q}\ln\left(\frac{N_C}{N_D}\right) \tag{4}$$

which was found to be 0.622 eV relative to the conduction band edge. It should be noted that this Fermi level value indicates a pronounced degree of semiconductor degeneracy, in which the carrier distribution deviates from the classical Maxwellian distribution and must be described using Fermi–Dirac statistics [38]. Such a shift of the Fermi level has a direct effect on the depletion layer width in the junction: at high impurity concentrations, the depletion layer becomes significantly narrower, which increases the probability of tunneling through the barrier and changes the dominant current transport mechanisms. Thus, the obtained parameters of the barrier height and Fermi level are consistent with the features of transport processes in multilayer metal–semiconductor structures and isotype heterojunctions. Accordingly, the difference between the conduction band edge and the Fermi level is 0.59 eV, and the difference between the barrier height and this value gives the contact potential differences for the junctions:

U_c^{Ag-nSi} = - 0.412 eV, $U_c^{nSi-n+Si}$ = 0.554 eV, $U_c^{n+Si-(In+Sn)}$ = 0.152 eV. The potential difference between the Ag-nSi and n⁺Si-(In+Sn) junctions is 0.625 eV.

Assuming an abrupt metal–semiconductor junction, the corresponding widths of the space-charge regions (W^{m_1-n} and W^{n-m_2}) can be determined based on the formula [37]:

$$W^{m-n} = \left[\frac{2\varepsilon\varepsilon_0}{qN_D}(U_C \pm U_{adj})\right]^{1/2} \tag{5}$$

In the absence of an external bias, the initial thicknesses of the space-charge regions formed by the rectifying barriers were calculated. The obtained values were $W_0^{m_1-n}$ =672.8 µm and $W_0^{n-m_2}$=5.49 nm, which reflects a significant contrast in the spatial distribution of the electric field at different junctions. Using the method for determining the voltage drop across each junction [39], based on the experimental I–V characteristics, the values of U_1^{Ag-nSi}, $U_2^{n+Si-nSi}$ and $U_3^{n+Si-(In+Sn)}$, were obtained, as well as the thicknesses of the space-charge layers of each junction, which are presented in Table 1.

Table 1. Calculated data of physical parameters at transitions

(-)Ag-nSi-n⁺Si-(In-Sn)(+)								
$U_{general}$ (V)	$I_{general}$ (µA)	U_1 (V)	U_2 (V)	U_3 (V)	E (V/см)	W_1(µm)	W_2(µm)	W_3(µm)
0.1	0.06	0	0.705	0.320	5.55	254.3	675.2	0.0037
0.5	0.37	0.106	1.125	0.712	27.74	568.6	845.3	0.0056
1.0	0.64	0.615	1.605	1.218	55.49	804.1	1018.7	0.0073
1.5	0.92	1.117	2.132	1.672	83.23	984.8	1166.6	0.0086
2.0	1.23	1.504	2.412	2.185	110.97	1137.2	1297.8	0.0098
2.5	1.57	2.119	3.113	2.720	138.72	1272.7	1417.6	0.0110
3.0	1.82	2.606	3.515	3.136	166.46	1395.4	1529.3	0.0121
3.5	2.11	3.107	4.088	3.697	194.20	1507.9	1636.0	0.0132
4.0	2.45	3.616	4.565	4.210	221.94	1612.8	1739.3	0.0143
4.5	2.73	4.099	5.133	4.703	249.69	1711.9	1840.2	0.0154
5.0	3.16	4.428	5.497	5.301	277.43	1806.6	1939.6	0.0165
10.0	6.78	9.701	10.605	9.327	554.86	2538.8	3089.0	0.0231
15.0	9.12	14.596	16.212	15.583	832.29	3114.3	3186.1	0.0290
20.0	12.0	19.606	21.101	20.158	1109.72	3577.7	3484.6	0.0346

Table 1 also shows the values of the maximum electric field strength in the turn-off junctions. It is important to note that the dependence of the current calculated relative to the falling voltage completely reproduces the course of the curve on the total turn-off voltage (Fig. 3), which indicates the identity of the current transfer mechanisms. As follows from the data in Fig. 3, in forward-biased junctions the current increases linearly with increasing falling voltage; the exponent γ ~ 1, corresponds to the thermionic emission mode. In this case, the applied voltage in the forward-biased junction cannot exceed the value of the contact potential difference, as a result of which its main part is distributed over the quasi-neutral region of the base r_{bases}, that is, $U_{straight}^{Ag-nSi} = U_{straight}^{Ag-nSi^*} + U_{r_{bases}}$, connected in

series with the junction. Such voltage redistribution directly affects the width of the depletion layer, decreasing it with increasing forward bias, which, in turn, facilitates the injection of carriers through the barrier and leads to a change in the current transfer conditions [40].

Based on the equivalent circuit (Fig. 4) describing the two-barrier model of the Ag–nSi–n⁺Si–(In+Sn) structure, the following features of the current transport mechanism can be distinguished:

- in the low-voltage region ($|U| < 0.3$ V), the current is dominated by generation–recombination through the barrier φ_{v1} in the depletion region, which is reflected in its quasi-linear increase;

- at medium voltages ($0.3 \div 1$ V), the main mechanism becomes thermionic emission through the φ_{v1} barrier, which is characterized by an exponential dependence of the current on the applied voltage;

- in the region of high voltages ($U > 1 \div 2$ V) the second barrier φ_{v2} is activated, tunneling processes with the participation of localized states are enhanced, which leads to a power dependence of the type $I \sim U^{\gamma}$ with fractional values of the exponent γ.

The measurements of the VEH were carried out in the voltage range from -15 V to +15 V. The dependences of the capacitance C(U) were recorded (Fig. 5), which were then recalculated into coordinates C^{-2} (U) [37]. The dependence of the capacitance on the voltage in coordinates $C^{-2} \sim U$ (Fig. 6) in the initial section gives a straight line, confirming the sharpness of the p-n junction.
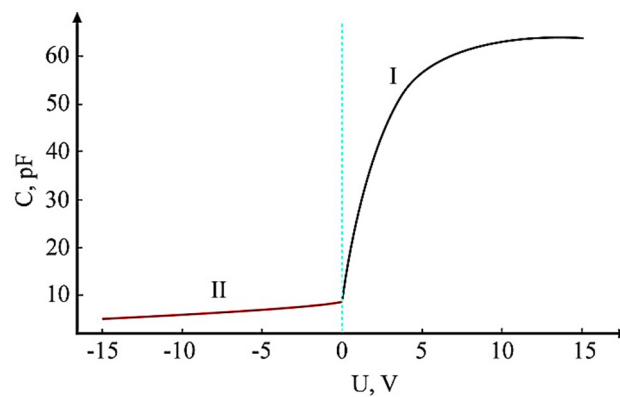
Figure 5. Volt-capacitive characteristic of the Ag-nSi-n⁺Si-(In+Sn) structure under forward (I) and reverse (II) bias

Fig. 5 shows the VEC of the studied Ag-nSi-n⁺Si-(In+Sn) structure. The experimental data show two characteristic modes of capacitance behavior depending on the magnitude of the applied voltage. In the region of reverse voltages ($0\ldots{-}15$ V), a monotonic decrease in capacitance from ~ 9 pF to ~ 5 pF is observed. This effect is due to the expansion of the depletion layer and corresponds to the barrier capacitance of the p-n junction, which is described by the expression [34,37]:

$$C_{bar} \cong S \sqrt{\frac{q \varepsilon \varepsilon_o N}{2(\phi_{con} - U)}},\qquad(6)$$

where, N is the impurity concentration in the lightly doped region, S is the area of the structure, U is the blocking voltage, ϕ is the height of the metal-semiconductor barrier.

Therefore, as the reverse bias modulus increases, the width of the depletion layer increases, which leads to a decrease in the barrier capacitance.

When moving to the region of forward biases ($0\ldots{+}15$ V), an exponential growth of capacitance is observed, reaching ~ 64 pF at +15 V. This effect is due to the dominance of the diffusion component associated with the injection and accumulation of charge carriers near the junction. The diffusion capacitance is described by the dependence [34]:

$$C_d \propto \exp(qV/kT),\qquad(7)$$

Thus, the analysis of the VEH shows that in the region of reverse voltages, the main mechanism of capacitance change is the redistribution of the space charge and the expansion of the depletion layer, whereas in the region of forward bias, the process of diffusion injection dominates.

Fig. 6 shows the dependence C^{-2} (U) for the studied structure; linear approximation in the reverse bias region allowed us to determine key parameters such as: charge carrier concentration, depletion layer width, and potential barrier height of the junction. In particular, the value of the built-in potential was $\varphi_v \approx 0.185$ V, and the concentration of donor impurities was $N_D \approx 5.2 \times 10^{11}$ cm⁻³. The analysis technique is based on the Mott-Schottky equation, which relates the capacitance of the barrier junction to the applied voltage [34, 37]:

$$C^{-2} = (2/q\varepsilon\varepsilon_0 N_D S^2) \cdot (\varphi_v - U),\qquad(8)$$

where, q is the electron charge, ε is the relative permittivity of silicon, ε_0 is the electric constant, S is the area of the structure, U is the external voltage, and φ_v is the built-in potential.
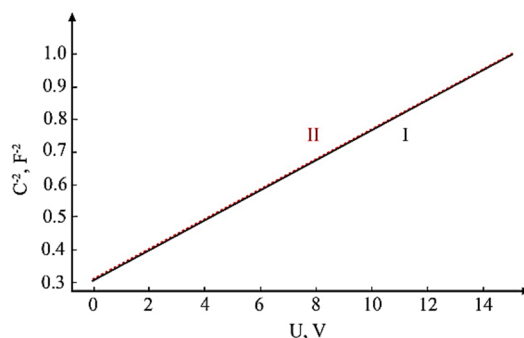
Figure 6. Dependence C^{-2} (U) by the Mott-Schottky method for the Ag–nSi–n⁺Si–(In+Sn)
structure with superimposed linear approximation

The linear section of the C^{-2} (U) graph indicates a uniform distribution of impurities in the semiconductor volume. The donor concentration N_D is determined from the slope of the straight line, and the intersection point with the voltage axis yields the value of φ_{con}. Optimization of the parameters of the base silicon region (thickness $\approx$36 μm and specific resistance 4.2×106 Ω·cm) leads to a decrease in the concentration of charge carriers and, as a consequence, a decrease in the barrier capacitance of the structure to $8 \div 10$ pF, which is almost an order of magnitude less compared to $70 \div 110$ pF for photodiodes based on GaAsSb solid solutions for the IR region, providing a twofold expansion of the operating frequency range and an increase in response time, which gives the structure under consideration a significant advantage over analogs based on gallium arsenide and antimony compounds [41, 42].

The dependences of the photocurrent on the operating voltage during excitation from the Ag-nSi junction side by integrated light with a maximum at λ=0.55 μm of the Ag-nSi-n⁺Si-(In+Sn) structure in the potential barrier locking mode under different illuminations are shown in Fig. 7 [43].

Figure 7. Illuminated current–voltage characteristics of the Ag–nSi–n⁺Si–(In+Sn) structure in the reverse-
bias mode: 1 – 0 lx, 2 – 100 lx, 3 – 200 lx, 4 – 1000 lx, 5 – 2000 lx

As can be seen from Fig. 7, in darkness the current–voltage dependence is nearly linear. Under the action of broadband light from a tungsten lamp with a spectral maximum near 0.86 μm, an increase in photocurrent is observed with increasing reverse bias voltage up to 2 V and illumination intensity, indicating a higher photocurrent compared to its initial value at 0.02 V. The optimal operating voltage range is $0.8 \div 1.2$ V.

The dependence of the response sensitivity on wavelength (Fig. 8) qualitatively corresponds to the characteristic curve of a silicon photodiode with a p–n junction, and the spectral sensitivity range extends from 0.48 to 1.26 μm.
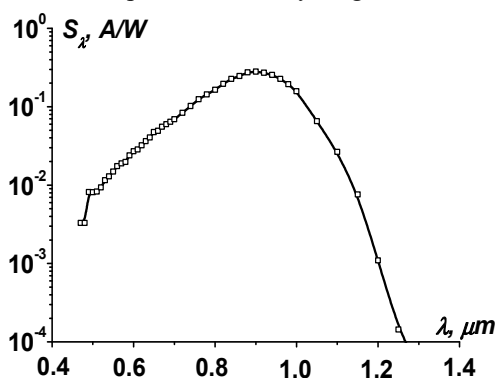
Figure 8. Wavelength dependence of the response sensitivity of the Ag–nSi–n⁺Si–(In+Sn) structure

The spectral optical range of the Ag–nSi–n⁺Si–(In+Sn) structure is relatively broad, extending from λ=0.48 to 1.26 μm, with a maximum response at 0.92 μm. This behavior is explained by the presence of a thin, high-resistivity layer located near the surface. The spectral range extends into the near-infrared region due to deep impurity levels positioned near the mid-gap in the subsurface region of silicon, which become ionized under reverse bias. As the operating voltage increases from 0.02 V to 2.0 V, the photocurrent rises correspondingly, particularly in the range of λ=0.9÷1.25 μm. The formation of an active near-surface layer with increased resistivity leads to enhanced photosensitivity across the investigated spectral range, reaching a value of 0.338 A/W [33, 44]. The spectral photocurrent exhibits a monotonic increase with applied voltage, which is attributed to the higher rate of photogenerated carriers in the space-charge region controlled by the Ag–nSi junction [45,46].

CONCLUSIONS

The homojunction structures Ag–nSi–n⁺Si–(In+Sn), obtained by the liquid-phase epitaxy method, exhibit a perfect single-crystalline film with (111) orientation and subcrystallite sizes exceeding 50 nm [47]. During the liquid-phase epitaxy of the solid solution, a compensated high-resistivity layer is formed at the interface between the n⁺-Si substrate and the n-Si epitaxial film, characterized by a resistivity of 3.2×10^4 Ω·cm at room temperature (293 K).

The analysis of the I–V characteristics of the Ag–nSi–n⁺Si–(In+Sn) structure revealed that charge transport is multifactorial, determined by thermionic emission, tunneling, and generation–recombination processes. A significant influence is exerted by the differences in the electrical characteristics of the Schottky barrier and the isotype junction, the dynamics of the depletion layer width, as well as localized states caused by defects and impurity centers. The power-law behavior of the current–voltage dependence indicates a change in the dominant conduction mechanisms under different bias regimes: from tunneling transport at low voltages to diffusion–thermionic and trap-assisted space-charge-limited current at higher voltages [48]. The photosensitivity of the studied structure covers a spectral photon energy range of 0.387÷1.016 eV, being shifted toward the long-wavelength region compared to conventional pSi–nSi silicon structures; additional formation of a high-resistivity near-surface layer enhances the response, allowing photosensitivity to reach 0.338 A/W. The maximum photocurrent increase at $E_{ph} \approx 0.74$ eV indicates the generation of nonequilibrium minority carriers (holes) in the electronic transitions. It should be emphasized that the highest photocurrent value in the impurity absorption region is achieved under the condition that the thermal generation rate of electrons from silicon impurity levels is comparable to the rate of photogeneration of minority carriers via electron transitions from the valence band to these levels [49]. Optimization of the parameters of the silicon base region ensures a reduction in barrier capacitance down to 8÷10 pF, which is almost an order of magnitude lower than that of GaAsSb photodiodes (70÷110 pF), thereby enabling an extended operating frequency range and improved response speed.

Ag–nSi–n⁺Si–(In+Sn) structures show potential for use as photodiodes in optoelectronic devices operating in the visible and infrared spectral regions. The results presented here can be applied to improve the photoelectric properties of silicon photodiode systems with metal–semiconductor junctions.

ORCID

Feruza A. Giyasova, https://orcid.org/0000-0003-0746-4986; **Murodjon A. Yuldoshev,** https://orcid.org/0000-0002-9722-9439
Khayot N. Bakhronov, https://orcid.org/0009-0000-4138-3149; **Farkhod A. Giyasov,** https://orcid.org/0009-0003-9882-0655
Nosirbek A. Sattarov, https://orcid.org/0009-0005-0506-0269

REFERENCES

[1] J. Davila-Rodriguez, X. Xie, J. Zang, C. J. Long, T. M. Fortier, H. Leopardi, T. Nakamura, J. C. Campbell, S.A. Diddams, F. Quinlan, "Optimizing the linearity in high-speed photodiodes," Instrumentation and Detectors, arXiv.1808.04429, (2018). https://doi.org/10.48550/arXiv.1808.04429

[2] T. Kauten, B. Pressl, T. Kaufmann, and G. Weihs, "Measurement and modeling of the nonlinearity of photovoltaic and Geiger-mode photodiode," Rev. Sci. Instrum. **85**, 063102 (2014). https://doi.org/10.1063/1.4879820

[3] C.A.R. Perini, G. Ferrari, J.-P. Correa-Baena, A. Petrozza and M. Caironi, "A solution processed metal oxide:polymer interlayer improves the perovskite photodetector response speed, dark current, and stability," The Royal Society of Chemistry's, EES Solar (2025). https://doi.org/1039/D5EL00043B

[4] Q. Zhao, W. Wang, F. Carrascoso-Plana, W. Jie, and T. Wang, A. Castellanos-Gomez, and R. Frisenda, "The role of traps in the photocurrent generation mechanism in thin InSe photodetectors," Materials Horizons, **7**, 252 (2020). https://doi.org/10.1039/C9MH01020C

[5] Q. Chen, X. Zhang, M.S. Sharawi, and R. Kashya, "Advances in High -Speed, High–Power Photodiodes: From Fundamentals to Applications," Appl. Sci. **14**, 3410 (2024). https://doi.org/10.3390/app14083410

[6] O.A. Abdulkhaev, G.O. Asanova, D.M. Yodgorova, and A.V. Karimov, "Investigation of the photoelectric characteristics of photodiode structures with silicon-based potential barriers," Journal of Engineering Physics and Thermophysics, **85**(3), 709-715 (2012). https://doi.org/10.1007/s10891-012-0705-y

[7] M. Casalino, G. Coppola, M. Iodice, I. Rendina, and L. Sirleto, "Near-Infrared Sub-Bandgap All-Silicon Photodetectors: State of the Art and Perspectives," Sensors, **10**, 10571-10600 (2010). https://doi.org/10.3390/s101210571

[8] O. Surucu, D.E. Yıldız, and M. Yıldırım, "A study on the dark and illuminated operation of Al/Si3N4/p Si Schottky photodiodes: optoelectronic insights," Applied Physics A, **130**, 103 (2024). https://doi.org/10.1007/s00339-024-07284-2

[9] S. Khudaverdyan, A. Vaseashta, G. Ayvazyan, L. Matevosya, A. Khudaverdyan, M. Khachatryan, and E. Makaryan, "On the Selective Spectral Sensitivity of Oppositely Placed Double-Barrier Structures," Photonics, **9**, 558 (2022). https://doi.org/10.3390/photonics9080558

[10] X. Guan, *et al.*, "Recent progress in short- to long-wave infrared photodetection using 2D materials and heterostructures," Advanced Optical Materials, **9**(4), 1-24 (2021). https://doi.org/10.1002/adom.202001708

[11] A. Bablich, *et al.*, "Few-Layer MoS2/a-Si:H Heterojunction Pin-Photodiodes for Extended Infrared Detection," ACS Photonics, **6**, 1372-1378 (2019). https://doi.org/10.48550/arXiv.1907.09592

[12] V.S. Varavin, S.A. Dvoretskii, N.N. Mikhailov, V.G. Remesnik, I.V. Sabinina, Yu.G. Sidorov, V.A. Shvets, *et al.*, "Molecular Beam Epitaxy of CdHgTe: Current State and Horizons," Optoelectronics, Instrumentation and Data Processing, **56**(5), 456-469 (2021). https://doi.org/10.3103/S8756699020050143

[13] I. Izhnin, A. Izhnin, H. Savytskyy, O. Fitsych, N. Mikhailov, V. Varavin, S. Dvoretsky, *et al.*, "Defects in HgCdTe grown by molecular beam epitaxy on GaAs substrates," Opto-electronics review, **20**(4), 375-378 (2012). https://doi.org/10.2478/s11772-012-0048-4

[14] M. Wittmer, "Carrier recombination and high barrier Schottky diodes on silicon," Solids and Materials, **51**, 451–454 (1990). https://doi.org/10.1007/BF00324725

[15] M Wittmer, and J.L. Freeouf, "Ideal Schottky diodes on passivated silicon," Phys. Rev. Lett. **69**(18), 2701-2704 (1992). https://doi.org/10.1103/PhysRevLett.69.2701

[16] T. Saito, "Spectral Properties of Semiconductor Photodiodes," in: *Advances in Photodiodes*, edited by G.-F.D. Betta, (IntechOpen, London, 2011), pp. 1-24. https://doi.org/10.5772/15300

[17] P. Pipinys, A. Pipiniene, and A. Rimeika, "Phonon-assisted tunneling in reverse biased Schottky diodes," J. Appl. Phys. **86**, 6875-6878 (1999). https://doi.org/10.1063/1.371766

[18] Z. Li, X. Jin, C. Yuan, and K. Wang, "Photon Detector Technology for Laser Ranging: A Review of Recent Developments," Coatings, **15**, 798 (2025). https://doi.org/10.3390/coatings15070798

[19] D. Ma, Y. Wang, and Y. Wang, "Performance enhancement of fiber-optic ultraviolet photodetector based on Ag/ZnO-microrod Schottky junction," in: *Proc. SPIE 12617, Ninth Symposium on Novel Photoelectronic Detection Technology and Applications, (NDTA 2022)*, vol. 126175D, (2023). https://doi.org/10.1117/12.2666501

[20] Y.-F. Xiong, J.-H. Chen, Y.-Q. Lu, and F. Xu, "Optical-Fiber-Compatible Photodetector Based on a Graphene-MoS2-WS2 Heterostructure with a Synergetic Photogenerating Mechanism," Advanced-Electronic-Materials, **5**(1), 1800562 (2018). https://doi.org/10.1002/aelm.201800562

[21] S. Rakhmanov, K. Matchonov, H. Yusupov, K. Nasriddinov, and D. Matrasulov, "Optical high harmonic generation in Dirac materials," Eur. Phys. J. B, **98**, 35 (2025). https://doi.org/10.1140/epjb/s10051-025-00885-7

[22] M. Wang, *et al.*, "Silicon-Based Intermediate-Band Infrared Photodetector Realized by Te Hyperdoping," Adv. Optical Mater. **9**, 2101798 (2021). https://doi.org/10.1002/adom.202101798

[23] Y. Jin, J. Seok, and K. Yu, "Highly Efficient Silicon-Based Thin-Film Schottky Barrier Photodetectors," ACS Photonics, **10**(5), 1-2 (2023). https://doi.org/10.1021/acsphotonics.2c01923

[24] A. Pelella, A. Grillo, E. Faella, G. Luongo, M.B. Askari, and A. Di Bartolomeo, "Graphene–Silicon Device for Visible and Infrared Photodetection," ACS Appl. Mater. **13**, 47895-47903 (2021). https://doi.org/10.1021/acsami.1c12050

[25] R. Aly, R. Tarek, O. Ramadan, and M. Khashan, "An Overview on Schottky Barrier Diodes," Faculty of Engineering-Alexandria University, 1-10 (2025). https://www.researchgate.net/publication/366763152

[26] B. Zhang, D. Ji, Y. Min, Y. Fan, and X. Chen, "A High-Efficiency 220 GHz Doubler Based on the Planar Schottky Varactor Diode," J. Electron. Mater. **48**, 3603–3611 (2019). https://doi.org/10.1007/s11664-019-07067-z

[27] M. Alathbah, "Development and Modelling of Gallium Nitride Based Lateral Schottky Barrier Diodes with Anode Recesses for mm Wave and THz Applications," Micromachines, **14**(2), 2-18 (2023). https://doi.org/10.3390/mi14010002

[28] C.-C. Hsieh, Y.-F. Chang, Y.-C. Chen, H.-L. Chang, and S.K. Banerjee, "Highly Non linear and Reliable Amorphous Silicon Based Back to Back Schottky Diode as Selector Device for RRAM Arrays," ECS Journal of Solid State Science and Technology, **6**(9), 143-147 (2017). https://doi.org/10.1149/2.0041709jss

[29] H. Chouaib, M. Aouassa, and M. Bouabdellaoui, "Highly photosensitive MIS structure with embedded silicon film for solar cell and photodetection applications," Journal of Materials Science: Materials in Electronics, **34**, 1815 (2023). https://doi.org/10.1007/s10854-023-11171-6

[30] F.A. Giyasova, "Development of Multilayer Photosensitive Structures Based on GaAs and Si for Optoelectronic Devices," D.Sci. thesis, Institute of Semiconductor Physics and Microelectronics, Uzbekistan (2024).

[31] A. Grillo, and A. Di Bartolomeo, "A Current-Voltage Model for Double Schottky Barrier Devices," Advanced Electronic Materials, **7**, 2000979 (2021). https://doi.org/10.1002/aelm.202000979

[32] N.N. Kononov, and S.G. Dorofeev, "Characteristics of the Schottky barriers of two-terminal thin-film Al/nano-Si film/ITO structures," Semiconductors, **51**, 608–616 (2017). https://doi.org/10.1134/S106378261705013X

[33] Sh. B. Utamuradova, F.A. Giyasova, M.S. Paizullakhanov, S.Yu. Gerasimenko, M.A. Yuldoshev, S.R. Boydedayev, and M.R. Bekchanova, "Investigation of the functional capability of modified silicon-based photodiodes structure," Chalcogenide Letters. **22**(8), 753-764 (2025). https://doi.org/10.15251/CL.2025.228.753

[34] A.G. Milnes, and D.L. Feucht, "Heterojunctions and Metal-Semiconductor Junctions," (Elsevier Science Imprint, 2012).

[35] V. Kumar, R. Singh, and P.K. Basu, "Current transport mechanisms in metal–semiconductor contacts," J. Appl. Phys. **110**(2), 024502-1–024502-7 (2011).

[36] R. Singh, and S. Kumar, "Trap-assisted space-charge-limited conduction in semiconductor structures," Solid-State Electronics, **45**(4), 625-630 (2001).

[37] S.M. Sze, and K.K. Ng, *Physics of Semiconductor Devices*, 3rd ed, (Wiley, Hoboken, NJ, USA, 2007).

[38] J.R. Yusupov, M. Ehrhardt, Kh.Sh. Matyokubov, and D.U. Matrasulov, "Driven transparent quantum graphs," Physica Scripta, **100**(7), (2025). https://doi.org/10.1088/1402-4896/ade014

[39] A.V. Karimov, and D.M. Yodgorova, "Determination of characteristics of double-barrier photodiode structures with metal-semiconductor junctions," Technology and design in electronic equipment, (5), 27-30 (2005). (in Ukrainian)

[40] D.M. Yodgorova, A.V. Karimov, F.A. Giyasova, R.A. Saidova, A.A. Yakubov, "Spectral photosensitivity m-n -n of structure on a basis epitaxy of layers," Semiconductor Physics Quantum Electronics Optoelectronics, **11**(1), 26-28 (2008). https://doi.org/10.15407/spqeo11.01.026

[41] E.V. Kunitsyna, I.A. Andreev, G.G. Konovalov, E.V. Ivanov, A.A. Pivovarova, N.D. Il'inskaya, and Yu.P. Yakovlev, "GaSb/GaAlAsSb Heterostructure Photodiodes for the Near-IR Spectral Range," Semiconductors, **52**, 1215-1220 (2018). https://doi.org/10.1134/S1063782618090099

[42] Sh.B. Utamuradova, F.A. Giyasova, K.N. Bakhronov, M.A. Yuldoshev, M.R. Bekchanova, B. Ismatov. Current Transfer Mechanism in A Thin-Based Heterosystem Based on A^2B^6 Compounds. East Eur. J. Phys. (2025), **3**, 325. https://doi.org/10.26565/2312-4334-2025-3-31

[43] D.M. Yodgorova, and F.A. Giyasova, "Photoelectric characteristics of silicon n^+-nSi-Ag structure," International Conference "Fundamental and Applied Issues of Physics". Section II: Physics of Semiconductors and Solids, Their Applied Aspects, **13-14**, 137-139 (2017).

[44] M.A. Yuldoshev, Z.T. Azamatov, A.B. Bakhromov, M.R. Bekchanova, East Eur. J. Phys. (4), 250 (2024), https://doi.org/10.26565/2312-4334-2024-4-25

[45] M. Akramov, B. Eshchanov, S. Usanov, Sh. Norbekov, and D. Matrasulov, "Second-harmonic generation in branched optical waveguides: Metric graphs based approach," Physics Letters A, **524**, 129827 (2024), doi.org/10.1016/j.physleta.2024.129827

[46] F.A. Giyasova, and M.A. Yuldoshev, "Investigation of temporal characteristics of photosensitive heterostructures based on gallium arsenide and silicon," Chalcogenide Letters, 22(2), 123–129 (2025). https://doi.org/10.15251/CL.2025.222.123

[47] A.S. Saidov, Sh.N. Usmonov, M.U. Kalanov, A.N. Kurmantayev, and A.N. Bahtybayev, "Structural and Some Electrophysical Properties of the Solid Solutions Si1–xSnx (0≤x≤0.04)," Phys. Solid State, **55**, 45-53 (2013). https://doi.org/10.1134/S1063783413010290

[48] A.V. Karimov, D.M. Yodgorova, F.A. Giyasova, E.M. Shpilevskiy, and N.I. Usmanova, "Photovoltaic Effect in Au-nSi-Au Structures with Schottky Barriers and Features of Spectral Characteristics," Applied Solar Energy, **54**(5), 330-332 (2018). https://doi.org/10.3103/S0003701X18050109

[49] A.S. Saidov, Sh.N. Usmonov, M. Kalanov, and Kh.M. Madaminov, "Structure and Photoelectric Properties of $Si_{1-x}Sn_x$ Epilayers," Tech. Phys. Lett. **36**, 827–829 (2010). https://doi.org/10.1134/S1063785010090154

ФІЗИЧНІ ПРИНЦИПИ ГЕНЕРАЦІЇ ФОТОСТРУМУ В КРЕМНІЄВІЙ ФОТОДІОДНІЙ СТРУКТУРІ З БАР'ЄРОМ ШОТТКІ

Ф.А. Гіясова[1]**, А.З. Рахматов**[2]**, Х.Н. Бахронов**[3]**, М.А. Юлдошев**[4]**, Ф.А. Гіясов**[1]**, А.Н. Олімов**[5]**, Н.А. Саттаров**[1]

[1]Міжнародний університет Кімьо в Ташкенті, Узбекистан
[2]ВАТ «Фотон», Ташкент, Узбекистан
[3]Ташкентський університет інформаційних технологій імені Мухаммада аль-Хорезмі, Узбекистан
[4]Міжнародний університет Туран, Наманган, Узбекистан
[5]Інститут іонно-плазмових та лазерних технологій Академії наук Узбекистану,
вул. Дурмон Юлі, 33, 100125, Ташкент, Узбекистан
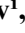
Гомоперехідні структури типу Ag–nSi–n^+Si–(In+Sn) з ідеальною монокристалічною (111) орієнтацією та шаром з високим опором, компенсованим на межі розділу n^+Si/n-Si, були отримані методом рідкофазної епітаксії. Представлено результати дослідження процесів фотогенерації та механізмів струмопереносу в кремнієвій фотодіодній структурі з бар'єром Шотткі. Було розроблено двобар'єрну модель структури, згідно з якою струмоперенос має багатофакторну природу та визначається комбінованим внеском термоелектронної емісії, тунелювання та процесів генерації-рекомбінації. Крім того, було встановлено, що фоточутливість досліджуваної структури охоплює діапазон енергій фотонів 0,387÷1,016 еВ, зміщений у довгохвильову область. Формування приповерхневого шару з високим опором сприяє підвищенню відгуку та дозволяє досягти значень фоточутливості до 0,338 А/Вт. Було виявлено, що зменшення бар'єрної ємності до 8÷10 пФ розширює діапазон частот та підвищує швидкість відгуку. Структури Ag–nSi–n^+Si–(In+Sn) є перспективними для використання у фотодіодах оптоелектронних пристроїв, що працюють у видимому та інфрачервоному діапазонах спектра.

Ключові слова: *структура; гомоперехід; характеристика; індекс; механізм; ємність; бар'єр; фотогенерація; фоточутливість; фотострум; інтенсивність; фотодіод*

MODIFICATION OF THE KINETIC PARAMETERS OF *SnSe* BY TERBIUM DOPING

T.A. Jafarov[1], ⬤O.M. Gasanov[1], Kh.A. Adgezalova[1], H.A. Aslanov[1], ⬤J.I. Huseynov[1]*, ⬤I.I. Abbasov[2], R.Sh. Ragimov[3]

[1]Azerbaijan State Pedagogical University, AZ-1000, Baku, Uz. Hajibeyli Str. 68, Azerbaijan
[2]Azerbaijan State Oil and Industry University, Az-1010, Baku, Azadlıq Avenue 20, Azerbaijan
[3]Baku State University, AZ-1148, Baku, Zahid Xalilov Str. 23, Azerbaijan
Corresponding Author email: jahangirhuseynov1958@gmail.com

The kinetic parameters of solid solutions $Tb_xSn_{1-x}Se$ ($0 \leq x \leq 0.05$), grown by the Bridgman method, were investigated at 300 K. It was found that doping with Tb significantly affects the electrical conductivity, Hall coefficient, Seebeck coefficient (thermoelectric power), thermal conductivity, and the concentration and mobility of charge carriers. At low Tb concentrations, a transition from p-type to n-type conductivity is observed, accompanied by a non-monotonic change in the Hall coefficient and the sign of the Seebeck coefficient. Electrical and thermal conductivities decrease due to enhanced scattering at defects caused by introducing Tb. The obtained data are important for controlling the properties of SnSe in its thermoelectric applications.

Keywords: *Solid solutions; Kinetic parameters; Doping; Thermoelectric properties; Seebeck coefficient; Electrical conductivity; Thermal conductivity; Carrier concentration; Conductivity type transition*
PACS: 71.20.Nr, 72.20.Pa, 61.72.-y

1. INTRODUCTION

Tin selenide $(SnSe)$ is a binary semiconductor compound with an orthorhombic ($Pnma$) layered structure, characterized by pronounced anisotropy, low thermal conductivity, and high thermoelectric performance. The presence of Sn atom vacancies in the crystal lattice results in $p-$type conductivity [1–3].

Due to its high Seebeck coefficient, low thermal conductivity, and sufficient electrical conductivity, $SnSe$ is considered one of the best thermoelectric materials, especially in single-crystal form ($ZT \approx 2.6 - 2.8$ $at \sim 900 K$). Its bandgap width ($0.9 - 1.3$ eV) also makes it promising for optoelectronic applications. The ease of mechanical cleavage further supports the use of $SnSe$ in flexible electronics [4–6].

The material consists of non-toxic and non-deficient elements, which is important from both environmental and economic perspectives. The properties of $SnSe$ can be effectively tuned through doping and cation substitution. The introduction of elements such as Na, Ag, and K (for $p-$type) or Bi, Cl, and I (for $n-$type) allows control over the charge carrier concentration. Substituting Sn with Pb, Ge, Mn, Co, and other cations affects the structure and functional properties, including reduced thermal conductivity and the emergence of new properties [7–10].

Particular interest lies in doping with rare-earth elements (e.g., La, Ce, Gd), which enhance conductivity and reduce thermal conductivity due to local lattice distortions [11–13]. Among them, terbium (Tb) is especially promising; its ions can act as donors, increasing the electron concentration and promoting $n-$type behavior. Substituting Sn with Tb also enhances phonon scattering, reduces thermal conductivity, and may introduce localized energy levels [14]. This study investigates the effect of Tb content on the key kinetic parameters of $Tb_xSn_{1-x}Se$ alloys at a temperature of $300 K$.

2. EXPERIMENTAL SECTION

For the synthesis of $Tb_xSn_{1-x}Se$ alloys, high-purity starting materials were used: tin of grade B4-000, selenium of grade OC417-4, and chemically pure terbium (99.98%). The synthesis was performed in evacuated quartz ampoules at a pressure of 0.1333 Pa using a two-step direct melting method. In the first stage, the ampoules containing the weighed components were heated at a rate of $4 - 5$ $°C/min$ to the melting point of selenium and held at that temperature for $3 - 4$ $hours.$ Subsequently, the temperature was gradually increased to $950 - 1000 °C$ (depending on the composition) and maintained for $8 - 9$ $hours$ [15].

The interaction in the $SnSe - TbSe$ system was investigated using differential thermal analysis (DTA), $X-$ray diffraction (XRD), microstructural analysis (MSA), as well as measurements of microhardness and density [16]. DTA was conducted using a PerkinElmer Simultaneous Thermal Analyzer STA 6000 (USA) to determine the thermal effects and phase transitions of the synthesized samples. Nitrogen was used as the purge gas at a flow rate of 20 $mL/s,$ and the samples were heated to their melting temperatures at a rate of 5 $°C/min.$

$X-$ray diffraction analysis was performed using a Rigaku Miniflex diffractometer operating at 30 kV and 10 mA with $CuK\alpha$ radiation ($\lambda = 1.5406$ Å). Diffraction peaks were recorded over a 2θ range of $0 - 80°$. The surface

morphology and microstructure of the samples were examined using a JEOL JSM-6610LV scanning electron microscope (Japan).

Electrical conductivity and the Hall coefficient were measured under direct current conditions in a constant magnetic field using an electromagnet setup [17]. The Seebeck coefficient and thermal conductivity were determined using a fully stationary method, as described in [18]. The experimental uncertainty did not exceed 4.2%.

3. RESULTS AND DISCUSSION
3.1. Physicochemical Analysis

The thermograms of the alloys in the $Tb_xSn_{1-x}Se$ system show sharp peaks during heating and cooling, which correspond to the melting and solidification temperatures, indicating the formation of congruently melting alloys. In the $SnSe$ compound, partial substitution of Sn with Tb lowers the melting temperature due to the incorporation of larger rare-earth (RE) ions, which distort the crystal lattice and weaken interatomic bonds. This leads to structural defects and an additional decrease in melting temperature. The microhardness of samples with $TbSe$ content up to $0.05\ mol.\%$ remains at the level of $\sim500\ MPa$.

Analysis of the intensity of $X-$ray reflections shows that the sample has a preferred crystal orientation and consists of a single phase. Indexing of the $X-$ray patterns indicate an orthorhombic crystal system with the space group $D_{2h}^{16} - Pcmn$ (Fig. 1). In the range $0 \leq x \leq 0.05$, no shift in diffraction lines is observed; only their intensity changes, which indicates the formation of solid solutions based on $SnSe$. When Sn atoms are partially replaced with RE atoms of larger ionic radius, the intensity of reflections decreases, and the lattice parameters increase additively. The increase in parameters is linear, with no deviations from Vegard's law observed.
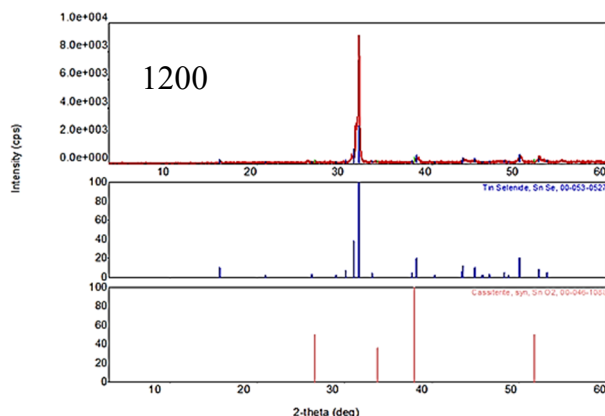
Figure 1. X-ray diffraction spectrum of crystals Tb$_x$Sn$_{1-x}$Se:x=0,0025. Below are X-ray diffraction patterns of SnSe and SnO for comparison

$X-$ray structural analysis shows that the addition of terbium selenides leads to an increase in the unit cell parameters of $SnSe$ as the concentration of Tb increases. This is accompanied by intense charge-carrier scattering due to lattice distortion, consistent with the low thermal conductivity of the alloys [16]. At the same time, the density of the $Tb_xSn_{1-x}Se$ system remains practically unchanged, indicating interstitial positioning of Tb atoms and the formation of Frenkel-type defects [19].

The increase in lattice parameters, the coherent substitution of Sn with Tb, and adherence to Vegard's law confirm the formation of a substitutional solid solution based on $SnSe$. $X-$ray structural analysis and pycnometry revealed that the solubility range of $TbSe$ in $SnSe$ at room temperature is limited to $2\ mol.\%$.

Comprehensive physicochemical analysis showed that the $Tb_xSn_{1-x}Se$ system alloys, like $SnSe$, crystallize in an orthorhombic crystal system. With an increase in $TbSe$ content, the lattice parameters, density, and microhardness increase slightly, while the thermal effects shift to lower temperatures. Due to differences in the electronic configuration of Sn and Tb, substitution in the $Tb_xSn_{1-x}Se$ solid solution leads to distortions in the $SnSe$ crystal lattice, while preserving its basic structure.

Atomic force microscopy of the surface topography of $Tb_xSn_{1-x}Se$ crystals revealed that the natural surface is inhomogeneous and has a roughness of about $25\ nm$. This is due to the presence of weak van der Waals forces between the layers, which lead to the formation of atomic clusters upon cleavage, giving the surface an uneven appearance. $X-$ray microanalysis revealed the phase composition and element distribution (Fig. 2). The surface was generally homogeneous; however, an excess of selenium was observed within the homogeneity range of $SnSe$.

Element	Weight %	Atomic %
Sn L	59.69	49.72
Se L	39.90	50.03
Tb L	0.41	0.25
Total	100	100
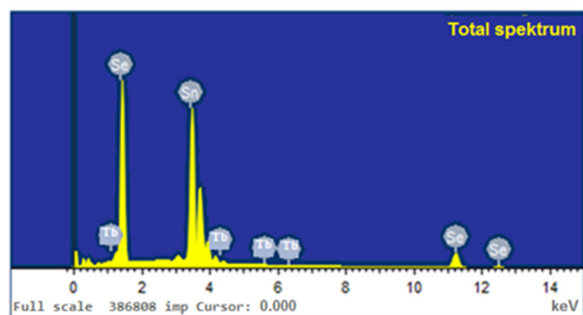
Figure 2. X-ray microanalysis of the crystal surface Tb$_x$Sn$_{1-x}$Se:(x=0.005)

3.2. Electrophysical and Thermal Properties of $Tb_xSn_{1-x}Se$ Alloys at Various Tb Concentrations

In the solid solution range of ($0 \leq x \leq 0.05$), several kinetic parameters were investigated at room temperature ($300\,K$) for $TbSe$ − containing samples grown by the Bridgman method. These parameters include electrical conductivity (σ), Hall coefficient (R), thermopower (S), thermal conductivity coefficient (k), charge carrier concentration (p, n), and Hall mobility (μ). The obtained results are summarized in Table 1.

$SnSe$ is typically a p −type semiconductor, and its charge transport properties are highly sensitive to doping. As seen from Table 1, with increasing $TbSe$ content in $Tb_xSn_{1-x}Se$ alloys, the resistivity and Hall coefficient increase, while the carrier concentration and mobility decrease.

In the binary compound $SnSe$, with partial cation-cation substitution of Sn atoms by Tb atoms at room temperature ($T = 300\,K$), the Hall coefficient (R) strongly depends on the percentage of Tb atoms and varies non-monotonically. This non-monotonic change in the absolute value of the Hall coefficient is explained by the competition of two or more mechanisms depending on impurity concentration.

The $SnSe$ compound, in the absence of doping impurities, consistently exhibits p-type conductivity, which has been confirmed both by experimental measurements and quantum-chemical calculations [20, 21]. The primary reason for this is the presence of intrinsic defects in the crystal lattice—primarily tin cation vacancies (V_{Sn}), which act as acceptor centers and promote hole generation.

The formation of such vacancies can be explained in terms of the atomic properties and electronic structure of $SnSe$. First, tin (Sn) has a relatively low ionization energy (first ionization energy ∼7.34 eV [22]), which facilitates the loss of valence electrons and the transition of Sn atoms to the Sn^{2+} ionic state. Second, selenium (Se), with its high electronegativity (2.55 on the Pauling scale [20]), strongly attracts electrons from the $Sn - Se$ covalent bond, thereby further polarizing and weakening this bond. As a result, Sn cations become less stable in the lattice, especially under Se −rich synthesis conditions, which promotes the formation of cation vacancies

Table 1. The main kinetic parameters of $Tb_xSn_{1-x}Se$ alloys at T = 300 K

Composition, x, mol%	R, cm³/K	S, μV/K	σ, Ω⁻¹·cm⁻¹	$k\times10^{-5}$, W/(m·K)	μ, cm²/(V·s)	p(n)×10¹⁷, cm⁻³
0.00	+8.68	+420	18	20	156	7.2
0.10	+25.7	+275	2.42	18	60.5	2.43
0.20	+32.3	+128	0.45	17	14.5	1.93
0.25	-180	-325	0.027	16.4	4.86	0.347
0.50	-1750	-298	0.012	14.5	21.12	0.036
1.00	-1260	-297	0.0063	12.5	6.50	0.05
1.5	-1040	-278	0.0061	12	6.34	0.06
2.00	-898	-262	0.006	11.8	5.39	0.07
2.5	-420	-258	0.012	11.2	5.04	0.15
3.00	-245	-250	0.028	10.7	6.86	0.26
3.5	-176	-246	0.035	9.9	6.16	0.36
4.00	-70	-235	0.04	9	2.82	0.89
4.5	-54	-227	0.043	11.3	2.3	1.16
5.00	-41.6	-210	0.047	14.5	3	1.5

From the standpoint of modern defect thermodynamics, the formation of a cation vacancy in SnSe under thermodynamic equilibrium can be described by the reaction:

$$Sn_{site} \rightarrow V_{Sn}^{''} + 2h^+ + Sn_{(qaz)},$$
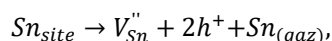
where $V_{Sn}^{''}$ is a doubly negatively charged Sn cation vacancy and h^+ denotes a hole (positive charge carrier) [23]. Such a defect type is thermodynamically stable under slight deviations from stoichiometry, particularly in the case of a tin deficit [19]. These holes can move freely, thus ensuring p-type conductivity [20]. Consequently, the formation of vacancies is accompanied by an increase in the hole concentration that determines the p-type conduction.

Density Functional Theory (DFT) calculations confirm that the formation energy of Sn cation vacancies is significantly lower than that of other intrinsic defects (such as Se vacancies or antisite defects), especially under Se −rich conditions [20]. This indicates the thermodynamic preference for such defects, consistent with p-type conductivity.

In binary $SnSe$, partial cation–cation substitution of Sn by Tb atoms lead to strong dependence of the Hall coefficient (R) on the Tb concentration at room temperature ($T = 300\,K$), with a non-monotonic variation (Fig. 3). The non-monotonic change in the absolute value of the Hall coefficient can be explained by the competition of two or more mechanisms depending on the impurity concentration.

At low Tb concentrations, the Hall coefficient is positive, indicating dominant hole-type conduction. As the Tb concentration increases in $Sn_{1-x}Tb_xSe$ alloys, the increase of R_H from +8.68 to +32.3 cm^3/C reflects a decrease in carrier concentration and possible formation of acceptor levels due to the substitution of Sn^{2+} by Tb^{3+}. The sharp sign reversal from positive to negative at 0.25 $mol\%\,Tb$ indicates an inversion of conduction type from hole to electron

conduction. This may be attributed either to the transition of Tb from acceptor to donor behavior or to band structure modifications that generate effective electron states.

During cation substitution, Tb atoms, according to their electronic configuration $(1s^2\ 2s^2\ 2p^6\ 3s^2\ 3p^6\ 4s^2\ 3d^{10}\ 4p^6\ 5s^2\ 4d^{10}\ 5p^6\ 6s^2\ 4f^9)$, act as donors. At low Tb concentrations, partial substitution of Sn^{2+} ions by Tb^{3+} introduces donor electrons. These donors compensate part of the holes, thereby neutralizing them. At low impurity levels, compensation starts and the charge carrier concentration decreases [24]. As a result, although the overall hole concentration decreases ($x \leq 0.002$), holes remain the dominant carriers. The compensation of holes leads to an increase in the positive value of the Hall coefficient.
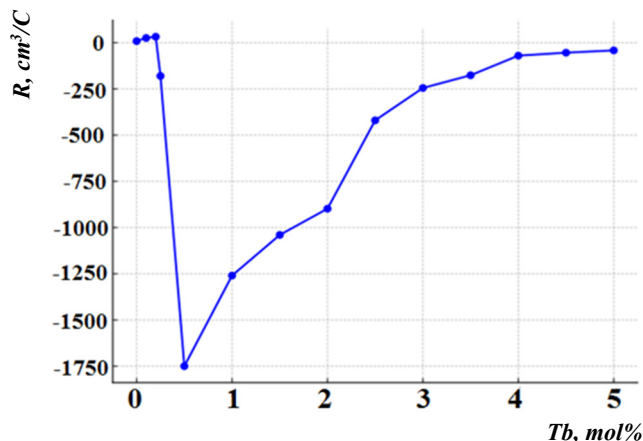

Figure 3. Composition dependence of the Hall coefficient of $Tb_xSn_{1-x}Se$ system alloys

However, at a critical impurity concentration ($x \approx 0.002 - 0.0025$), donor electrons fully compensate holes, reducing the net carrier concentration to nearly zero (the compensation point). This represents a typical conductivity-type transformation in semiconductors, and the corresponding composition can be characterized as the compensation point. Near this transition, the electron concentration approaches that of holes ($p \approx n$), indicating maximum compensation.

At the inversion point of conductivity type (transition from hole to electron conduction), the Hall coefficient R_H is described by the two-carrier model, since both electrons and holes are present and contribute competitively. The generalized expression for the Hall coefficient in a two-carrier system is:

$$R_H = \frac{p\mu_p^2 - n\mu_n^2}{e(p\mu_p + n\mu_n)^2},$$

where $p -$ is the hole concentration, n- is the electron concentration, μ_p and μ_n are the mobilities of holes and electrons, respectively, and $e -$ is the elementary charge [25]. At the inversion point, the condition $p\mu_p^2 = n\mu_n^2$ is satisfied, and $R_H = 0$. When $p\mu_p^2 < n\mu_n^2$, R_H becomes negative, indicating electron dominance.

Thus, the observed sign reversal and sharp increase in the absolute value of the Hall coefficient at $x = 0.0025$ (0.25 $mol\%$) in $Tb_xSn_{1-x}Se$ alloys is a key transition point in the electronic structure of the material. The transition to negative values demonstrates a shift to electron-type conduction, showing that Tb acts effectively as a donor, introducing electrons into the conduction band [13].

At the composition corresponding to $x = 0.0025$, the sign of the Hall coefficient becomes negative, and its absolute value sharply increases, reaching approximately $-1750\ cm^3/C$, indicating a sudden change in the dominant charge carriers from holes to electrons. With further increase in dopant content, the hole carriers are compensated, and then electrons begin to dominate, resulting in a change in the Hall coefficient's sign from positive to negative. The change in conductivity type, i.e., the transition from $p -$ to $n -$ type, is explained by the substitution of Sn^{2+} ions with Tb^{3+} ions, which leads to the generation of additional electrons and the dominance of donor-type defects in the system. Consequently, $p -$type conductivity transforms into $n -$type, causing a sharp change in the alloy's electrophysical properties [26]. Such transition points are of particular significance in terms of controlling the functional properties of materials and open up possibilities for their tuning in future applications.

With increasing terbium (Tb) content, the absolute value of the Hall coefficient decreases, while its sign remains negative across the entire concentration range, indicating the predominance of electrons as the main charge carriers. In the concentration range $0.0025 < x < 0.025$, the Hall coefficient decreases especially sharply. This is presumably due to the effective donor action of Tb, which significantly increases the concentration of free electrons.

As the Tb content further increases ($x > 0.025$), the decrease slows down. This behavior may be due to donor state saturation, where further introduction of Tb no longer leads to a significant increase in carrier concentration. Additionally, enhanced scattering effects or the formation of localized states may occur, reducing carrier mobility and thereby stabilizing the Hall coefficient value [27].

As shown in the table, the carrier concentration (P) initially decreases from $7.2 \times 10^{17} \, cm^{-3}$ to a minimum value of about $0.036 \times 10^{17} \, cm^{-3}$ at $0.5 \, mol\%$, indicating carrier compensation due to charge capture or the formation of recombination centers. With further increase in Tb content, the carrier concentration rises, reaching $1.5 \times 10^{17} \, cm^{-3}$ at $5 \, mol\%$. This indicates a shift in the role of Tb in the material – from a compensator to a donor capable of generating free electrons in the conduction band [27].

As seen from the table, the carrier concentration (p) decreases from $7.2 \times 10^{17} \, cm^{-3}$ to a minimum value of approximately $0.036 \times 10^{17} \, cm^{-3}$ with the initial introduction of Tb up to $0.5 \, mol\%$, indicating compensation of carriers due to charge trapping or the formation of recombination centers. With a further increase in Tb content, the carrier concentration rises, reaching $1.5 \times 10^{17} \, cm^{-3}$ at $5 \, mol\%$. This indicates a change in the role of Tb in the material – from a compensator to a donor capable of generating free electrons in the conduction band [28].

For pure SnSe at room temperature, the Seebeck coefficient lies in the range of $S \approx +400 \, to +500 \, \mu V/K$ (in the table, this value is approximately $+420 \, \mu V/K$). Such a high value is attributed to the low carrier concentration and to an anomalous density-of-states function at the energy levels. As the temperature increases, the Seebeck coefficient in $SnSe$ rises, reaching values around $600 - 800 \, \mu V/K$ at elevated temperatures $(500 - 800 \, K)$ [29]. These characteristics highlight the high potential of $SnSe$ as a thermoelectric converter at elevated temperatures. The combination of these properties gives this material a leading position among high-efficiency thermoelectric materials.

With an increase in terbium content in solid solutions of $Tb_xSn_{1-x}Se$, the Seebeck coefficient (S) initially decreases sharply and then, after crossing into negative values, becomes relatively stabilized (see Fig. 4). In the initial region $(0 \leq x \leq 0.002 \, mol\%)$, a rapid decrease in the positive Seebeck coefficient is observed—from $+420 \, \mu V/K$ to $+128 \, \mu V/K$. This indicates a reduction in the contribution of positive charge carriers (holes) to the thermoelectromotive force. This decrease is explained by the partial substitution of Sn^{2+} ions with Tb^{3+} ions, leading to the emergence of a donor effect and the formation of additional electronic states contributing to the generation of electrons in the conduction band. This partial substitution disrupts the crystal lattice's symmetry, enhances carrier scattering, and thus reduces their transport efficiency.
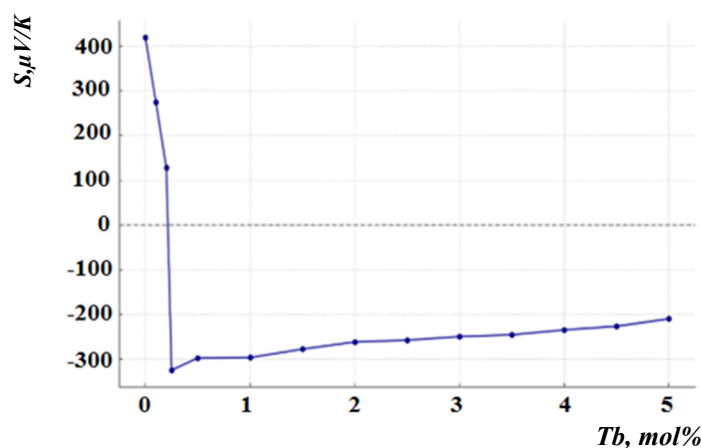
Figure 4. Composition dependence of theSeebeck coefficient of
$Tb_xSn_{1-x}Se$ system alloys $Sn_{1-x}Tb_x$

In the narrow interval of $0.002 < x < 0.0025 \, mol\% \, Tb$, a sign inversion of the Seebeck coefficient is observed: its value changes from $+128 \, \mu V/K$ to $-325 \, \mu V/K$, indicating a change in the dominant type of charge carriers – from hole-type $(p-\text{type})$ to electron-type $(n-\text{type})$ conductivity. This is associated with reaching a critical concentration of Tb at which the Fermi level shifts close to the conduction band, and electrons become the predominant carriers [30]. Terbium atoms create localized energy levels near the conduction band, which are easily ionized and participate in electron transport.

After the change in conductivity type, in the range of $0.0025 < x < 0.015 \, mol\% \, Tb$, the Seebeck coefficient stabilizes in the negative region. This indicates the formation of a new carrier balance dominated by electrons, saturation of the Tb donor levels, stabilization of the energy structure, and an increase in the material's homogeneity.

In the interval of $0.02 < x < 0.05 \, mol\% \, Tb$, a gradual decrease in the absolute value of the Seebeck coefficient is observed, which is caused by an increase in free electron concentration, reducing the chemical potential gradient – the main factor determining the thermoelectromotive force. Possible interactions between Tb atoms that lead to electron localization or changes in their effective mass, as well as the ordering of bulk defects in the crystal lattice due to the elevated Tb content, also contribute to the reduction in thermoelectric voltage [31].

As shown in Figure 5, the dependence of the electrical conductivity of $Tb_xSn_{1-x}Se$ solid solutions on the Tb content exhibits a non-monotonic character based on experimental data. According to the presented table, at x = 0, the system's electrical conductivity is high, amounting to $\sigma = 18 \, \Omega^{-1} \cdot cm^{-1}$. However, with an increase in Tb concentration from 0.1 to $2 \, mol.\%$, the conductivity sharply decreases, reaching a minimum value $(\sigma \approx 0.006 \, \Omega^{-1} \cdot cm^{-1})$. This effect

is consistent with the literature data [32], which indicate that the introduction of Tb^{3+} ions into the $SnSe$ lattice leads to distortions in the crystal structure, the formation of local energy levels and recombination centers, thereby reducing the concentration of free charge carriers and, consequently, the electrical conductivity.

Figure 5. Composition dependence of the specific electrical conductivity
of $Tb_xSn_{1-x}Se$ system alloys

This process is explained by the occurrence of lattice distortions due to the incorporation of Tb^{3+} ions into the SnSe crystal lattice, the appearance of localized energy levels, and increased scattering of charge carriers. The difference in valence between Tb and Sn ions ($Tb^{3+} \rightarrow Sn^{2+}$) leads to the formation of compensation and recombination centers in the system, which in turn reduces the concentration of free charge carriers [17].
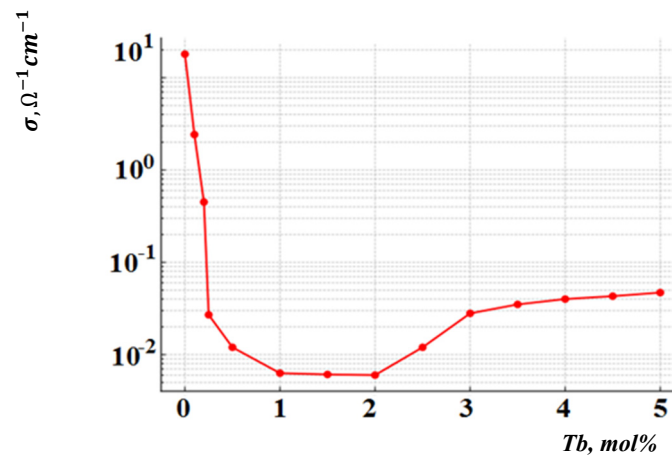
With a further increase in Tb content above $2\ mol.\%$, the electrical conductivity begins to gradually increase. This growth can be explained by the formation of additional conductive levels in the energy band after reaching the critical concentration of Tb atoms, the manifestation of the percolation effect, and the weakening of the degree of carrier localization. Thus, the mobility of charge carriers in the system is partially restored, resulting in an increase in electrical conductivity.

These observations indicate that the electrical conductivity in the $Tb_xSn_{1-x}Se$ system significantly depends not only on the number of free carriers but also on their energy state and scattering processes within the crystal structure. Such non-monotonic dependence is typically explained by the localization-delocalization transition, structural distortions, and percolation theory.

The study of the dependence of the alloys' thermal conductivity on the terbium (Tb) content revealed that as the Tb concentration increases from 0 to $4.0\ mol\%$, the material's thermal conductivity gradually decreases—from $20 \times 10^{-5}\ W/(m \cdot K)$ to $9 \times 10^{-5}\ W/(m \cdot K)$. However, with further increases in Tb concentration, the opposite trend is observed—thermal conductivity rises to $14.5 \times 10^{-5}\ W/(m \cdot K)$ at $5.0\ mol\%$. This behavior can be explained by changes in the alloy's microstructure. At the initial stage of Tb incorporation, impurity atoms distort the crystal lattice due to differences in atomic radii and mass, which enhances phonon scattering—the main carriers of heat in solids. Moreover, increasing Tb concentration leads to a higher number of point defects and disorder, further hindering heat transport. These effects account for the observed decrease in thermal conductivity [33].

When the threshold concentration ($\sim 4\ mol\%$) is exceeded, it is likely that a new phase or an ordered structure forms, in which the level of phonon scattering decreases. This may be associated with a phase transition accompanied by structural stabilization and a reduction in defect density. As a result, an increase in thermal conductivity is observed despite the continued increase in Tb content [34]. The obtained data indicate a complex dependence of thermal conductivity on alloy composition, driven by the competition between phonon scattering at defects and structural rearrangement of the material at high Tb concentrations.

The dependence of the Hall mobility of free carriers on Tb concentration in the alloys is distinctly nonlinear. As the Tb content increases from 0 to $\sim 2.5\ mol\%$, there is a sharp decrease in mobility, attributed to enhanced scattering of charge carriers at lattice defects introduced by Tb atoms. Terbium atoms, differing in size and valence, induce distortions in the crystal lattice and promote the formation of localized states that serve as effective scattering centers. Additionally, the possible formation of traps associated with $Tb\ 4f-$electron levels also contributes to reduced mobility. At higher concentrations ($2.5-4.5\ mol\%$), the character of the dependence becomes more complex: fluctuations are observed, likely due to Tb atom clustering, secondary phase formation, or changes in the charge transport mechanism [35]. Magnetic scattering associated with local magnetic moments of Tb may also play a role. Thus, the reduction in mobility with increasing Tb concentration is determined by a complex interplay of structural, electronic, and magnetic factors.

In summary, doping $SnSe$ with terbium leads to complex changes in thermal and electrical properties, caused by structural and electronic transformations within the system. These results are essential for understanding the

mechanisms of heat and charge transport in doped semiconductors and enable optimization of compositions for thermoelectric and other functional applications.

CONCLUSIONS

The study demonstrated that doping the SnSe semiconductor with terbium (Tb) significantly alters its electronic and thermal properties, thereby altering the mechanisms of charge and heat transport. Depending on the Tb content, phase and functional transitions are observed, including a change in the type of conductivity from $p-$type to $n-$type, which is accompanied by a sharp restructuring of kinetic parameters — the Hall coefficient, thermoelectric power (Seebeck coefficient), electrical conductivity, and others.

A charge carrier compensation point has been identified, at which maximum suppression of conductivity occurs — an important characteristic for tuning the functional properties of the material. Doping leads to a significant decrease in thermal conductivity due to enhanced phonon scattering, which is a favorable factor for thermoelectric applications. The observed nonmonotonic dependencies of parameters on Tb concentration are associated with the competition between donor and compensating effects, carrier localization, and structural changes in the crystal lattice.

The obtained results provide a basis for the targeted control of the properties of $SnSe-$like materials and for optimizing their composition for thermoelectric and sensor applications.

ORCID

O.M. Gasanov, https://orcid.org/0000-0003-4888-7686; **J.I. Huseynov**, https://orcid.org/0000-0002-4498-2400
I.I. Abbasov, https://orcid.org/0000-0001-8111-2642

REFERENCE

[1] A.T. Buruiana, C. Mihai, V. Kuncser, and A. Velea, "Advances in 2D Group IV Monochalcogenides: Synthesis, Properties, and Applications," Materials, **18**(7), 1530 (2025). https://doi.org/10.3390/ma18071530

[2] J. Rundle, and S. Leoni, "Layered Tin ChalcogenidesSnS and SnSe: Lattice Thermal Conductivity Benchmarks and Thermoelectric Figure of Merit," The Journal of Physical Chemistry C, **126**(33), 14036–14046, (2022); https://doi.org/10.1021/acs.jpcc.2c02401

[3] J.M. Flitcroft, I. Pallikara, and J. M. Skelton, "Thermoelectric Properties of Pnma and RocksaltSnS and SnSe," Solids, **3**(1), 155–176 (2022). https://doi.org/10.3390/solids3010011

[4] M. Yadav, V. Singh, S.K. Sharma, *et al.* "Temperature driven n- to p-type conduction switching in SnSe and its mitigation through Zn doping with added advantage of Improved thermoelectric performance," Emergent Materialse, **8**, 3753–3760 (2024). https://doi.org/10.1007/s42247-024-00873-0

[5] N. Zakay, A. Schlesinger, U. Argaman, *et al*. "Electrical and Optical Properties of γ-SnSe: A New Ultra-narrow Band Gap Material," ACS Applied Materials &Interfaces, **15**(12), 15668–15675 (2023). https://doi.org/10.1021/acsami.2c22134

[6] M. Kumar, S. Rani, P. Vashishtha, *et al*. "Exploring the optoelectronic properties of SnSe: a new insight," Journal of Materials Chemstry C**, 10,** 16714-16722 (2022). https://doi.org/10.1039/D2TC03799H

[7] A.Q. Zhao, B. Qin, D. Wang, Y. Qiu, and L.-D. Zhao, "Realizing High Thermoelectric Performance in Polycrystalline SnSe via Silver Doping and Germanium," ACS Appl. Energy Mater. **3**, 2049−2054 (2020). https://doi.org/10.1021/acsaem.9b01475

[8] A. Duong, V. Nguyen, G. Duvjir, *et al.* "Achieving ZT=2.2 with Bi-doped n-type *SnSe* single crystals," Nat Commun, **7**, 13713 (2016). https://doi.org/10.1038/ncomms13713

[9] Y. Shu, X. Su, H. Xie, *et al*. "Modification of Bulk Heterojunction and Cl Doping for High-Performance Thermoelectric SnSe₂/SnSe Nanocomposites." ACS Appl Mater Interfaces, **10**(18), 15793-15802 (2018). https://doi.org/10.1021/acsami.8b00524

[10] R.Md. Aspan, N. Fatima, R. Mohamed, U. Syafiq, and M.A. Ibrahim, "An Overview of the Strategies for Tin Selenide Advancement in Thermoelectric Application," Micromachines, **12**, 1463 (2021). https://doi.org/10.3390/mi12121463

[11] F. Li, W. Wang, Z-H. Ge, *et al*. "Enhanced Thermoelectric Properties of Polycrystalline SnSe via LaCl₃ Doping," Materials (Basel), **11**(2), 203 (2018). https://doi.org/10.3390/ma11020203

[12] Y. Qin, T. Xiong, J-F. Zhu, *et al.* "Realizing high thermoelectric performance of Cu and Ce co-doped p-type polycrystalline SnSe via inducing nanoprecipitation arrays," Journal of Advanced Ceramics, **11**, 1671–1686 (2022). https://doi.org/10.1007/s40145-022-0639-6

[13] I.I. Abbasov, Sh.S. Ismailov, V.A. Abdurahmanova, *et al*. "Concentration dependences of electrical conductivity and the Hall effect of the *CeₓSn₁-ₓSe* single crystals," Low Temperature Physics, **45**, 1277–1280 (2019). https://doi.org/10.1063/10.0000209

[14] J.I. Huseynov, and T.A. Jafarov, "Effect of γ-ray radiation on electrical properties of heat-treated *TbₓSn₁-ₓSe* single crystals," Semiconductors, **46**, 430–432 (2012). https://doi.org/10.1134/S1063782612040082

[15] J.I. Huseynov, and T.A. Jafarov, "The Influence of γ-Irradiation on Thermoemf and Heat Conduction of *Ln₀.₀₁Se₀.₉₉* (*Ln – Pr, Tb, Er*) Monocrystals," World Journal of Condensed Matter Physics, **4**(1), 1-5 (2014). http://dx.doi.org/10.4236/wjcmp.2014.41001

[16] I.I. Aliev, M.I. Murguzov, Sh.S. Ismailov, *et al.* "Phase relations and properties of alloys in the SnSe-DySe system," Inorg. Mater. **50**, 237–240 (2014). https://doi.org/10.1134/S0020168514030029

[17] J.I. Huseynov, M.I. Murguzov, and S.S. Ismayilov, "Specific features of self-compensation in *ErₓSn₁-ₓSe* solid solutions," Semiconductors, **47**, 323–326 (2013). https://doi.org/10.1134/S106378261303010X

[18] J.I. Huseynov, M.I. Murguzov, S.S. Ismayilov, *et al. "*On the thermopower and thermomagnetic properties of *ErₓSn₁-ₓSe* solid solutions." Semiconductors, **51**, 153–157 (2017). https://doi.org/10.1134/S1063782617020075

[19] J.I. Huseynov, K.A. Hasanov, T.A. Jafarov, and I.I. Abbasov, "Compensating Effect of Terbium Impurity on the Conductivity of *TbₓSn₁-ₓSe* Solid Solutions," Ukrainian journal of physics, **65**(3), 225-230 (2020). https://doi.org/10.15407/ujpe65.3.225

[20] Y. Huang, C. Wang, X. Chen, *et al*. "First-principles study on intrinsic defects of SnSe," RSC Advances, (44), 27139 – 27832 (2017).https://doi.org/10.1039/c7ra03367b

[21] S. Gowthamaraju, U.P. Deshpande, S. Anwar, *et al.* "Effect of vacancy on thermoelectric properties of polycrystalline SnSe," J. Mater. Sci: Mater. Electron. **32**, 11568–11576 (2021). https://doi.org/10.1007/s10854-021-05750-8

[22] Y. Gong, W. Dou, B. Lu, *et al.* "Divacancy and resonance level enables high thermoelectric performance in n-type SnSe polycrystals," Nat Commun. **15**(1), 4231 (2024). https://doi.org/10.1038/s41467-024-48635-0

[23] A.K. Tolloczko, S.J. Zelewski, J. Ziembicki, *et al.* "Photoemission Study of the Thermoelectric Group IV-VI van der Waals Crystals (GeS, SnS, and SnSe)," Advanced Optical Materials, **12**(6), 2302049 (2024). https://doi.org/10.1002/adom.202302049

[24] M.R. Shankar, A.N. Prabhu, A.M. Ashok, *et al.* "Role of Bi/Te co-dopants on the thermoelectric properties of SnSepolycrystals: an experimental and theoretical investigation,"Journal of Materials Science,**59**, 13055–13077 (2024). https://doi.org/10.1007/s10853-024-09984-9

[25] J.E. Dill, C.F.C. Chang, D. Jena, and H.G. Corre, "Two-carrier model-fitting of Hall effect in semiconductors with dual-band occupation: A case study in GaN two-dimensional hole gas," J. Appl. Phys. **137**, 025702 (2025). https://doi.org/10.1063/5.0248998

[26] C. Zhang, X-G. He, H. Chi, *et al.* "Electron and hole contributions to normal-state transport in the superconducting system $Sn_{1-x}In_xTe$," Phys. Rev. B, **98**, 054503 (2018). https://doi.org/10.1103/PhysRevB.98.054503

[27] X. Cui, T. Hu, H. Wu, *et al.* "Charge Carrier Transport Behavior and Dielectric Properties of BaF_2:Tb^{3+} Nanocrystals," Nanomaterials, **10**(1), 155 (2020). https://doi.org/10.3390/nano10010155

[28] I.I. Abbasov, and J.I. Huseynov, "Charge-transfer Processes in $(SnS)_{1-x}(PrS)_x$ Alloys," Ukr. J. Phys. **62**(10), 883-888 (2017). https://doi.org/10.15407/ujpe62.10.088

[29] A. Golabek, N.K. Barua, E. Niknam, L.T. Menezes, and H. Kleinke, "Large Improvements in the Thermoelectric Properties of SnSe by Fast Cooling," Materials, **18**(2), 358 (2025). https://doi.org/10.3390/ma18020358

[30] K.A. Hasanov, V.V. Dadashova, F.F. Aliyev, *et al.* "Effect of Phonon Drag on the Thermopower in a Parabolic Quantum Well," Semiconductors, **50**, 295–298 (2016). https://doi.org/10.1134/S106378261603009X

[31] J.I. Huseynov, M.I. Murquzov, and R.F. Mamedova, "Thermal Conductivity and Termal EMF of Materials for Thermal Energy Converters," in: *TPE-06 3rd Intern. Conf. on Technical and Physical Problems in Power Engineering*, (Ankara, 2008).

[32] D.I. Huseynov, M.I. Murguzov, and S.S. Ismailov, "Thermal conductivity of $Er_xSn_{1-x}Se$ ($x \leq 0.025$) solid solutions." Inorg Mater, **44**, 467–469 (2008). https://doi.org/10.1134/S0020168508050063

[33] Sh.S. Ismailov, M.A. Musaev, I.I. Abbasov, V.A. Abdurahmanova, *et al.* "Effect of doping level and compensation on thermal conductivity in $Ce_xSn_{1-x}Se$ solid solutions," Low Temperature Physics,**46**, 1114–1120 (2020). https://doi.org/10.1063/10.0002155

[34] C.-W.T. Lo, Sh. Song, Y-Ch. Tseng, *et al.* "Microstructural Instability and Its Effects on Thermoelectric Properties of SnSe and Na-Doped SnSe," ACS Appl. Mater. Interfaces, **16**(37), 49442–49453 (2024). https://doi.org/10.1021/acsami.4c11319

[35] X. He, H. Zhang, T. Nose, *et al.* "Degenerated Hole Doping and Ultra-Low Lattice Thermal Conductivity in Polycrystalline SnSe by Nonequilibrium Isovalent Te Substitution," Advanced Science, **9**(13), 2105958 (2022). https://doi.org/10.1002/advs.202105958

МОДИФІКАЦІЯ КІНЕТИЧНИХ ПАРАМЕТРІВ SnSe ШЛЯХОМ ЛЕГУВАННЯ ТЕРБІЄМ

Т.А. Джафаров[1], О.М. Гасанов[1], Х.А. Адгезалова[1], Х.А. Асланов[1], Я.І. Хусейнов[1], І.І. Аббасов[2], Р.Ш. Рагімов[3]

[1]Азербайджанський державний педагогічний університет, AZ-1000, Баку, вул. Уз. Гаджибейлі, 68, Азербайджан
[2]Азербайджанський державний університет нафти та промисловості, Az-1010, Баку, проспект Азадлик, 20, Азербайджан
[3]Бакинський державний університет, AZ-1148, Баку, вул. Західа Халілова, 23, Азербайджан

Кінетичні параметри твердих розчинів $Tb_xSn_{1-x}Se$ ($0 \leq x \leq 0{,}05$), вирощених методом Бріджмена, досліджувалися при 300 K. Було виявлено, що легування Tb суттєво впливає на електропровідність, коефіцієнт Холла, коефіцієнт Зеєбека (термоЕРС), теплопровідність, а також концентрацію та рухливість носіїв заряду. При низьких концентраціях Tb спостерігається перехід від p-типу до n-типу провідності, що супроводжується немонотонною зміною коефіцієнта Холла та знака коефіцієнта Зеєбека. Електро- та теплопровідність зменшуються через посилене розсіювання на дефектах, спричинених введенням Tb. Отримані дані важливі для контролю властивостей SnSe в його термоелектричних застосуваннях.

Ключові слова: *тверді розчини; кінетичні параметри; легування; термоелектричні властивості; коефіцієнт Зеєбека; електропровідність; теплопровідність; концентрація носіїв; перехід типу провідності*

MEMRISTIVE SWITCHING BEHAVIOR OF SOL–GEL DERIVED Ga2O3 THIN FILMS

Jamoliddin X. Murodov[1,2]*, Shavkat U. Yuldashev[2], Azamat O. Arslanov[3], Noiba U. Botirova[2], Javohir Sh. Xudoyqulov[3,4], Ilyos Kh. Khudaykulov[5], Marguba S. Mirkamilova[1], Utkur E. Jurayev[1], Azlarxon M. Tillaboyev[6]

[1]Tashkent State Technical University named after Islam Karimov, Tashkent, Uzbekistan
[2]Center of Nanotechnology Development, National University of Uzbekistan, Tashkent, Uzbekistan
[3]National University of Uzbekistan named after Mirzo Ulugbek, Tashkent, Uzbekistan
[4]Central Asian University, Tashkent, Uzbekistan
[5]Arifov Institute of Ion-Plasma and Laser Technologies of Uzbekistan Academy of Sciences, Tashkent, Uzbekistan
[6]Chirchik State Pedagogical University, Chirchik, Uzbekistan
*Corresponding Author e-mail: jamoliddinmilliy@gmail.com

Gallium oxide (Ga_2O_3) is an ultrawide-bandgap semiconductor (~4.8–5.0 eV) that has recently gained considerable attention for next-generation nanoelectronic and memory devices owing to its superior breakdown field, chemical durability, and thermal robustness. In this study, Ga_2O_3 thin films were fabricated through a sol-gel spin-coating route and subsequently annealed at 1000 °C. X-ray diffraction revealed that annealing led to structural evolution from an amorphous state to the stable monoclinic β-Ga_2O_3 phase. Electrical measurements exhibited reproducible bipolar resistive switching with an ON/OFF resistance ratio exceeding 10^2 and relatively low set/reset voltages. The observed switching is interpreted within the framework of conductive filament formation and rupture, predominantly governed by oxygen vacancy dynamics. The combination of low-cost synthesis, scalable processing, and robust memristive performance highlights sol–gel derived Ga_2O_3 thin films as strong contenders for future resistive random-access memory (RRAM) architectures and neuromorphic computing technologies.

Keywords: *Gallium oxide; Sol–gel method; Thin films; Memristor*
PACS: 73.40.-c; *85*.30.Tv; 73.6 Ga

INTRODUCTION

Wide-bandgap (WBG) semiconductors such as SiC, GaN, and Ga_2O_3 have attracted significant attention due to their potential applications in high-power electronics, high-frequency devices, and deep-ultraviolet optoelectronics [1,2]. Among these, gallium oxide (Ga_2O_3) is particularly attractive because of its ultrawide bandgap (~4.8–5.0 eV), exceptionally high breakdown electric field (~8 MV/cm), excellent thermal stability, and chemical robustness [3]. Furthermore, Ga_2O_3 possesses five polymorphs (α, β, γ, δ, ε), with the monoclinic β-Ga_2O_3 phase being the most thermodynamically stable, making it highly suitable for device applications [4].

In addition to its role in power and optoelectronic devices, Ga_2O_3 has recently been investigated for resistive random-access memory (RRAM) devices, where resistive switching (RS) behavior plays a central role [5–7]. RRAM is considered a strong candidate for next-generation non-volatile memory due to its high switching speed, scalability, low power consumption, and compatibility with neuromorphic computing architectures [8-11]. The resistive switching mechanism in oxide memristors is typically associated with the formation and rupture of conductive filaments, primarily governed by the migration of oxygen vacancies.

Various fabrication methods, including pulsed laser deposition (PLD), molecular beam epitaxy (MBE), and RF sputtering, have been employed to grow Ga_2O_3 thin films [12–14]. Although these techniques produce high-quality films, they require expensive equipment and are not ideal for large-area or low-cost processing. In contrast, the sol–gel spin-coating technique provides a simple, low-cost, and highly scalable approach, making it attractive for industrial applications [15,16]. Nevertheless, systematic studies of memristive switching in sol–gel derived Ga_2O_3 thin films remain limited, with most prior works focusing primarily on structural and optical characteristics.

Furthermore, research on other oxide-based memristors has demonstrated how doping and defect engineering can introduce new functionalities. For example, Murodov *et al.* recently reported tunable negative differential resistance (NDR) in SnO_2:Co memristors fabricated on p-Si substrates, showing that controlled nanocluster formation can significantly influence switching behavior [17]. In addition to single-oxide memristors, bilayer and heterojunction systems have also been investigated to enhance switching performance. For instance, our recent study on SnO_2/ZnO heterojunction thin films demonstrated stable bipolar resistive switching with an ON/OFF ratio above 10^2 and forming-free operation, highlighting the role of interface engineering and oxygen vacancy dynamics in modulating device characteristics [18]. Such works emphasize the importance of material engineering in tailoring memristive responses and inspire further exploration of wide-bandgap oxides, such as Ga_2O_3.

In this context, the present study investigates sol–gel derived Ga₂O₃ thin films annealed at 1000°C. Structural analysis revealed evolution from an amorphous to β-Ga₂O₃ phase, and electrical measurements confirmed reproducible bipolar resistive switching with a high ON/OFF ratio ($>10^2$) and low set/reset voltages. The switching behavior is interpreted in terms of oxygen vacancy-mediated conductive filament formation. These findings establish sol–gel derived Ga₂O₃ thin films as promising candidates for cost-effective, scalable, and high-performance RRAM and neuromorphic computing applications.

METHODS

Gallium oxide (Ga₂O₃) thin films were prepared using a sol–gel spin-coating method. The overall preparation process is schematically illustrated in Figure 1, which depicts the main steps of solution preparation, coating, drying, and high-temperature annealing. Gallium nitrate hydrate [Ga(NO₃)₃·xH₂O] served as the precursor, dissolved in 2-methoxyethanol ($C_3H_8O_2$), while monoethanolamine (MEA, C_2H_7NO) was employed as a stabilizing agent at a 1:1 molar ratio with respect to gallium nitrate. The precursor concentration was adjusted to 0.5 M. The solution was continuously stirred at 60°C for 2 hours, then aged at room temperature for 36 hours to achieve uniformity and stability. Silicon (100) substrates were thoroughly cleaned in hydrofluoric acid, acetone, ethanol, and deionized water to eliminate native oxides and organic residues. The sol–gel solution was spin-coated onto the substrates at 3000 rpm for 30 seconds. After each deposition, the coated layers were dried at 120 °C for 10 minutes on a hot plate and subsequently pre-annealed in air at 500°C for 15 minutes. This deposition and treatment sequence was repeated six times, yielding films with thicknesses ranging from 100 to 150 nm. Finally, the films were annealed at 1000 °C for 30 minutes in air to induce crystallization.
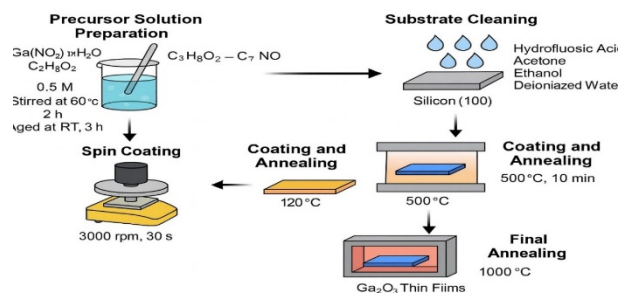
Figure 1. Schematic of the Ga₂O₃ thin films preparation method
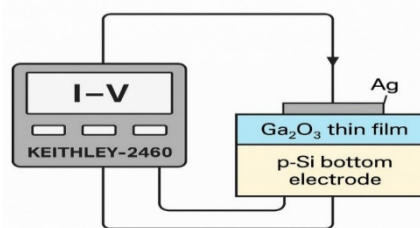
Figure 2. Electrical measurement scheme for Ga₂O₃ films with Keithley-2460

The structural properties of the films were examined using X-ray diffraction (XRD) (Cu Kα radiation, λ = 1.5406 Å). The optical absorption spectra were measured with a UV–Vis spectrophotometer in the range of 200–800 nm. For electrical characterization, the measurement setup is shown schematically in Figure 2, where current–voltage (I–V) curves were obtained using a Keithley-2460 source meter in a two-probe configuration with Ag top electrodes on the Ga₂O₃ thin films and a p-Si bottom electrode. For electrical measurements, Ag top electrodes (~100 nm) were deposited onto the Ga₂O₃ thin films through thermal evaporation using a shadow mask, forming circular pads with a diameter of 200 μm. The bottom electrode was p-type Si (100) substrate, which served simultaneously as a mechanical support and as the bottom contact. This configuration resulted in a vertical Ag/Ga₂O₃/p-Si memristor structure. The use of Ag top electrodes facilitates the formation of conductive filaments during resistive switching, while the p-Si bottom electrode provides good ohmic contact with the Ga₂O₃ layer.

RESULTS

Structural properties: XRD analysis revealed that the as-prepared Ga₂O₃ thin films were predominantly amorphous, with only substrate-related diffraction peaks corresponding to Si (100) being observed. This indicates that the deposited layers did not form a well-ordered crystalline lattice in the as-grown state. However, after thermal annealing at 1000°C, distinct diffraction peaks assigned to the β-Ga₂O₃ phase appeared, confirming crystallization into the thermodynamically stable monoclinic structure [19,20].

The transition from the amorphous state to the crystalline β-phase demonstrates that high-temperature annealing plays a crucial role in improving the structural ordering of sol–gel derived Ga₂O₃ films. This observation is consistent with previous reports, which have shown that metastable phases of Ga₂O₃ (α, γ, δ, ε) tend to transform into the stable β-phase upon sufficient thermal treatment. Thus, annealing at 1000°C is confirmed to be effective in enhancing crystallinity and stabilizing the β-Ga₂O₃ phase in sol–gel processed thin films (Figure 3).

Optical properties: The optical absorption spectra of the Ga₂O₃ thin films showed a pronounced absorption edge, which sharpened after annealing at 1000°C, indicating improved crystallinity and a reduction in defect states. The optical bandgap was estimated using Tauc plots derived from the absorption data. The calculated bandgap for the annealed films was approximately 4.9 eV, which is in good agreement with reported values for β-Ga₂O₃ [21-23]. The corresponding Tauc plot for the annealed films is shown in Figure 4.
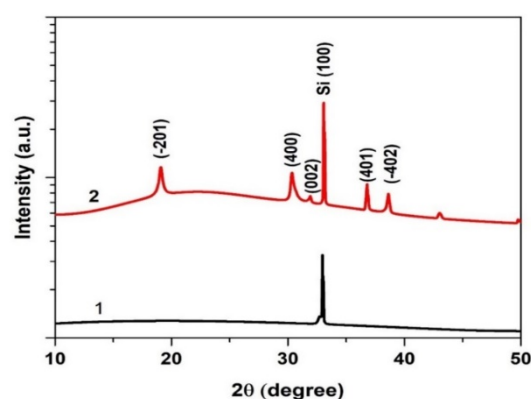
Figure 3. XRD patterns of sol–gel derived Ga₂O₃ thin films
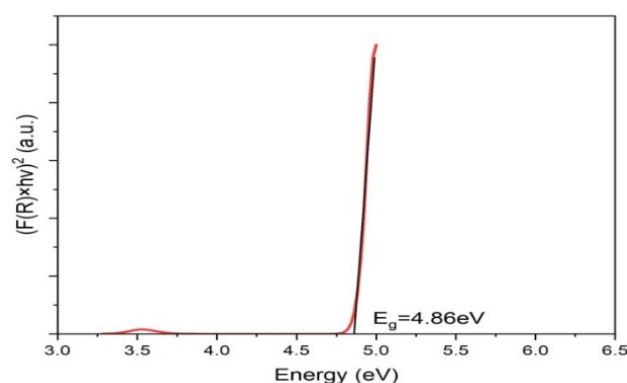
Figure 4. Tauc plot of Ga₂O₃ thin films annealed at 1000 °C, indicating an optical bandgap of ~4.86 eV

A noticeable blue shift in the absorption edge was observed as the annealing temperature increased. This shift can be attributed to the improved structural ordering of the films, which reduces sub-bandgap defect states, thereby widening the effective bandgap. Such behavior is commonly observed in oxide thin films and is typically attributed to the reduction of localized defect levels and the improvement of stoichiometry upon thermal treatment.

These results confirm that high-temperature annealing not only stabilizes the β-Ga₂O₃ phase but also enhances its optical quality, making sol–gel–derived Ga₂O₃ thin films suitable for optoelectronic and memory device applications that require a wide bandgap and high thermal stability.

Electrical properties: The current–voltage (I–V) characteristics of the Ga₂O₃ thin films demonstrated reproducible bipolar resistive switching behavior. During the voltage sweep, the devices switched from a high-resistance state (HRS) to a low-resistance state (LRS) at a relatively low set voltage, and returned to the HRS at the reset voltage. The observed ON/OFF resistance ratio exceeded 10^2, ensuring a clear distinction between the two resistance states and making the films suitable for non-volatile memory applications (Figure 5). The fabricated device exhibited stable bipolar resistive switching in the Ag/Ga₂O₃/p-Si configuration. The Ag top electrode played a crucial role in filament formation, as silver cations can drift under bias, assisting the creation of localized conductive paths in addition to oxygen vacancy migration. This hybrid filamentary mechanism contributed to the low set/reset voltages and stable endurance observed in our device.

Logarithmic I–V plots further confirmed the presence of well-defined HRS and LRS states across an extended voltage range (Figure 6). The resistive switching mechanism is attributed to the formation and rupture of conductive filaments, predominantly governed by oxygen vacancy migration within the Ga₂O₃ layer. In the SET process, oxygen vacancies drift under an electric field, forming localized conductive paths that reduce the resistance. Conversely, in the RESET process, these conductive filaments rupture, restoring the device to its high-resistance state.

These findings are consistent with previously reported Ga₂O₃-based memristors fabricated using physical vapor deposition techniques, such as RF sputtering and pulsed laser deposition [5–8]. However, the present results highlight that the sol–gel approach provides a cost-effective, solution-processable, and scalable alternative, while still achieving competitive switching performance parameters.
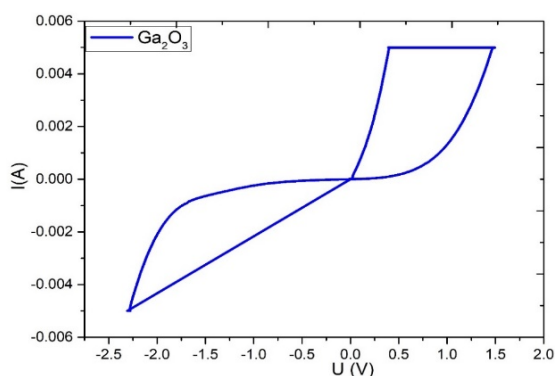
Figure 5. Current-voltage (I–V) characteristics of Ga₂O₃ thin film demonstrating memristive switching behavior
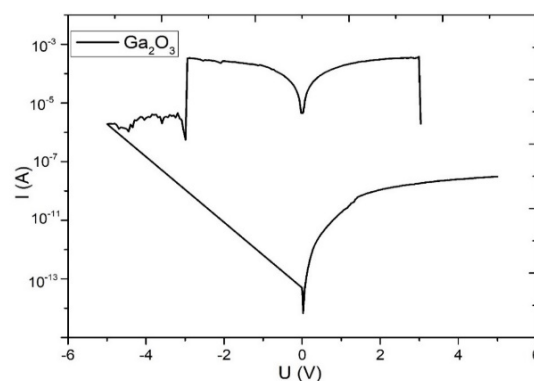
Figure 6. Log-scale I–V characteristics of Ga₂O₃ thin film showing high-resistance and low-resistance states over extended voltage range

The resistive switching behavior in Ag/Ga₂O₃ memristors can be explained by the formation and rupture of conductive filaments, mediated by both oxygen vacancies and Ag cations (Figure 7). Under a positive bias, oxygen vacancies migrate and Ag ions drift from the top electrode into the Ga₂O₃ layer, combining to form a localized filamentary

path that reduces the device resistance (SET process). When the polarity is reversed, Joule heating and electrochemical dissolution lead to the rupture of these filaments, restoring the high-resistance state (RESET process). This filamentary model is consistent with the observed bipolar switching and stable ON/OFF ratio in our devices.
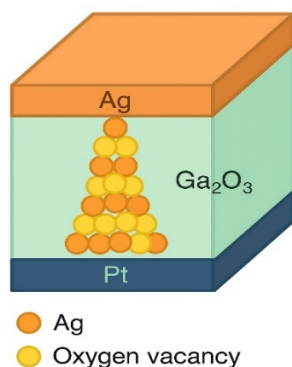
Figure 7. Schematic of filament formation and rupture in
Ag/Ga$_2$O$_3$/Pt memristor (orange: Ag ions, yellow: oxygen vacancies)

CONCLUSION

In this work, Ga$_2$O$_3$ thin films were successfully synthesized by a low-cost sol–gel spin-coating technique followed by annealing at 1000°C. Structural analysis confirmed the phase transformation from an amorphous state to the thermodynamically stable β-Ga$_2$O$_3$ phase. Optical characterization revealed a sharp absorption edge with an estimated bandgap of ~4.9 eV, accompanied by a blue shift that can be attributed to improved crystallinity and reduced defect states. Electrical measurements demonstrated reliable bipolar resistive switching with a high ON/OFF resistance ratio ($>10^2$) and low set/reset voltages. The switching mechanism was explained by the formation and rupture of oxygen-vacancy-mediated conductive filaments.

These results highlight the potential of sol–gel derived Ga$_2$O$_3$ thin films as scalable, cost-effective, and high-performance candidates for resistive random-access memory (RRAM) and neuromorphic computing applications. Furthermore, this study demonstrates that solution-processed Ga$_2$O$_3$ can achieve memristive characteristics comparable to those obtained by expensive physical vapor deposition techniques, thus opening new avenues for the development of next-generation memory technologies. Unlike many previous works that primarily emphasized Ga$_2$O$_3$ film growth, our study highlights the memristive behavior of a complete device structure (Ag/Ga$_2$O$_3$/p-Si). The explicit consideration of contact engineering is essential, since both the choice of top electrode (Ag) and bottom electrode (p-Si) strongly influence resistive switching performance.

ORCID

Jamoliddin X. Murodov, https://orcid.org/0009-0006-3088-4881; **Shavkat U. Yuldashev,** https://orcid.org/0000-0002-2187-5960
Azamat O. Arslanov, https://orcid.org/0009-0000-4817-8770, **Noiba U. Botirova,** https://orcid.org/0009-0002-2294-9981

REFERENCES

[1] G. Akbar, A. Di Fatta, G. Rizzo, G. Ala, P. Romano, and A. Imburgia, "Comprehensive review of wide-bandgap (WBG) devices: SiC MOSFET and its failure modes affecting reliability," PhysChem, **5**(1), 10 (2025). https://doi.org/10.3390/physchem5010010
[2] S. Musumeci, "Gallium nitride power devices in power electronics," Energies, **16**(9), 3894 (2023). https://doi.org/10.3390/en16093894
[3] D. Kaur, A. Ghosh, and M. Kumar, "A strategic review on gallium oxide based power electronics: Recent progress and future prospects," Materials Today: Proceedings, **33**, 104244 (2022). https://doi.org/10.1016/j.matpr.2022.104244
[4] F. Safieddine, *et al.*, "Comparative study of the fundamental properties of Ga$_2$O$_3$," Journal of Solid State Chemistry, **312**, 123272 (2022). https://doi.org/10.1016/j.jssc.2022.123272
[5] R.T. Velpula, B. Jain, and H.P.T. Nguyen, "Low-power multilevel resistive switching in β-Ga$_2$O$_3$ based RRAM devices," Nanotechnology, **34**(7), 075201 (2023). https://doi.org/10.1088/1361-6528/aca418
[6] Z. Yang, K. Zhang, R. Guo, J. Wu, P. Li, Y. Chen, and W. Mi, "Resistive random access memory based on gallium oxide thin films for self-powered pressure sensor systems," Ceramics International, **46**(13), 21141–21148 (2020). https://doi.org/10.1016/j.ceramint.2020.05.191
[7] L.-W. Wang, C.-W. Huang, K.-J. Lee, S.-Y. Chu, and Y.-H. Wang, "Multi-level resistive Al/Ga$_2$O$_3$/ITO switching devices with interlayers of graphene oxide for neuromorphic computing," Nanomaterials, **13**(12), 1851 (2023). https://doi.org/10.3390/nano13121851

[8] B. Oh, *et al*., "Wake-up effects on improving gradual switching and variation in resistive random-access memory (RRAM)," Electronics, **14**(10), 1921 (2025). https://doi.org/10.3390/electronics14101921

[9] K. Sato, Y. Hayashi, N. Masaoka, T. Tohei, and A. Sakai, "High-temperature operation of gallium oxide memristors up to 600 K," Scientific Reports, **13**, 1261 (2023). https://doi.org/10.1038/s41598-023-28075-4

[10] H.J. Lee, J.-H. Kim, J. Choi, Y.S. Kim, and S.-N. Lee, "Correlation between oxygen flow-controlled resistive switching and capacitance behavior in gallium oxide memristors grown via RF sputtering," Heliyon, **9**(12), e23157 (2023). https://doi.org/10.1016/j.heliyon.2023.e23157

[11] D. Cui, M. Pei, Z. Lin, H. Zhang, M. Kang, Y. Wang, X. Gao, *et al*., "Versatile optoelectronic memristor based on widebandgap Ga$_2$O$_3$ for artificial synapses and neuromorphic computing," Nanomaterials, **15**(2), 367 (2025). https://doi.org/10.3390/nano15020367

[12] I. Rahaman, "Epitaxial growth of Ga$_2$O$_3$: A review," Materials, **17**(17), 5678 (2024). https://doi.org/10.3390/ma17175678

[13] Y. Yang, "Compact Ga$_2$O$_3$ thin films deposited by plasma and RF magnetron sputtering," Thin Solid Films, **757**, 139139 (2022). https://doi.org/10.1016/j.tsf.2022.139139

[14] T. Yamaguchi, Y. Oshima, H. Murakami, and S. Fujita, "Structural evolution and nucleation dynamics of RF-sputtered gallium oxide thin films," APL Materials, **13**(4), 041130 (2025). https://doi.org/10.1063/5.0205673

[15] H. Zhang, D. Niu, J. Yang, X. Zhang, and W. Li, "β-Ga$_2$O$_3$ thin films via an inorganic sol–gel spin coating: Preparation and characterization," Nanomaterials, **15**(4), 277 (2025). https://doi.org/10.3390/nano15040277

[16] V.A. Spiridonov, D.I. Panov, and X. Zhang, "Ga$_2$O$_3$ deposition methods by low-cost techniques: A review," Journal of Sol-Gel Science and Technology, **101**, 222–245 (2024). https://doi.org/10.1007/s10971-024-06543-1

[17] J.X. Murodov, S.U. Yuldashev, A.O. Arslanov, M.S. Mirkamilova, and U.E. Jurayev, "Tunable negative differential resistance in SnO$_2$:Co memristors on p-Si," East Eur. J. Phys., (2), 115–122 (2025). https://doi.org/10.26565/2312-4334-2025-2-22

[18] J.X. Murodov, Sh.U. Yuldashev, A.O. Arslanov, N.U. Botirova, J.Sh. Xudoyqulov, R.Sh. Sharipova, R.A. Nusretov, *et al.*, Resistive switching behavior of SnO$_2$/ZnO heterojunction thin films for non-volatile memory applications, East Eur. J. Phys. (3), 348–352 (2025). https://doi.org/10.26565/2312-4334-2025-3-34

[19] W. Shan, W. Walukiewicz, K.M. Yu, J.W. Ager, E.E. Haller, H. Lu, and W.J. Schaff, "Structural evolution of Ga$_2$O$_3$ thin films: Amorphous to β-Ga$_2$O$_3$ transition upon high-temperature annealing," AIP Conf. Proc. **1466**, 197–200 (2012). https://doi.org/10.1063/1.4740301

[20] N. Makeswaran, R. Arivazhagan, T. Balasubramanian, "Crystallization and phase stabilization of Ga$_2$O$_3$ nanofibers under thermal treatments (700–900 °C): Evidence of β-Ga$_2$O$_3$ formation at 900 °C," Journal of Nanomaterials, 2022, 9476513 (2022). https://doi.org/10.1155/2022/9476513

[21] A.M. Hassanien, A.A. Atta, M.M. El-Nahass, S.I. Ahmed, A.A. Shaltout, A.M. Al-Baradi, A. Alodhayb, and A.M. Kamal, "Effect of annealing temperature on structural and optical properties of gallium oxide thin films deposited by RF-sputtering," J. Mater. Sci.: Mater. Electron., **31**(9), 7355–7366 (2020). https://doi.org/10.1007/s10854-020-03203-7

[22] L.B. Cheah, R.A.M. Osman, and P. Poopalan, "Ga$_2$O$_3$ thin films by sol-gel method and its optical properties," AIP Conf. Proc. **2203**, 020015 (2020). https://doi.org/10.1063/1.5142120

[23] N.U. Botirova, A.O. Arslanov, G.B. Eshonkulov, J.X. Murodov, R.Sh. Sharipova, J.Sh. Khudoykulov, and Sh.U. Yuldashev, "Effect of SiO$_2$ and Post-Annealed Ga$_2$O$_3$ Buffer Layers on Ga$_2$O$_3$ Thin Film Growth and Properties," Cryst. Growth Des. (2025) https://doi.org/10.1021/acs.cgd.5c01075

**МЕМРИСТИВНА ПОВЕДІНКА ПЕРЕМИКАННЯ ТОНКИХ ПЛІВОК Ga₂O₃,
ОТРИМАНИХ ЗОЛЬ-ГЕЛЬ МЕТОДОМ**

**Джаموліддін Х. Муродов[1,2], Шавкат У. Юлдашев[2], Азамат О. Арсланов[3], Нойба У. Ботірова[2],
Джавохір Ш. Худайкулов[3,4], Ільос Х. Худайкулов[5], Маргуба С. Міркамілова[1],
Уткур Е. Джураєв[1], Азлархон М. Тіллабоєв[6]**

[1]*Ташкентський державний технічний університет імені Іслама Карімова, Узбекистан*
[2]*Центр розвитку нанотехнологій, Національний університет Узбекистану, Ташкент, Узбекистан*
[3]*Національний університет Узбекистану імені Мірзо Улугбека, Ташкент, Узбекистан*
[4]*Центральноазіатський університет, Ташкент, Узбекистан*
[5]*Інститут іонно-плазмових та лазерних технологій імені Аріфова Академії наук Узбекистану, Ташкент, Узбекистан*
[6]*Чирчикський державний педагогічний університет, Чирчик, Узбекистан*

Оксид галію (Ga₃O₃) – це напівпровідник з надширокою забороненою зоною (~4,8–5,0 еВ), який нещодавно привернув значну увагу для наноелектронних пристроїв та пристроїв пам'яті наступного покоління завдяки своєму чудовому полю пробою, хімічній стійкості та термостійкості. У цьому дослідженні тонкі плівки Ga₂O₃ були виготовлені методом золь-гель спінінгу та потім відпалені при 1000°C. Рентгенівська дифракція виявила структурну еволюцію від аморфного стану до стабільної моноклінної фази β-Ga₂O₃ після відпалу. Електричні вимірювання показали відтворюване біполярне резистивне перемикання з коефіцієнтом опору ввімкнення/вимкнення, що перевищує 10², та відносно низькими напругами встановлення/скидання. Спостережуване перемикання інтерпретується в рамках формування та розриву провідних ниток, переважно керованих динамікою вакансій кисню. Поєднання недорогого синтезу, масштабованої обробки та надійної мемристивної продуктивності підкреслює тонкі плівки Ga₂O₃, отримані методом золь-гель, як сильних претендентів на майбутні архітектури резистивної пам'яті з довільним доступом (RRAM) та нейроморфні обчислювальні технології.
Ключові слова: *оксид галію; золь-гель метод; тонкі плівки; мемристор*

INVESTIGATION OF THE OPTICAL PROPERTIES OF METAL ION-INTERCALATED GaSe SEMICONDUCTOR MONOCRYSTALS

Rahim Madatov[1,2], Lamiya Sadigli[1]*, Rakshana Mamishova[1,3], Aydan Khaligzadeh[1]

[1]Ministry of Science and Education Republic of Azerbaijan, Institute of Radiation Problems,
B. Vagabzadeh street 9, AZ 1141, Baku, Azerbaijan
[2]National Aviation Academy, Mardakan Avenue, 30, Az 1045, Baku, Azerbaijan
[3]Azerbaijan University of Architecture and Construction, Ayna Sultanova Street 5, Az1073, Baku, Azerbaijan
*Corresponding Author E-mail: Sadiglilamiye@gmail.com

In this study, the XRD method was used to characterise the structural and phase properties of GaSe monocrystals, and the impact of Cu ion intercalation on their optical properties was investigated. An increase in absorption (ABS) was observed in the 200–400 nm region as a result of the addition of Cu ions, and new optical transitions occurred around 600 nm. Overall, observable variations in absorption levels have been observed over the 200–800 nm spectral range. Tauc analysis revealed that the band gap narrowed from approximately 2 eV to about 1.88 eV upon intercalation and slightly widened to about 2.15 eV with photo-intercalation. These results suggest that Cu ion intercalation can be applied to modify the optical properties of GaSe monocrystals, increasing their potential for use in nonlinear optical devices, photonics, and sensor technologies. The findings also demonstrate that intercalation is an appropriate technique for regulating the physical characteristics of layered materials.

Keywords: *Band gap; Absorption; Intercalation; XRD diffraction*
PACS: 64.60.-i.621.315.592

INTRODUCTION

Due to their significant potential in optoelectronics, photonics, and sensor technologies, layered semiconductor materials have been the subject of extensive research in recent years. Gallium selenide (GaSe) is unique among these materials due to its unique layered crystal structure, broad band gap (around 2 eV), and significant nonlinear optical characteristics. GaSe may crystallise in both orthorhombic and hexagonal systems, and its layered structure makes it possible to adjust its electrical and optical characteristics using a variety of modification techniques [1]. GaSe is a potential material for use in laser technologies, photodetectors, and nonlinear optical devices because of these characteristics [2–5].

The process of intercalation, which is the insertion of atoms, molecules, or ions into the interlayer spaces in such layered crystals, can have a major impact on the electronic structure and functional characteristics of the material [6]. The research suggests that intercalation may result in the creation of new localised energy states, band gap change, optical absorption spectrum broadening, and photoluminescence intensity regulation. In GeI_2 crystals intercalated with pyridine molecules, for example, band gap widening has been seen, whereas electrochemical intercalation has enhanced electrical conductivity in materials like MoS_2 and $ZrSe_2$, even causing a change from semiconducting to metallic behaviour [7–10].

The combined results of these investigations show that the intercalation process is a popular and efficient way to intentionally adjust the electrical and optical characteristics of materials with little structural harm. Intercalated layered materials have a wide range of potential applications in optoelectronic devices, as confirmed by the literature now under publication. This highlights the need for more study in this area [11-12,13].

However, the effects of intercalation on the optical properties of layered semiconductors like GaSe, such as absorption spectra, optical transitions, and energetic modifications of the band gap, have not yet been thoroughly examined. Previous study published in the scientific literature [1, 14-18] has concentrated chiefly on structural features and electrical conductivity. Electrochemical intercalation was chosen for this investigation because to its quick, energy-efficient, and economical application, as well as its repeatable and controllable nature. Additionally, it provides a viable approach for the creation of novel functional nanostructures. Because of their potential to improve electrical conductivity, modify the band gap, contribute to memory, energy storage, and more effectively thermal and chemical stability, copper ions were specifically chosen as intercalants. Nevertheless, little is known about the specific optical changes brought about by the intercalation of transition metals like Cu into GaSe crystals, especially with regard to wavelength-dependent effects and structural changes of the band gap. This emphasizes the necessity of additional experimental research. Therefore, by investigating the impact of Cu intercalation on the optical properties of GaSe crystals and exploring the potential applications of the ensuing alterations, this work aims to fill the existing gap.

EXPERIMENTAL METHODOLOGY

The layered GaSe single crystals investigated in this study were grown using the Bridgman–Stockbarger directional crystallization technique [1]. This method was specifically chosen due to its ability to produce high-quality

single crystals with a homogeneous structure and excellent crystallinity, yielding large, optically smooth GaSe crystals with a characteristic bright red appearance. The technique enabled the growth of samples with high purity and well-preserved layered morphology, which are essential for accurate optical investigations.

A detailed sample preparation protocol was implemented before measurements. High-quality specimens were selected based on their mirror-like surface morphology and scanned along the layer planes to ensure structural uniformity. Structural and compositional analyses were performed, including X-ray diffraction (XRD), to verify the crystalline order and homogeneity of the samples. These characterizations were essential not only to confirm the composition of the GaSe crystals but also to monitor changes induced by the intercalation process.

The intercalation itself was carried out via electrochemical intercalation under a constant electric field. The GaSe single crystal samples were placed between electrodes separated by a 2.5 cm distance and subjected to the process for 1 hour. Experiments were conducted under two different conditions – illuminated and dark environments – to examine the effect of external excitation on ion diffusion. The electrolyte consisted of a 4% aqueous copper sulfate solution ($CuSO_4 \cdot 5H_2O$)+H_2O (distilled), prepared by dissolving 30 g of copper sulfate in 700 ml of distilled water. Before the intercalation, the solution was heated to 70°C, and the process was initiated at this temperature. During the experiment, a potential difference of 0.3 V was applied, while a constant current of 0.22 mA was maintained between the electrodes, enabling the effective insertion of copper ions into the GaSe crystal lattice. A copper sulfate ($CuSO_4$) aqueous solution was employed as the electrolyte, facilitating the insertion of copper ions into the GaSe crystal lattice.

To investigate the influence of intercalation on the optical properties of GaSe single crystals, the optical spectra of the samples were measured across a wide spectral range of 190–1100 nm, encompassing both ultraviolet (UV) and visible regions. A high-sensitivity Varian Cary 50 UV-Visible spectrophotometer was used for spectrometric analysis, allowing precise measurement of the samples' absorption and transmission characteristics. The results revealed notable changes in the optical spectra due to the incorporation of copper ions into the crystal lattice, particularly the shift of the absorption edge and the modulation of the optical band gap energy. These findings provide critical insights into how intercalation affects the electronic structure of GaSe crystals, offering a valuable foundation for assessing their potential in future optoelectronic applications.

Absorbance spectra in the range of 200–800 nm were calibrated by subtracting the dark signal prior to analysis. The absorption coefficient was calculated as:

$$\alpha(\lambda) = \frac{2.303 A(\lambda)}{d}$$

where d is the sample thickness (uncertainty: ±3%). Wavelength calibration uncertainty was ±1 nm, as specified by the manufacturer, corresponding to ±0.005–0.02 eV in the 300–600 nm range.

The optical bandgap (E_g) was determined under the assumption of a direct allowed transition using Tauc analysis, plotting $(\alpha h\nu)^2$ versus $h\nu$. The linear fitting region was selected by visual inspection (pure GaSe: 1.95–2.15 eV; Cu-intercalated: 1.75–1.95 eV) and fitted using the least-squares method. E_g values were obtained from the x-intercept of the linear extrapolation.

Total uncertainty was estimated as the quadratic sum of contributions from: (i) absorbance noise and fitting error (95% confidence interval of the linear fit), (ii) wavelength calibration, and (iii) thickness measurement. For each sample, three replicate spectra were recorded; where applicable, the 95% CI from the fit and the standard deviation across replicates were combined.

3. RESULTS AND DISCUSSION
3.1. Structural Characterisation of the Layered GaSe Single Crystal by XRD

To analyse the structural properties of the studied GaSe single crystals, X-ray diffraction (XRD) measurements were carried out in the angular range of $2\theta = 0°–120°$. The XRD technique plays a crucial role in identifying the crystallographic phase and structural order of materials. In the diffraction pattern, the 2θ angle provides information about the atomic arrangement. At the same time, the intensity (measured in counts per second, cps) reflects the strength of the diffracted signal and indicates how densely atoms are packed along specific planes.

In the recorded diffraction pattern, a dominant peak with an intensity of approximately 300,000 cps appears near $2\theta \approx 20°$, which corresponds to the primary crystallographic phase of GaSe and confirms the high degree of ordering within the material (Fig. 1). The sharpness and narrow width of the peaks across the entire scan range are indicative of a well-ordered single-crystalline structure. We identified seven distinct diffraction peaks, each corresponding to specific crystallographic planes within the GaSe lattice.

The most intense peak observed around 20° is indexed as the (002) reflection plane. This peak is characteristic of layered semiconductors, such as GaSe, and reflects the strong periodicity along the crystallographic c-axis. A weaker peak located between 30° and 40° corresponds to the (004) plane, which typically exhibits lower intensity in layered compounds due to the nature of interlayer interactions. Another significant peak appears around 60°, associated with the (006) plane, further validating the material's layered periodicity. The (008) reflection is detected near 70° and is generally observed in high-quality GaSe single crystals.

In addition, a peak near 80°, indexed as the (101) plane, reveals information about the lateral atomic arrangement within the basal layers. Two further low-intensity reflections observed between 90° and 100°, corresponding to the

(112) and (114) planes, provide evidence for the full three-dimensional crystallographic symmetry of the crystal lattice. These reflections, though less intense, help affirm that the crystal exhibits long-range order in multiple directions.

Figure 2 presents the compositional analysis derived from the XRD pattern of the investigated GaSe crystal. In this plot, the red and green peaks correspond to the experimental reflections obtained from the sample, while the blue markers represent the standard diffraction data for the GaSe phase (ICDD card: 00-037-0931). A comparison of the measured and reference patterns reveals a high degree of correspondence, confirming that the studied material is consistent with the stoichiometric GaSe phase. This agreement indicates that the crystal is single-phased and exhibits high purity.
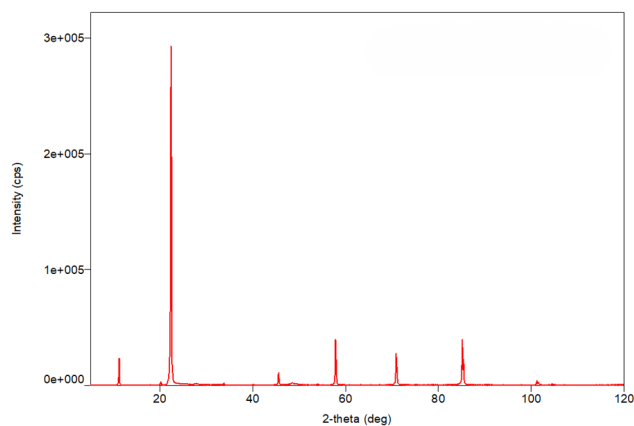
Figure 1. XRD image of a GaSe crystal
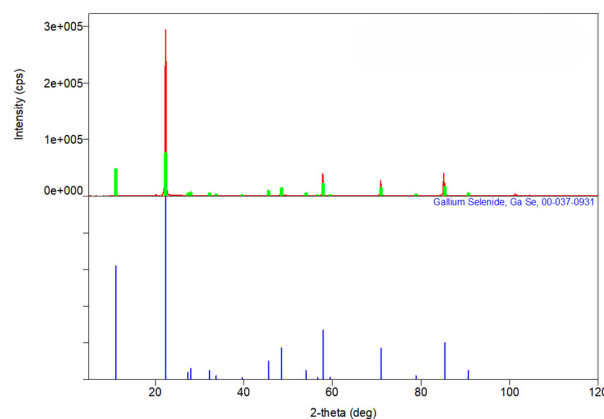
Figure 2. Compositional analysis of GaSe crystal

Gallium selenide (GaSe) is a III–VI group layered semiconductor that crystallizes in an orthorhombic system and typically displays p-type conductivity. The presence of acceptor-like defects, particularly selenium vacancies, is a characteristic feature contributing to its p-type behavior. The confirmation of a monocrystalline nature implies that the entire crystal has grown uniformly along a single crystallographic direction, exhibiting minimal grain boundaries or internal fractures.

The orthorhombic symmetry of the GaSe structure implies that the crystal possesses three mutually perpendicular axes of unequal lengths (Υ-modification, $a = 3.755 \times 10^{-4}$ μm and $c = 2.392 \times 10^{-3}$ μm.). This structural system is distinct from the more symmetric hexagonal configuration and is considered a more specific and directionally anisotropic phase. A major advantage of single-crystalline materials over polycrystalline or nanocrystalline forms is their superior and more predictable physical properties, as the uniform crystal orientation enables more coherent charge transport and reduced scattering at interfaces.

In the case of p-type GaSe, the charge transport is primarily governed by positively charged carriers (holes), resulting from an intrinsic deficit of electrons. This type of conductivity is particularly relevant for tuning the material's electronic response under external stimuli. The combination of a layered structure and intrinsic p-type behavior makes GaSe a promising host material for intercalation-based modifications, enabling targeted tuning of its physical and optoelectronic properties.

3.2. Effect of electrochemical intercalation with copper ions on optical properties

In Figure 3a, the wavelength-dependent absorption (ABS) of the layered GaSe single crystal is presented. The main features of the graph can be described as follows:

- At short wavelengths (high absorption region) – in the range of 200–350 nm, a strong absorption is observed. This indicates the spectral region where electronic transitions from the valence band to the conduction band occur intensely in the GaSe single crystal. The sharp peaks observed during the measurement are attributed to the sensitivity of the device.

- Sharp decrease in absorption (300–400 nm region) – after 300 nm, a noticeable drop in absorbance is observed. This suggests that the material's band gap lies within this spectral range. In this region, the photon energy is no longer sufficient to induce major electronic transitions in the GaSe crystal, leading to a decrease in absorption.

- Low absorption region (beyond 400 nm) – for wavelengths greater than 400 nm, the absorbance appears to stabilize around 2. This indicates that the material does not significantly absorb light in this region and is mainly transparent.

- Stable absorption up to 800 nm – at longer wavelengths (approaching the infrared spectral region), the absorption remains very low. This is due to the increase in optical transmission of the material and the fact that the photon energy is insufficient for electronic transitions.

Figure 3b shows the wavelength-dependent absorption of the GaSe single crystal after electrochemical intercalation with copper ions.

High absorption region (200–350 nm) – compared to the pure GaSe, intense absorption peaks are also observed at short wavelengths in this spectrum. These peaks are associated with changes in the electronic structure of the crystal due to the incorporation of copper ions between the GaSe layers.

Sharp decrease in absorption (350–600 nm) – after intercalation, the absorption decrease shows a slightly different behaviour. Compared to the previous (non-intercalated) spectrum, it can be seen that absorption persists to some extent even at longer wavelengths. This is explained by the modification of energetic levels and the emergence of new optical transitions as a result of copper ion incorporation into the crystal structure.

New features (600–800 nm) – in this region, a sharp change is observed around 600 nm in the intercalated sample. This is related to the influence of newly formed energy levels, induced by copper ions between the GaSe layers, on the optical properties. The fact that absorption drops to nearly zero beyond 600 nm indicates that the material becomes less sensitive to light in this region.

a)   b)
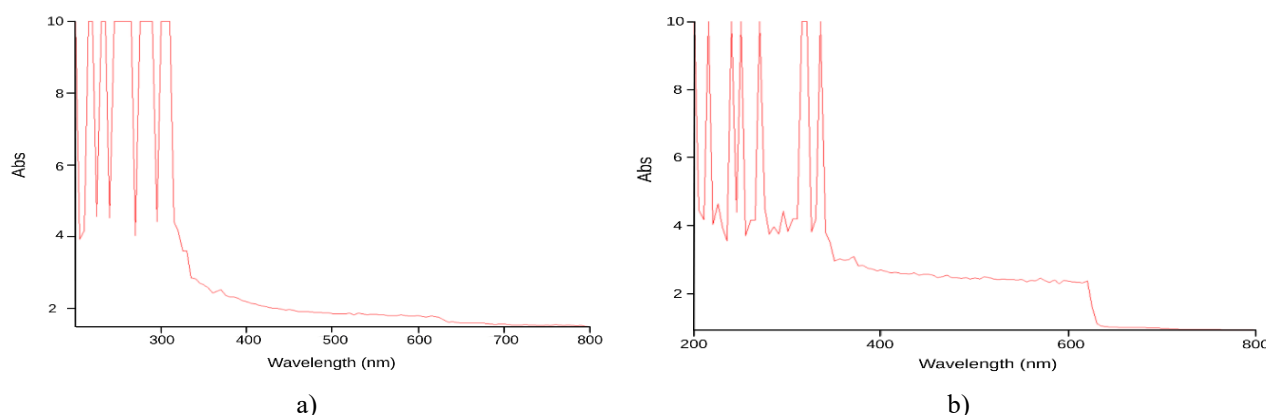
Figure 3. a) Wavelength dependence of absorption before intercalation; b) Wavelength dependence of absorption after intercalation with Cu ions

In Figure 4, the Tauc method is used to analyze the effect of intercalation on the band gap more precisely. By applying the Tauc method, the band gap energy of the GaSe single crystal is accurately determined. For this purpose, the Tauc equation is used:

$$(\alpha h\nu)^n = A(h\nu - E_g)$$

Here:

α - absorption coefficient, $h\nu$ - photon energy, E_g - band gap width, A - proportionality coefficient, n - a parameter that depends on the type of transition. Since this coefficient is a direct transition for GaSe, n=2 is taken.
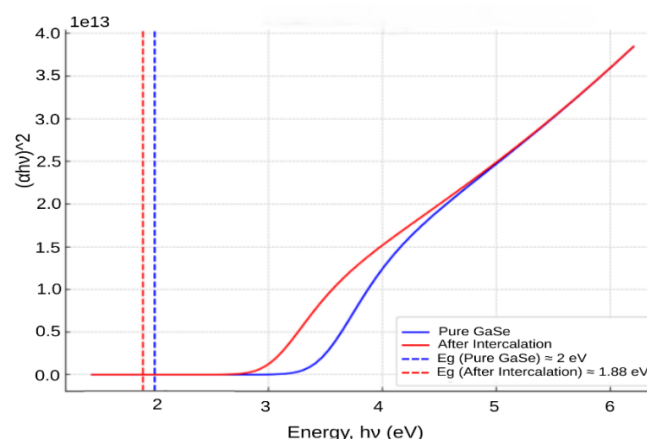
Figure 4. Determination of the prohibited zone according to the Tauc method

The linear fit windows are shown as gray bands; solid lines represent least-squares fits; the shaded area indicates the 95% confidence interval. The band gaps extracted from the intersections are: E_g (pure) = 2.00 ± 0.03 eV, E_g (Cu-intercalated) = 1.86 ± 0.03 eV.

In Figure 4, the narrowing of the band gap in the GaSe crystal is related to structural and electronic changes in the crystal lattice caused by intercalation with copper ions.

Before intercalation, the band gap width of the GaSe crystal (blue line) was observed to be approximately 2 eV. This value corresponds to the expected band gap of pure GaSe. For copper-intercalated GaSe (red line), the band gap is approximately 1.88 eV. As shown, the band gap narrows due to copper intercalation.

The insertion of copper ions between the layers leads to changes in the energetic levels and gives rise to new optical transitions at lower energy states. In the spectrum of pure GaSe, the transmittance (Tm%) sharply decreases at high energies (short wavelengths), indicating the absorption edge and the band gap energy (Eg) of the material. This steep drop is a clear indicator of the band edge position.

During the electrochemical intercalation process, copper ions enter between the layers of the GaSe single crystal and affect the crystal lattice. As a result, lattice deformation occurs, where the incorporation of copper ions alters interatomic distances, thereby influencing the mobility of electrons and the configuration of the energy bands. At the same time, new localised energy states are formed.

When copper ions (Cu^{2+}) are intercalated into the GaSe crystal lattice, the type of energy levels they generate depends on several factors. These factors are as follows:

- The electronic configuration of Cu^{2+} ions – The electron configuration of the Cu^{2+} ion is $3d^9$. The d-orbital electrons of this ion create localized energy states within the GaSe crystal lattice.
- Increase in conductivity and narrowing of the band gap – As seen from the graph, copper intercalation enhances conductivity and narrows the band gap by approximately 0.1 eV. This implies that Cu^{2+} ions are more likely to form acceptor levels rather than donor levels.
- Type of levels formed by copper ions – Acceptor levels (energy levels near the valence band) – When Cu^{2+} ions are intercalated into the layered GaSe structure, they tend to attract electrons, which leads to the formation of new energy levels just above the valence band. In this case, the valence band effectively expands, resulting in a narrower band gap. The energy required for electrons to transition into the conduction band decreases, which accounts for the 0.12 eV narrowing of the band gap. As a result, conductivity increases because electrons in the valence band can more easily reach the conduction band.
- Spectral manifestation of band gap narrowing – In the spectrum of pure GaSe, the absorption edge is located at a higher energy (around 2 eV). However, after copper intercalation, this edge shifts toward lower energies (around 1.88 eV), indicating a narrowing of the band gap, as the material begins to absorb lower-energy photons.
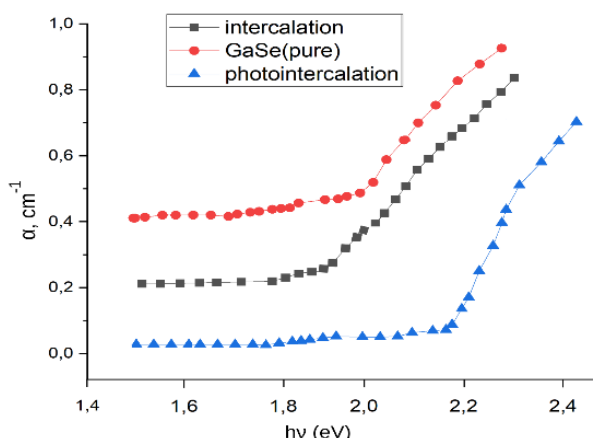
Figure 5. Dependence of the absorption coefficient (α) on photon energy (hν) for pure GaSe (black squares), Cu-ion-intercalated (red circles), and photo-intercalated (blue triangles) GaSe single crystals

Figure 5 presents the dependence of the absorption coefficient (α) on photon energy (hν) for pure GaSe, Cu-ion-intercalated GaSe, and photo-intercalated GaSe single crystals. Layered semiconductor GaSe, in its pure state, possesses high crystalline perfection and a relatively low defect density. High-energy photons (in the UV region) induce strong absorption; however, as the photon energy approaches the band gap, the absorption decreases sharply. The absorption edge is observed at approximately 2.0 eV, which corresponds to the typical band gap of pure GaSe. The incorporation of Cu^{2+} ions into the interlayer spaces creates localized energy states in the crystal lattice. These states enable additional transitions between the valence and conduction bands, allowing electrons to be excited by photons of lower energy (~1.88 eV) (red shift). At the same time, defects and lattice deformation caused by the ions increase light scattering and the probability of carrier recombination, which in turn reduces the overall absorption coefficient. During photo-intercalation, both the positioning of the ions and the formation of photo-induced defects occur under illumination. The photo-induced effect generates additional lattice strain and changes the relative positions of atoms, thereby increasing the distance between the valence and conduction bands (~2.15 eV) (blue shift). In this process, some defects act as "trapping centers" in the conduction band, reducing the absorption of low-energy photons. As a result, the overall absorption coefficient becomes even lower compared to ion intercalation.

Figure 6 shows the dependence of light transmittance on photon energy for all three samples.

As seen in the pure sample, the transmittance remains relatively high (~65%) up to approximately 2 eV, followed by a sharp drop. This drop corresponds to the fundamental band gap of the material, indicating that the GaSe single crystal absorbs light with photon energies above ~2 eV and does not transmit it.

After intercalation, the initial transmittance level starts around ~43%, and a steep decrease is observed near 1.88 eV. This indicates that the intercalation slightly narrows the band gap and introduces changes in the crystal structure or electronic states.

In the case of photo-intercalation, the transmittance is further reduced (~35%), and the onset of absorption appears around ~2.15 eV. This suggests that even lower-energy photons are now being absorbed by the material, resulting in an earlier and more pronounced drop in transmittance.
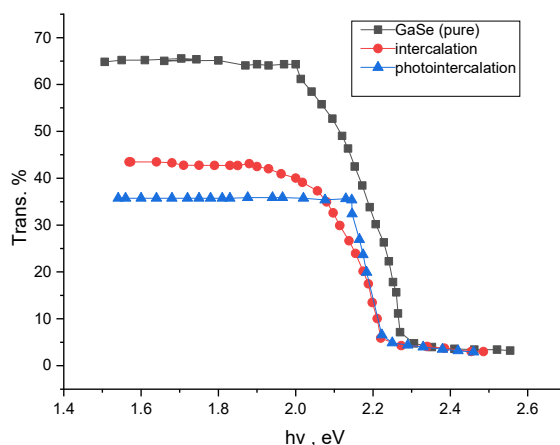
Figure 6. Dependence of light transmission rate on energy

CONCLUSIONS

The experimental investigations revealed that the most intense diffraction peak (002) in the XRD pattern confirms the layered structure and high degree of ordering along the c-axis. Additional major diffraction peaks such as (004), (006), and (008) indicate a well-organised layered phase, while reflections corresponding to planes like (101), (110), and (112) demonstrate the lateral structural arrangement of the crystal. The narrow and sharp nature of these peaks reflects the high crystalline quality of the single crystal (99.99999%).

As a result of Cu ion intercalation into GaSe single crystals, the band gap decreased from 2 eV to 1.88 eV, leading to the formation of new energetic levels. This caused a notable increase in the absorption coefficient within the 200–400 nm range and the appearance of new optical transitions around 600 nm. In the case of photo-intercalation, approximately 35% of the incident light is transmitted through the material, while the remaining 65% is absorbed, with the band gap widening slightly to about 2.15 eV.

Using the applied approach, the band gap for pure GaSe was determined as $E_g = 2.00 \pm 0.03$ eV and for Cu-intercalated GaSe as $E_g = 1.86 \pm 0.03$ eV (95% CI). Thus, intercalation reduces the band gap by $\Delta E_g = -0.14 \pm 0.04$ eV.

DISCUSSION

This work presents results for a single intercalation level; nevertheless, considering the measurement uncertainty, the observed narrowing of the band gap (Eg) is clear and exceeds the experimental errors. In the future, we plan to prepare a series of samples with varying Cu intercalation levels (confirmed by EDS) to investigate changes in Eg over a broader range.

ORCID

®**Rahim Madatov,** https://orcid.org/0000-0003-2420-2654; ®**Lamiya Sadigli,** https://orcid.org/0009-0001-3091-401X
®**Rakshana Mamishova,** https://orcid.org/0000-0002-1760-8384; ®**Aydan Khaligzadeh,** https://orcid.org/0009-0001-6325-0440

REFERENCES

[1] A.Z. Abasova, R.S. Madatov, and V.I. Stafeev, *Radiation-stimulated processes in chalcogenide structures*, (Elm, Baku, 2011). (in Russian)
[2] G.B. Sakr, "Optical and electrical properties of GaSe thin films," Materials Science and Engineering: B, **138**(1), 1–6 (2007). https://doi.org/10.1016/j.mseb.2006.10.008
[3] N.N. Kolesnikov, E.B. Borisenko, D.N. Borisenko, and V.K. Gartman, "Influence of growth conditions on microstructure and properties of GaSe crystals," Journal of Crystal Growth, **300**(2), 294–298 (2007). https://doi.org/10.1016/j.jcrysgro.2007.01.001
[4] Z.D. Kovalyuk, and V.Y. Duplavyy, "Preparation and properties of electrets based on iodine-intercalated InSe and GaSe," Inorganic Materials, **48**, 776–780 (2012). https://doi.org/10.1134/S0020168512080092
[5] Y. Zhirko, V. Grekhov, N. Skubenko, Z. Kovalyuk, and T. Feshak, "Characterization and optical properties of layered InSe and GaSe crystals intercalated with hydrogen and hydrogen-containing molecules," in: *Advanced Materials for Renewable Hydrogen Production, Storage and Utilization*, edited by J. Liu, (InTech, 2015), pp. 11–50. https://doi.org/10.5772/61051
[6] T. Nakato, H. Kamase, and R. Shinozaki, "Visible-light-induced electron transfer in intercalation-type composites organized on photocatalytically active layered niobate," Journal of the Ceramic Society of Japan, **119**(6), 528–531 (2011). https://doi.org/10.2109/jcersj2.119.528

[7] A. Dhingra, R.G. Blair, and P.A. Dowben, "Effects of intercalation on bandgap of pristine two-dimensional layered GeI$_2$," MRS Advances, **7**, 763–765 (2022). https://doi.org/10.1557/s43580-022-00302-6

[8] M. Mengjuan, X. Han, W. Shilei, S. Yitong, L. Bingbing, B. Lihui, S. Bing, *et al*., "Intercalation-induced monolayer behavior in bulk NbSe$_2$," ACS Applied Materials and Interfaces, **16**(43), 59049–59055 (2024). https://doi.org/10.1016/j.commatsci.2024.113468

[9] R. Liu, C. Wang, Y. Li, Y. Xie, Q. Chen, Z. Chen, and Q. Liu, "Intercalating copper into layered TaS$_2$ van der Waals gaps," RSC Advances, **7**, 46699–46703 (2017). https://doi.org/10.1039/C7RA08630J

[10] N. Shehzad, I. Shahid, F. Subhan, W. Rahman, and M. Cai, "Structural, electronic, and optical properties of two-dimensional bilayer MgCl$_2$ intercalated with Be and Mg single atom: Insulator to semiconductor transformation," Computational Materials Science, **247**, 113468 (2025). https://doi.org/10.1016/j.commatsci.2024.113468

[11] C. Julien, "Electrical and optical properties of intercalated In–Se layered materials," in: *Intercalation in Layered Materials*, vol. 148, (Springer, Boston, 1986), pp. 159–160. https://doi.org/10.1007/978-1-4757-5556-5_11

[12] J. Zhou, Z. Lin, H. Ren, X. Duan, I. Shakir, Y. Huang, and X. Duan, "Layered intercalation materials," Advanced Materials, **33**(25), 2004557 (2021). https://doi.org/10.1002/adma.202004557

[13] M. Rajapakse, B. Karki, U.O. Abu, S. Pishgar, M.R.K. Musa, S.M.S. Riyadh, M. Yu, *et al*., "Intercalation as a versatile tool for fabrication, property tuning, and phase transitions in 2D materials," npj 2D Materials and Applications, **5**(1), 30 (2021). https://doi.org/10.1038/s41699-021-00211-6

[14] V.B. Bolędziuk, Z.D. Kovalyuk, Z.R. Kudrynskyi, M.N. Pyrlya, T.N. Feshak, and A.D. Shevchenko, "Electrochemical, optical and magnetic properties of Ni$_x$GaSe intercalation compounds," Inorganic Materials, **51**(11), 1086–1089 (2015). https://doi.org/10.1134/S0020168515100039

[15] Z. Muhammad, K. Mu, H. Lv, C. Wu, Z. Rehman, M. Habib, Z. Sun, *et al*., "Electron doping induced semiconductor to metal transitions in ZrSe$_2$ layers via copper atomic intercalation," Nano Research, **11**, 4914–4922 (2018). https://doi.org/10.1007/s12274-018-2081-1

[16] R. Madatov, A. Najafov, A. Alakbarov, T. Tagiev, and A. Khaliqzadeh, "Features of electrical and photoelectric properties of GaS(Yb) monocrystals," Journal of Physical Sciences, **74**(9), 1–5 (2019). https://doi.org/10.1515/zna-2018-0475

[17] Y. Torita, K. Kushida, T. Nishimura, K. Kuriyama, and T. Nakamura, "Lattice displacement and electrical property of Li-ion implanted GaN single crystal," Procedia Engineering, **215**, 66–76 (2017). https://doi.org/10.1016/j.proeng.2017.11.152

[18] R. Madatov, R. Mamishova, M. Mamedov, J. Ismayilov, and U. Faradjova, "Electrophysical properties of Pb$_{1-x}$Mn$_x$Se epitaxial films irradiated by γ-quanta," Turkish Journal of Physics, **44**(2), 214-221 (2020). https://doi.org/10.3906/fiz-1906-14

ДОСЛІДЖЕННЯ ОПТИЧНИХ ВЛАСТИВОСТЕЙ МОНОКРИСТАЛІВ НАПІВПРОВІДНИКІВ GaSe, ІНТЕРКАЛЬОВАНИХ ІОНАМИ МЕТАЛІВ

Рахім Мадатов[1,2], Ламія Садіглі[1], Ракшана Мамішова[1,3], Айдан Халігзаде[1]
[1]*Міністерство науки та освіти Азербайджанської Республіки, Інститут радіаційних проблем,*
вулиця Б. Вагабзаде, 9, AZ 1141, Баку, Азербайджан,
[2]*Національна авіаційна академія, проспект Мардакана, 30, Az 1045, Баку, Азербайджан*
[3]*Азербайджанський університет архітектури та будівництва, вулиця Айни Султанової, 5, Az1073, Баку, Азербайджан*

У цьому дослідженні для характеристики структурних та фазових властивостей монокристалів GaSe було використано метод рентгенівської дифракції, а також досліджено вплив інтеркаляції іонів Cu на їх оптичні властивості. Збільшення поглинання (ABS) спостерігалося в області 200–400 нм в результаті додавання іонів Cu, а нові оптичні переходи відбувалися близько 600 нм. Загалом, спостережувані варіації рівнів поглинання спостерігалися в спектральному діапазоні 200–800 нм. Таус аналіз а показав, що ширина забороненої зони звузилася приблизно з 2 еВ до приблизно 1,88 еВ при інтеркаляції та дещо розширилася до приблизно 2,15 еВ при фотоінтеркаляції. Ці результати свідчать про те, що інтеркаляцію іонів Cu можна застосовувати для модифікації оптичних властивостей монокристалів GaSe, збільшуючи їхній потенціал для використання в нелінійних оптичних пристроях, фотоніці та сенсорних технологіях. Результати також демонструють, що інтеркаляція є відповідним методом регулювання фізичних характеристик шаруватих матеріалів.
Ключові слова: *ширина забороненої зони; поглинання; інтеркаляція; рентгенівська дифракція*

ADVANCED FIRST-PRINCIPLE STUDY OF AgGaTe$_2$ AND AgInTe$_2$ CHALCOPYRITE SEMICONDUCTORS: STRUCTURAL, ELECTRONIC, AND OPTICAL PROPERTIES VIA FPLAPW WITHIN WIEN2K

Abdelghani Koubil[1], Mohamed Khettal[1], ⬤Yousra Megdoud[1], ⬤Mosbah Laouamer[2],
⬤Yamina Benkrima[3]*, Latifa Tairi[4], ⬤Redha Meneceur[2]
[1]Institute of Sciences, University Center of Tipaza, Algeria
[2]UDERZA Unit, Faculty of Technology, University of El-Oued, 3900 Algeria
[3]Ecole Normale Superieure de Ouargla 3000 Algeria
[4]Research Center in Industrial Technologies CRTI, P.O. Box 64, Cheraga, 1, 6014 Algiers, Algeria
*Corresponding Author Email: b-amina1@hotmail.fr

In this paper, we present a detailed theoretical exploration of the ternary chalcopyrite semiconductors AgGaTe$_2$ and AgInTe$_2$ using first-principles calculations grounded in Density Functional Theory (DFT). The simulations are carried out within the Full-Potential Linearized Augmented Plane Wave (FPLAPW) formalism as implemented in the WIEN2k computational package. Structural properties are optimized using the WC-GGA exchange–correlation functional, whereas the electronic and optical responses are refined through the modified Becke–Johnson (mBJ) potential, known for its improved bandgap estimation accuracy. The study involves a thorough evaluation of the electronic band structures and various optical parameters, including the complex dielectric function, absorption coefficient, refractive index, energy-loss function, and reflectivity. The findings reveal that both materials possess direct bandgaps that lie within the optimal range for solar cell absorption. Additionally, these compounds show strong light absorption in the visible and near-infrared regions, high refractive indices, and marked interband transitions. Such features highlight their suitability for photovoltaic technologies, especially in thin-film configurations where enhanced light capture and carrier generation are critical. Moreover, the observed optical and electronic properties also suggest possible utilization in infrared detection and nonlinear optoelectronic systems. Overall, the results contribute valuable theoretical insight into the optoelectronic characteristics of silver-based telluride chalcopyrites, reinforcing their potential as environmentally friendly and efficient materials for future solar energy solutions.
Keywords: *FPLAPW; Density Functional Theory; Modified Becke–Johnson; Electronic structure; Optical analysis*
PACS: 73.20.At, 78.20.Ci

1. INTRODUCTION

Ternary I–III–VI2 chalcogenide semiconductors, notably AgGaTe$_2$ and AgInTe$_2$, have garnered substantial attention from the scientific community owing to their remarkable structural and physicochemical characteristics.

These compounds are part of a wider family of tellurium-rich materials that adopt a crystal structure based on the chalcopyrite prototype [2]**.** Their combination of adaptable crystal geometry, adjustable bandgap energy, and superior optical activity across the visible and infrared spectra renders them highly suitable for innovative energy-related and optoelectronic applications [3–8].

AgGaTe$_2$ and AgInTe$_2$ crystallize in a chalcopyrite-type tetragonal lattice (space group I-42d, No. 122) [9], derived from the zincblende structure through an ordered arrangement of cations. This structural configuration exhibits a distinct distribution of atoms at cationic and anionic positions, leading to anisotropic electronic properties and notable dielectric responses.

Thanks to their relatively narrow and direct bandgaps, both materials are highly suited for use in thin-film solar cells, infrared photodetectors, thermoelectric converters, and nonlinear optical applications [10–15]. Furthermore, their optoelectronic characteristics can be engineered through compositional modifications or lattice strain, enhancing their adaptability for tailored device integration.

Despite their promising functionalities, rigorous theoretical investigations, particularly those employing accurate ab initio techniques, remain limited. Among such methods, the Full-Potential Linearized Augmented Plane Wave (FPLAPW) approach [16] is widely regarded for its high precision in solving the Kohn–Sham equations within the Density Functional Theory (DFT) framework [17], especially for systems exhibiting structural anisotropy or complex bonding environments.

In this study, we utilize the WIEN2k computational platform [18], a well-established implementation of the FPLAPW formalism, to explore the structural, electronic, and optical properties of AgGaTe$_2$ and AgInTe$_2$. Geometry optimization is conducted using the Wu–Cohen Generalized Gradient Approximation (WC-GGA), while the electronic and optical responses are computed via the modified Becke–Johnson (mBJ) potential [19], which offers superior bandgap accuracy compared to traditional GGA or LDA functionals.

The objective is to provide a thorough characterization of these compounds, including their:

• electronic band structures and bandgap nature (direct vs. indirect),

• and Optical parameters, such as the dielectric function, absorption coefficient, refractive index, and reflectivity [15].

The findings provide valuable theoretical insights for optimizing Ag-based chalcopyrite semiconductors in energy harvesting and optoelectronic applications, while supporting their development as efficient and sustainable materials for next-generation technologies.

2. COMPUTATIONAL METHODOLOGY

All computational analyses in this study were conducted using the WIEN2k package [18], which implements the Full-Potential Linearized Augmented Plane Wave (FPLAPW) method [16] recognized as one of the most precise first-principles techniques for solving the Kohn–Sham equations of Density Functional Theory (DFT) [17]. This approach is particularly effective for handling materials with strongly localized or correlated electrons, such as those containing transition metals or heavy elements.

For structural relaxation and total energy determination, we employed the Generalized Gradient Approximation (GGA) with the Perdew-Burke-Ernzerhof (PBE) exchange correlation functional [20]. To enhance the accuracy of the computed electronic bandgaps and optical properties, we adopted the modified Becke Johnson (mBJ) potential, which is known to yield bandgap estimates that align more closely with experimental results than those obtained using standard GGA or LDA methods.

Given the presence of the heavy tellurium (Te) atom ($Z = 52$), spin–orbit coupling (SOC) effects were explicitly considered, as they significantly influence the electronic states near the valence band maximum. Computational parameters were carefully selected to ensure numerical accuracy and convergence: the plane-wave cutoff parameter RK_{max} was set to 8.0, and the Brillouin zone was sampled with a $12\times12\times12$ Monkhorst Pack k-point mesh.

Muffin-tin radii (R_{MT}) were assigned as follows: 2.5 atomic units (a.u.) for Ag, 2.3 a.u. for Ge or In, and 2.4 a.u. for Te, ensuring there was no overlap between atomic spheres. Self-consistent field (SCF) cycles were considered converged when the total energy difference between iterations was less than 10^{-5} Ry, and the charge convergence threshold was set to 10^{-4} Ry.

3. RESULTS AND INTERPRETATION
3.1. Structural Optimization

The structural optimization of the ternary chalcopyrite compounds AgInTe$_2$ and AgGaTe$_2$ offers crucial insights into their crystal stability, atomic-scale arrangement, and the structural parameters that influence their physical behavior. Both compounds crystallize in the tetragonal chalcopyrite structure with space group I-42d, **[9]** which can be regarded as a derivative of the cubic zinc blende structure. This configuration arises through the ordered substitution of Group III elements (In or Ga) and the resulting doubling of the unit cell along the c-axis. The ordered arrangement of cations (Ag and In or Ga) in this tetragonal lattice breaks the cubic symmetry and introduces anisotropy into the physical properties an essential feature for applications in directional optoelectronics and thermoelectrics **[21]**.

The optimized lattice parameters obtained using the GGA-WC results illustrated in **(Table 1),** in good agreement with reported experimental and theoretical data. The c/a ratio in both compounds is approximately 1.98, which is slightly lower than the ideal value of 2.0. This subtle deviation signifies the presence of a minor tetragonal distortion, commonly observed in real chalcopyrite structures. Such a small distortion indicates that the systems maintain a high degree of lattice symmetry and structural integrity, essential for minimizing crystal imperfections, lattice strain, and potential defect states that can trap carriers or act as non-radiative recombination centers.

Table 1. Lattice parameters (a, c) (Å), internal parameter (u), bulk modulus B (GPa), and its pressure derivative *B′* for the AgGaTe$_2$ and AgInTe$_2$ compounds

Compound		*a*(Å)	*C*(Å)	*c/a*	$\eta=c/2a$	*U*(Å)	*B*(GPa)	*B′*
AgGaTe$_2$	Our Calcul.	6.221	12.558	1.99	1.00	0.250	50.123	5.347
	Exp.	6.288[a]	11.940[a]	1.898[a]	0.949[a]	-	-	-
		6.283[b]	11.918[b]	1.897[b]	0.948[b]	0.26[b]	48.6[b]	-
AgInTe$_2$	Our calcul.	6.442	12.925	1992	0.997	0.231	45.540	5.6122
	Exp.	6.467[a]	12.633[a]	1.85[a]	0.977[a]	0.262[a]	-	-

[a]**Ref [32],** [b]**Ref [33]**

The variation of Energy as function a volume **(Fig. 1).** The slight differences in lattice constants and unit cell volumes between AgInTe$_2$ and AgGaTe$_2$ can be attributed primarily to the difference in covalent radii of the Group III elements. Indium (In), with a covalent radius of 1.56 Å, is significantly larger than gallium (Ga), which has a radius of 1.36 Å. This difference leads to a lattice expansion in AgInTe$_2$ along both the a-axis and c-axis, resulting in a larger unit cell volume compared to AgGaTe$_2$. This observation is consistent with Vegard's law, which states that the lattice parameters of a solid solution or alloy vary linearly with the atomic radii of the substituting elements. From a materials physics perspective, such atomic substitution not only alters the geometrical framework but also subtly affects bond lengths and bond angles, especially the Ag–Te and In/Ga–Te bonds, which are critical for orbital hybridization and

bandgap formation. For example, a longer In–Te bond in AgInTe$_2$ leads to weaker orbital overlap compared to the shorter Ga–Te bond in AgGaTe$_2$, which can influence both the band dispersion and the effective mass of charge carriers.

Moreover, the bond alternation parameter (u) and internal displacement of atoms though not detailed here also play a role in the spatial electron density distribution, anisotropic dielectric response, and polarization effects, which are significant in nonlinear optical applications and in understanding carrier localization phenomena.
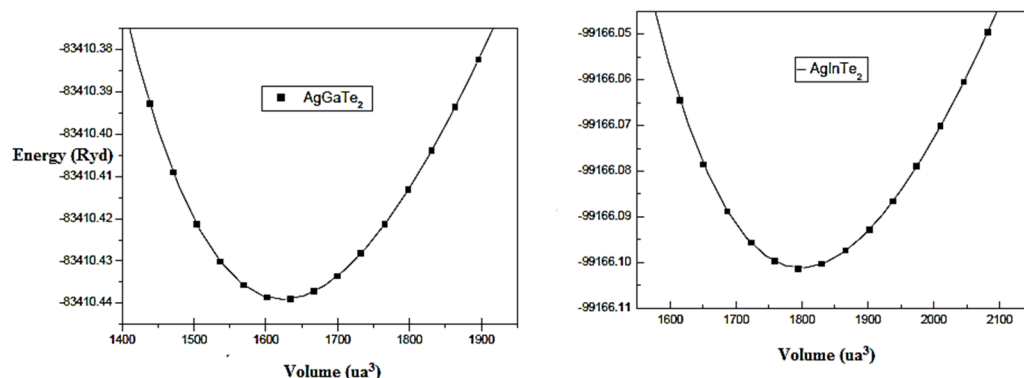
Figure 1. The dependence of the total energy on volume was examined for the AgInTe$_2$ and AgGaTe$_2$ compounds, aiming to analyze their thermodynamic and structural characteristics

The precision of the computed structural parameters highlights the strength and reliability of the employed computational approach. Although the GGA-WC functional is recognized for its limited accuracy in bandgap predictions, it proves effective in capturing equilibrium structures and volumetric behavior. This consistency in structural modeling provides a dependable foundation for further exploration of the electronic band structure, density of states, and optical characteristics, especially considering that even slight discrepancies in lattice parameters may lead to significant variations in observable physical properties.

In conclusion, both AgInTe$_2$ and AgGaTe$_2$ exhibit stable, well-ordered chalcopyrite structures with minimal tetragonal distortion and expected trends in lattice expansion due to atomic substitution. These structural characteristics contribute directly to the favorable semiconducting and optical properties of these materials. Their mechanical stability, structural uniformity, and adaptability to lattice engineering make them strong candidates for advanced applications in photovoltaic energy conversion, infrared photodetection, and thermoelectric energy harvesting.

3.2. Electronic Structure Band

The electronic band structure calculations for AgInTe$_2$ and AgGaTe$_2$ indicate that both compounds possess a direct bandgap, with the valence band maximum (VBM) and conduction band minimum (CBM) located at the Γ-point in the Brillouin zone (see Figure 2). This direct transition is particularly beneficial for optoelectronic and photovoltaic technologies, as it enables efficient photon absorption and emission without the necessity of phonon involvement. The band structures were derived using the Generalized Gradient Approximation (GGA), based on either prior literature or current computational results (refer to Table 2). These findings align with the well-documented limitation of GGA in underestimating bandgap values due to its inadequate treatment of exchange–correlation interactions. To achieve more reliable electronic gap predictions, the modified Becke–Johnson (mBJ) potential was employed. This semi-local exchange potential significantly improves the description of the electronic structure, resulting in corrected bandgap values of around 0.98 eV for AgInTe$_2$ and approximately 1.15 eV for AgGaTe$_2$. These values are in much closer agreement with available experimental data, confirming that mBJ is more suitable for accurately capturing the quasi-particle bandgap of semiconducting chalcopyrite materials.

Figure 2. Electronic band structures of (a) AgGaTe$_2$ and (b) AgInTe$_2$ were computed using the modified Becke–Johnson (mBJ) potential

Table 2. Band gap (Eg) values of the $AgInTe_2$ and $AgGaTe_2$ compounds.

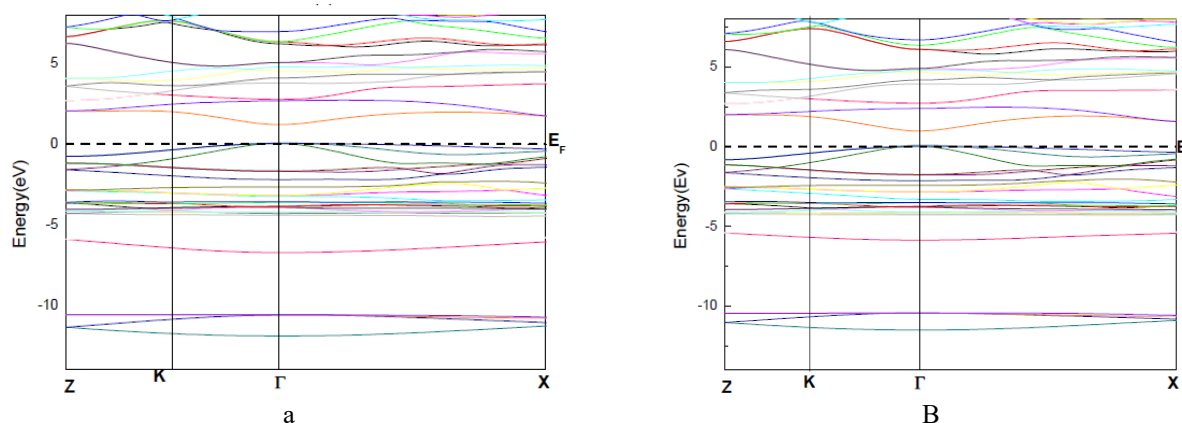|	Eg (eV)			
	Our Calcul.		Exp.	Other calcul.
	WC-GGA	mBj		
$AgGaTe_2$	0.5	1.18	1.1[a], 1.36[b], 1.32[c]	1.10[a], 1.21[b]
$AgInTe_2$	0.04	1.01	0.93-0.96[a], 1.04[b]	1.09[b]

[a]Ref [32], [b]Ref [33]

In terms of orbital character, the valence band region in both compounds is predominantly composed of Te-5p states, which are strongly hybridized with Ag-4d orbitals. This p–d hybridization plays a vital role in shaping the upper valence bands, leading to relatively flat band dispersion near the VBM and contributing to the high hole effective mass. The conduction band edge, however, exhibits material-specific characteristics: in $AgInTe_2$, the CBM is largely formed by In-5p orbitals, while in $AgGaTe_2$, it consists mainly of Ga-4p states. Due to the smaller and more localized nature of Ga-4p orbitals compared to In-5p, the conduction band in $AgGaTe_2$ is slightly more dispersive, which can contribute to a lower electron effective mass and potentially better n-type transport behavior.

The separation between the valence and conduction bands defines the electronic bandgap, and the precise alignment and nature of these bands are crucial in determining the absorption edge, carrier recombination dynamics, and overall efficiency of optoelectronic devices. The clear direct bandgap at the Γ-point and the dominant p–d and p–p interactions in both materials are consistent with what is expected in chalcopyrite semiconductors and support their use as light-absorbing layers in thin-film solar cells, infrared sensors, and photoelectronic modulators.

In summary, the electronic structure analysis demonstrates that $AgInTe_2$ and $AgGaTe_2$ are both direct gap semiconductors with bandgaps suitable for infrared and near-infrared applications. The mBJ correction effectively mitigates the bandgap underestimation typical of GGA, and the detailed orbital analysis highlights the significant role of Te–Ag hybridization and Group III p-orbitals in shaping the band structure. These characteristics reinforce the potential of these compounds for integration into next-generation optoelectronic and photovoltaic technologies.

3.3 Optical Properties

The optical response of $AgInTe_2$ and $AgGaTe_2$ was investigated through first-principles calculations of the complex dielectric function, expressed as $\varepsilon(\omega) = \varepsilon_1(\omega) + i\varepsilon_2(\omega)$, [31] where $\varepsilon_1(\omega)$ represents the real part (describing dispersion) and $\varepsilon_2(\omega)$ the imaginary part (related to absorption). From these fundamental optical quantities, additional key parameters such as the refractive index (n), absorption coefficient (α), and reflectivity (R) were derived, providing a comprehensive view of the materials' interaction with electromagnetic radiation.

The static dielectric constants $\varepsilon_1(0)$ were found to be approximately 12.6 for $AgGaTe_2$ and 13.1 for $AgInTe_2$, indicating strong polarization response at zero photon energy. These high values suggest significant electronic polarizability, which is favorable for materials intended for nonlinear optical or capacitive applications. Similarly, the static refractive index n(0) shows high values of ~3.55 for $AgGaTe_2$ and ~3.60 for $AgInTe_2$, **(Figure 3)** indicating that both compounds are optically dense. Such high refractive indices imply efficient light confinement, which is crucial for enhancing the optical path length in thin-film solar cell structures and improving light absorption efficiency. **(Table 3).**
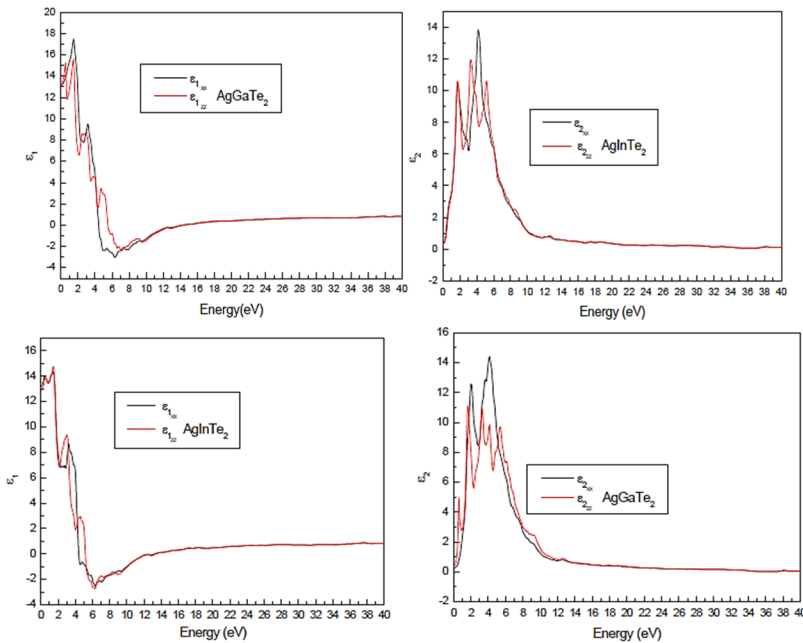

Figure 3. The energy-dependent behavior of both the real and imaginary components of the electronic dielectric function ε(ω) was analyzed for $AgGaTe_2$ and $AgInTe_2$ compounds

Table 3. Static Dielectric Function (ε1(0)) and Static Refractive Index (n(0)) Calculations for AgInTe2 and AgGaTe2 Compounds.

	n(0)		$\varepsilon_1(0)$	
	Our Calcul. WC-GGA	Other calcul. Ref.	Our Calcul.	Other calcul. Ref.
AgInTe$_2$	Xx: 3.591	Xx: 2.756	Xx:12.942	-
	Zz:3.623	Zz: 2.775	Zz: 13.193	-
AgGaTe$_2$	Xx: 3.631	Xx: 2.891	Xx: 13.193	Xx: 12.72
	Zz: 3.513	Zz: 2.466	Zz: 13.103	Zz: 12.90

Ref [32,33]

The analysis of the imaginary component of the dielectric function, $\varepsilon_2(\omega)$, indicates that the principal absorption peaks are located at approximately 4.1 eV for AgGaTe$_2$ and 3.9 eV for AgInTe$_2$. These prominent features are attributed to strong interband transitions, notably from Te-5p and Ag-4d states in the valence band to conduction band states largely comprised of Ga-4p or In-5p orbitals. Moreover, the computed absorption coefficient α(ω) (as shown in Figure 4) surpasses 10^5 cm^{-1} within the visible and near-infrared regions, highlighting the materials' pronounced interaction with light. This high absorption performance is particularly advantageous for photovoltaic applications, as it facilitates efficient solar energy capture even in devices employing ultrathin active layers.
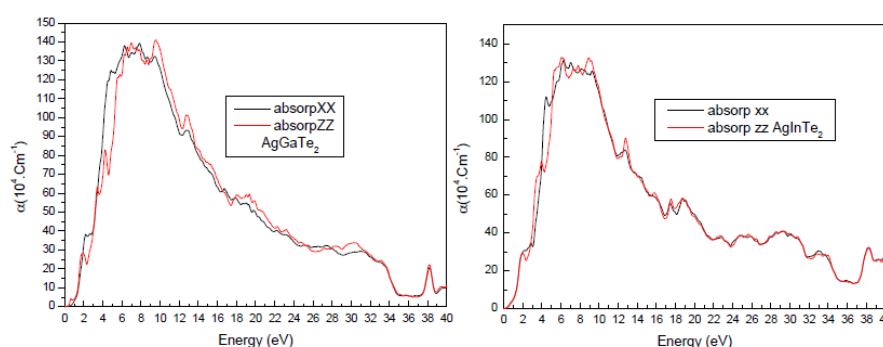
Figure 4. The energy-dependent optical conductivity of AgInTe$_2$ and AgGaTe$_2$ compounds was examined to assess their electromagnetic response characteristics
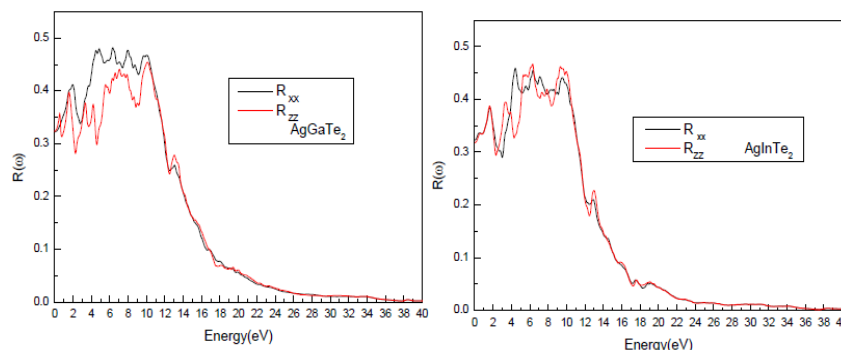
Figure 5. The photon energy dependence of the optical reflectivity R(ω) was investigated for the AgInTe$_2$ and AgGaTe$_2$ compounds to understand their reflective behavior across different spectral regions

The reflectivity spectra demonstrate that both AgInTe$_2$ and AgGaTe$_2$ compounds display moderate reflectance approximately 45% in the ultraviolet (UV) region, followed by a gradual decline as the wavelength extends into the visible and infrared ranges. This behavior, characterized by efficient absorption in the visible spectrum alongside partial UV reflectivity (See Figure5), suggests these materials are well-suited for multifunctional optical coatings. In particular, their UV-reflective properties can enhance device longevity and serve as effective radiation filters, making them valuable in optoelectronic and protective applications.

The variation of the refractive index $n(\omega)$ and the extinction coefficient $k(\omega)$ as a function of energy is presented in Figure 6. According to the refractive index spectrum, we observe anisotropic behavior, characterized by $\Delta n(0) = 0.05$ and 0.02 for AgInTe$_2$ and AgGaTe$_2$, respectively. The refractive index increases with energy until it reaches a maximum value in the visible region for both compounds. Beyond these energies 1.542 eV for AgInTe$_2$ and 1.589 eV for AgGaTe$_2$ it decreases. It is also noted that the peaks shift towards lower energies when moving from Ga to In.

The extinction coefficient $k(\omega)$ is related to the damping of the oscillation amplitude of the incident electric field. The maximum peak in the extinction coefficient curve appears at the energy value (2.771 eV for AgGaTe$_2$ and 2.489 eV for AgInTe$_2$) where the real part of the dielectric function crosses zero. This is clearly verified for both compounds. Subsequently, the extinction coefficient $k(\omega)$ decreases with increasing incident photon energy.

Optical conductivity plays a crucial role in evaluating photoelectric conversion efficiency, as it reflects the material's response under illumination. Figure (7) illustrates the energy-dependent optical conductivity profiles of AgGaTe$_2$ and

AgInTe$_2$. Notably, both compounds demonstrate substantial conductivity within the visible spectrum (1.64–3.12 eV), highlighting their suitability for solar energy applications.

Overall, the optical analysis confirms that AgInTe$_2$ and AgGaTe$_2$ exhibit highly favorable properties – such as elevated refractive indices, robust absorption across the visible to near-infrared range, and moderate reflectivity in the ultraviolet. These characteristics render them excellent candidates for cutting-edge technologies, including thin-film photovoltaic cells, IR photodetectors, and nonlinear optical components. Furthermore, their capacity to achieve efficient light absorption while maintaining selective transparency enhances their potential integration into advanced multilayer optoelectronic and photonic architectures.
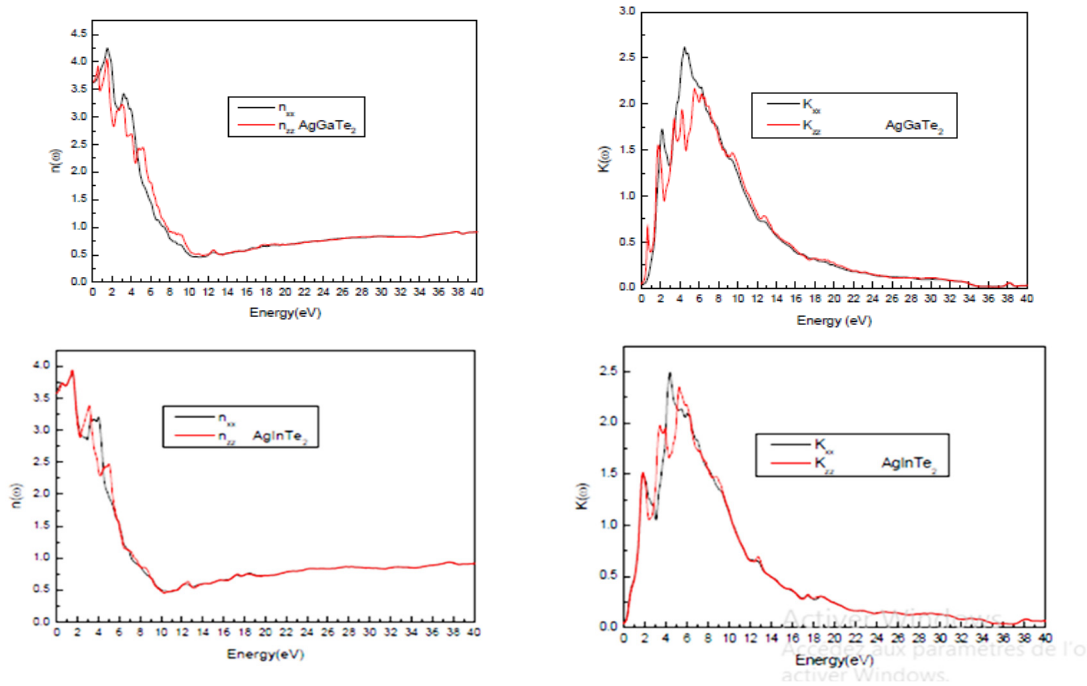
Figure 6. Optical Behavior of AgInTe$_2$ and AgGaTe$_2$: Spectral Variation of n(ω) and extinction *k(ω)*
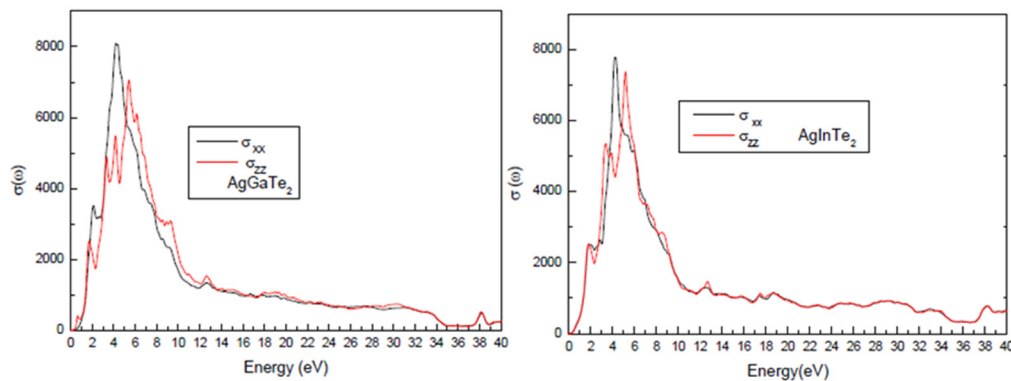
Figure 7. The variation in optical conductivity with photon energy was explored for AgInTe$_2$ and AgGaTe$_2$ compounds to assess their light-induced electronic response characteristics

5. CONCLUSIONS

In this study, we conducted a comprehensive theoretical investigation of the chalcopyrite-type semiconductors AgGaTe$_2$ and AgInTe$_2$ using the Full-Potential Linearized Augmented Plane Wave (FPLAPW) method as implemented in the WIEN2k code. Our first-principles calculations provided detailed insights into the structural, electronic, and optical properties of these compounds.

- The optimized lattice parameters are in excellent agreement with available experimental data, confirming the reliability of the computational approach based on the GGA-PBE functional.

- Band structure calculations using the mBJ potential reveal that both materials possess direct bandgaps of approximately 1 eV, which is ideal for optoelectronic and infrared applications.

- The optical analysis demonstrates strong absorption in the visible and near-infrared regions, high static refractive indices, and robust dielectric responses, all of which are critical for efficient light harvesting and photonic functionality.

These findings highlight the potential of AgGaTe$_2$ and AgInTe$_2$ as promising candidates for next-generation photovoltaic devices, infrared detectors, and nonlinear optical systems.

6. OUTLOOK AND FUTURE DIRECTIONS

To further advance the understanding and technological potential of these materials, future studies may focus on:

- Defect engineering, including the investigation of vacancies, substitutional dopants, or antisite defects, to tailor electronic and optical behavior.
- Alloying strategies, such as partial substitution of Ga, Sb, or Se, to tune the bandgap and optimize performance for specific applications.
- Inclusion of many-body effects, through GW approximation and Bethe–Salpeter Equation (BSE) methods, to more accurately describe excitonic interactions and optical spectra.
- Evaluation of thermal conductivity and carrier mobility, which are crucial for thermoelectric applications and overall device efficiency.

This work lays a strong theoretical foundation for the practical development of Ag-based ternary tellurides and opens avenues for their integration into high-performance optoelectronic and energy conversion technologies.

ORCID

Mosbah Laouamer, https://orcid.org/0000-0002-6374-6075; **Yamina Benkrima**, https://orcid.org/0000-0001-8005-4065
Redha Meneceur, https://orcid.org/0000-0002-1801-0835; **Yousra Megdoud,** https://orcid.org/0000-0001-8999-8134

REFERENCES

[1] A.S. Verma, Philos. Mag. **89**, 183 (2009). https://doi.org/10.1080/14786430802593814
[2] C. Catella, and D. Burlage, Mater. Res. Bull. **23**, 28 (1998). https://doi.org/10.1557/S0883769400029055
[3] M.C. Ohmer, J.T. Goldstein, D.E. Zelmon, A. Waxler, S.M. Hegde, J.D. Wolf, P.G. Schunemann, and T.M. Pollak, J. Appl. Phys. **86**, 94 (1999). https://doi.org/10.1063/1.370704
[4] A.S. Verma, and S.R. Bhardwaj, Phys. Scr. **79**, 015302 (2009). https://doi.org/10.1088/0031-8949/79/01/015302
[5] V.V. Badikov, O.N. Pivovarov, Y.V. Skokov, O.V. Skrebneva, and N.K. Trotsenko, Sov. J. Quantum Electron. **5**, 3502 (1975). https://doi.org/10.1070/qe1975v005n03abeh011027
[6] T. Plirdpring, K. Kurosaki, A. Kosuga, T. Day, S. Firdosy, V. Ravi, G.J. Snyder, *et al.*, Adv. Mater. **24**, 3622 (2012). https://doi.org/10.1002/adma.201200732
[7] T. Plirdpring, K. Kurosaki, A. Kosuga, M. Ishimaru, A. Harnwunggmoung, T. Sugahara, Y. Ohishi, *et al.* Mater. Trans. **53**, 1212 (2012). https://doi.org/10.2320/matertrans.e-m2012810
[8] R. Liu, L. Xi, H. Liu, X. Shi, W. Zhang, and L. Chen, Chem. Commun. (Camb.) **48**, 3818 (2012). https://doi.org/10.1039/C2CC30318C
[9] J. Yao, N. Takas, M. Schliefert, D. Paprocki, P. Blanchard, H. Gou, A. Mar, *et al.* J. Aitken, Phys. Rev. B, **84**, 075203 (2011). https://doi.org/10.1103/PhysRevB.84.075203
[10] Y. Li, Q. Meng, Y. Deng, H. Zhou, Y. Gao, Y. Li, J. Yang, and J. Cui, Appl. Phys. Lett. **100**, 231903 (2012). https://doi.org/10.1063/1.4726109
[11] A. Kosuga, T. Plirdpring, R. Higashine, M. Matsuzawa, K. Kurosaki, and S. Yamanaka, Appl. Phys. Lett. **100**, 042108 (2012). https://doi.org/10.1063/1.3678044
[12] A.V. Kopytov, and A.V. Kosobutsky, Phys. Solid State, **52**, 1359 (2010). https://doi.org/10.1134/s1063783410070061
[13] D. Xue, K. Betzler, and H. Hesse, Phys. Rev. B, **62**, 13546 (2000). https://doi.org/10.1103/physrevb.62.13546
[14] A.H. Reshak, Physica B, **369**, 243 (2005). https://doi.org/10.1016/j.physb.2005.08.038
[15] S. Sharma, A.S. Verma, and V.K. Jindal, Mater. Res. Bull. **53**, 218 (2014). https://doi.org/10.1016/j.materresbull.2014.02.021
[16] E. Wimmer, "Computational methods for atomistic simulations of materials," Materials Science and Engineering: B, **37**(1-3), 72 (1996). https://doi.org/10.1016/0921-5107(95)01459-4
[17] P. Kiréev, la physique des semi-conducteur, (Mir, Moscow, 1979).
[18] M. Born, j., and R. Oppenheimer, Ann. Phys. **87**, 457 (1927). https://doi.org/10.1002/andp.19273892002
[19] D.R. Hartree, Mathematical Proceedings of the Cambridge Philosophical Society, **24**(1), 89 (1928). https://doi.org/10.1017/S0305004100011919
[20] V. Fock, Z. Phys. **61**, 126 (1930). http://dx.doi.org/10.1007/BF01340294
[21] A. Zunger, and A.J. Freeman, Phys. Rev. B, **16**, 2901 (1977). https://doi.org/10.1103/PhysRevB.16.2901
[22] J.P. Perdew, and A. Zunger, Phys. Rev. B, **23**, 5048 (1981). https://doi.org/10.1103/physrevb.23.5048
[23] L.H. Thomas, "The calculation of atomic fields," Mathematical Proceedings of the Cambridge Philosophical Society, **23**(5), 542 (1927). Published online by Cambridge University Press: 24 October 2008. https://doi.org/10.1017/S0305004100011683
[24] E. Fermi, Z. Phys. **48**, 73 (1928). https://doi.org/10.1007/bf01351576
[25] P. Hohenberg, and W. Kohn, Phys. Rev. **136**, B864 (1964). https://doi.org/10.1103/PhysRev.136.B864
[26] J.P. Perdew, and Y. Wang, Phys. Rev. B, **45**, 13244 (1992). https://doi.org/10.1103/physrevb.45.13244
[27] A. Chahed, O. Benhelal, H. Rozale, S. Laksari, and N. Abbouni, Phys. Status Solidi, B, **244**, 629 (2007). https://doi.org/10.1002/pssb.200642050
[28] S. Ullah, U.D. Haleem, G. Murtaza, T. Ouahrani, R. Khenata, S. Naeemullah, Bin Omran, J. Alloys Compd. **617**, 575 (2014). https://doi.org/10.1016/j.jallcom.2014.08.058
[29] E. Jaffe, A. Zunger, Phys. Rev. B, **29**, 1882 (1983). https://doi.org/10.1103/PhysRevB.29.1882
[30] J.L. Shay, and J.H. Wernick, *Ternary Chalcopyrite Semiconductors: Growth, Electronic Properties and Applications*, (Pergamon Press, Oxford, 1975). https://doi.org/10.1016/C2013-0-02602-3

[31] W.N. Honeyman, K.H. Wilkinson, J. Phys. D, **4**, 1182 (1971). https://doi.org/10.1088/0022-3727/4/8/319
[32] K. Beggas, *et al*., Indian J. Phys. **98**, 2755 (2024). http://dx.doi.org/10.1007/s12648-023-03049-4
[33] S.A. Bendehiba, *et al*. Materials Science in Semiconductor Processing, **183**, 108772 (2024), https://doi.org/10.1016/j.mssp.2024.108772

ПОКРАЩЕНЕ ДОСЛІДЖЕННЯ НАПІВПРОВІДНИКІВ ХАЛЬКОПІРИТУ AgGaTe₂ ТА AgInTe₂ НА ОСНОВІ ПЕРШОПРИНЦИПІВ ЗА ДОПОМОГОЮ FPLAPW В РАМКАХ WIEN2K: СТРУКТУРНІ, ЕЛЕКТРОННІ ТА ОПТИЧНІ ВЛАСТИВОСТІ

Абдельгані Кубіл[1], Мохамед Хеттал[1], Юсра Мегдуд[1], Мосбах Лауамер[2], Яміна Бенкрима[3], Латіфа Тайрі[4], Редха Менесер[2]

[1]Інститут наук, Університетський центр Тіпаза, Алжир
[2]Підрозділ UDERZA, Технологічний факультет, Університет Ель-Уед 3900, Алжир
[3]Вища нормальна школа Уаргла 3000 Алжир
[4]Дослідницький центр промислових технологій CRTI, P.O. Скринька 64, Cheraga16014 Алжир, Алжир

У цій статті ми представляємо детальне теоретичне дослідження потрійних халькопіритових напівпровідників AgGaTe₂ та AgInTe₂ з використанням розрахунків з перших принципів, заснованих на теорії функціоналу густини (DFT). Моделювання проводиться в рамках формалізму повнопотенціальної лінеаризованої доповненої плоскої хвилі (FPLAPW), реалізованого в обчислювальному пакеті WIEN2k. Структурні властивості оптимізовані за допомогою функціоналу обміну-кореляції WC-GGA, тоді як електронні та оптичні відгуки уточнюються за допомогою модифікованого потенціалу Бекке-Джонсона (mBJ), відомого своєю покращеною точністю оцінки ширини забороненої зони. Дослідження включає ретельну оцінку електронних зонних структур та різних оптичних параметрів, включаючи комплексну діелектричну функцію, коефіцієнт поглинання, показник заломлення, функцію втрат енергії та відбивну здатність. Результати показують, що обидва матеріали мають прямі заборонені зони, які знаходяться в оптимальному діапазоні для поглинання сонячними елементами. Крім того, ці сполуки демонструють сильне поглинання світла у видимому та ближньому інфрачервоному діапазонах, високі показники заломлення та помітні міжзонні переходи. Такі особливості підкреслюють їхню придатність для фотоелектричних технологій, особливо в тонкоплівкових конфігураціях, де покращене захоплення світла та генерація носіїв заряду є критично важливими. Більше того, спостережувані оптичні та електронні властивості також вказують на можливе використання в інфрачервоному детектуванні та нелінійних оптоелектронних системах. Загалом, результати надають цінне теоретичне розуміння оптоелектронних характеристик телуридних халькопіритів на основі срібла, підкреслюючи їхній потенціал як екологічно чистих та ефективних матеріалів для майбутніх рішень у сфері сонячної енергетики.

Ключові слова: *FPLAPW; теорія функціоналу густини; модифікований аналіз Бекке-Джонсона; електронна структура; оптичний аналіз*

ELECTROPHYSICAL CHARACTERIZATION OF PHOTODETECTORS BASED ON SEMICONDUCTOR STRUCTURES Si (Li) AND Si(Au)

Ilhom I. Maripov[1*], Sali A. Radzhapov[2], Sardor F. Xasanov[1], Damir B. Istamov[2],
Yusuf T. Yuldashev[1], Diyora Axnazarova[3], Shamshiddin A. Ashirov[3]

[1]Tashkent State Agrarian University, Tashkent Region, 111160, Uzbekistan
[2]Physical-Technical Institute of Uzbekistan Academy of Sciences, Tashkent 100084, Uzbekistan
[3]Gulistan State University, 4 micro districts, 120100, Gulistan, Uzbekistan
*Corresponding Author e-mail: maripov1988@gmail.com

This paper explores the technological and physical principles for developing silicon-lithium (Si(Li)) nuclear radiation detectors with a thickness greater than 1.5 mm and a surface area of at least 50 cm^2. The formation of large-area p–i–n structures via lithium-ion drift and diffusion mechanisms was analyzed. To evaluate the electrophysical parameters of the detectors, current-voltage (I–V) and capacitance-voltage (C–V) characteristics were measured. The I–V results under reverse bias in the range of $U = 0 – 200$ V showed extremely low leakage currents $I \leq 0.5$ nA, indicating the formation of high-quality p – i – n junctions. Beyond 100 V, the current remained nearly constant, forming a plateau region. The findings propose effective technological solutions for developing highly sensitive, stable, and low-noise radiation detectors.

Keywords: *Detector; Heterostructure; Silicon; Germanium; Semiconductor p–i–n structure; p–n junction; Electrophysical properties*
PACS: 73.40. Sx, 73.61.Cw, 73.61.Ey, 72.20.Ee

INTRODUCTION

In recent years, semiconductor-based detectors have been widely applied in various fields such as nuclear physics, medical diagnostics, environmental monitoring, and cosmic radiation detection [1–5]. In particular, detectors based on semiconductor materials such as silicon (Si) and germanium (Ge) are distinguished by their high sensitivity and accuracy. The electrical and physical properties of these materials enable their effective use as radiation-responsive detectors [6-9]. This study focuses on the electrophysical and radiometric properties of detectors fabricated with $Al − nGe(p − i − n) − Au$ and $Au − nSi − Al$ structures. The $Al − nGe(p − i − n) − Au$ detector, based on germanium, exhibits high sensitivity due to the presence of a p–i–n junction. Meanwhile, the $Au − nSi − Al$ detector, based on silicon, is characterized by its low-noise operational regime. During the research, the current-voltage (I–V) and capacitance-voltage (C–V) characteristics of the detectors were analyzed, along with investigations into their radiation sensitivity, temperature dependence, and physical phenomena arising under irradiation. The results of this work contribute to the advancement of modern semiconductor detectors by enhancing their sensitivity and expanding their applicability across different technological fields [10–13]. The development of such detectors begins with a thorough study of the parameters of the materials used in their fabrication. Accordingly, we have theoretically analyzed the energetic properties of Si and Ge, the primary semiconductor materials used in this research. The analysis involved understanding the interaction between metal and semiconductor layers, as well as the variations in these properties across the material's depth. We specifically examined the physical processes occurring in these regions and evaluated their influence on the detector's performance [14–16]. In this work, we conducted an in-depth study of the electrophysical and radiometric characteristics of $Al − nGe(p − i − n) − Au$ and $Au − nSi − Al$ structures. Through this, we determined their optical and electrical parameters. Globally, the development of compact semiconductor detectors has made significant advancements. To date, detectors with dimensions of up to 50 mm based on the $Al − nGe(p − i − n) − Au$ structures have been developed by researchers worldwide. A critical aspect of $Al − nGe(p − i − n) − Au$ structured semiconductor detectors is ensuring a uniform concentration of lithium ions within a defined depth of the silicon crystal. This uniform distribution is essential for achieving optimal detector performance [17–18]. Therefore, technological processes based on diffusion and drift methods, which are widely used to introduce dopant atoms into the crystal lattice, require optimization to ensure homogeneous dopant distribution throughout the bulk of the crystal.

RESEARCH METHODOLOGY

In the development of semiconductor detectors used for recording nuclear radiation, the energy levels and potential barrier diagrams of key elements — silicon (Si) and germanium (Ge) — are of primary importance. These parameters are illustrated in Figure 1. The analysis was conducted explicitly for the detector based on the $Au − nSi − Al$ structure, and the results are presented using the corresponding energy band diagram.

As shown in Figure 1, the energy transitions and theoretical energy band structure of the semiconductor material silicon (Si) are depicted. The upper part of the diagram illustrates the energy levels across the detector structure. Region No. 0 (the Au electrode) has an energy level of approximately 5.00 eV, indicating that gold (Au), due to its high work function, forms a potential barrier at the interface with silicon. This barrier makes it somewhat more difficult for electrons to move from the gold contact into the silicon region. Region No. 1 represents n-type silicon, where the bandgap energy is approximately 1.1 eV. However, in this diagram, the vertical axis indicates an energy value of around 4.20 eV. The Fermi level (indicated by the red dotted line) lies between the conduction and valence bands, but given the n-type nature of the silicon, the Fermi level is positioned closer to the conduction band. This confirms that the majority charge carriers in the n-type Si are electrons, and their preferred direction of motion is from left to right ($Au \rightarrow Al$). The energy level of the Al electrode is approximately 4.24 eV, which suggests that at the $Al - nSi$ interface, the potential barrier is relatively small – significantly lower than that at the $Au - Si$ junction. As a result, electron transport toward the Al side is more favorable in this detector. Considering that the central region of the detector is composed of n-type silicon, it can be concluded that electrons are the primary charge carriers in the device. The energy band diagram also indicates the presence of an internal electric field across the structure, which facilitates the rapid separation and collection of charge carriers under the influence of this field.
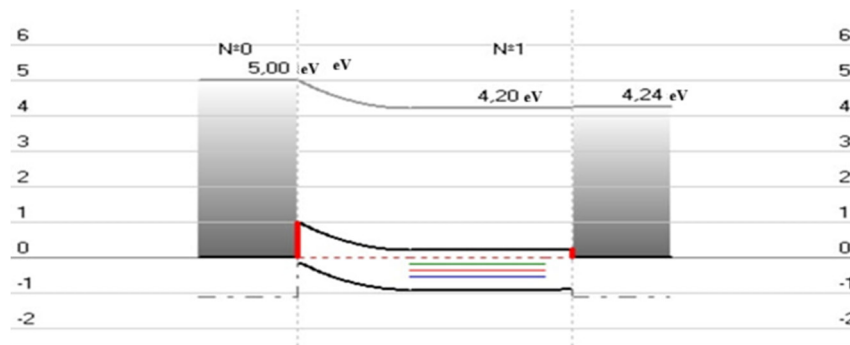
Figure 1. Energy band diagram of the $Au - nSi - Al$ structured detector based on silicon
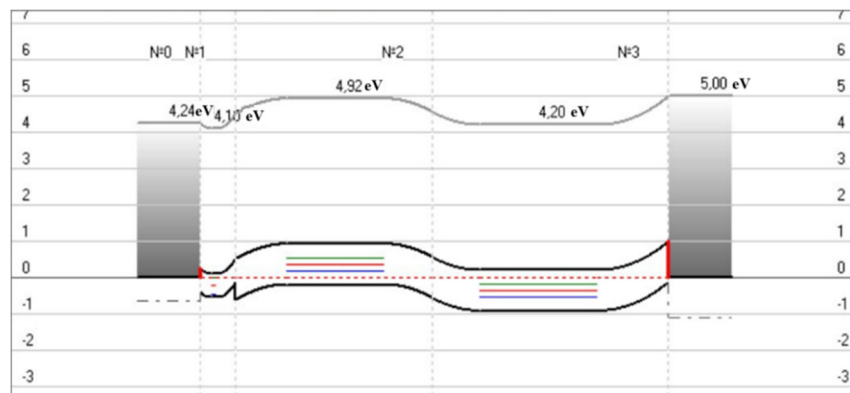
Figure 2. Energy band diagram of the $Al - pGe(p - i - n) - Au$ structured detector based on germanium

As shown in Figure 2, energy barriers, Fermi level positions (red dotted lines), and the movement of charge carriers are illustrated for each layer of the structure. $N0 \rightarrow N1$ (*Al contact to $p - Ge$*)**:** This region represents the interface between the aluminum electrode and the p-type germanium layer. The downward slope of energy barriers indicates a favorable path for electron movement. The Fermi level is located close to the valence band, confirming the p-type character of this region. $N1 \rightarrow N2$ ($p - Ge \rightarrow i - Ge \rightarrow n - Ge$) This is the core of the p–i–n structure. The energy gap of 4.92 eV corresponds to the intrinsic region of germanium. The bent portion between black lines reflects the internal potential gradient. The Fermi level is nearly centered, which is typical for intrinsic semiconductors. In this i-region, charge carriers (electron-hole pairs) are generated when photons or ionizing particles interact. $N2 \rightarrow N3$ ($n - Ge$ to Au) This segment extends from the n-type Ge to the gold (Au) contact. The Fermi level lies higher, which aligns with n-type behavior. A gradual upward slope of the energy levels reflects the internal electric field generated under external bias. Under radiation exposure, the electron–hole pairs created in the i-region are quickly separated and directed towards their respective electrodes, resulting in a measurable signal. The spatial variation of the Fermi level across the layers indicates the formation of an internal electric field. Additionally, adjusting the electrode thickness allows fine-tuning of key detector parameters (Figure 2). Technological Fabrication Overview. The fabrication of $Au - nSi - Al$ and $Al - pGe(p - i - n) - Au$ semiconductor detectors for nuclear radiation detection is a complex process involving mechanical, chemical, and thermal operations, as well as precise structural design. Each step has a specific purpose and requires meticulous control. Refined

semiconductor processing technologies determine the ability of these detectors to preserve radiation sensitivity over extended periods. In this study, silicon wafers with diameters of $\theta = 10 - 30 \, mm$ and thicknesses of $d = 1 - 2 \, mm$ were prepared using $p - type$ monocrystalline silicon ($\rho = 0.01 - 5 \, k\Omega \cdot cm, \tau = 50 - 1000 \, \mu s$). The wafers were cut with a diamond internal arc saw. To remove the mechanically damaged layer, double-sided grinding was performed using M-14 and M-5 micropowders. Each side was ground to a depth of at least 50 μm. After grinding, the wafers were cleaned with non-alkaline soap and deionized water and subjected to ultrasonic treatment. The mechanical damage often exceeds the abrasive grain size, particularly when using diamond powders. Therefore, chemical etching was employed to remove residual defects. Before etching, the wafers were rinsed in distilled water for at least 15 minutes. The chemical solution was prepared using hydrofluoric acid (HF), nitric acid (HNO₃), and acetic acid (CH₃COOH) in a 1:5:1 ratio, and cooled to 5°C. This slow etching process allowed better control. The wafers were rotated in a fluoroplastic bath for 15–20 minutes using a motorized platform to ensure uniform surface processing. The optimal etch rate was 4 μm/min.

RESULTS AND DISCUSSION

The condition of the silicon wafers prepared for experimental research after completing the step-by-step processing stages described above is illustrated in Figure 3 (a–b–c).

a) Appearance of the silicon wafer after cutting

b) Appearance of the silicon wafer after mechanical processing

c) Appearance of the silicon wafer after chemical treatment

a) Appearance of the silicon wafer after cutting

b) Appearance of the silicon wafer after mechanical processing

c) Appearance of the silicon wafer after chemical treatment
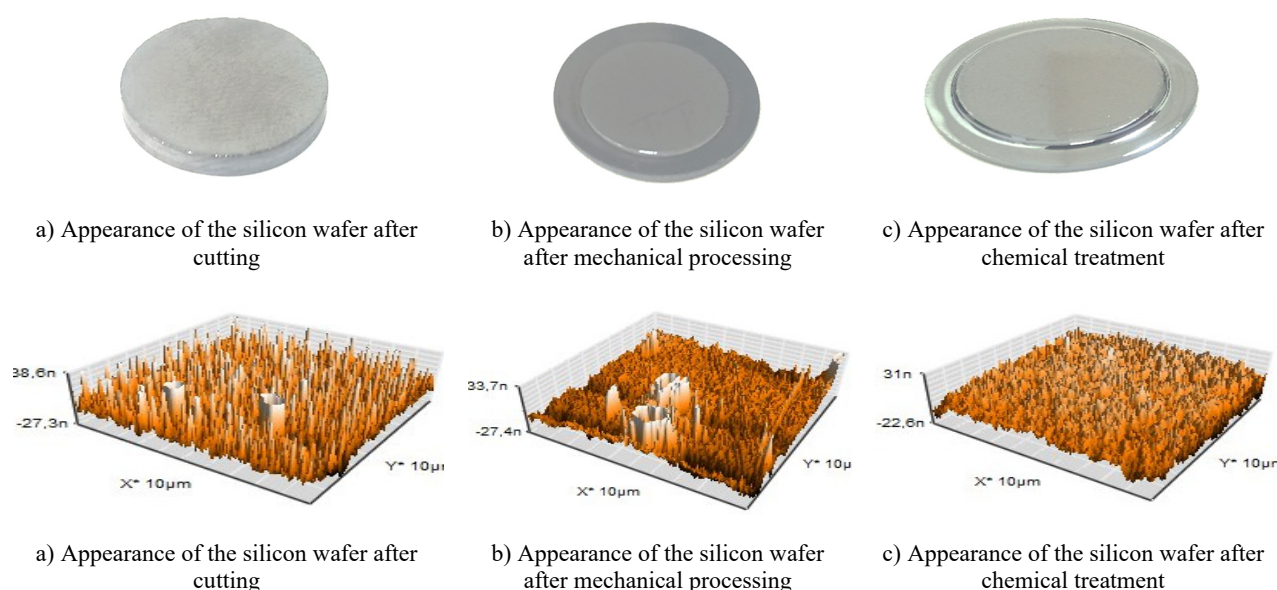
Figure 3 (a–b–c) shows images of the silicon wafers obtained using Atomic Force Microscopy (AFM) after the technological processing steps

As shown in Figure 3(a), surface irregularities of approximately 38 nm are formed on the silicon wafer after the cutting process. In Figure 3 (b), these irregularities are reduced to 33.7 nm after mechanical processing. Finally, Figure 3(c) shows that the asymmetrical layer is further reduced to 31 nm after chemical cleaning. This demonstrates the gradual decrease in surface non-uniformity through successive technological steps. Achieving high energy resolution in semiconductor detectors is one of the more complex challenges in detector development. This primarily depends on the growth technologies of the initial semiconductor materials and their electrical and structural properties. Localized defects and impurity bands in the sensitive volume significantly degrade the detector's radiometric characteristics. A key advantage of lithium-doped silicon and germanium is their ability to create large, nearly intrinsic regions exceeding 1 mm in thickness. This is made possible due to the high mobility of lithium ions in Group IV crystals and their low ionization energies – 0.033 eV in silicon and 0.0043 eV in germanium.

Figure 4. Schematic diagram of the device used for lithium diffusion: 1 – quartz tube, 2 – lithium sample, 3 – needle valve

For example, the diffusion coefficient of lithium in germanium is approximately 10⁷ times higher than that of conventional donor atoms. Lithium ions, due to their small radius, do not occupy lattice sites but instead migrate through interstitial positions. In silicon, lithium ions form an extended intrinsic zone, which significantly enhances sensitivity to X-rays and gamma radiation. This region generates a high-resistance volume inside the crystal, facilitating charge collection and signal generation within the detector. To implement lithium diffusion in small-sized crystals, a GSL-1100X furnace was

used. The furnace consists of a quartz tube for sample placement. Diffusion was performed across the entire surface of the wafers at a vacuum of $\sim 10^{-5}$ mmHg, to a depth of (50–200) μm, for 1 to 3 minutes, at temperatures between 380°C and 450°C (Figure 4). After diffusion, the crystals were slowly cooled to 250°C to prevent defect formation and lithium ejection, which typically occurs during rapid cooling. Diffusion depth was controlled using a step-grinding technique. The depth of lithium diffusion into p-type silicon can be determined using the following formula:

$$x_j = 2\sqrt{Dt}\ erfc^{-1}\left(\frac{N_A}{N_0}\right) \tag{1}$$

Here, D is the diffusion coefficient, which is calculated for p-type silicon with a specific resistivity of approximately $\rho \approx 1000\ \Omega \cdot cm$, as follows:

$$D = 6 \cdot 10^{-4} \exp\left(\frac{-0{,}61\,q}{k_B\,T}\right)\left[cm^2/_s\right] \tag{2}$$

Here, q is the elementary charge, k_B is the Boltzmann constant and T is the temperature in Kelvin.

In p-type material, compensation of acceptor atoms through lithium diffusion is carried out as follows: First, lithium is directed into the p-type material. The temperature is then raised to approximately 430 °C, initiating the diffusion of lithium into the sample. The diffusion process lasts for several minutes, during which lithium penetrates to a depth of approximately 0.01 μm. Subsequently, lithium ions begin to migrate from the n-side back toward the p-side of the p–n junction. In this region, they compensate for the acceptor atoms present in the p-type material. The thickness of the depleted layer formed as a result of this diffusion process can be calculated using the following formula:

$$d = \sqrt{2\mu_{Li}Ut}, \tag{3}$$

Here, d is thickness of the depleted layer, μ_{Li} is the ion mobility in semiconductors at the given diffusion temperature, U is the drift bias voltage and t is the drift time.

The diffusion time is determined as follows:

$$t = \frac{W^2}{2U\mu_{Li}}, \tag{4}$$

Here, W is the thickness (width) of the compensated intrinsic (i) region in the Si(Li) detector.

The relationship between mobility and the diffusion coefficient is as follows:

$$\mu_{Li} = \frac{q}{k_BT} \cdot D\left[sm^2/_{(V\cdot s)}\right] \tag{5}$$

The thermal regime of lithium-ion drift is described in detail to ensure the required compensation at minimal redistribution of the lithium profile within the sensitive volume.

Drift was performed unidirectionally at a temperature of T = (60–100)°C, under a reverse bias voltage of 70–600V, for a duration of four days. The completion of the drift process was monitored by a sharp increase in the reverse current. To determine the i-region, after drift termination, one side of the crystal (with an $n^+ - i - p^+$ structure) was polished using silicon carbide (SiC) micro powder on a glass disc. The thickness of the removed layer was estimated considering partial washout of the diffusion profile. The polished layer typically had a thickness ranging from 50 to 400 μm. The i-region was then selectively removed using an etching solution of HNO₃:HF in a 1:1000 ratio. The i-region was considered entirely removed when its contour matched the diameter of the diffused region and appeared close to a circular shape.

The geometry of Si(Li) p–i–n detectors play an important role in determining their electrical and detection characteristics. Two typical structural configurations are illustrated in Figure 5: the planar geometry (Figure 5a), where the p–i–n layers extend uniformly across the detector surface, and the T-type reference geometry (Figure 5b), which is widely used to reduce surface leakage currents and improve charge collection efficiency. The key design parameters include the detector diameter (D), the thickness of the intrinsic (i) region (d), the thickness of the p-region (h), and the diameter of the n-region (2r).

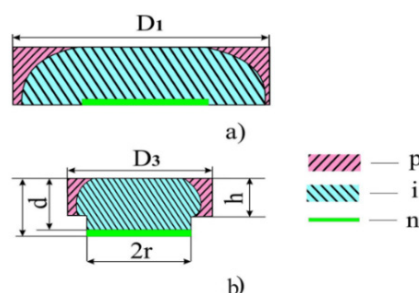
Figure 5. Cross-sectional view of the detector: a – planar, b – T-type reference geometry
D – detector diameter; d – thickness of the intrinsic (i) region; h – thickness of the p region; 2r – diameter of the n region.

It should be emphasized that when performing diffusion doping of silicon, it is essential to consider the thermal and temporal regimes to avoid the formation of thermally induced defects. In the technology of Si(Li) p–i–n detectors, lithium is typically diffused at temperatures ranging from 300°C to 500°C, with a critical threshold at 450°C, beyond which the intensive generation of donor-type thermodefects occurs. In known Si(Li) p–i–n detector fabrication processes, a rapid cooling step is applied after diffusion to preserve the desired lithium profile and prevent redistribution. However, this high cooling rate (on the order of 10^2–10^3 °C/s) can induce stable thermodefects, which may negatively affect the final characteristics of the semiconductor detector. The formation of electrical contacts on the prepared silicon wafers was carried out using a VPS-4 universal vacuum post system. The sample holders were specially designed using molybdenum and tungsten, cleaned in alcohol, and then preheated in a vacuum for 10–15 minutes. The molybdenum filament had a length of 40 mm, and the distance between the evaporator and the silicon wafer was set at 80 mm. The silicon wafers were placed in the evaporation chamber, and contacts were deposited under a vacuum of 5×10^{-5} mmHg. As a contact material, gold layers with a thickness of approximately 200 Å were deposited on the silicon wafers.

The visual appearance of the silicon wafers before and after contact formation is shown in Figure 6. In particular, Figure 6a illustrates the surface morphology of the Si(Li) wafer after the lithium drift process, whereas Figure 6b demonstrates the post-diffusion appearance of the Au-coated silicon wafer. This comparison highlights the transition from the initial lithium-compensated structure to the final detector surface with gold contact deposition.

a   **b**

Figure 6. Appearance of the detector after contact formation
a) Post-drift appearance of Si(Li), b) Post-diffusion appearance of Si(Au)

The current–voltage (I–V) characteristics of Si(Li) p–i–n structured detectors were investigated in accordance with the GOST 26222-86 standard methodology. To study the characteristics mentioned above, a specialized device was developed and assembled for measuring reverse current, which allows for the simultaneous acquisition of dark current values across different bias conditions. The applied reverse bias voltage $U_{rev.}$ was set in the range of 0.1 to 800 V, and the current measurement ranges $I_{rev.}$ were configured for 1 μA, 10 μA, and 100 μA, respectively.
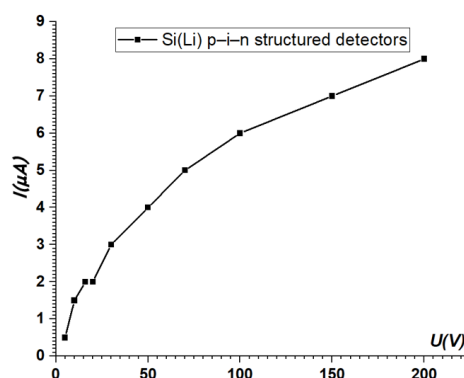
Figure 7. Current–voltage (I–V) characteristics of semiconductor Si(Li) p–i–n structured detectors

Figure 7 illustrates the dependence of the output current. I_{output} on the output voltage U_{output} for a detector with a T-shaped cross-section, showing both the minimum and maximum current values. As shown in the graph, the output current across the entire detector volume ranges from 0.5 to 9 μA at an applied voltage of 200 V.

This indicates that a uniform compensation has been achieved within the silicon volume (30 mm in diameter and 2 mm in thickness) by lithium ions. As the voltage increases, the current also rises; however, this increase is non-linear and gradually approaches a saturation-like regime. In the initial voltage region (0–30 V), the current increases sharply with voltage, indicating the onset of the drift process. In this zone, the detector exhibits high sensitivity. In the intermediate region (30–100 V), the growth of the current slows down. This suggests that the drift region is expanding, although a significant portion of the lithium ions in the silicon has already been positioned. At high voltages (100–200 V and beyond), the current increase becomes nearly negligible and deviates significantly from linearity, indicating saturation. This means the drift layer has reached its maximum extent, and the detector operates in a stable regime at these voltages. It is well known that capacitance-voltage (C–V) characteristics can be used to determine both the density of surface states and their distribution function across the energy bandgap at the semiconductor–dielectric interface of monocrystalline silicon. Several methods have been developed to analyze these parameters based on C–V measurements.

It is well established that capacitance–voltage (C–V) characteristics provide valuable insights into the density of surface states and their energy distribution at the semiconductor–dielectric interface. This type of C–V analysis is particularly significant for evaluating the physical - parametric properties of $Si(Li)$ −based detectors. Figure 8 presents the C–V characteristic of an $Al - nGe(p - i - n) - Au$ detector, which is based on a $p - i - n$ (positive–intrinsic–negative) type semiconductor structure. In such detectors, due to the narrow width of the intrinsic (i) layer, the depletion region extends significantly, resulting in a low overall capacitance. As the applied voltage increases, the capacitance decreases slowly. The C–V curve generally shows a downward trend with increasing bias voltage, ultimately reaching a plateau region where the capacitance becomes nearly constant. From the graph, it can be observed that in the initial voltage range (~0–20 V), the capacitance decreases rapidly, indicating the expansion of the depletion region. In the 30–35 V range, a plateau forms, indicating that the structure has reached complete depletion, and further increase in voltage no longer significantly affects the capacitance. The capacitance starts at approximately 300 pF and stabilizes as it approaches the plateau. Under this condition of complete depletion, the detector yields a clean and well-defined signal, indicating its optimal operating state. Any additional voltage serves only to stabilize the operation and does not affect the capacitance further. On the other hand, the $Au - nSi - Al$ detector features a structure based on a classical n-type semiconductor (Si) and behaves similarly to a Schottky barrier or p–n junction detector. In this case, applying a voltage causes the depletion region to deepen, but since there is no intrinsic layer (i-region), the capacitance remains relatively high. Consequently, the C–V characteristic of such detectors exhibits a steeper and more abrupt decrease. Due to the shorter depletion width, the capacitance begins at a higher level (approximately 300–400 pF) and decreases rapidly as the voltage increases. The $C = f(V)$ graph for this detector type shows a rapid drop in capacitance with little to no observable plateau.
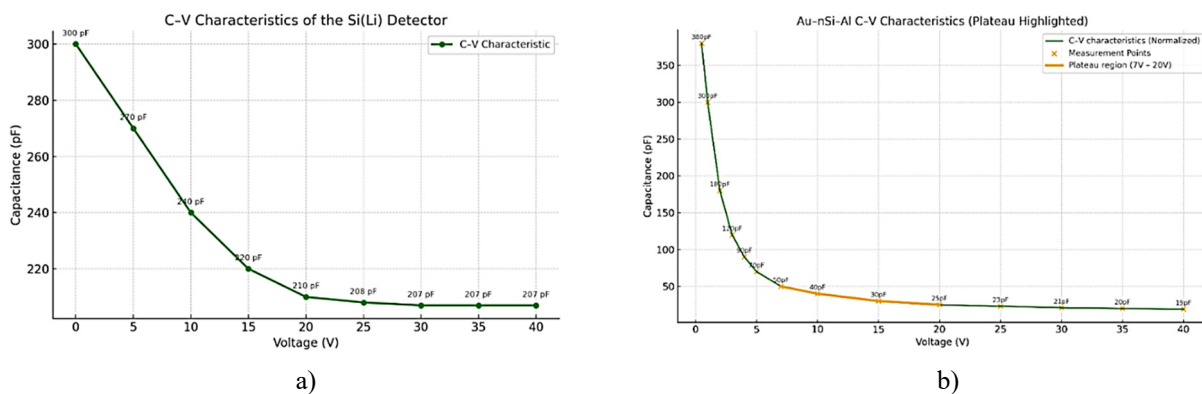

a)   b)

Figure 8. Capacitance-voltage $(C - V)$ characteristics
a*) $Al - nGe(p - i - n) - Au$. b*) $Au - nSi - Al$ detectors

The capacitance-voltage (C–V) characteristics were studied using the E7-12 instrument at a frequency of 1 MHz, and a modernized L2-7-1M instrument was employed for measurements in the 0.465 MHz to 10 MHz frequency range. These instruments ensured that the amplitude of the applied AC signal did not exceed 5–7 mV. All measurements were carried out at a temperature of T = 300 K, using both parallel and series equivalent circuit configurations. The measurement error did not exceed 0.1pF. The voltage-capacitance characteristics investigated for detectors of different types demonstrate that a high compensation quality was achieved during fabrication, owing to the drift process of lithium ions within the detector material.

The obtained results are considered to be optimal for semiconductor detectors. Consequently, through investigations and technological processes, the fabrication technology of $Si(Li)$ −based semiconductor detectors with a $p - i - n$ structure has been developed and optimized.

CONCLUSIONS

The choice of detector material and structure directly affects their electrophysical and radiometric properties. In particular, detectors with a $p - i - n$ structure stands out from other types due to their high resolution and low current noise. High sensitivity and stability were achieved in low-defect p-type silicon (pSi) samples due to deep lithium diffusion. The high resistance and extremely low leakage current of the detector demonstrated its excellent energy resolution capability. Measurements of detectors based on the $Au - nSi - Al$ structure showed that this type of detector has greater radiation tolerance, making it suitable for continuous operation. The capacitance–voltage (C–V) and current-voltage (I–V) characteristics were measured for both types of detectors, revealing that the depletion region is fully formed within the voltage range of 30 – 35 V. The plateau region observed in the C–V characteristics indicates full activation of the detector, while the low current observed under reverse bias in the I–V characteristics confirms the formation of a high-quality p–n junction. These detectors have high potential for use in various applications, including cosmic radiation detection, nuclear medicine, environmental monitoring, and security systems.

ORCID

⊙**Ilhom I. Maripov,** https://orcid.org/0009-0005-1683-2260

REFERENCES

[1] E. Fortunato, M. Vieira, L. Ferreira, *et al*. "Large Area Position Sensitive Detector Based on Amorphous Silicon Technology," MRS Online Proceedings Library, **297**, 981–986 (1993). https://doi.org/10.1557/PROC-297-981

[2] D. Protić, T. Krings, and R**.** Schleichert, "Development of double-sided microstructured Si(Li) detectors," IEEE Transactions on Nuclear Science, **49**(4), 1829–1832 (2002). https://doi.org/10.1109/TNS.2002.801541

[3] J. Wang, P. Mulligan, L. Brillson, and L.R. Cao, "Review of using gallium nitride for ionizing radiation detection," Applied Physics Reviews, **2**(3) 031102 (2015). https://doi.org/10.1063/1.4929913

[4] Z. Xie, K. Jiang, S. Zhang, Z. Wang, X. Shan, B. Wang, and J. Ben, *et al*. "Ultraviolet Optoelectronic Synapse Based on AlScN/p-i-n GaN Heterojunction for Advanced Artificial Vision Systems," Advanced Materials, **37**(19), e2419316 (2025). https://doi.org/10.1002/adma.202419316

[5] A. Keffousa, M. Siad, A. Cheriet, N. Benrekaa, Y. Belkacem, H. Menari, W. Chergui, and A**.** Dahmani, "Comparison of electrical and optical parameters of Au/n-Si and Ag/n-Si Schottky barrier photodiodes,". Applied Surface Science, **236**(1–4), 42-49 (2004). https://doi.org/10.1016/j.apsusc.2004.03.233

[6] M. Kozai, H. Fuke, M. Yamada, K. Perez, T. Erjavec, C. J. Hailey, N. Madden, *et al*. "Developing a mass-production model of large-area Si(Li) detectors with high operating temperatures," Nuclear Instruments and Methods in Physics Research Section A: Accelerators, Spectrometers, Detectors and Associated Equipment, **947**, 162695 (2019). https://doi.org/10.1016/j.nima.2019.162695

[7] R.A. Muminov, A.K. Saymbetov, N.M. Japashov, Y. Toshmurodov, S.A. Radzhapov, N.B. Kuttybay, and M.K**.** Nurgaliyev, "Physical Features of Double Sided Diffusion of Lithium into Silicon for Large Size Detectors," Journal of Nano- and Electronic Physics, **11**(2), 02031-1–4 (2019). https://doi.org/10.21272/jnep.11(2).02031

[8] J. Grant, C. Buttar, M. Brozel, A. Keffous, A. Cheriet, K. Bourenane, A. Bourenane, *et al*. "Lithium-drifted, silicon radiation detectors for harsh radiation environments," Journal of Materials Science: Materials in Electronics, **19**(S1), S14–S18 (2008). https://doi.org/10.1007/s10854-008-9707-0

[9] D. Alexiev, M.I. Reinhard, L. Mo, A. R. Rosenfeld, and M. L. Smith, "Review of Ge detectors for gamma spectroscopy," Australasian Physics & Engineering Sciences in Medicine, **25**(3), 102–109 (2002). https://doi.org/10.1007/BF03178770

[10] A. Keffous, M. Siad, A. Cheriet, Y. Belkacem, H. Menari, W. Chergui, and A. Dahmani, "Effect of the lithium diffusion into n-type silicon on the spectral response of the Schottky photodiodes," Optics Communications*,* **222**(4–6), 299–304 (2003). https://doi.org/10.1016/S0030-4018(03)01604-3

[11] M. Xiao, A. Stoessl, B. Roach, C. Gerrity, I. Bouche, G. Bridges, P. von Doetinchem, *et al*. "Large-Scale Detector Testing for the GAPS Si(Li) Tracker," IEEE Transactions on Nuclear Science, **70**(8), 2125-2133 (2023). https://doi.org/10.1109/tns.2023.3291235

[12] D.B. Istamov, O.A. Abdulkhayev, and Sh.M. Kuliyev, "Limiting characteristics of silicon diode temperature sensors for determining the maximum temperature with specified measurement accuracy," UNEC J. Eng. Appl. Sci. 5(1), 63-69 (2025). https://doi.org/10.61640/ujeas.2025.0507

[13] D.B. Istamov, O.A. Abdulkhayev, Sh.M. Kuliyev, N. Abdullayev, A.Sh. Ashirov, and D.M. Yodgorova, "Temperature response curve of silicon diode temperature sensors," East Eur. J. Phys. (2), 287-291 (2025), https://doi.org/10.26565/2312-4334-2025-2-35

[14] R.R. Bebitov, O.A. Abdulkhaev, D.M. Yodgorova, D.B. Istamov, G.M. Hamdamov, Sh.M. Kuliyev, A.A. Khakimov and A.Z. Rakhmatov, "Dependence of the accuracy of the silicon diode temperature sensors for cryogenic thermometry on the spread of their parameters," Low Temperature Physics, **49**(2), 277–282 (2023). https://doi:10.1063/10.0016843

[15] R.R. Bebitov, O.A. Abdulkhaev, D.M. Yodgorova, D.B. Istamov, Sh.M. Kuliyev, A.A. Khakimov, A.B. Bobonazarov, *et al*. "Distribution of impurities in base-depleted region of diode temperature sensor," Low Temperature Physics, **50**(5), 418–424 (2024). https://doi.org/10.1063/10.0025635.

[16] I.M. Isakovich, O. S. Komilovich, and M. F. Gallievna, "Electrophysical Properties of Al-pGe(p-i-n)-Au and Au-nSi-Al Structural Detectors Prepared on the Basis of Si and Ge," Physical and mathematical sciences, (2), 23-29 (2024). https://doi.org/10.24412/2709-1201-2025-28-23-29

[17] J. Grant, C. Buttar, M. Brozel, A. Keffous, A. Cheriet, K. Bourenane, A. Bourenane, *et al*. "Lithium-drifted, silicon radiation detectors for harsh radiation environments," J. Mater. Sci: Mater. Electron. **19**, S14–S18 (2008). https://doi.org/10.1007/s10854-008-9707

[18] W.R. Leo, *Techniques for Nuclear and Particle Physics Experiments*, (Springer-Verlag Berlin Heidelberg GmbH, 1994). https://doi.org/10.1007/978-3-642-57920-2

ЕЛЕКТРОФІЗИЧНА ХАРАКТЕРИЗАЦІЯ ФОТОДЕТЕКТОРІВ НА ОСНОВІ НАПІВПРОВІДНИКОВИХ СТРУКТУР Si(Li) ТА Si(Au)

Ілхом І. Маріпов¹, Салі А. Раджапов², Сардор Ф. Хасанов¹, Дамір Б. Істамов², Юсуф Т. Юлдашев¹, Діора Ахназарова³, Шамшіддін А. Ашіров³

¹Ташкентський державний аграрний університет, Ташкентська область, 111160, Узбекистан
²Фізико-технічний інститут Академії наук Узбекистану, Ташкент 100084, Узбекистан
³Гулістанський державний університет, 4-й мікрорайон, 120100, Гулістан, Узбекистан

У цій статті досліджено технологічні та фізичні принципи створення ядерних детекторів випромінювання на основі кремній-літієвих (Si(Li)) структур із товщиною понад 1,5 мм та площею поверхні не менше 50 см². Аналізується формування великогабаритних p–i–n структур шляхом дрейфу та дифузії іонів літію. Для оцінки електрофізичних параметрів детекторів були проведені вимірювання вольт-амперних (I–V) та ємнісно-напругових (C–V) характеристик. Результати I–V при зворотному зміщенні в діапазоні U = 0–200 В показали надзвичайно низькі струми витоку (I ≤ 0,5 нА), що свідчить про формування високоякісних p–i–n переходів. При напрузі понад 100 В струм залишався практично сталим, утворюючи плато. Отримані результати пропонують ефективні технологічні рішення для розробки високочутливих, стабільних детекторів випромінювання з низьким рівнем шуму.

Ключові слова: *детектор; гетероструктура; кремній; германій; напівпровідникова p–i–n структура; p–n перехід; електрофізичні властивості*

BANDGAP-ENGINEERED pSi/n-Cd$_x$S$_{1-x}$ HETEROJUNCTIONS: EFFECT OF COMPOSITION ON OPTOELECTRONIC BEHAVIOR

Ibrokhim B. Sapaev[1,2,4,5]*, Jamoliddin I. Razzokov[6,7], Jo'shqin Sh. Abdullayev[1],
Dildora A. Qalandarova[3], Madinabonu Sh. Ibragimova[3]
[1]National Research University TIIAME, Department «Physics and Chemistry»,
Kori Niyoziy 39, Tashkent 100000, Uzbekistan
[2]Tashkent University for Applied Sciences, 28 Universitetskaya Street, Tashkent 100095, Uzbekistan
[3]Urgench State University, Hamid Olimjon Street, 14, Urgench, 220100 Uzbekistan
[4]School of Engineering, Central Asian University, Tashkent 111221, Uzbekistan
[5]Azerbaijan State Oil and Industry University (ASOIU), Faculty of Chemical Technology,
20 Azadlig Avenue, Baku AZ1010, Azerbaijan
[6]Institute of Fundamental and Applied Research, National Research University TIIAME,
Kori Niyoziy 39, Tashkent 100000, Uzbekistan
[7]Department of Biotechnology, Tashkent State Technical University, Universitet 2, 100095, Tashkent, Uzbekistan
*Corresponding Author e-mail: j.sh.abdullayev6@gmail.com
Received June 28, 2025; revised October 11, 2025; in final form October 20, 2025; accepted October 21, 2025

This study provides a comprehensive analysis of the electrophysical properties of the pSi/n-Cd$_x$S$_{1-x}$ heterojunction, where the cadmium composition x varies continuously from 0 to 1. The investigation integrates theoretical modeling, numerical simulations, and experimental validation employing typical doping concentrations of p = 2×10^{17} cm^{-3} for p-type porous silicon and n = 1×10^{18} cm^{-3} for n-type Cd$_x$S$_{1-x}$. Particular attention is devoted to the temperature-dependent evolution of key material parameters, including the bandgap energy Eg(T), intrinsic carrier concentration n$_i$(T), and the Debye temperature Θ(x). As the cadmium fraction increases, the bandgap narrowing in Cd$_x$S$_{1-x}$ becomes evident, while porous silicon maintains a relatively wide and thermally stable Eg(T), resulting in a substantial band offset (ΔEg) that enhances charge carrier separation across the interface. Furthermore, the reduction of Θ(x) with increasing cadmium concentration modulates phonon scattering and recombination dynamics, thereby influencing charge transport characteristics. The analysis of current transport mechanisms indicates that the junction behavior is predominantly controlled by temperature- and composition-dependent band alignment and carrier recombination processes. The obtained results validate the proposed physical model and demonstrate the promising potential of pSi/n-Cd$_x$S$_{1-x}$ heterostructures for high-temperature and acoustically tunable optoelectronic devices.
Keywords: *Optoelectronic properties; Electrostatic analysis; Band gap engineering; pSi/n-Cd$_x$S$_{1-x}$; Debye temperature; Built-in potential modulation; Calibration*
PACS: 73.40. Lq, 73.61.Cw, 73.61.Ey, 72.20.Jv

INTRODUCTION

The rapid advancement of semiconductor technology increasingly requires precise electrostatic control and a thorough understanding of complex junction architectures [1–3]. Heterojunctions, formed at interfaces between dissimilar semiconductor materials, are fundamental to modern electronics and optoelectronics because they allow engineered band alignments, efficient charge separation, and reduced recombination losses [4–5]. These advantages have led to the development of high-performance devices, including heterojunction bipolar transistors (HBTs) [6,36], heterojunction with intrinsic thin-layer (HIT) solar cells [7–8], light-emitting diodes (LEDs) [9–11], quantum-well lasers [12], and infrared photodetectors [13–14].

Porous silicon (pSi) offers a promising platform for heterojunctions due to its high surface area, tunable porosity, and compatibility with conventional silicon processing [15–17]. When combined with cadmium sulfide (CdS) or its compositionally tunable alloy Cd$_x$S$_{1-x}$, pSi-based heterostructures demonstrate enhanced optical absorption, spectral selectivity, and controllable band alignment [18–21]. Despite these advantages, existing studies provide limited understanding of how temperature variations, ultrasonic excitation, and dopant ionization jointly influence the electrophysical properties of pSi/Cd$_x$S$_{1-x}$ heterojunctions [22–30]. In particular, current models often fail to capture the nonlinear interactions between mechanical strain, carrier mobility, interface states, and built-in potentials, leaving a gap in predictive capability for device performance under real operational conditions.

To address these shortcomings, this study investigates the electrophysical behavior of pSi/n-Cd$_x$S$_{1-x}$ heterojunctions across the full compositional range. By combining analytical modeling, numerical simulations, and experimental validation at typical doping levels (p = 2×10^{17} cm^{-3}, n = 1×10^{18} cm^{-3}), we systematically explore the effects of temperature and ultrasonic perturbation on key parameters such as bandgap Eg(T), intrinsic carrier concentration n$_i$(T), Debye temperature Θ(x), and current transport mechanisms. Our results reveal that increasing Cd content reduces Θ(x) and

narrows the Cd$_x$S$_{1-x}$ bandgap, producing a stable band offset (ΔEg) that enhances charge separation. Furthermore, the thermal behavior of n$_i$(T) confirms junction robustness, while analysis of space-charge distribution, built-in potential, and C–V characteristics under ultrasonic modulation provides new insights into device physics. This work fills a critical gap in the literature and highlights the potential for acoustically tunable, high-temperature optoelectronic devices based on pSi/n-Cd$_x$S$_{1-x}$ heterojunctions.

METHODS AND MATERIAL

The investigated heterojunction structure consists of a p-type porous silicon (pSi) substrate and a thin film of n-type cadmium sulfide alloy (Cd$_x$S$_{1-x}$), where the cadmium composition x varies from 0 to 1. The pSi substrate has a thickness of approximately 400 μm, while the n-Cd$_x$S$_{1-x}$ layer is about 10 μm thick and exhibits a compositionally graded profile, ranging from Cd-rich ($x \approx 1$) near the interface to S-rich ($x \approx 0$) at the surface. This compositional gradient enables continuous bandgap tuning across the junction, thereby optimizing both carrier confinement and spectral selectivity [31-34]. The Cd$_x$S$_{1-x}$ thin films are assumed to be deposited using either chemical bath deposition (CBD) or close-spaced sublimation (CSS) methods—both of which are well-established for fabricating high-quality II–VI compound semiconductors [35–36]. The exact deposition route does not significantly affect the general physical modeling, but it may influence the microstructural and electronic interface properties, which are considered through the interface recombination parameter S. The dielectric constant of the Cd$_x$S$_{1-x}$ alloy, $\varepsilon(x)$, was estimated using an empirical composition-dependent relation that accounts for nonlinear variations due to alloy disorder:

$$\varepsilon(x) \approx x \cdot \varepsilon_{CdS} + (1-x) \cdot \varepsilon_S - \delta \cdot x(1-x) \tag{1}$$

In equation (1), ε_{CdS} represents the contribution of pure CdS to the dielectric constant when the mole fraction of cadmium is x, while ε_S corresponds to the sulfur-rich phase, when the mole fraction is $1-x$. The variable $x \in [0,1]$ denotes the molar fraction of CdS in the Cd$_x$S$_{1-x}$ alloy. The parameter δ is an empirical bowing constant that accounts for the non-linear deviation from Vegard-type linear interpolation between the dielectric constants of the two binary compounds. Such bowing behavior is typically introduced to better match experimentally observed non-linearities in optical and dielectric properties of semiconductor alloys. However, in this study, due to the absence of reliable experimental data for intermediate compositions and to maintain analytical tractability, the bowing term δ is neglected. Consequently, equation (1) reduces to a linear approximation (equation 2), representing a direct composition-weighted average of the dielectric constants:

$$\varepsilon(x) \approx x \cdot \varepsilon_{CdS} + (1-x) \cdot \varepsilon_S \tag{2}$$

This formula provides an estimate of the Debye temperature, $\Theta(x)$, of the Cd$_x$S$_{1-x}$ alloy as a function of the composition parameter x. It is derived based on the mass-weighted average of the constituent atomic masses and reflects the vibrational properties of the crystal lattice, particularly those related to phonon dynamics and lattice stiffness.

$$\Theta(x) = \Theta_{D0} \cdot \sqrt{\frac{M_{Cd} + M_S}{x \cdot M_{Cd} + (1-x) \cdot M_S}} \tag{3}$$

In the expression for $\Theta(x)$, M_{Cd} and M_S denote the atomic masses of cadmium and sulfur, respectively; $\Theta(x)$ represents the Debye temperature as a function of composition x; and Θ_{D0} is the reference Debye temperature. The Debye temperature $\Theta(x)$ is a fundamental material parameter that characterizes the maximum phonon energy (or frequency) in a crystal lattice. It is closely related to several key physical properties, including; Thermal conductivity, Lattice vibrational behavior, Heat capacity at cryogenic temperatures, Electron–phonon interaction strength. This model illustrates that as the composition x varies, the average atomic mass of the alloy changes, which in turn modifies the vibrational spectrum of the lattice and thus alters the Debye temperature $\Theta(x)$. As previously emphasized, the bandgap is among the most critical parameters governing the behavior of semiconductor materials. Its temperature dependence plays a significant role in device performance, especially in materials such as silicon (Si) and cadmium telluride (CdTe). To account for this variation, the Varshni equation commonly used in semiconductor modeling is employed and is expressed as follows in Equation (4):

$$E_g(T) = E_g(0) - \frac{\alpha \cdot T^2}{T + \Theta(x)}. \tag{4}$$

In equation (3), $E_g(T)$ denotes the bandgap energy at temperature T, while $E_g(0)$ represents the bandgap at absolute zero (0 K). The parameter α is a material-specific coefficient that quantifies the temperature dependence of the bandgap and is typically determined experimentally for each semiconductor material [29]. The temperature dependence of the bandgap for both pSi and n-Cd$_x$S$_{1-x}$ layers was modeled using the Varshni relation, allowing accurate prediction of bandgap narrowing at elevated temperatures. To validate the theoretical model, the calculated temperature-dependent bandgap values were compared with numerical simulations performed for doping concentrations of $p = 2 \times 10^{17}$ cm^{-3} and $n = 1 \times 10^{18}$ cm^{-3}. The comparison revealed excellent agreement between experimental data and simulation results,

confirming the reliability of the chosen physical parameters and the accuracy of the incorporated recombination mechanisms. In the energy band diagram, the conduction band (E_C), valence band (E_V), and Fermi level (E_F) are shown with characteristic band bending near the interface due to space-charge formation and built-in potential development. Distinct band discontinuities (ΔE_C, ΔE_V) arise from differences in electron affinity and bandgap between Si and Cd_xS_{1-x}, typical of type-II heterojunctions. The composition- and temperature-dependent bandgap, $E_g(T, x)$, governs carrier confinement, recombination dynamics, and optical absorption. This pSi/n-Cd_xS_{1-x} heterojunction exhibits strong potential for: Optoelectronic applications, including high-sensitivity photodiodes and broadband solar cells; Bandgap engineering, achieved by controlling the Cd-to-S ratio (x) to tune electronic and optical response; Thermal behavior analysis, as its $E_g(T, x)$ dependence makes it a promising candidate for temperature-sensitive or high-temperature optoelectronic devices.

RESULTS AND DISCUSSION

The compositional tuning of the Cd_xS_{1-x} layer provides precise control over the bandgap energy (Eg), which is critical for optimizing heterojunction performance. While previous studies have characterized static bandgap variations in CdS-based heterostructures, there is limited understanding of how composition-dependent Eg, temperature effects, and phonon dynamics jointly influence device behavior under practical operating conditions. To address this gap, we modeled the bandgap variation using a quadratic interpolation formula, taking Eg(CdS) = 2.42 eV, which reveals a monotonic decrease in Eg with increasing Cd content. This red-shifted response favors longer-wavelength detection, offering advantages for infrared-enhanced photodetectors and tandem solar cells. Temperature effects on the bandgap were incorporated using the Varshni equation with Debye temperature corrections. Cd-rich compositions ($x > 0.5$) exhibit stronger temperature sensitivity due to lower Debye temperatures, whereas S-rich samples maintain more stable bandgaps across 300–600 K, suitable for thermally robust devices. Modeling the Debye temperature as a function of composition shows a nonlinear decrease in $\Theta(x)$ with increasing Cd content, indicating softer phonon modes that enhance phonon–electron interactions. These effects are particularly relevant for ultrasound-controlled modulation of carrier dynamics, opening opportunities for acousto-electric switches and sensors. The tunability of the pSi/n-Cd_xS_{1-x} system has clear implications for device applications, including: photodetectors with wavelength-specific sensitivity, solar cells with thermally stable efficiency, acousto-optoelectronic devices that exploit ultrasound to modulate current or light output.

The combination of stable heterojunction alignment, low intrinsic carrier concentration $n_i(T)$, and Debye-tunable recombination rates makes this material system highly promising for advanced optoelectronic devices. Figure 1 illustrates the model structure of the pSi/n-Cd_xS_{1-x} heterojunction, showing both its geometrical configuration and energy band alignment. The heterojunction consists of a 400 µm-thick p-type porous silicon substrate and a 10 µm-thick n-type Cd_xS_{1-x} layer with a compositional gradient from Cd-rich ($x \approx 1$) to S-rich ($x \approx 0$), enabling continuous bandgap tuning, spectral selectivity, and optimized carrier transport.
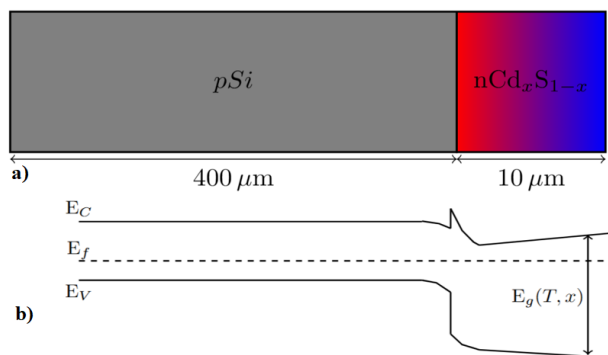

Figure 1. Model sample a) 2D view of the pSi/nCd_xS_{1-x} heterojunction, b) Band gap diagram of the pSi/nCd_xS_{1-x} heterojunction

Figure 2 shows the variation of the Debye temperature, $\Theta(x)$, as a function of cadmium composition x in the ternary alloy Cd_xS_{1-x}, based on a simplified mass-weighted model. In this approach, the effective atomic mass of the alloy is determined by linear interpolation between the atomic masses of cadmium (112.41 u) and sulfur (32.07 u). Assuming that the Debye temperature is inversely proportional to the square root of the effective mass, $\Theta(x)$ is calculated accordingly.

The results reveal a nonlinear decrease in $\Theta(x)$ with increasing cadmium content. At the sulfur-rich limit (x = 0), $\Theta(x)$ reaches a maximum of approximately 318 K, reflecting a stiffer lattice and higher phonon frequencies. As cadmium content increases, $\Theta(x)$ steadily declines, reaching a minimum of about 170 K at x = 1 (pure CdS). This nonlinear trend arises from the square-root dependence of $\Theta(x)$ on the effective mass, producing a gradual curvature rather than a linear decrease.

At intermediate composition (x = 0.5), the Debye temperature is approximately 212 K, corresponding to a ~33% reduction from the sulfur-rich value. This compositional dependence of $\Theta(x)$ has important implications for the physical behavior of pSi/n-Cd_xS_{1-x} heterojunctions, as softer phonon modes in Cd-rich alloys enhance phonon–electron interactions, influencing carrier dynamics, recombination rates, and the potential for acousto-electric modulation in device applications.
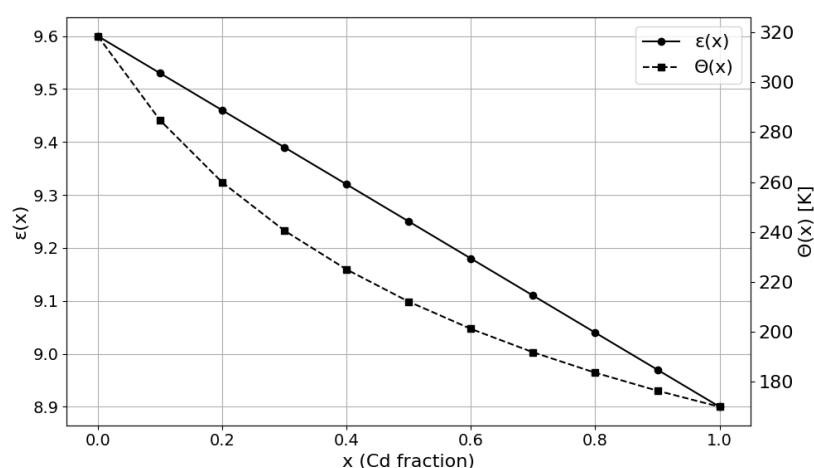
Figure 2. ε(x) and Θ(x) for Cd$_x$S$_{1-x}$.

The Debye temperature plays a critical role in phonon-mediated mechanisms, including: Lattice thermal conductivity, where lower Θ values indicate softer lattices and increased phonon scattering; Electron–phonon coupling, which affects carrier mobility and recombination rates; Acousto-electric effects, particularly under ultrasonic excitation.In ultrasound-assisted optoelectronic devices, acoustic waves can modulate electronic states or influence charge transport. Therefore, understanding the compositional dependence of Θ(x) is essential for predicting device behavior. The observed variation in Debye temperature indicates that tuning the Cd/S ratio in Cd$_x$S$_{1-x}$ allows deliberate engineering of the phonon spectrum, enabling control over thermal dissipation, recombination dynamics, and defect sensitivity under acoustic perturbation. Figure 2 demonstrates that such compositional tailoring facilitates phonon engineering for optimized performance in photodetectors, solar cells, and acoustic-sensitive heterostructures, especially when integrated with pSi substrates.
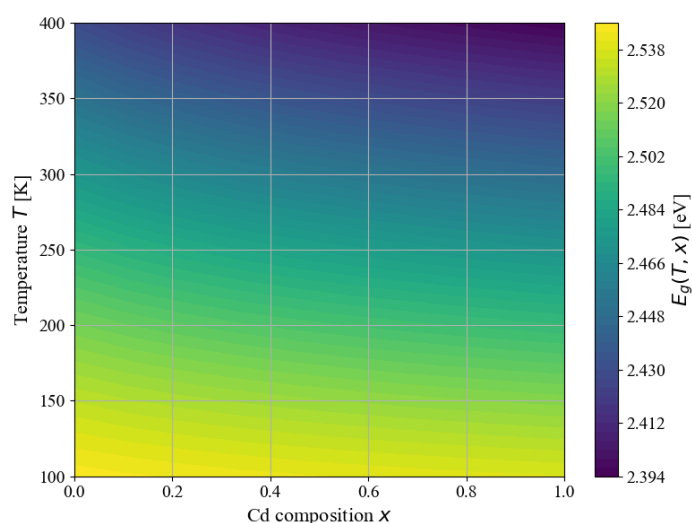

Figure 3. Bandgap variation $E_g(T, x)$ in Cd$_x$S$_{1-x}$ as a function of temperature and composition

Figure 3 presents a contour map of the bandgap energy, Eg(T, x), as a function of cadmium composition x ∈ [0.0, 1.0] and temperature T ∈ [100 K, 400 K] for the ternary alloy Cd$_x$S$_{1-x}$. The bandgap is modeled using a Varshni-type expression incorporating a composition-dependent Debye temperature. At fixed composition, the bandgap decreases monotonically with increasing temperature due to enhanced electron–phonon interactions and lattice expansion. For example, for x = 0 (pure sulfur), Eg decreases from ~2.536 eV at 100 K to ~2.323 eV at 400 K (ΔEg ≈ 0.213 eV). For x = 1 (pure cadmium), Eg decreases from ~2.518 eV to ~2.278 eV (ΔEg ≈ 0.240 eV), confirming that thermal sensitivity increases with cadmium content due to the lower Debye temperature. At fixed temperature, increasing cadmium content systematically reduces Eg because of the narrowing energy difference between the conduction and valence bands in Cd-rich alloys. For instance, at T = 300 K, Eg decreases from ~2.370 eV for x = 0 to ~2.316 eV for x = 1 (ΔEg ≈ 0.054 eV). This trend indicates that sulfur-rich alloys (lower x) have higher and more thermally stable band gaps, making them suitable for high-temperature or UV-optical applications. The calculated Debye temperature varies nonlinearly with composition due to mass weighting: Θ(x = 0) ≈ 150 K, Θ(x = 0.5) ≈ 211 K, Θ(x = 1) ≈ 276 K. Higher Θ(x) values in Cd-rich alloys suppress the Varshni temperature correction, resulting in flatter Eg(T, x) curves at lower x, as shown in the contour plot. Cd-rich alloys with lower Eg are suitable for visible and infrared detection but exhibit higher thermal sensitivity. S-rich alloys (x < 0.4)

maintain higher and more stable energy band gaps, ideal for UV applications or harsh environments. Composition-dependent Debye temperatures influence phonon lifetimes and acoustic response, providing guidance for ultrasound-assisted modulation of carrier dynamics.
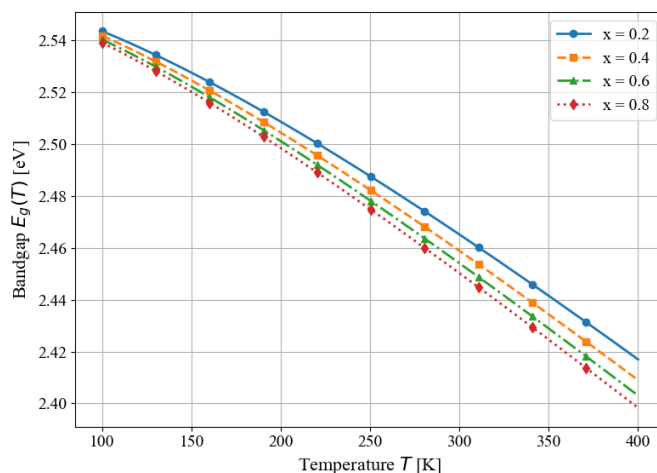

Figure 4. Temperature dependence of the bandgap Eg(T) for different Cd fractions in Cd_xS_{1-x}

Figure 4 illustrates the temperature-dependent bandgap, Eg(T), of the ternary compound Cd_xS_{1-x} for cadmium compositions x = 0.2, 0.4, 0.6, and 0.8. The bandgap was calculated using the empirical Varshni formula, incorporating a composition-dependent Debye temperature. As cadmium content increases, $\Theta(x)$ decreases due to the heavier atomic mass of Cd relative to S, which enhances the thermal sensitivity of Eg.

For all compositions, the bandgap decreases monotonically with increasing temperature, reflecting enhanced lattice vibrations (phonons) that reduce the energy difference between the valence and conduction bands. At T = 100 K, the bandgaps are approximately 2.531 eV ($x = 0.2$), 2.528 eV ($x = 0.4$), 2.524 eV ($x = 0.6$), and 2.519 eV ($x = 0.8$). At T = 400 K, these values decrease to 2.311 eV, 2.303 eV, 2.293 eV, and 2.282 eV, respectively. The overall bandgap reduction (~0.22–0.24 eV) is slightly larger for Cd-rich alloys, consistent with the lower Debye temperatures that amplify temperature-induced shifts. These results highlight the dual influence of composition and temperature on the electronic structure of Cd_xS_{1-x} alloys. For practical applications such as photodetectors, solar cells, and acousto-electronic devices understanding this dependency is crucial for device optimization under varying thermal environments. Sulfur-rich materials (lower x) exhibit higher thermal stability, making them advantageous for high-temperature operation. Moreover, using a composition-dependent Debye temperature provides more physically accurate predictions than models with a fixed Θ, particularly in multi-element semiconductor alloys where mass differences significantly impact lattice dynamics.

CONCLUSIONS

This study comprehensively analyzed the optoelectronic and thermal behavior of pSi/n-Cd_xS_{1-x} heterojunctions over the full composition range ($0 \leq x \leq 1$). Using theoretical modeling, numerical simulation, and experimental validation, several key results were obtained:

1. The bandgap of Cd_xS_{1-x} decreases from ~2.42 eV (CdS) to ~1.74 eV (CdSe) with increasing Cd content, while pSi maintains a stable Eg(T) $\approx$ 1.12 eV. This contrast forms a strong band offset $\Delta Eg \approx$ 0.6–1.3 eV, promoting efficient carrier separation.

2. The Varshni model accurately described Eg(T) behavior for doping levels of p = 2×10^{17} cm^{-3} and n = 1×10^{18} cm^{-3}. Cd-rich alloys exhibited greater thermal narrowing ($\Delta Eg \approx$ 70–90 meV from 100–400 K), while S-rich compositions showed superior thermal stability.

3. The Debye temperature $\Theta(x)$ decreased from ~350 K (S-rich) to ~220 K (Cd-rich), reflecting increased atomic mass and phonon softening. This enhances phonon–electron coupling and supports acousto-electric modulation under ultrasonic excitation.

Overall, the pSi/n-Cd_xS_{1-x} heterojunction demonstrates strong compositional tunability, thermal robustness, and phonon-controlled carrier dynamics, making it a promising candidate for high-temperature, infrared-sensitive, and ultrasound-responsive optoelectronic devices.

ORCID
Jo'shqin Sh. Abdullayev, https://orcid.org/0000-0001-6110-6616; Ibrokhim B. Sapaev, https://orcid.org/0000-0003-2365-1554

REFERENCES
[1] W. Duncan, and A.R. Smellie, "Si–CdS heterojunction memory diodes," J. Appl. Phys. **49**(8), 4098–4104 (1978). https://doi.org/10.1063/1.325371

[2] N.D. Akhavan, I. Ferain, P. Razavi, R. Yu, and J.-P. Colinge, "Junctionless multigate transistors : fabrication and performance," Appl. Phys. Lett. **98**(10), 103510 (2011). https://doi.org/10.1063/1.3559625

[3]   A.V. Babichev, H. Zhang, P. Lavenus, F.H. Julien, A.Y. Egorov, Y.T. Lin, and M. Tchernycheva, "Nanowire heterojunction optoelectronics," Appl. Phys. Lett. **103**(20), 201103 (2013). https://doi.org/10.1063/1.4829756

[4]   B. Pal, K.J. Sarkar, and P. Banerji, "Optical and electronic properties of nanostructured solar cells," Sol. Energy Mater. Sol. Cells **204**, 110217 (2020). https://doi.org/10.1016/j.solmat.2019.110217

[5]   I. Aberg, G. Vescovi, D. Asoli, U. Naseem, J.P. Gilboy, C. Sundvall, and L. Samuelson, "III–V nanowire photovoltaics on silicon," IEEE J. Photovoltaics, **6**(1), 185–190 (2016). https://doi.org/10.1109/JPHOTOV.2015.2484967

[6]   P. Dubey, B. Kaushik, and E. Simoen, "Analytical modeling of advanced nano-CMOS devices," IET Circuits Devices Syst. (2019). https://doi.org/10.1049/iet-cds.2018.5169.

[7]   A.M. de Souza, D.R. Celino, R. Ragi, and M.A. Romero, "Emerging devices modeling," Microelectron. J. **119**, 105324 (2021). https://doi.org/10.1016/j.mejo.2021.105324

[8]   D.B. Istamov, O.A. Abdulkhayev, and Sh.M. Kuliyev, "Limiting characteristics of silicon diode temperature sensors for determining the maximum temperature with specified measurement accuracy," UNEC J. Eng. Appl. Sci. **5**(1), 63-69 (2025). https://doi.org/10.61640/ujeas.2025.0507

[9]   D.B. Istamov, O.A. Abdulkhayev, Sh.M. Kuliyev, N. Abdullayev, A.Sh. Ashirov, and D.M. Yodgorova, "Temperature response curve of silicon diode temperature sensors," East Eur. J. Phys. (2), 287-291 (2025). https://doi.org/10.26565/2312-4334-2025-2-35

[10] R. Seoudi, A.A. Shabaka, M. Kamal, E.M. Abdelrazek, and W. Eisa, "Size-dependent CdS nanoparticle characteristics," Physica E, **45**, 47–55 (2012). https://doi.org/10.1016/j.physe.2012.07.006

[11] J.Sh. Abdullayev, and I.B. Sapaev, "Optimization of temperature effects in radial p–n junctions," East Eur. J. Phys. (3), 344–349 (2024). https://doi.org/10.26565/2312-4334-2024-3-39

[12] J.Sh. Abdullayev, and I.B. Sapaev, "Temperature and doping optimization in p–n and p–i–n devices," Eurasian Phys. Tech. J. **21**(3), 21–28 (2024). https://doi.org/10.31489/2024No3/21-28

[13] J.Sh. Abdullayev, "Effect of linear doping on p–n junction properties," East Eur. J. Phys. (1), 245–249 (2025). https://doi.org/10.26565/2312-4334-2025-1-26

[14] R.D. Trevisoli, R.T. Doria, M. de Souza, S. Das, I. Ferain, and M.A. Pavanello, "Repetition," IEEE Trans. Electron Devices, **59**(12), 3510 (2012). https://doi.org/10.1109/TED.2012.2219055

[15] J.Sh. Abdullayev, and I.B. Sapaev, "Ideality factor variation at cryogenic temperatures," East Eur. J. Phys. (4), 329–333 (2024). https://doi.org/10.26565/2312-4334-2024-4-37

[16] A.V. Babichev, H. Zhang, P. Lavenus, F.H. Julien, A.Y. Egorov, Y.T. Lin, and M. Tchernycheva, "GaN nanowire ultraviolet photodetector with a graphene transparent contact," Appl. Phys. Lett. **103**(20), 201103 (2013). https://doi.org/10.1063/1.4829756

[17] J.Sh. Abdullayev, I.B. Sapaev, and Kh.N. Juraev, "Incomplete ionization analysis in radial p–n junctions," Low Temp. Phys. **51**, 60–64 (2025). https://doi.org/10.1063/10.0034646

[18] J.Sh. Abdullayev, and I.B. Sapaev, "GaAs/Si heterojunction analysis," East Eur. J. Phys. (1), 204–210 (2025). https://doi.org/10.26565/2312-4334-2025-1-21

[19] R. Bebitov, O. Abdulkhaev, D. Yodgorova, D. Istamov, G. Khamdamov, Sh. Kuliyev, J.Sh. Abdullaev, *et al*., "Potential distribution over temperature sensors of p-n junction diodes with arbitrary doping of the base region," E3S Web Conf. **401**, 03062 (2023). https://doi.org/10.1051/e3sconf/202340103062

[20] R.R. Bebitov, O.A. Abdulkhaev, D.M. Yodgorova, D.B. Istamov, G.M. Hamdamov, Sh.M. Kuliyev, A.A. Khakimov, and A.Z. Rakhmatov, "Dependence of the accuracy of the silicon diode temperature sensors for cryogenic thermometry on the spread of their parameters," Journal "Low Temperature Physics, **49**(2), 277–282 (2023). https://doi:10.1063/10.0016843

[21] R.R. Bebitov, O.A. Abdulkhaev, D.M. Yodgorova, D.B. Istamov, Sh.M. Kuliyev, A.A. Khakimov, A.B. Bobonazarov, *et al*, "Distribution of impurities in base-depleted region of diode temperature sensor," Low Temperature Physics, **50**(5), 418–424 (2024). https://doi:https://doi.org/10.1063/10.0025635

[22] J.Sh. Abdullayev, and I.B. Sapaev, "Modeling Si and GaAs junctions," Phys. Sci. Technol. **11**(3–4), 39–48 (2024). https://doi.org/10.26577/phst2024v11i2b05

[23] O. Toqtarbayuly, M. Baysariev, A. Qaysha, *et al*., "Enhancing dye-sensitized solar cell efficiency using gas-phase CVD GaN," Eurasian Phys. Tech. J. **21**(4), 131–139 (2024). https://doi.org/10.31489/2024No4/131-139

[24] I. Sapaev, I.B. Sapaev, *et al*., "Conference paper on p–n junction features," E3S Web Conf. **383**, 04022 (2023). https://doi.org/10.1051/e3sconf/202338304022

[25] J.Sh. Abdullayev, I. Sapaev, N. Esanmuradova, S. Kadirov, and S. Kuliyev, "Temperature and concentration in radial p–n junctions," East Eur. J. Phys. (2), 220–225 (2025). https://doi.org/10.26565/2312-4334-2025-2-24

[26] J.Sh. Abdullayev, I.B. Sapaev, and S.R. Kadirov, "Recombination's effect on radial p–n junction efficiency," East Eur. J. Phys. (2), 252–257 (2025). https://doi.org/10.26565/2312-4334-2025-2-30

[27] N.V. Deshmukh, T.M. Bhave, A.S. Ethiraj, *et al*., "PL and I–V characteristics of CdS-nanoparticles/porous-Si," Nanotechnology **12**(3), 290–294 (2001). https://doi.org/10.1088/0957-4484/12/3/316

[28] R. Zellagui, H. Dehdouh, M. Adnane, M.S. Akhtar, and M.A. Saeed, "CBD deposition of Cd$_x$Zn$_{1-x}$S thin films," Optik, **164**, 164377 (2020). https://doi.org/10.1016/j.ijleo.2020.164377

[29] N.A. Shah, A. Ali, S. Hussain, A. Maqsood, "CdCl$_2$-treated CdTe films via sublimation," J. Coatings Technol. Res. **7**(1), 105–110 (2008). https://doi.org/10.1007/s11998-008-9146-0

[30] J.Sh. Abdullayev, L. Abdullayeva, L. Agamalieva, and R. Ismailova, "Correlating Ni microstructure with Schottky barrier homogeneity in monolayer MoS$_2$ field-effect transistors," Advanced Physical Research, **7**(3), 350–357 (2025). https://doi.org/10.62476/apr.73350

[31] O.O. Akinwunmi, G.O. Egharevba, and E.O.B. Ajayi, "CdS, ZnS, CdZnS nanoparticles embedded in polystyrene," J. Modern Phys. **5**(5), 416–423 (2014). https://doi.org/10.4236/jmp.2014.55036

[32] C.-F. Wang, B. Hu, H.-H. Yi, and W.-B. Li, "Optoelectronic characterization of ZnS/silicon systems," Chin. Opt. Lett. **7**(6), 481-484 (2009). https://doi.org/10.3788/COL20090705.0432

[33] J.Sh. Abdullayev, I.B. Sapaev, J.Sh. Abdullayev, D.A. Juraev, M.J. Jalalov, and E.E. Elsayed, "Mathematical Modeling of Incomplete Ionization in Radial p-Si/n-GaAs Heterojunctions: Temperature and Doping Effects," Journal of Electronic Materials, **54**, 1–9 (2025). https://doi.org/10.1007/s11664-025-12391-8

[34] A. Laouid, A.A. Belghiti, K. Wisniewski, *et al.*, "Mn/Ca-doped ZnS thin films: morphology and PL," Mater. Chem. Phys. **290**, 127870 (2024). https://doi.org/10.1016/j.matchemphys.2024.129270

[35] J. Xiang, H. Wang, X. Wang, X. Chen, T. Wu, H. Wan, Y. Liu, and H. Wang, "$Cd_xZn_{1-x}S$ nanocrystals for visible-light photocatalysis," RSC Adv. **9**(7), 4001–4007 (2019). https://doi.org/10.1039/C8RA09408J

[36] M. Wang, A. Debernardi, Y. Berencén, R. Heller, C. Xu, Y. Yuan, *et al.*, "Breaking doping limit in silicon via deep impurities," Phys. Rev. Appl. **11**(5), 054039 (2019). https://doi.org/10.1103/PhysRevApplied.11.054039

ГЕТЕРОПЕРЕХОДИ pSi/n-Cd_xS_{1-x}, СТВОРЕНІ ЗА ДОПОМОГОЮ ТЕХНОЛОГІЇ BANDGAP: ВПЛИВ СКЛАДУ НА ОПТОЕЛЕКТРОННІ ВЛАСТИВОСТІ

Іброхім Б. Сапаєв[1,2,4,5*], Джамоліддін І. Раззоков[6,7], Джошкін Ш. Абдуллаєв[1], Дільдора А. Каландарова[3], Мадінабону Ш. Ібрагімова[3]

[1]*Національний дослідницький університет ТІІАМЕ, кафедра «Фізика та хімія», Корі Нійозій 39, Ташкент 100000, Узбекистан*

[2]*Ташкентський університет прикладних наук, вул. Університетська, 28, Ташкент 100095, Узбекистан*

[3]*Ургенчський державний університет, вул. Хаміда Олімджона, 14, Ургенч, 220100, Узбекистан*

[4]*Інженерний факультет, Центральноазіатський університет, Ташкент 111221, Узбекистан*

[5]*Азербайджанський державний університет нафти та промисловості (АДУНП), факультет хімічної технології, проспект Азадлиг, 20, Баку AZ1010, Азербайджан*

[6]*Інститут фундаментальних та прикладних досліджень, Національний дослідницький університет ТІІАМЕ, Корі Нійозій 39, Ташкент 100000, Узбекистан*

[7]*Кафедра біотехнології, Ташкентський державний технічний університет, Університет 2, 100095, Ташкент, Узбекистан*

У цьому дослідженні представлено всебічне вивчення електрофізичних властивостей гетеропереходу pSi/n-Cd_xS_{1-x}, у якому кадмієва складова x змінюється в межах від 0 до 1. Аналіз базується на поєднанні теоретичного моделювання, чисельного моделювання та експериментальної перевірки, виконаних для типових рівнів легування: $p = 2 \times 10^{17}$ см⁻³ для пористого p-кремнію та $n = 1 \times 10^{18}$ см⁻³ для n-Cd_xS_{1-x}. Особливу увагу приділено температурозалежній поведінці ключових матеріальних параметрів, зокрема ширини забороненої зони $E_9(T)$, концентрації власних носіїв $n_i(T)$ та температури Дебая $\Theta(x)$. Встановлено, що зі збільшенням частки кадмію спостерігається звуження забороненої зони Cd_xS_{1-x}, тоді як пористий кремній зберігає відносно широку та термічно стабільну $E_9(T)$, що забезпечує значне зонне вирівнювання (ΔE_9) і сприяє ефективному розділенню носіїв заряду на межі поділу. Зменшення $\Theta(x)$ зі зростанням вмісту кадмію впливає на інтенсивність фононного розсіювання та рекомбінаційні процеси, змінюючи механізм перенесення струму. Аналіз струмопереносу показує, що поведінка гетеропереходу значною мірою визначається температурно- та композиційно-залежним вирівнюванням зон і динамікою рекомбінації. Отримані результати підтверджують адекватність запропонованої фізичної моделі та демонструють перспективність структур pSi/n-Cd_xS_{1-x} для використання у високотемпературних та акустично керованих оптоелектронних пристроях.

Ключові слова: *оптоелектронні властивості; електростатичний аналіз; інженерія забороненої зони; гетероперехід pSi/n-Cd_xS_{1-x}; температура Дебая; модуляція вбудованого потенціалу; калібрування параметрів*

EFFECT OF SUBSTRATE TEMPERATURE ON THE MORPHOLOGY AND CRYSTALLINITY OF TiO$_2$ THIN FILMS GROWN BY ALD USING TTIP AND H$_2$O

Temur K. Turdaliev*, Khojiakhmad Kh. Zokhidov, Shukhrat Ch. Iskandarov,
Usmonjon F. Berdiyev

Arifov Institute of Ion-Plasma and Laser Technologies of Uzbekistan Academy of Sciences
100125, Durmon yuli st. 33, Tashkent, Uzbekistan
Corresponding Author E-mail: turdaliev@iplt.uz

This study investigates the influence of substrate temperature on the morphological and structural characteristics of TiO$_2$ thin films synthesized by thermal atomic layer deposited (ALD) using titanium tetraisopropoxide and water as precursors. The substrate temperature was varied from 200 to 275°C in 25°C increments. Surface morphology was examined using atomic force microscopy, while the crystalline structure was analyzed by XRD and Raman spectroscopy. It was found that films deposited at 200 °C exhibited an amorphous structure and a smooth, conformal surface with minimal roughness. Increasing the temperature to 225 °C led to the formation of microstructures and the emergence of initial signs of crystallization, accompanied by an increase in surface roughness. At 250-275 °C, a well-defined polycrystalline anatase structure was formed, characterized by grain development and nanostructure agglomeration, as evidenced by the increased intensity of diffraction peaks and higher surface roughness parameters. According to the XRD analysis, the average crystallite size ranged from 32 to 71 nm, depending on the synthesis temperature. The results demonstrate that deposition temperature exerts a comprehensive effect on both the phase composition and surface morphology of TiO$_2$ films, which must be considered for their application in functional nanostructures, photocatalytic systems, sensors, and microelectronic devices.

Keywords: *TiO$_2$; ALD; Anatase; Crystallinity; Morphology; Substrate temperature; XRD; Raman*
PACS: 81.07.Bc, 81.15.Gh, 68.37.Ps, 61.05.C-

INTRODUCTION

TiO$_2$ is one of the most extensively studied oxide materials due to its high thermal and chemical stability, environmental safety, and the diversity of its structural modifications. It is widely employed as a functional material in micro- and nanoelectronics, sensing technologies, photocatalysis, as well as in buffer and protective layers within multilayered heterostructures [1,2,3]. Of particular interest is the ability to deliberately control the surface morphology and structural state of TiO$_2$ thin films, as these characteristics directly influence the material's mechanical, electrical, and diffusion properties [4,5]. The type of crystalline phase, such as anatase, rutile, or brookite, along with crystallite size and orientation, the presence of amorphous components, and surface topography, collectively determine the performance of the film in practical applications [6]. Among the modern techniques for TiO$_2$ thin film fabrication, ALD stands out as one of the most precise and controllable methods, capable of producing highly uniform coatings even on substrates with complex geometries [7,8].

ALD enables angstrom-level control over film thickness, uniformity, and conformality, making it particularly attractive for the fabrication of nanostructured materials, especially on substrates with complex geometries [9]. In the synthesis of TiO$_2$ thin films via ALD, various titanium-containing precursors are commonly employed, such as titanium tetrachloride [10], tetrakis(dimethylamido)titanium [11], and titanium tetraisopropoxide (TTIP) [12], in combination with oxidizing agents like water, oxygen, or ozone. Among these, the thermal ALD process using TTIP and water as precursors is especially advantageous due to its low toxicity, high process stability, and the absence of corrosive by-products such as hydrochloric acid, which are typically generated when using chloride-based precursors [13]. This approach ensures high chemical purity of the resulting films and offers precise control over their thickness and phase composition, which is essential for tailoring the structural and functional properties of TiO$_2$ layers. One of the most critical parameters in the ALD process is the substrate temperature, which has a pronounced effect on growth mechanisms, the degree of crystallinity, and the surface morphology of the resulting films. At low deposition temperatures, films typically remain amorphous, whereas elevated temperatures can induce crystallization, surface roughening, grain growth, and, beyond the optimal range, agglomeration and loss of uniformity [14].

This work aims to investigate the effect of substrate temperature on the formation of surface morphology and crystalline structure of TiO$_2$ thin films synthesized by thermal ALD using TTIP and water as precursors. Particular attention is given to the analysis of surface evolution and crystallinity as a function of deposition temperature in the range of 200 - 275°C with 25°C increments, using atomic force microscopy, XRD, and Raman spectroscopy.

EXPERIMENT

TiO$_2$ thin films were deposited by thermal ALD using an SI PEALD system (SENTECH Instruments GmbH, Germany). Polished monocrystalline silicon wafers with a thickness of 0.4 mm, p-type conductivity, and (100)

crystallographic orientation were used as substrates. TTIP served as the metalorganic precursor, while deionized water was employed as the oxidizing agent. Nitrogen was used as both the carrier and purge gas. The substrate temperature was varied from 200 to 275 °C in 25 °C increments to investigate its effect on the morphology and crystallinity of the resulting films. All other deposition parameters were kept constant and corresponded to previously optimized conditions [12]: nitrogen flow rate of 120 cm³/min, chamber pressure of approximately 60 Pa, and a total cycle duration of 8 s. Each deposition cycle included five steps carried out in sequence: an initial purge with nitrogen, injection of the TTIP precursor for 0.5 s, a nitrogen purge for 3 s, introduction of H_2O for 1.5 s, and a final nitrogen purge for 3 s. The deposition was carried out for 500 cycles under the conditions described above.

The structural properties of the films were investigated using a Renishaw InVia Raman spectrometer operating in the visible range with a laser wavelength of λ = 532 nm. Phase analysis of the samples was performed by XRD using a Rigaku SmartLab diffractometer equipped with a copper anode (Cu Kα, λ = 1.5406 Å). Diffraction data were collected in the 2θ range from 20° to 75° with a step size of 0.02°. The resulting diffraction patterns were analyzed using the ICSD (Inorganic Crystal Structure Database) to identify the crystalline phases. Surface morphology of the synthesized TiO_2 films was examined by AFM using an AFM-NT MDT Solver Next system operating in contact mode.

Surface Morphology

Surface scanning was performed over areas of 5 × 5 μm² for each deposition temperature. Both two-dimensional topographic images and cross-sectional surface profiles were analyzed, enabling assessment of the influence of substrate temperature on surface relief evolution.

Topographic AFM images of the films deposited at temperatures ranging from 200 to 275°C are presented in Figure 1(a). A progressive transformation of the surface structure is observed with increasing deposition temperature. At 200°C, the surface is nearly flat and featureless, indicating a conformal growth mode. At 225 °C, isolated microstructures appear, likely associated with the onset of crystallization and the formation of initial growth centers. At 250°C, these microstructures become more pronounced and well-defined, suggesting intensified crystallization and the emergence of crystalline phase regions. At 275 °C, a substantial morphological transformation is observed, with the formation of agglomerated spherical nanostructures exhibiting particle sizes of 50-100 nm and an overall cluster diameter of approximately 0.5 μm. This indicates that the upper limit of the optimal ALD process window may have been exceeded, resulting in enhanced surface diffusion and aggregation due to precursor molecule desorption and re-adsorption. Analysis of the surface profiles extracted from the AFM scans is presented in Figure 1(b).
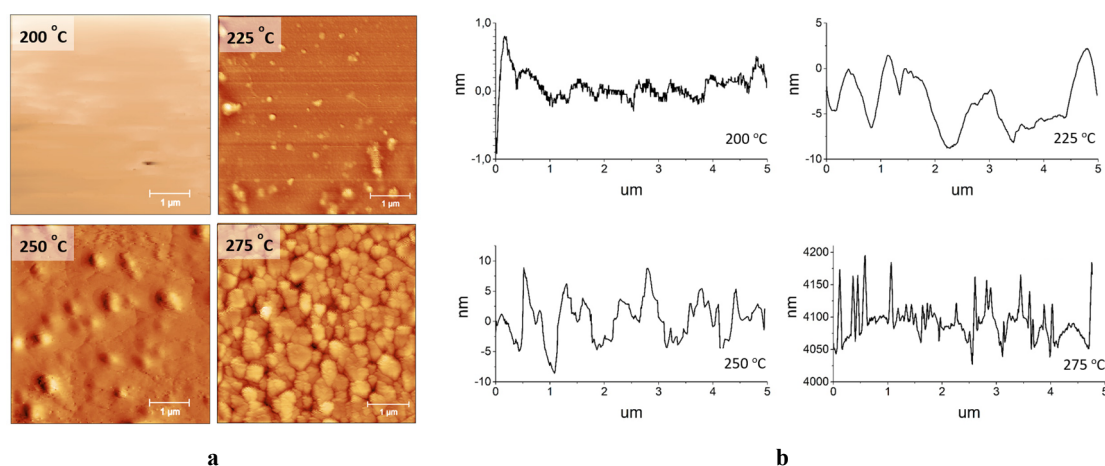

Figure 1. AFM images (a) and cross-sectional profiles (b) of TiO_2 films deposited at 200-275°C

Quantitative analysis of the AFM surface profiles enabled the determination of key roughness parameters, which are summarized in Table 1. The values of surface roughness and maximum height difference were calculated using standard formulas commonly applied in the interpretation of AFM data.

Table 1. Surface roughness parameters of TiO_2 films deposited at different substrate temperatures

	200 °C	225 °C	250 °C	275 °C
R_a	0.14 nm	2.4 nm	2.69 nm	18.64 nm
R_z	1.73 nm	10.97 nm	17.44 nm	167.92 nm

At 200°C, the R_a was measured to be 0.14 nm, indicating a highly smooth surface and uniform growth without the formation of local clusters. The film growth at this temperature was predominantly governed by saturated surface reactions. At 225°C, an increase in surface roughness to 2.40 nm was observed, along with the appearance of microstructures, suggesting the onset of conformality loss and the emergence of crystallization centers. This trend continued at 250°C, where R_a reached 2.69 nm and Rz was 17.44 nm, reflecting the development of grains and the intensification of grain boundaries. The most significant changes were observed at 275°C, where R_a increased to 18.64 nm

and R$_z$ to 167.92 nm. These values indicate the formation of a coarse-grained agglomerated structure and a pronounced loss of growth uniformity, likely due to the exceedance of the ALD process temperature window and enhanced thermally driven diffusion processes.

Structural Analysis

The Raman spectrum of the investigated sample exhibits well-defined peaks at 143, 194, 392, and 637 cm^{-1}, along with an intense band at 520 cm^{-1} (Figure 2). Peak identification was performed based on factor group analysis and comparison with literature data. It is well established that anatase phase TiO$_2$ exhibits six Raman active modes with symmetries A1g, B1g, and Eg, typically observed at 144, 194, 397, 513, 517, and 639 cm^{-1} [15]. The peaks recorded at 143, 194, and 637 cm^{-1} correspond to phonon modes with Eg symmetry, while the band at 392 cm^{-1} is assigned to the B1g mode. The strong signal at 520 cm^{-1} originates from Si-Si vibrations and is attributed to the monocrystalline silicon substrate [16]. This substrate-related peak overlaps with the anatase-related A1g and B2g modes at 513 and 517 cm^{-1}, respectively, hindering their unambiguous identification. The rutile phase of TiO$_2$ is characterized by principal Raman modes at 144, 243, 447, and 612 cm^{-1} [17]. None of which was observed in the acquired spectrum. Similarly, no bands corresponding to brookite-typically found at 153, 247, 322, 366, 398, 414, and 632 cm^{-1}-were detected [18]. This indicates the absence of both rutile and brookite phases in the film.

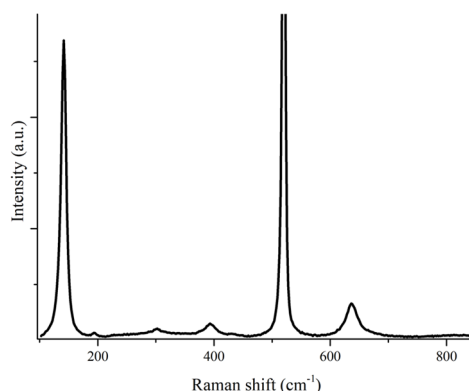**Figure 2.** Raman scattering spectrum of the sample

Identification and physical interpretation of the observed Raman peaks: The peak at 143 cm^{-1} is the most intense and prominent feature of anatase-phase TiO$_2$. It corresponds to the Eg symmetry phonon mode, associated with symmetric in-plane vibrations of oxygen atoms relative to titanium ions. Its intensity and sharpness are indicative of a high degree of crystallinity and lattice order. The 194 cm^{-1} peak represents a low-frequency mode with Eg symmetry, attributed to collective oxygen vibrations directed along the crystallographic axis. The 392 cm^{-1} peak arises from oxygen vibrations perpendicular to the titanium atoms and is characteristic of the B$_1$g mode, reflecting the local symmetry of the anatase crystal lattice. The strong peak at 520 cm^{-1} originates from the Si-Si bond vibrations of the monocrystalline silicon substrate. In cases of low TiO$_2$ film thickness, this peak appears as a pronounced background signal, which can mask the intrinsic Raman features of TiO$_2$, particularly those near 513 and 517 cm^{-1}. The 637 cm^{-1} peak is a high-frequency mode associated with symmetric oxygen vibrations within the anatase lattice and serves as an additional signature of this crystalline phase. Taken together, the presence and assignment of these peaks confirm that the TiO$_2$ films synthesized at substrate temperatures of 225-275°C exhibit a well-defined anatase crystalline structure, while the film grown at 200 °C retains an amorphous phase.

The crystallinity and phase composition of TiO$_2$ films synthesized at substrate temperatures of 200°C, 225°C, 250°C, and 275°C were investigated using XRD. In the sample deposited at 200°C, no diffraction peaks were detected, indicating an amorphous structure with the absence of long-range crystalline order. For the samples synthesized at 225 °C, 250 °C, and 275°C, the corresponding XRD patterns are shown in Figure 3 (a). At 225°C, weak but clearly distinguishable diffraction peaks appear, characteristic of the anatase phase of TiO$_2$. In particular, a peak near 2θ ≈ 25.3° corresponds to the (101) crystallographic plane, indicating the initial formation of crystalline nuclei, i.e., growth centers [19]. At the same time, the presence of a broad amorphous background suggests a two-phase composition-comprising both amorphous and crystalline components.

To quantitatively evaluate the phase composition, Rietveld refinement [20] was performed using the reference anatase structure from the ICSD database (entry No. 83795). The analysis revealed that the crystalline phase content in the sample deposited at 225°C was approximately 25-30%, with the remaining fraction being amorphous. The emergence of crystalline growth centers at this temperature may be attributed to substrate surface characteristics, including morphology, surface energy, and the presence of structural defects that promote localized adsorption and structural ordering. However, crystallization does not extend throughout the entire film, and the majority of the volume remains amorphous.

In contrast, XRD analysis of the samples synthesized at 250 °C and 275 °C revealed sharp and intense diffraction peaks corresponding to the anatase phase of TiO$_2$. Reflections from the (101), (004), (200), (105), and (211) planes were identified at 2θ angles of approximately 25.3°, 37.8°, 48.0°, and 54.0°, respectively [20]. The presence of narrow and intense peaks indicates a high degree of long-range crystalline order. The absence of a broad amorphous background further confirms the

fully crystallized anatase structure in these films, with no detectable amorphous component. Comparison of the obtained diffraction patterns with the reference anatase phase revealed complete agreement in both peak positions and relative intensities, indicating a polycrystalline anatase structure. The crystallites are randomly oriented, and the diffraction intensity is evenly distributed across all crystallographic directions. Based on the results of XRD and AFM analyses, a schematic representation of the TiO$_2$ film growth process via ALD at different substrate temperatures is provided in Figure 3(b).
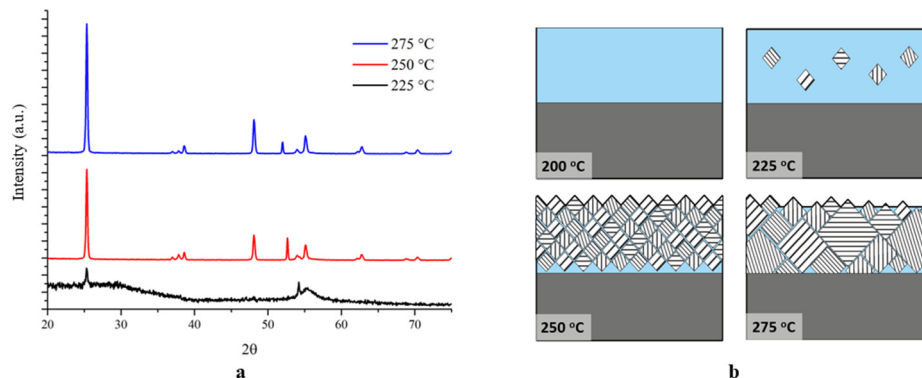

Figure 3. XRD patterns of TiO$_2$ films (a) and schematic illustration of the temperature-dependent growth mechanism (b)

At 200°C, the film is amorphous, exhibiting a smooth surface with no signs of crystallization. The layer demonstrates high conformality. At 225°C, localized crystallization centers begin to emerge, accompanied by the initial formation of anatase domains. The conformality of the film is partially disrupted. At 250°C, the crystallization process intensifies, resulting in the development of a continuous polycrystalline anatase structure throughout the film. The crystallites are randomly oriented, and the structure appears stabilized. At 275°C, a coarse-grained structure composed of large crystallites is formed. Enhanced surface diffusion results in agglomeration, and the film grows with a loss of uniformity. The average crystallite size was calculated using the Scherrer equation [21]:

$$D = \frac{K\lambda}{\beta cos\theta}$$

Where D is the average crystallite size, K is the Scherrer constant, λ is the wavelength of Cu Kα radiation (0.15406 nm), β is the full width at half maximum (FWHM) of the diffraction peak, and θ is the Bragg angle. For the calculations, five diffraction peaks corresponding to different crystallographic planes were selected, and the FWHM values (β) were measured for each of them. According to the results, the crystallite sizes ranged from 32.2 nm to 71.3 nm, indicating an average crystallite size of approximately 40-70 nm in the investigated TiO$_2$ samples.

CONCLUSIONS

Structural and morphological characterization of TiO$_2$ thin films synthesized by thermal ALD using TTIP and H$_2$O as precursors has demonstrated a strong dependence on substrate temperature. At 200°C, the films exhibit an amorphous structure with conformal surface morphology, as confirmed by the absence of diffraction peaks and a low surface roughness. The onset of crystallization is observed at 225°C, with the emergence of weak diffraction features and microstructural formations, indicating the formation of anatase-phase nuclei. At elevated deposition temperatures of 250–275°C, the TiO$_2$ films exhibit complete crystallization into the anatase polymorphic phase, as confirmed by the appearance of sharp and intense diffraction peaks corresponding to the (101), (004), (200), and other characteristic crystallographic planes. The crystallite size increases significantly with temperature, reaching ~70 nm, and the films exhibit a coarse-grained polycrystalline structure. AFM analysis reveals a progressive increase in surface roughness, consistent with crystallite growth and agglomeration driven by enhanced surface diffusion. These results confirm that substrate temperature is a critical parameter governing the nucleation, growth mode, and final structural configuration of ALD-deposited TiO$_2$ films. Control over this parameter enables precise tuning of crystallinity and surface topology, which is essential for optimizing film performance in applications such as photocatalysis, sensors, and nanostructured functional coatings.

ORCID
Temur K. Turdaliev, https://orcid.org/0000-0002-0732-9357; **Shukhrat Ch. Iskandarov,** https://orcid.org/0000-0002-3002-9141
Usmonjon F. Berdiyev, https://orcid.org/0000-0003-2808-0105

REFERENCES
[1]   V. Morgunov, S. Lytovchenko, V. Chyshkala, D. Riabchykov, and D. Matviienko, "Comparison of Anatase and Rutile for Photocatalytic Application: the Short Review," East Eur. J. Phys. (4), 18–30 (2021). https://doi.org/10.26565/2312-4334-2021-4-02

[2]   V. Yadav, S. Chaudhary, S.K. Gupta, and A.S. Verma, "Synthesis and characterization of TiO2 thin film electrode based dye sensitized solar cell," East Eur. J. Phys. (3), 129–133 (2020). https://doi.org/10.26565/2312-4334-2020-3-16

[3]   Y. Song, J. Yuan, Q. Chen, X. Liu, Y. Zhou, J. Cheng, S. Xiao, M.K. Chen, and Z. Geng, "Three-dimensional varifocal meta-device for augmented reality display," PhotoniX, **6**(1), (2025). https://doi.org/10.1186/s43074-025-00164-9

[4]   P.P. Conti, E. Scopel, E.R. Leite, and C.J. Dalmaschio, "Nanostructure morphology influences in electrical properties of titanium dioxide thin films," J. Mater. Res. **35**(21), 3012–3020 (2020). https://doi.org/10.1557/jmr.2020.235

[5]   E. Kumi-Barimah, R. Penhale-Jones, A. Salimian, H. Upadhyaya, A. Hasnath, and G. Jose, "Phase evolution, morphological, optical and electrical properties of femtosecond pulsed laser deposited TiO2 thin films," Sci. Rep. **10**(1), 1–12 (2020). https://doi.org/10.1038/s41598-020-67367-x

[6]   D.A.S. Mulus, M.D. Permana, Y. Deawati, and D.R. Eddy, "A current review of TiO2 thin films: synthesis and modification effect to the mechanism and photocatalytic activity," Appl. Surf. Sci. Adv. **27**, 100746 (2025). https://doi.org/10.1016/j.apsadv.2025.100744

[7]   J.P. Niemelä, G. Marin, and M. Karppinen, "Titanium dioxide thin films by atomic layer deposition: A review," Semicond. Sci. Technol. **32**(9), 1–20 (2017). https://doi.org/10.1088/1361-6641/aa78ce

[8]   J.P. Klesko, R. Rahman, A. Dangerfield, C.E. Nanayakkara, T. L'Esperance, D.F. Moser, L. Fabián Peña, E.C. Mattson, C.L. Dezelah, R.K. Kanjolia, and Y.J. Chabal, "Selective Atomic Layer Deposition Mechanism for Titanium Dioxide Films with (EtCp)Ti(NMe2)3: Ozone versus Water," Chem. Mater. **30**(3), 970–981 (2018). https://doi.org/10.1021/acs.chemmater.7b04790

[9]   T.K. Turdaliev, K.B. Ashurov, and R.K. Ashurov, "Morphology and Optical Characteristics of TiO2 Nanofilms Grown by Atomic-Layer Deposition on a Macroporous Silicon Substrate," J. Appl. Spectrosc. **91**(4), 769–774 (2024). https://doi.org/10.1007/s10812-024-01783-z

[10]   L. Aarik, T. Arroval, R. Rammula, H. Mändar, V. Sammelselg, and J. Aarik, "Atomic layer deposition of TiO2 from TiCl4 and O3," Thin Solid Films **542**, 100–107 (2013). https://doi.org/10.1016/j.tsf.2013.06.074

[11]   J.-J. Park, W.-J. Lee, G.-H. Lee, I.-S. Kim, B.-C. Shin, and S.-G. Yoon, "Very Thin TiO2 Films Prepared by Plasma Enhanced Atomic Layer Deposition (PEALD)," Integr. Ferroelectr. **68**(1), 129–137 (2004). https://doi.org/10.1080/10584580490895815

[12]   T.K. Turdaliev, "Optical Performance and Crystal Structure of TiO$_2$ Thin Film on Glass Substrate Grown by Atomic Layer Deposition," East Eur. J. Phys. (1), 250–255 (2025). https://doi.org/10.26565/2312-4334-2025-1-27

[13]   C. Armstrong, L.-V. Delumeau, D. Muñoz-Rojas, A. Kursumovic, J. MacManus-Driscoll, and K.P. Musselman, "Tuning the band gap and carrier concentration of titania films grown by spatial atomic layer deposition: a precursor comparison," Nanoscale Adv. **3**(20), 5908–5918 (2021). https://doi.org/10.1039/D1NA00563D

[14]   N.K. Chowdhary, and T. Gougousi, "Temperature-Dependent Properties of Atomic Layer Deposition-Grown TiO2 Thin Films," Adv. Mater. Interfaces **2400855**, (2025). https://doi.org/10.1002/admi.202400855

[15]   A.E. Maftei, A. Buzatu, G. Damian, N. Buzgar, H.G. Dill, and A.I. Apopei, "Micro-Raman—a tool for the heavy mineral analysis of gold placer-type deposits (Pianu Valley, Romania)," Minerals **10**(11), 1–17 (2020). https://doi.org/10.3390/min10110988

[16]   M. Kadlečíková, Ľ. Vančo, J. Breza, M. Mikolášek, K. Hušeková, K. Fröhlich, P. Procel, M. Zeman, and O. Isabella, "Raman spectroscopy of silicon with nanostructured surface," Optik (Stuttg). **257**, 168869 (2022). https://doi.org/10.1016/j.ijleo.2022.168869

[17]   T. Lan, X. Tang, and B. Fultz, "Phonon anharmonicity of rutile TiO2 studied by Raman spectrometry and molecular dynamics simulations," Phys. Rev. B - Condens. Matter Mater. Phys. **85**(9), (2012). https://doi.org/10.1103/PhysRevB.85.094305

[18]   M.N. Iliev, V.G. Hadjiev, and A.P. Litvinchuk, "Raman and infrared spectra of brookite (TiO2): Experiment and theory," Vib. Spectrosc. **64**, 148–152 (2013). https://doi.org/10.1016/j.vibspec.2012.08.003

[19]   S. Prachakiew, S. Boonphan, Y. Keereeta, C. Boonruang, and A. Klinbumrung, "Structural Influence of Vanadium on the Anatase-to-Rutile Phase Transition and Bandgap Modification in TiO2 Nanocrystals," Arab. J. Sci. Eng. (2025). https://doi.org/10.1007/s13369-025-10150-9

[20]   M.T. Islam, S. Aman, T. Bayzid, M.A. Rahaman, U. Podder, G.M. Arifuzzaman Khan, and M.A. Alam, "Crystal growth behavior of nanocrystal anatase TiO2: A Rietveld refinement in WPPF analysis," Chem. Inorg. Mater. **6**, 100108 (2025). https://doi.org/10.1016/j.cinorg.2025.100108

[21]   T. Theivasanthi, and M. Alagar, "Titanium dioxide (TiO2) Nanoparticles XRD Analyses: An Insight," ArXiv:1307.1091, (2013). https://doi.org/https://doi.org/10.48550/arXiv.1307.1091

ВПЛИВ ТЕМПЕРАТУРИ ПІДКЛАДКИ НА МОРФОЛОГІЮ ТА КРИСТАЛІЧНІСТЬ ТОНКИХ ПЛІВОК TiO₂, ВИРОЩЕНИХ МЕТОДОМ ALD З ВИКОРИСТАННЯМ TTIP ТА H₂0

Темур К. Турдалієв, Ходжіахмад Х. Зохідов, Шухрат Ч. Іскандаров, Усмонджон Ф. Бердієв

Інститут іонно-плазмових та лазерних технологій ім. Аріфова Академії наук Узбекистану

100125, вул. Дурмон йулі, 33, Ташкент, Узбекистан

У цьому дослідженні досліджується вплив температури підкладки на морфологічні та структурні характеристики тонких плівок TiO₂, синтезованих методом термічного ALD з використанням тетраізопропоксиду титану та води як прекурсорів. Температура підкладки змінювалася від 200 до 275°C з кроком 25°C. Морфологію поверхні досліджували за допомогою атомно-силової мікроскопії, а кристалічну структуру аналізували за допомогою рентгенівської дифракції та раманівської спектроскопії. Було виявлено, що плівки, нанесені при 200°C, мали аморфну структуру та гладку, конформну поверхню з мінімальною шорсткістю. Підвищення температури до 225°C призвело до утворення мікроструктур та появи початкових ознак кристалізації, що супроводжувалося збільшенням шорсткості поверхні. При 250-275°C утворилася чітко виражена полікристалічна структура анатазу, що характеризується розвитком зерен та агломерацією наноструктур, про що свідчить підвищена інтенсивність дифракційних піків та вищі параметри шорсткості поверхні. Згідно з рентгенівським дифракційним аналізом, середній розмір кристалітів коливався від 32 до 71 нм, залежно від температури синтезу. Результати показують, що температура осадження має комплексний вплив як на фазовий склад, так і на морфологію поверхні плівок TiO₂, що необхідно враховувати для їх застосування у функціональних наноструктурах, фотокаталітичних системах, сенсорах та мікроелектронних пристроях.

Ключові слова: *TiO₂; ALD; анатаз; кристалічність; морфологія; температура підкладки; XRD; раманівська спектроскопія*

DESIGN AND DEVELOPMENT OF FERRITE-TIO$_2$ NANOCOMPOSITES WITH TUNABLE MAGNETIC PROPERTIES

Hanaa Sh. Ahmed[1],   **A.K. Sijo[2]*,**   **Ali M. Mohammad[1#], Hero S. Ahmed Al-Jaf[1], Balen H. Ahmed[1],**
J. Mazurenko[3]

[1]University of Garmian, College of Education, Department of Physics, Kurdistan region, Kalar-46021, Iraq
[2]Department of Physics, Mary Matha Arts & Science College, Mananthavady, Kannur University-670645, India
[3]Department of Medical Informatics, Ivano-Frankivsk National Medical University, 2 Halytska Str., 76018, Ivano-Frankivsk, Ukraine
Corresponding Author e-mail: *aksijo@marymathacollege.ac.in; #alimustaf392@gmail.com
Received August 14, 2025; revised October 2, 2025; accepted October 23, 2025

Ni-ferrite-TiO$_2$ nanocomposites with varying TiO$_2$ content (0%, 25%, 50% and 75%) were synthesized using the sol-gel auto-combustion method and characterized through XRD, FE-SEM, VSM, and Raman spectroscopy. The XRD analysis confirmed the coexistence of ferrite and TiO$_2$ phases. FE-SEM images revealed uniform particle distribution and a reduction in particle size as TiO$_2$ content increased. Raman spectroscopy showed strong TiO$_2$-related vibrational modes, with the highest intensity observed in the 75% TiO$_2$ sample, diminishing as TiO$_2$ content decreased. Peaks observed in pure Ni-ferrite (283, 402, 469 and 689 cm^{-1}) shifted to lower wavelengths with increasing TiO$_2$ doping, indicating altered vibrational modes due to phase interactions. These interactions likely contributed to changes in the magnetic properties. VSM analysis revealed a decrease in saturation magnetization and magnetic remanence with increasing TiO$_2$ content, while coercivity remained stable. The magnetic behavior was attributed to TiO$_2$ dilution and phase interfaces, offering valuable insights for the design of magnetic materials with customized properties.
Keywords: *Ferrite; Nanocomposites; Magnetic properties; Nanoparticles; Hybrid ferrite*
PACS: 75.75.+a ; - 81.16.-c

1. INTRODUCTION

The pursuit of advanced magnetic materials with tailored properties has become a central focus of modern technological innovation. Magnetic nanomaterials offer promising opportunities for applications in spintronics, magnetic storage, biomedical devices, and energy storage systems [1][2]. Among these, nickel ferrite (NiFe) nanoparticles stand out due to their remarkable magnetic characteristics, stability, and biocompatibility [3].

Ni ferrite nanoparticles are known for their excellent magnetic properties, such as high saturation magnetization and coercivity, making them suitable for various high-performance applications [4,5]. Moreover, the magnetic behavior of these nanoparticles can be further optimized by altering their composition, structure, and morphology [6]. Studies on similar ferrite-based nanocomposites, such as cobalt ferrite (CoFe) and zinc ferrite (ZnFe), have demonstrated distinct magnetic properties. CoFe nanoparticles exhibit high magnetic anisotropy and coercivity [7], while ZnFe nanoparticles are recognized for their magnetic stability and biocompatibility [8].

The potential of NiFe nanoparticles can be expanded through hybridization with other materials, creating multifunctional nanocomposites with enhanced magnetic and structural properties. Titanium dioxide (TiO$_2$) emerges as an excellent material for this purpose due to its unique optical, electrical, and magnetic properties [9]. Integrating TiO$_2$ with NiFe nanoparticles can yield nanocomposites with enhanced magnetic properties, improved thermal stability, and increased surface area [10].

In this study, Ni-ferrite-TiO$_2$ nanocomposites with varying TiO2 content were synthesized using the sol-gel auto-combustion method. This technique provides precise control over the composition, structure, and morphology of the nanocomposites, enabling a systematic investigation of how TiO$_2$ incorporation influences their magnetic properties [11]. Our research investigates the structural, morphological, and magnetic properties of NiFe-TiO$_2$ nanocomposites to gain a deeper understanding of the mechanisms underlying their enhanced magnetic behavior. The insights gained from this study will aid in the development of multifunctional nanomaterials with customized magnetic properties, opening new possibilities for applications in magnetic storage, spintronics, biomedical devices, and energy storage technologies.

2. Materials and methods
2.1 Synthesis

NiFe$_2$O$_4$ spinel nanoferrite was synthesized using a sol-gel auto-combustion method [12,13]. Stoichiometric amounts of analytical grade of ferric nitrate (Fe(NO$_3$)$_3$·9H$_2$O), nickel nitrate (Ni(NO$_3$)$_2$·6H$_2$O), and citric acid (C$_6$H$_8$O$_7$) were dissolved in deionized water, maintaining a 1:1 molar ratio [14]. The pH was adjusted to neutral (pH 7) by adding ammonia while stirring. The mixture was then heated to 90°C, forming a dense gel, which was subsequently heated to 275°C, initiating a combustion reaction that produced as-burnt ferrite powder. The powder was calcined at 500°C for 3

hours in air to remove organic residues and achieve a uniform particle size distribution [15]. To explore the impact of TiO$_2$ content on the nanocomposite properties, TiO$_2$ nanoparticles were introduced into the ferrite nanopowder at various ratios (0%, 25%, 50%, and 75%). The structural, morphological, and magnetic properties of the resulting ferrite-TiO$_2$ nanocomposites were comprehensively characterized.

2.2 Material characterization

The crystalline structure of the ferrite nanocomposites was examined using X-ray diffraction (XRD) analysis performed on a PANalytical X'pert Pro instrument (Netherlands) with a Cu Kα radiation source (λ = 1.54048 Å) [16]. The surface morphology of the nanoparticles was investigated using field emission-scanning electron microscopy (FE-SEM) with a MIRA3-XMU model (TESCAN, Czech Republic) [17]. Raman spectra using XploRa-HOBIBA with a 785 nm laser were employed to identify the spinel ferrite phase [18]. The magnetic properties of the ferrite nanocomposites were characterized at room temperature using a vibrating sample magnetometer (VSM) from LBKFB Meghnatis Daghigh Kavir Company, with an applied magnetic field ranging from -10 to +10 kOe [19].

3. RESULTS AND DISCUSSION

The XRD patterns of the NiFe$_2$O$_4$/TiO$_2$ nanocomposites with varying TiO$_2$ content (0%, 25%, 50%, and 75%) are presented in Figure 1. The FullProf-fitted spectra reveal well-defined peaks at (220), (311), (222), (400), (422), and (440), which are characteristic of the spinel ferrite phase [20]. These peaks confirm the presence of the NiFe$_2$O$_4$ spinel structure and indicate that the samples are free from detectable impurities [21]. In addition to the ferrite phase, the TiO$_2$ phase was identified through spectral fitting techniques [22]. The XRD patterns correspond well with known reference patterns for the cubic spinel phase of NiFe$_2$O$_4$ (JCPDS card no. 00-054-0964) and the tetragonal anatase phase of TiO$_2$ (JCPDS card no. 00-021-1272) [23]. The accurate matching of these patterns with standard reference cards validates the successful incorporation of TiO$_2$ into the NiFe$_2$O$_4$ matrix and confirms the preservation of the distinct crystal structures of both components within the nanocomposites. This indicates that TiO$_2$ is present in its anatase form and does not interfere with the spinel structure of the ferrite, thus allowing for the exploration of combined properties of these materials.
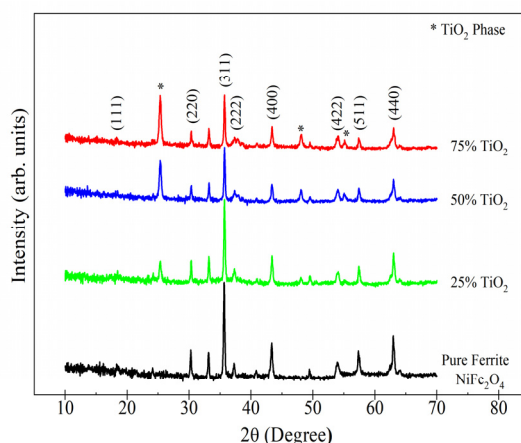

Figure 1. XRD patterns of 0%, 25%, 50%, and 75% NiFe$_2$O$_4$/TiO$_2$ nanocomposites

The structural parameters of the NiFe$_2$O$_4$/TiO$_2$ nano composites, determined through FullProf fitting, are summarized in Table 1. The crystallite size (D$_{XRD}$) and particle size (D$_{FE-SEM}$) values show a slight variation with increasing TiO$_2$ content. Specifically, a minimum crystallite size of 41.72 nm is observed for the 25% TiO$_2$ sample. This reduction in crystallite size can be attributed to the grain refinement effect induced by the incorporation of TiO$_2$. The presence of TiO$_2$ may disrupt the growth of NiFe$_2$O$_4$ grains, leading to smaller crystallite sizes [24]. The lattice parameter (a) values range from 5.347 Å to 7.213 Å, reflecting a subtle expansion of the crystal lattice with increasing TiO$_2$ content. This lattice expansion is likely due to the substitution of larger Ti^{4+} ions for the smaller Fe^{3+} ions in the NiFe$_2$O$_4$ lattice. As Ti^{4+} ions are larger than Fe^{3+} ions, their incorporation into the NiFe$_2$O$_4$ lattice increases the lattice dimensions, which is consistent with the observed increase in the lattice parameter [25].

Table 1. Structural Parameters from XRD & SEM analysis- crystallite size (D$_X$), particle size (D$_S$), lattice parameter (a), density (ρx), microstrain(ε) and dislocation density (δ)

TiO$_2$ %	D$_{XRD}$ (nm)	D$_{SEM}$ (nm)	a (Å)	ρx	ε×10^{-3}	δ×10^{15}
0	44.85	17.9	8.350	5.35	1.5	0.599
25	41.72	19.9	8.335	7.21	1.91	0.824
50	45.01	22.1	8.333	7.21	1.80	0.720
75	49.08	21.9	8.335	7.21	1.61	0.591

The density (ρ_x) of the nanocomposites is found to be lowest for the 0% TiO₂ sample and remains relatively constant for the composites with higher TiO₂ content. This suggests that the addition of TiO₂ does not significantly alter the overall density of the nanocomposites. The lack of significant change in density might indicate that the TiO₂ particles are well-dispersed within the NiFe₂O₄ matrix, without causing substantial changes in the overall packing density of the material [25]. Additionally, the microstrain ($\varepsilon \times 10^{-3}$) values decrease with increasing TiO₂ content, indicating a relaxation of the crystal structure. Microstrain is a measure of local lattice distortions and defects. The decrease in microstrain with higher TiO₂ content suggests that the incorporation of TiO₂ reduces lattice distortions and helps to relieve internal stresses within the NiFe₂O₄ lattice. This reduction in microstrain is likely due to the reduced lattice mismatch between the NiFe₂O₄ and TiO₂ phases, leading to a more coherent and less strained crystal structure [26].

The surface morphology of the NiFe₂O₄/TiO₂ nano composites was examined using field emission scanning electron microscopy (FESEM), with the resulting images presented in Figure 2a-d. The FESEM images provide detailed insights into the particle size, shape, and distribution of the nanocomposites. These images reveal that the nanoparticles exhibit a relatively uniform distribution across the sample, with variations in particle size that are dependent on the TiO₂ content. The observations from the FESEM analysis are crucial for understanding the impact of TiO₂ incorporation on the surface characteristics of the NiFe₂O₄ matrix, which can influence the material's overall performance in various applications [27].
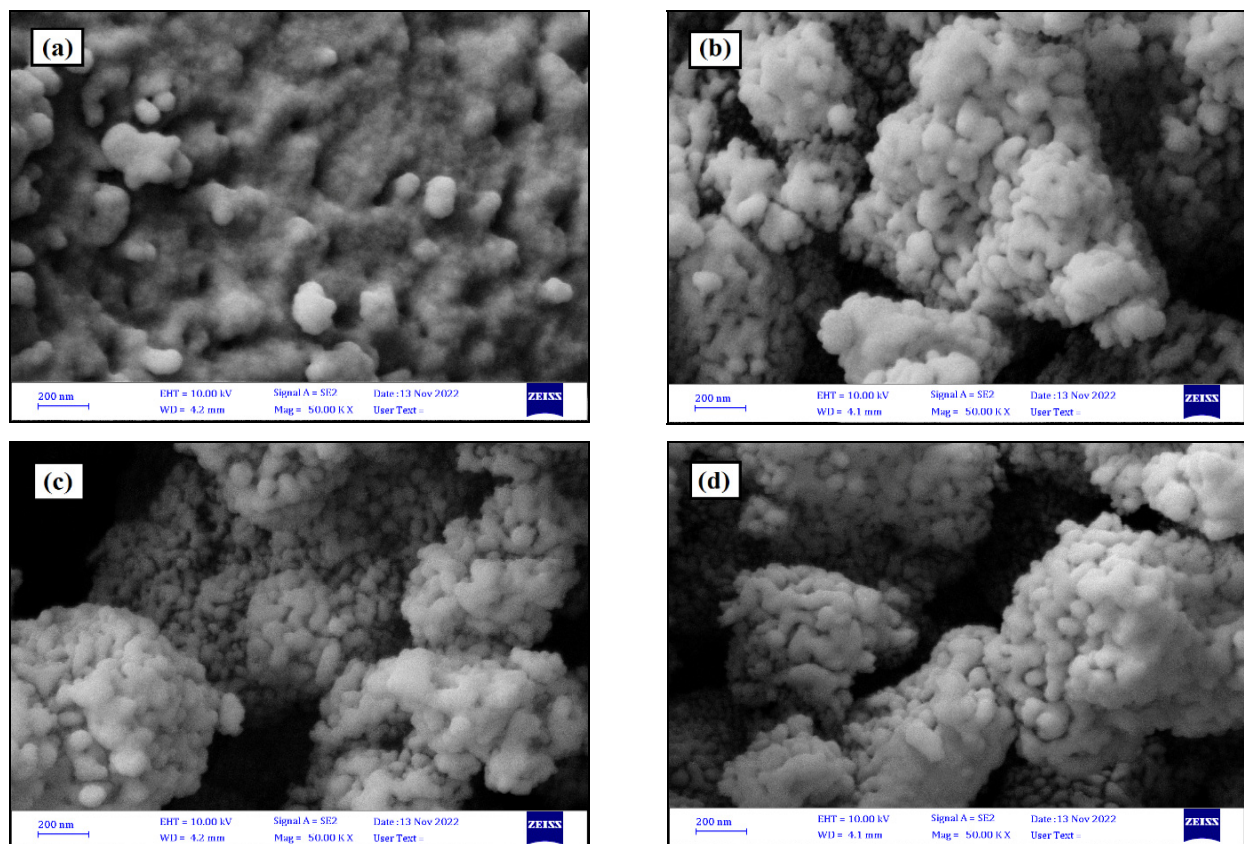

Figure 2. FE-SEM images of 0%, 25%, 50%, and 75% NiFe₂O₄/TiO₂ nanocomposites

The FE-SEM microstructural analysis (Figure 3a-d) revealed a nearly homogeneous particle size distribution across the surface, with particles predominantly exhibiting semi-spherical shapes. This analysis highlights the significant effect of TiO₂ doping on particle size, demonstrating that higher TiO₂ content (75%) results in noticeable particle enlargement. The microstructural examination provides detailed insights into the average size and grain growth characteristics, which are essential for understanding the material's physical, electrical, and magnetic properties. Particle agglomeration is evident, with smaller particles coalescing to achieve a lower free energy state, a trend that is more pronounced with increased TiO₂ doping. Additionally, there is a noticeable tendency for aggregation among numerous ferrite nanoparticles. The observed porous structures may result from substantial gas release during the combustion process, while the formation of agglomerated regions is likely due to the inherent interactions among magnetic nanoparticles [28].

The average crystallite size (D_{XRD}) and particle size (D_{FE-SEM}) show a significant dependence on TiO₂ content, as summarized in Table 1. The images also indicate that the particle sizes of the two phases vary with the relative content of each component. As TiO₂ content increases, the size of the nanocomposite particles also increases. Uniform structures are observed in the intermediate compositions, suggesting coherent grain growth within the constituent phases of the composites.
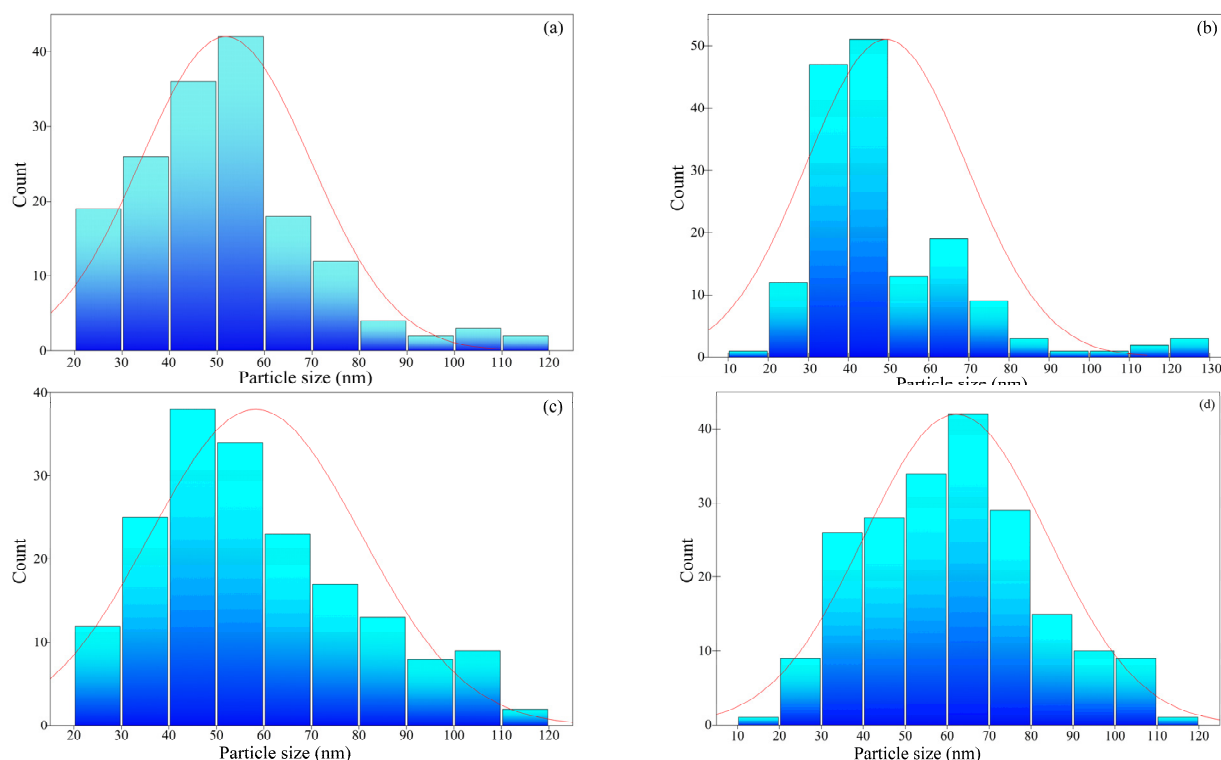
Figure 3. FE-SEM images of 0%, 25%, 50%, and 75% NiFe$_2$O$_4$/TiO$_2$ nanocomposites

Figure 4 presents the Raman spectra of NiFe$_2$O$_4$/TiO$_2$ nanocomposites with varying TiO$_2$ content (0%, 25%, 50%, and 75%). The Raman spectroscopy results reveal a prominent vibrational mode associated with the TiO$_2$ phase, as evidenced by the high-intensity peaks observed in the 75% TiO$_2$ sample [29]. As the TiO$_2$ content decreases, the intensity of these TiO$_2$-related peaks diminishes, highlighting the influence of TiO$_2$ concentration on the Raman signal. In contrast, the pure Ni-ferrite sample exhibits characteristic peaks at 283, 402, 469, and 689 cm^{-1}. These peaks shift towards lower wavelengths with increasing TiO$_2$ doping percentages, suggesting changes in the vibrational modes of the Ni-ferrite phase due to interactions with the TiO$_2$. The observed shift in peak positions and variations in peak intensities indicate a strong interaction between the Ni-ferrite and TiO$_2$ phases. This interaction likely influences the material's vibrational properties and is correlated with changes in the magnetic properties of the nanocomposites as TiO$_2$ content varies [30].
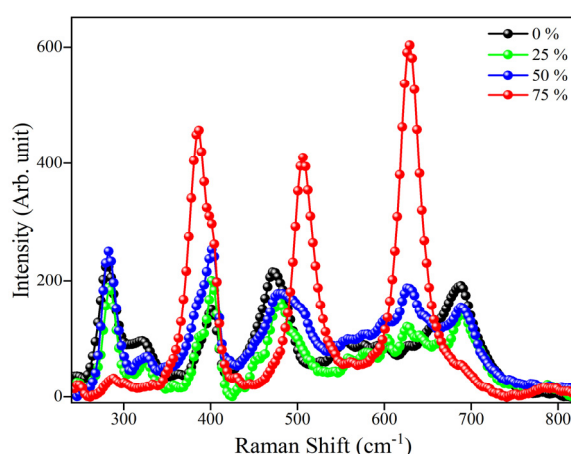

Figure 4. Raman spectra of 0%, 25%, 50%, and 75% NiFe$_2$O$_4$/TiO$_2$ nanocomposites

Figure 5 displays the room temperature hysteresis loops derived from Vibrating Sample Magnetometry (VSM) measurements. The magnetic properties, saturation magnetization (Ms), coercivity (Hc), and remanence magnetization (M$_R$), are summarized in Table 2.

Figure 6 presents the variation curves for Ms and M$_R$ with different TiO$_2$ concentrations. The results reveal a decline in Ms and magnetic moment (μ) as TiO$_2$ content increases, indicating a systematic reduction in the magnetic properties of the NiFe$_2$O$_4$/TiO$_2$ nanocomposites. This reduction is attributed to the dilution effect caused by the incorporation of TiO$_2$, which progressively diminishes the magnetic properties of the NiFe$_2$O$_4$ phase [31,32]. Since TiO$_2$

is non-magnetic, its presence reduces the concentration of the magnetic $NiFe_2O_4$ phase, leading to an overall decrease in the magnetic moment of the nanocomposites. Notably, Hc remains relatively stable across different TiO_2 concentrations, suggesting that the incorporation of TiO_2 does not significantly affect the magnetic anisotropy of the nanocomposites [33,34]. The consistent coercivity indicates that TiO_2 does not substantially alter the magnetic domain structure or the magnetization reversal process in the $NiFe_2O_4$ phase.
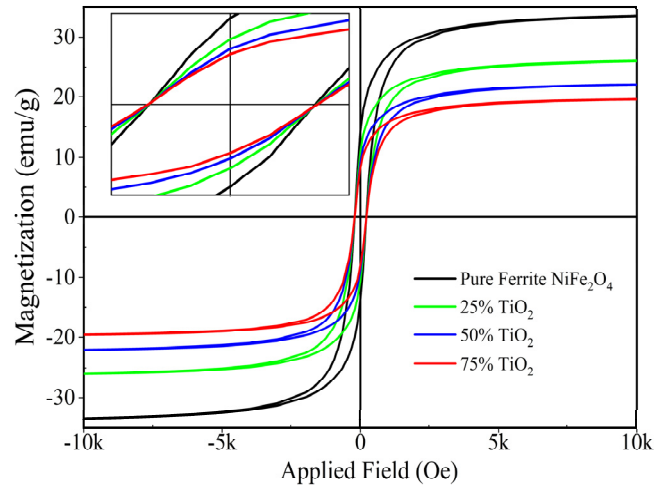

Figure 5. RT Magnetic curves of 0%, 25%, 50%, and 75% $NiFe_2O_4/TiO_2$ nanocomposites

Table 2. RT Magnetic parameters

TiO_2 %	M_S (emu/g)	M_R (emu/g)	H_C (Oe)	ηB (μB)	$K \times 10^3$ (emu.Oe/g)
0	33.73	14.29	204.1	1.416	7.17
25	26.28	10.86	204.7	1.479	5.60
50	22.24	9.19	205.9	1.251	4.77
75	19.75	8.3	206.9	1.111	4.26

The observed decrease in saturation magnetization and magnetic moment with increasing TiO_2 content may also be related to changes in particle size and surface effects, as indicated by the FESEM analysis [35]. Variations in particle size and potential surface phenomena, such as increased porosity or agglomeration, could further impact the magnetic properties of the nanocomposites. These factors must be considered when interpreting the changes in magnetic behavior with varying TiO_2 concentrations.
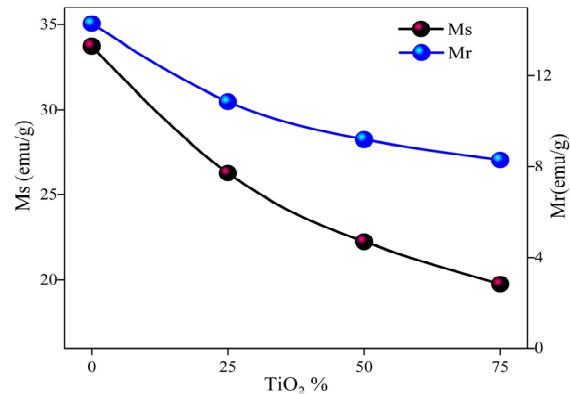

Figure 6. RT Magnetic Saturation (Ms) and Remanence (M_R) variation curves of 0%, 25%, 50%, and 75% $NiFe_2O_4/TiO_2$ nanocomposites

4. CONCLUSIONS

This study provides significant insights into $NiFe_2O_4/TiO_2$ nanocomposites, focusing particularly on their magnetic properties alongside structural and morphological aspects. X-ray diffraction (XRD) confirmed the successful synthesis of these nanocomposites, revealing the presence of both $NiFe_2O_4$ and TiO_2 phases. Field emission scanning electron microscopy (FESEM) demonstrated a uniform distribution of TiO_2 within the $NiFe_2O_4$ matrix, with particle size decreasing as TiO_2 content increased, suggesting that TiO_2 acts as a grain refiner. Raman spectroscopy further revealed strong interactions between $NiFe_2O_4$ and TiO_2, leading to changes in vibrational modes that influence the material's magnetic behavior.

The magnetic studies, conducted via Vibrating Sample Magnetometry (VSM), are particularly noteworthy. The results showed a significant decrease in saturation magnetization and magnetic moment as TiO$_2$ content increased, highlighting a pronounced dilution effect on the magnetic properties of the NiFe$_2$O$_4$ phase. This reduction is a direct consequence of the non-magnetic TiO$_2$ phase diluting the magnetic contribution of NiFe$_2$O$_4$. Despite this decrease, the coercivity remained stable across different TiO$_2$ concentrations, indicating that TiO$_2$ incorporation does not significantly affect the magnetic anisotropy or the magnetization reversal process. This stability in coercivity suggests that the fundamental magnetic characteristics of the NiFe$_2$O$_4$ phase are preserved, even as its magnetic moment is diluted.

Looking ahead, future research should prioritize optimizing synthesis parameters to further refine these magnetic properties, exploring different TiO$_2$ doping levels and alternative materials. Additionally, practical applications in spintronics, magnetic sensors, and catalysis could benefit from these findings, making it crucial to evaluate how these nanocomposites perform in specific technological contexts. Comparative studies with other materials will also be valuable to highlight the relative advantages of NiFe$_2$O$_4$/TiO$_2$ nanocomposites. Overall, this work advances our understanding of TiO$_2$ doping effects on NiFe$_2$O$_4$ nanocomposites, emphasizing their potential for applications requiring tailored magnetic properties.

ORCID
A.K. Sijo, https://orcid.org/0000-0002-1478-2088; **Ali M. Mohammad,** https://orcid.org/0000-0003-1659-8855
J. Mazurenko, https://orcid.org/0000-0002-8446-5280

REFERENCES
[1] H. Wang, T.N. Lamichhane, and M.P. Paranthaman, "Review of additive manufacturing of permanent magnets for electrical machines: A prospective on wind turbine," Materials Today Physics, **24**, 100675 (2022). https://doi.org/10.1016/j.mtphys.2022.100675
[2] A. Hirohata, K. Yamada, Y. Nakatani, I.L. Prejbeanu, B. Diény, P. Pirro, and B. Hillebrands, "Review on spintronics: Principles and device applications," Journal of Magnetism and Magnetic Materials, **509**, 166711 (2020). https://doi.org/10.1016/j.jmmm.2020.166711
[3] S.J. Salih, and W.M. Mahmood, "Review on magnetic spinel ferrite (MFe2O4) nanoparticles: From synthesis to application," Heliyon, **9**(6), e16601 (2023). https://doi.org/10.1016/j.heliyon.2023.e16601
[4] G. Rana, P. Dhiman, A. Kumar, D-V.N. Vo, G. Sharma, S. Sharma, and M. Naushad, "Recent advances on nickel nano-ferrite: A review on processing techniques, properties and diverse applications," Chemical Engineering Research and Design, **175**, 182-208 (2021). https://doi.org/10.1016/j.cherd.2021.08.040
[5] J. Mazurenko, A.K. Sidjo, L. Kaykan, J.M. Michalik, L. Gondek, E. Szostak, and Ż. Antoni, "Impact of cation distribution in shaping the structural and magnetic characteristics of Ni-Cu ferrite," Physica Scripta, **100**, 035940 (2025). https://doi.org/10.1088/1402-4896/adb2c3
[6] T. Dippong, E.A. Levei, and O. Cadar, "Correlation between structure, morphology and magnetic properties in ZnxCo0.8−xNi0.2Fe2O4@SiO2 (0.1÷0.7) nanocomposites," Journal of Alloys and Compounds, **938**, 168503 (2023). https://doi.org/10.1016/j.jallcom.2022.168503
[7] T. Tatarchuk, M. Bououdina, W. Macyk, et al. "Structural, Optical, and Magnetic Properties of Zn-Doped CoFe2O4 Nanoparticles," Nanoscale Research Letters, **12**, 141 (2017). https://doi.org/10.1186/s11671-017-1899-x
[8] P. Sahoo, P. Choudhary, S.S. Laha, A. Dixit, and O.T. Mefford, "Recent advances in zinc ferrite (ZnFe2O4) based nanostructures for magnetic hyperthermia applications," Chemical Communications, **59**, 12065-12090 (2023). https://doi.org/10.1039/D3CC01637D
[9] R. Javed, et al. "Diverse biotechnological applications of multifunctional titanium dioxide nanoparticles: an up-to-date review," IET Nanobiotechnology, **16**(5), 171-189 (2022). https://doi.org/10.3390/ma15051863
[10] X. Chen, W. Zhu, J. Chen, Q. Cao, Y. Chen, and D. Hu, "TiO2 Nanoparticle/Polyimide Nanocomposite for Ultrahigh-Temperature Energy Storage," Nanomaterials, **12**(24), 4458 (2022). https://doi.org/10.3390/nano12244458
[11] A.A. Nassar, A.A.E.A. Elfiky, A.K. El-Sawaf, et al. "Sustainable green synthesis and characterization of nanocomposites for synergistic photocatalytic degradation of Reactive Orange 16 in textile wastewater using CuO@A-TiO2/Ro-TiO2," Scientific Reports, **14**, 16188 (2024). https://doi.org/10.1038/s41598-024-63294-3
[12] A.K. Sijo, V.K. Jha, L.S. Kaykan, and D.P. Dutta, "Structure and cation distribution in superparamagnetic NiCrFeO4 nanoparticles using Mössbauer study," Journal of Magnetism and Magnetic Materials, **497**, 166047 (2020). https://doi.org/10.1016/j.jmmm.2019.166047
[13] J. Mazurenko, L. Kaykan, A.K. Sijo, M. Moiseienko, M. Kuzyshyn, N. Ostapovych, and M. Moklyak, "The influence of reaction medium pH on the structure, optical, and mechanical properties of nanosized CU-FE ferrite synthesized by the Sol-Gel autocombustion method," Journal of Nano Research, **81**, 65–84 (2023). https://doi.org/10.4028/p-d2fqah
[14] A.K. Sijo, "Magnetic and structural properties of CoCrxFe2−xO4 spinels prepared by solution self combustion method," Ceramics International, **43**(2), 2288-2290 (2017). https://doi.org/10.1016/j.ceramint.2016.11.010
[15] A. Varma, A.S. Mukasyan, A.S. Rogachev, and K.V. Manukyan, "Solution Combustion Synthesis of Nanoscale Materials," Chemical Reviews, **116**(23), 14493-14586 (2016). https://doi.org/10.1021/acs.chemrev.6b00279

[16] M. Ginting, S. Taslima, K. Sebayang, D. Aryanto, T. Sudiro, and P. Sebayang, "Preparation and characterization of zinc oxide doped with ferrite and chromium," AIP Conf. Proc. **1862**, 030062 (2017). https://doi.org/10.1063/1.4991166

[17] B. Jaleh, M. Kashfi, B.F. Mohazzab, "Experimental characterization and finite element investigation of SiO2 nanoparticles reinforced dental resin composite," Sci. Rep. **14**, 7794 (2024). https://doi.org/10.1038/s41598-024-58114-7

[18] Y. Li, Y. Sun, J. Wu, G. Ren, X. Xu, B. Corcoran, S.T. Chu, *et al*. "Performance Analysis of Microwave Photonic Spectral Filters based on Optical Microcombs," Advanced Photonics Research, 1(1), 2400084 (2024). https://doi.org/10.1002/apxr.202400084

[19] A.M. Mohammad, S.M.A. Ridha, and T.H. Mubarak, "Structural and magnetic properties of Mg-Co ferrite," Digest Journal of Nanomaterials and Biostructures, **13**(3), 615-623 (2018). https://chalcogen.ro/615_MohammadAM.pdf

[20] A. Sijo, and D.P. Dutta, "Size-dependent magnetic and structural properties of CoCrFeO4 nano-powder prepared by solution self-combustion," Journal of Magnetism and Magnetic Materials, **451**, 450–453 (2017). https://doi.org/10.1016/j.jmmm.2017.11.092

[21] A. Kumar, P. Sharma, and D. Varshney, "Structural, vibrational and dielectric study of Ni doped spinel Co ferrites: Co1−xNixFe2O4 (x=0.0, 0.5, 1.0)," Ceramics International, **40**(8), 12855-12860 (2014). https://doi.org/10.1016/j.ceramint.2014.04.140

[22] I. Ran, H. Liu, H. Dong, P. Gao, H. Cheng, J. Xu, H. Wang, *et al*. "Accurate quantification of TiO2(B)'s phase purity via Raman spectroscopy," Green Energy and Environment, **8**(5),1371-1379 (2023). https://doi.org/10.1016/j.gee.2022.02.008

[23] X. Liu, and J. Fu, "Electronic and elastic properties of the tetragonal anatase TiO2 structure from first principle calculation," Optik, **206**, 164342 (2020). https://doi.org/10.1016/j.ijleo.2020.164342

[24] K.R. Ramkumar, and S. Natarajan, "Effects of TiO2 nanoparticles on the microstructural evolution and mechanical properties of accumulative roll bonded Al nanocomposites," Journal of Alloys and Compounds, **793**, 526-532 (2019). https://doi.org/10.1016/j.jallcom.2019.04.218

[25] S. Kobayashi, Y. Ikuhara, and T. Mizoguchi, "Lattice expansion and local lattice distortion in Nb- and La-doped SrTiO3 single crystals investigated by x-ray diffraction and first-principles calculations," Physical Review B, **98**(13), 134114 (2018). https://doi.org/10.1103/PhysRevB.98.134114

[26] W. Qin, T. Nagase, Y. Umakoshi, and J.A. Szpunar, "Relationship between microstrain and lattice parameter change in nanocrystalline materials," Philosophical Magazine Letters, **88**(3), 169–179 (2008). https://doi.org/10.1080/09500830701840155

[27] H. Zhang, Q. Tang, Q. Li, Q. Song, H. Wu, and N. Mao, "Enhanced Photocatalytic Properties of PET Filaments Coated with Ag-N Co-Doped TiO2 Nanoparticles Sensitized with Disperse Blue Dyes," Nanomaterials, **10**(5), 987 (2020). https://doi.org/10.3390/nano10050987

[28] C. Liang, Z. Jia, and R. Chen, "An Automated Particle Size Analysis Method for SEM Images of Powder Coating Particles," Coatings, **13**(9), 1547 (2023). https://doi.org/10.3390/coatings13091547

[29] E.J. Ekoi, A. Gowen, R. Dorrepaal, and D.P. Dowling, "Characterisation of titanium oxide layers using Raman spectroscopy and optical profilometry: Influence of oxide properties," Results in Physics, **12**, 1574-1585 (2019). https://doi.org/10.1016/j.rinp.2019.01.054

[30] M.K. Kokare, N.A. Jadhav, Y. Kumar, K.M. Jadhav, and S.M. Rathod, "Effect of Nd3+ doping on structural and magnetic properties of Ni0.5Co0.5Fe2O4 nanocrystalline ferrites synthesized by sol-gel auto combustion method," Journal of Alloys and Compounds, **748**, 1053-1061 (2018). https://doi.org/10.1016/j.jallcom.2018.03.168

[31] L.S. Kaykan, J.S. Mazurenko, N.V. Ostapovych, A.K. Sijo, and N.Y. Ivanichok, "Effect of PH on structural morphology and magnetic properties of ordered phase of cobalt doped lithium ferrite nanoparticles synthesized by SoL-Gel auto-combustion method," Journal of Nano- and Electronic Physics, **12**(4), 04008–7 (2020). https://doi.org/10.21272/jnep.12(4).04008

[32] E.D. Smolensky, H.Y. Park, Y. Zhou, G.A. Rolla, M. Marjańska, M. Botta, and V.C. Pierre, "Scaling Laws at the Nano Size: The Effect of Particle Size and Shape on the Magnetism and Relaxivity of Iron Oxide Nanoparticle Contrast Agents," Journal of Materials Chemistry B, **1**(22), 2818-2828 (2013). https://doi.org/10.1039/C3TB00369H

[33] J. Mazurenko, A.K. Sidjo, L. Kaykan, J.M. Michalik, Ł. Gondek, E. Szostak, A. Żywczak, and V. Moklyak, "Magneto-Structural properties of MG-Substituted copper ferrite nanoparticles," Materials Research Express, **11**(12), 125003 (2024). https://doi.org/10.1088/2053-1591/ad9c19

[34] D. Dey, N. Halder, K.P. Misra, S. Chattopadhyay, S.K. Jain, P. Bera, N. Kumar, and A.K. Mukhopadhyay, "Systematic study on the effect of Ag doping in shaping the magnetic properties of sol-gel derived TiO2 nanoparticles," Ceramics International, **46**(17), 27832-27848 (2020). https://doi.org/10.1016/j.ceramint.2020.07.282

ПРОЕКТУВАННЯ ТА РОЗРОБКА НАНОКОМПОЗИТІВ ФЕРИТ-TiO₂ З НАСТРОЮВАНИМИ МАГНІТНИМИ ВЛАСТИВОСТЯМИ

Ханаа Ш. Ахмед[1], А.К. Сіджо[2], Алі М. Мохаммад[1], Геро С. Ахмед Аль-Джаф[1], Бален Х. Ахмед[1], Ю. Мазуренко[3]

[1]Університет Гарміана, Коледж освіти, Кафедра фізики, Курдистан, Калар-46021, Ірак

[2]Кафедра фізики, Коледж мистецтв та наук імені Мері Матха, Манантаваді, Університет Каннур-670645, Індія

[3]Кафедра медичної інформатики, Івано-Франківський національний медичний університет,

вул. Галицька, 2, 76018, Івано-Франківськ, Україна

Нанокомпозити Ni-ферит-TiO₂ з різним вмістом TiO₂ (0%, 25%, 50% та 75%) були синтезовані за допомогою методу золь-гель автогоріння та охарактеризовані за допомогою рентгенівської дифракції (XRD), FE-SEM, VSM та раманівської спектроскопії. Рентгенівський дифракціональний аналіз підтвердив співіснування фаз фериту та TiO₂. Зображення FE-SEM показали рівномірний розподіл частинок та зменшення розміру частинок зі збільшенням вмісту TiO₂. Раманівська спектроскопія продемонструвала сильні коливальні моди, пов'язані з TiO₂, причому найвища інтенсивність спостерігалася у зразку з 75% TiO₂, зменшуючи її зі зменшенням вмісту TiO₂. Піки, що спостерігалися в чистому Ni-фериті (283, 402, 469 та 689 см⁻¹), зміщувалися до нижчих довжин хвиль зі збільшенням легування TiO₂, що вказує на змінені коливальні моди через фазові взаємодії. Ці взаємодії, ймовірно, сприяли змінам магнітних властивостей. Аналіз VSM виявив зменшення намагніченості насичення та залишкової магнітної напруги зі збільшенням вмісту TiO₂, тоді як коерцитивна сила залишалася стабільною. Магнітна поведінка була пов'язана з розведенням TiO₂ та межами розділу фаз, що дає цінні знання для розробки магнітних матеріалів з індивідуальними властивостями.

Ключові слова: *ферит; нанокомпозити; магнітні властивості; наночастинки; гібридний ферит*

STUDY OF THE INFLUENCE OF TEMPERATURE ON THE TRANSITIONS OF THE CdS/Si/CdTe HETEROSYSTEM

Feruza A. Giyasova[1], Khayot N. Bakhronov[2], Murodjon A. Yuldoshev[3]*, Ibrokhim B. Sapaev[4], Rustamjon G. Ikramov[5], Farkhod A. Giyasov[1], Mira R. Bekchanova[6], Maxmudjon M. Qaxxarov[5], Hakimjon O. Abdullayev[5]

[1]*Kimyo International University in Tashkent, Uzbekistan*
[2]*Tashkent University of Information Technologies named after Muhammad al-Khwarizmi, Uzbekistan*
[3]*Turan International University, Namangan, Uzbekistan*
[4]*Tashkent Institute of Irrigation and Agricultural Mechanization Engineers National Research University, Tashkent, Uzbekistan*
[5]*Namangan State Technical University, Uzbekistan*
[6]*University of Public Security of the Republic of Uzbekistan*
*Corresponding Author e-mail: murod.yuldoshev1993@gmail.com
Received September 4, 2025; revised October 18, 2025; accepted October 25, 2025

The study presents the results of an investigation into the temperature dependence of the current–voltage characteristics of CdS/Si/CdTe heterostructures fabricated by thermal evaporation. The study establishes that, as the temperature increases, an exponential rise in current is observed, attributed to the thermally activated nature of conductivity and the reduction of the potential barrier at the interfacial boundaries. In the low-temperature region, the structure exhibits diode-like behavior, whereas at higher applied voltages (20–40 V), an injection transport mechanism becomes dominant. The activation energy of 0.61 eV confirms that the thermal release of carriers from localized states governs charge transport. The results indicate the stability of the barrier height and conduction mechanism over the studied temperature range, highlighting the need to account for thermal effects in the design of photoelectric and optoelectronic devices based on CdS/Si/CdTe structures.

Keywords: *Temperature; Heterosystem; Layer; Carrier; Mobility; Mechanism; Current; Voltage; Structure*
PACS: 64.70.kg, 73.40.Kp, 68.37.Hk

INTRODUCTION

In recent years, there has been growing interest in the development and investigation of thin-film heterostructures based on group II–VI compounds, which are distinguished by their high photoelectric efficiency and thermal stability under operating conditions [1–3]. Among these materials, cadmium-containing compounds such as CdS and CdTe have attracted particular attention due to their direct bandgap nature, strong optical activity, and the technological simplicity of their deposition processes. These properties make them widely applicable in solar cells, photodetectors, and various optoelectronic devices [4–7]. The incorporation of a silicon layer into CdS/CdTe-based heterostructures enables more effective lattice parameter matching between the constituent layers, reduces defect density at the interfaces, and improves charge-carrier transport conditions, thereby enhancing the overall functional performance of the structure [8-10]. Such a heterostructure is considered a promising platform for developing photoconverters with a broad spectral sensitivity range. In this system, the CdS layer-a wide-bandgap semiconductor ($E_g \approx 2.4$ eV)-acts as a transparent window; silicon ($E_g \approx 1.12$ eV) serves as a buffer and transport layer; while CdTe-a narrow-bandgap semiconductor ($E_g \approx 1.5$ eV)-provides efficient light absorption and charge-carrier generation [11,12]. The operational parameters of such structures are largely determined by temperature conditions, which influence the recombination rate, the potential barrier height of the p–n junction, and the carrier mobility.

The influence of temperature on the operating parameters of a photodiode is primarily determined by two fundamental diode characteristics-the ideality factor and the reverse saturation current density [13,14]. Direct-bandgap semiconductor materials such as CdS and CdTe have demonstrated high efficiency in the fabrication of thin-film photodiode structures [15,16].

To achieve the highest efficiency of photodiodes based on A^2B^6 compounds, the solid solution should possess a continuously graded composition across a thickness of d << 1 μm, ranging from CdS to CdTe [17]. The use of high-temperature processing during the formation of CdS/CdTe-based heterostructures incorporating a silicon layer leads to an increased concentration of uncontrolled impurities throughout the entire structure, including within the compound layers [18]. In CdS/CdTe heterostructures, a junction with pronounced rectifying behavior and high photosensitivity is typically formed [19, 20]. In addition to parameters such as layer thickness, doping level, bandgap width, charge-carrier mobility, and density of states, temperature effects exert a significant influence on the photoelectric characteristics and operational stability of photodiodes. Therefore, the investigation of the temperature dependence of current–voltage characteristics in CdS/Si/CdTe heterostructures represents a relevant and timely task aimed at optimizing their

photoelectric properties and enhancing stability under various operating conditions. In the present study, the influence of temperature on the key operating parameters of CdS/Si/CdTe photodiode heterosystems was analyzed within the temperature range of 293–333 K. The results obtained provide insights into the temperature stability of these structures and contribute to the optimization of the performance characteristics of single- and multi-junction photodiodes, taking thermal effects into account.

EXPERIMENTAL PART

The investigated CdS/Si/CdTe heterosystem [21,22] was fabricated in a quasi-closed volume using the vacuum thermal evaporation method of CdS and CdTe powders onto an n-type monocrystalline silicon substrate. The substrate used was monocrystalline silicon of the KEF-600 grade, oriented along the (111) crystallographic direction, with a thickness of d=130 μm, a diameter of D=42 mm, and a specific resistivity of ρ=607.47 Ω·cm. The concentration of the majority charge carriers was $N_n=7\times10^{12}$ cm^{-3}, and the area of the resulting structure was 29 mm². The thickness of the deposited films was d = 0.55 μm and was determined using a MII-4 microinterferometer [21]. The films consist of microcrystalline blocks with a columnar grain structure, oriented along the growth direction and azimuthally disoriented. The grain sizes range from 50 to 100 μm, extending through the entire film thickness. This combination of structural parameters and technological conditions ensures the formation of a high-quality heterojunction with good crystallinity and minimal interfacial defects, which is a prerequisite for obtaining stable current–voltage characteristics of the photodiode over a wide temperature range [17].

The temperature dependence of the investigated photodiode samples of the CdS/Si/CdTe heterosystem was recorded in the measuring chamber of a Carl Zeiss Jena monochromator. The temperature regime in the investigated samples was set using a heater mounted in the sample holder placed inside the measuring chamber. The set temperature from room temperature to 60 ºC was measured with a copper-constantan thermocouple and maintained with a thermostat, as shown in Fig. 1.

The temperature in the studied sample 5 was controlled using a specially made low-inert heater – 4, mounted in the sample holder – 3, placed inside the measuring chamber. The temperature was set from room temperature to 60°C, with an accuracy of ±1°C It was measured by thermocouple 6 (chromel-droplet) and maintained by digital thermostat 2, taking into account the inertia of the system. Using a high-precision adjustable voltage source – 1, a fixed voltage was set, supplied to the studied sample – 5. From the output of the studied sample 5, the current flowing through the semiconductor structure was supplied to a digital current meter – 7, SH-300, used in the DC measurement mode.

Based on the obtained results, the dependence of current change on temperature was constructed using OriginPro 7.0.
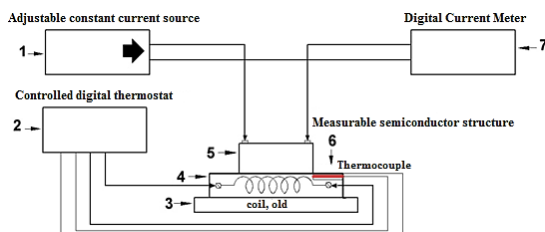

Figure 1. Block diagram for measuring the temperature dependence of the volt-ampere characteristic

RESULTS AND DISCUSSION

The current–voltage (I–V) characteristics of the structure were recorded in the forward direction over a wide range of current and voltage values. Assuming electrically active defects, analyzing I–V characteristics allows conclusions to be drawn about the defect structure formed within the heterosystem. Fig. 2 presents the forward branch of the I–V characteristic of the CdS/Si/CdTe heterosystem obtained at room temperature (293 K).
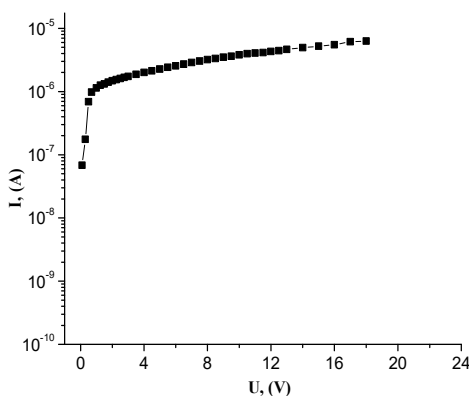

Figure 2. Volt-ampere characteristic of the CdS/Si/CdTe heterosystem in the forward direction at T=293 K

The current-voltage dependence is plotted on a semi-logarithmic scale. The analysis of the I-V characteristics indicates that the structure exhibits pronounced rectifying behavior. At 18 V, the rectification coefficient is ~10, confirming the diode-like behavior of the structure. Previously published research [23] presents the results of an analysis of the I-V characteristics of the CdS/Si/CdTe heterosystem.

The temperature dependence of the CdS/Si/CdTe heterosystem is shown in Fig. 3 and was recorded in the forward direction over wide current change ranges at fixed voltage. The study was conducted in the temperature range T=293÷333 K.
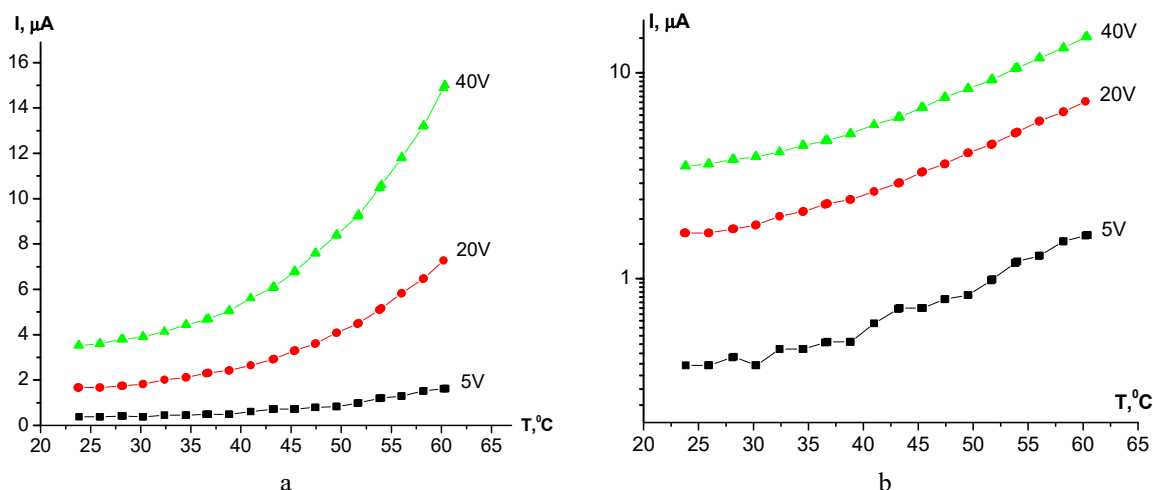

Figure 3. Current–voltage characteristics of the CdS/Si/CdTe heterosystem in the forward direction (a) and their sublinear regions (b) at fixed voltage values of 5 V, 20 V, and 40 V

In the obtained dependence (Fig. 3), an exponential increase in current with rising temperature was observed, indicating a thermally activated conduction mechanism. The forward branch of the I–V characteristics at low fixed voltages (5 V) followed an exponential dependence, whereas at higher voltages (up to 40 V) a sublinear increase in current with voltage was observed. In the low-temperature region, the current remained small due to the insufficient concentration of thermally excited carriers, while at low voltages (~5 V) an exponential current growth typical of diode structures with a diffusion-controlled conduction mechanism was evident. As the temperature increased, a noticeable enhancement of conductivity occured, associated with the intensification of thermal carrier generation and a reduction in the potential barrier at the CdS/Si and Si/CdTe heterointerfaces. At a fixed voltage of 20 V, the current increase was moderate, indicating a diode-type transition dominated by thermally activated charge transport processes. However, when the fixed voltage was increased to 40 V, the current rises much more rapidly, suggesting the onset of an injection-type conduction mechanism and an additional lowering of the barrier height at the heterojunction interface upon heating. An increase in temperature above 330 K was accompanied by a growth in leakage currents, which is likely associated with the thermal ionization of deep impurity and defect levels localized at the CdS/Si and Si/CdTe interfaces. The initial portion of the temperature dependence (Fig. 3) was well approximated by a known empirical law [24].

$$I = I_0 exp\ (eV/ckT) \tag{1}$$

The values of the exponent c in the exponent and the pre-exponential factor I_0, calculated from the temperature dependence (Fig. 3) for different temperatures, are given in Table 1.

Table 1. Values of the exponent c in the exponent and the pre-exponential factor I_0 at different temperatures

T, K	C	I_0, A
293	2.92	$5.17 \cdot 10^{-8}$
303	2.15	$8.02 \cdot 10^{-8}$
323	1.78	$2.53 \cdot 10^{-7}$
333	1.09	$3.02 \cdot 10^{-7}$

The transitions formed between the CdS/Si and Si/CdTe layers were high-resistance [25-27] and they mainly determined the electronic processes in the structure and the current transfer mechanism.

Dependence (1) is typical for the so-called "long" p-n diode, i.e. when $d/L_p > 1$, where d is the base length, $L_p=(D_p\tau_p)^{1/2}$ is the diffusion length of minority carriers, D_p is the diffusion coefficient, τ_p is the lifetime of minority carriers. Since the electronic processes [28, 29] associated with charge modulation during current flow through the structure are largely determined by the transition high-resistance layers of CdS and CdTe, it is reasonable to take the thickness of these layers, which is approximately d≈0.55 μm, as the base length.

Exponential dependence of current on voltage (1) for p-i-n structures, the exponent c in the exponent has the following form:

$$c = \frac{2b + ch(d/L_p) + 1}{b+1}, \tag{2}$$

where, $b = \mu_n/\mu_p$ is the ratio of electron and hole mobilities in the CdS/Si and Si/CdTe transition layers, $b = 9.12$ [30, 31]. Knowing b, we can find $d/L_p = 2.84$, then we can find the diffusion length of minority carriers: $L_p = 0.71$ μm. This allowed us to determine the product of the mobility and the minority carrier lifetime $\mu_p\tau_p = qL_p^2/kT$, which was obtained at room temperature (293 K) as 1.38×10^{-7} см²/V. At T=313 K, $\mu_p\tau_p = 4.12 \times 10^{-7}$ см²/V, which is e times greater than the value at room temperature; the increase in μpτp with temperature is explained by the recharging of deep centers.

The minority carrier lifetime (τ_p) was determined by the relaxation process of nonequilibrium carriers at a low excitation level both in the mode without external voltage and at different values of the applied voltage [32, 33]. Nonequilibrium carriers were created using an electric pulse generated by a G5-63 rectangular pulse generator. The pulses had a sharp front and tail with a duration of 500-600 ns. The rise time did not exceed 3×10^{-9} s, and the duty cycle was at least 6×10^{-4} s. In the absence of external voltage, the change in the concentration of nonequilibrium carriers n over time is described by an exponential dependence:

$$\Delta n = \Delta n_0 exp(-t/\tau), \tag{3}$$

where, t is the time and τ is the relaxation time constant. Based on dependence (5), the value of this constant was obtained: $\tau \approx 3.16 \times 10^{-7}$ s. Since in the structures under consideration the relaxation process was determined by the modulation of currents by minority carriers, the characteristic relaxation time corresponds to the lifetime of minority carriers, i.e. $\tau_p \approx 3.16 \times 10^{-7}$ s.

To avoid losses caused by the voltage drop in the bulk of the CdTe film, the Fermi level should be no further than approximately 0.2 eV from the upper boundary of the valence band, and for CdS, no further than 0.08 eV from the conduction band. The situation was complicated by the fact that even ultrapure CdTe and CdS samples inevitably contain residual impurities such as Cu, Fe, Au, Ag, As, P, and others in concentrations reached 10^{15}-10^{16} cm⁻³ [34-35]. In addition to uncontrolled impurities, electrically active defects arised in the material, which were formed during its synthesis, as well as during mechanical or chemical treatment. For example, Cd vacancies are capable of forming singly or doubly charged acceptor states, and in combination with impurities such as Cl, they form donor complexes (known as A-centers). Te vacancies and Te atoms in interstitial sites or at Cd sites also behaved similarly to impurities of various natures. As a result, both shallow and deep acceptor and donor levels were inevitably present in the CdTe band gap, making this material a partially compensated semiconductor [36].

Fig. 4 shows SEM images of a thin-base CdS film grown on a silicon substrate of n-type CdS/Si/CdTe heterosystem and mass fractions of cadmium (Cd) elements and residual impurities in percentage. It can also be seen that the back side of the sample, consisting of silicon, is partially covered with a thin CdS film.
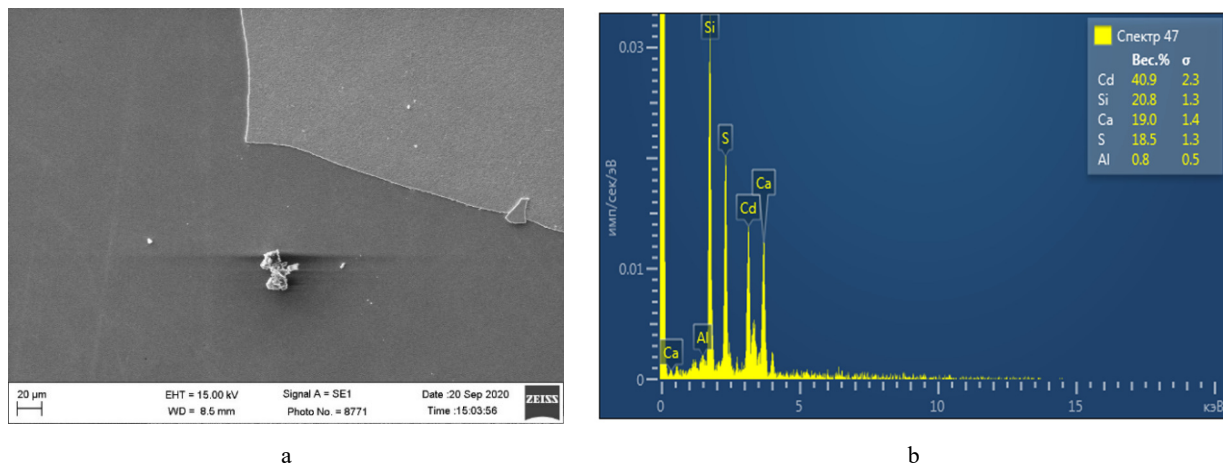

| | a | | b |

Figure 4. SEM images of the surface (a) and elemental analysis (b) of a thin base layer based on n-type CdS of the CdS/Si/CdTe heterosystem

It is known that, in the general case, the current–voltage characteristic (I–V characteristic) of a p–n junction under forward bias can be expressed by the following formula [24]:

$$I = I_s exp \frac{qV}{nkT}, \tag{4}$$

determine the voltage drop across the p-n junction, which has the following expression:

$$V = \frac{nkT}{q} ln \frac{I}{I_s}, \tag{5}$$

According to the dependencies (Fig. 5) measured on experimental samples at different temperatures, it was noted that with a change in temperature, the coefficient of non-ideality also changed. In this case, the coefficient of non-ideality changes linearly inversely proportional to the temperature ($1/T$) and is expressed as follows:

$$n = n_0 + \frac{T_0}{T} \tag{6}$$

where, n_0 and T_0 are constants of the empirical formula describing the dependence of the non-ideality coefficient on temperature. For the experimental samples under study at $T_0=310$ K, the value of n_0 is 0.72.

In practical calculations, the ideality factor is determined from the slope of the linear section of the I–V characteristic (Fig. 5) in semilogarithmic coordinates using the following expression:

$$n = \frac{q}{kT}\left(\frac{dV}{d(\ln(I_s))}\right) \tag{7}$$
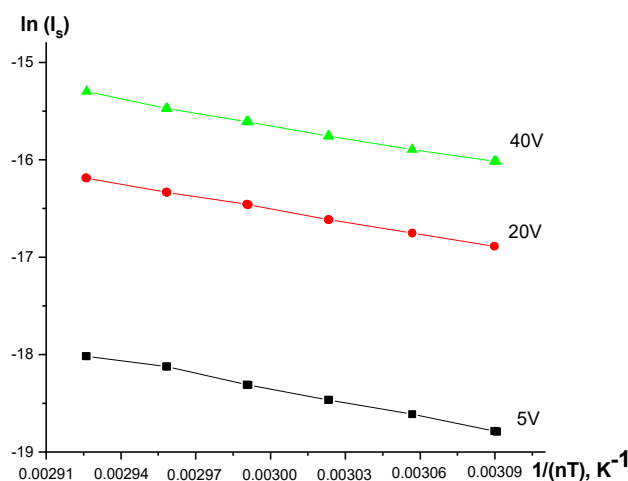

Figure 5. Arrhenius dependence of the pre-exponential factor for the CdS/Si/CdTe heterosystem

The graph shown in Fig. 5 illustrates the dependence of the logarithm of the saturation current ($\ln I_s$) on the inverse temperature ($1/(nT)$) for the CdS/Si/CdTe heterosystem at various fixed voltages: 5 V, 20 V, and 40 V. The linear nature of the dependencies corresponding to voltages of 20 V and 40 V indicates a thermally activated mechanism of saturation current conduction, which follows an exponential relationship described by expression (8) [24, 37].

$$I_s = I_{s0}exp\left(-\frac{\Delta E}{nkT}\right), \tag{8}$$

where, ΔE - activation energy, k is the Boltzmann constant, T is the absolute temperature, and n is the ideality factor of the junction.

The negative slope of the temperature dependences of the logarithm of the saturation current indicates an increase in current with rising temperature (decreasing $1/(nT)$), which is characteristic of diode structures where charge transport occurs via thermoelectronic emission across the potential barrier. The parallelism of the lines corresponding to different applied voltage values indicates that the activation energy remains constant within the studied temperature range, confirming the stability of the barrier height and the preservation of the charge transport mechanism [23,38]. At higher fixed voltages, an increase in the saturation current values is observed, which is associated with a reduction in the effective potential barrier height and an enhancement of injection processes in the heterojunction region. The linear dependence:

$$\ln(I_s) = f(1/nT) \tag{9}$$

confirms the thermally activated nature of the saturation current and allows for the evaluation of the energy parameters of the barrier junction in the CdS/Si/CdTe structure.

From the temperature dependence (Fig. 5) of the CdS/Si/CdTe heterosystem, the activation energy of charge carriers was estimated to be $\Delta E \approx 0.61$ eV, while the saturation current at the junctions was $I_{s0}=6.3\times10^{-8}$ A. The obtained activation energy value indicates a thermally activated conduction mechanism, in which charge transport is governed by the thermal release of carriers from localized energy states or by their overcoming of the potential barrier at the heterojunction interface. Based on the dependence shown in Fig. 5 and according to expression (7), the ideality factor was calculated to be n=3.6, which indicates a combined current transport mechanism in the CdS/Si/CdTe heterosystem [39,15]. Along with the diffusion transport of charge carriers, recombination and injection processes make a significant contribution to conductivity, as well as the influence of localized energy states and the inhomogeneity of the potential barrier at the interfacial boundaries [15].

According to the literature [24], the specific resistance of the material at a given temperature is determined by the concentration of the majority charge carriers (n) according to the expression $\rho=1/q\mu_n n$. In the CdS/Si/CdTe heterosystem at room temperature (293 K), the carrier concentration is about 10^{11} cm^{-3} and increases with increasing temperature, reaching up to 2×10^{12} cm^{-3} at 333 K. This indicates that the studied structure is a highly compensated material in which the concentration of ionized defect complexes of the $(V^{-2}_{Cd} D^+)$ - type is about 10^{11} cm^{-3} at room temperature.

CONCLUSIONS

The conducted studies have shown that temperature has a significant effect on the I–V characteristics of the CdS/Si/CdTe heterosystem. With increasing temperature, an exponential rise in current was observed, which is attributed to the thermally activated nature of conductivity and the reduction of the potential barrier at the interfacial boundaries. In the low-temperature region, the current remained small, whereas at low voltages (~5 V) the structure exhibited diode-like behavior characteristic of a diffusion-controlled carrier transport mechanism. When the applied voltage was increased to 40 V, an injection-type conduction mechanism stayed dominant, caused by a reduction in the barrier height upon heating. The observed increase in current with temperature indicates a decrease in the effective barrier height, confirming the stability of the electronic properties of the junction within the investigated temperature range.

The study of the temperature dependence in the sublinear region revealed that the deep energy levels within the structure are continuously distributed, with their concentration increasing toward the mid-gap region. It was established that the $\mu_p\tau_p$ parameter in the heterosystem increases with temperature: at T=293 K, $\mu_p\tau_p=1.38\times10^{-7}$ см^2/V, while at T=313 K, $\mu_p\tau_p=4.12\times10^{-7}$ см^2/V. Based on the measured specific resistivity of the heterostructure at the corresponding temperatures, the concentration of the majority charge carriers was determined to be approximately 10^{11}cm^{-3}, increasing to about 2×10^{11} cm^{-3} with rising temperature.

The temperature dependence of the pre-exponential factor I_0 in the exponential region of the current–voltage characteristics indicates a complex variation in the equilibrium charge carrier concentration within the CdS/Si/CdTe heterosystem. This behavior is attributed to the influence of deep energy levels, recombination centers, and the potential distribution features at the interfacial boundaries. It has been established that the conduction process in the CdS/Si/CdTe heterosystem exhibits a thermoactivated character. The activation energy of 0.61 eV suggests that charge transport was governed by the thermal release of carriers from localized states or by their surmounting of the potential barrier at the heterojunction interface.

The obtained results confirm the stability of the barrier height and the invariance of the carrier transport mechanism within the investigated temperature range, while also demonstrating the enhancement of injection processes under higher applied voltages. The revealed regularities highlight the necessity of accounting for temperature effects in the design and operation of photoelectric and optoelectronic devices based on CdS/Si/CdTe structures. The findings can be utilized to optimize the parameters of photoconverters and optical memory devices operating over a wide temperature range.

ORCID
Feruza A. Giyasova, https://orcid.org/0000-0003-0746-4986; **Murodjon A. Yuldoshev,** https://orcid.org/0000-0002-9722-9439
Khayot N. Bakhronov, https://orcid.org/0009-0000-4138-3149; **Farkhod A. Giyasov,** https://orcid.org/0009-0003-9882-0655
Rustamjon G. Ikramov, https://orcid.org/0000-0003-1629-1300; **Ibrokhim B. Sapaev,** https://orcid.org/0000-0003-2365-1554

REFERENCES

[1] C. Cao, Q. An, "Elucidating thin film growth mechanisms for high-performance II–VI photovoltaic semiconductors: simulation-driven insights and challenges," CrystEngComm, **27**(21), 3404-3415 (2025). https://doi.org/10.1039/D5CE00244C

[2] S.M. Sivasankar, C. de Oliveira Amorim, and A.F. da Cunha, "Progress in Thin-Film Photovoltaics: A Review of Key Strategies to Enhance the Efficiency of CIGS, CdTe, and CZTSSe Solar Cells," J. Compos. Sci. **9**(3), 143 (2025). https://doi.org/10.3390/jcs9030143

[3] K.G. Zayas-Bazán, P.G. Zayas-Bazán, F. de Moure-Flores, and D. Jiménez-Olarte, "Development of a CdCl$_2$ thermal treatment process for improving CdS/CdTe ultrathin solar cells," Journal of Materials Science: Materials in Electronics, (2019). https://doi.org/10.1007/s10854-019-01694-2

[4] M. Mathew, "i- ZnO and CdS Buffer Layers for Improving the Efficiency of Copper Tin Sulphide Quantum Dot Sensitized Solar Cells," East Eur. J. Phys. (2), 258 (2025). https://doi.org/10.26565/2312-4334-2025-2-31

[5] V.T. Mirzayev, B.J. Akhmadaliev, I.I. Yulchiev, and M.M. Madraximov, "Temperature and Infrared Quenching of Equilibrium Conductivity in CdSe$_x$S$_{1-x}$ Film," East Eur. J. Phys. (2), 247 (2025), https://doi.org/10.26565/2312-4334-2025-2-29

[6] T.M. Razykov, K.M. Kuchkarov, A.A. Nasirov, M.P. Pirimmatov, R.R. Khurramov, R.T. Yuldashev, D.Z. Isakov, *et al*. "Mechanism of Current Performance in Thin-Film Heterojunctions n-CdS/p-Sb$_2$Se$_3$ Obtained by the CMBD Method," East Eur. J. Phys. (4), 279 (2024). https://doi.org/10.26565/2312-4334-2024-4-29

[7] Sh.B. Utamuradova, Z.T. Azamatov, A.I. Popov, M.R. Bekchanova, M.A. Yuldoshev, and A.B. Bakhromov, East Eur. J. Phys. (3), 278 (2024), https://doi.org/10.26565/2312-4334-2024-3-27

[8] M. Isah, C. Doroody, K.S. Rahman, M.N. Rahman, A.A. Goje, M.E. Soudagar, T.S. Kiong, *et al*. "Exploring the impact of defect energy levels in CdTe/Si dual-junction solar cells using wxAMPS," Sci Rep. **27**(14), 4804 (2024). https://doi.org/10.1038/s41598-024-55616-2

[9] Sh.B. Utamuradova, Kh.S. Daliev, Sh.Kh. Daliev, S.A. Muzafarova, K.M. Fayzullaev, and G.A. Muzafarova, "Volt-Ampere Characteristics of Hetero Film Photosensitive Structure Au-CdS-nSi-CdTe-Au," East Eur. J. Phys. (4), 256 (2024). https://doi.org/10.26565/2312-4334-2024-4-26

[10] M.S. Kukurudziak, V.M. Lipka, and V.V. Ryukhtin, "Silicon p-i-n Mesa-Photodiode Technology, East Eur. J. Phys. (3), 385 (2024). https://doi.org/10.26565/2312-4334-2024-3-47

[11] G. Sürücü, H.H. Güllü, and Ö. Bayraklı, "Enhancement in Photovoltaic Characteristics of CdS/CdTe Heterojunction. Journal of Polytechnic, **20**(4), 801-805 (2017). https://doi.org/10.2339/politeknik.368993

[12] M. Akramov, B. Eshchanov, S. Usanov, Sh. Norbekov, and D. Matrasulov, "Second-harmonic generation in branched optical waveguides: Metric graphs based approach," Physics Letters A, **524**, 129827 (2024). https://doi.org/10.1016/j.physleta.2024.129827

[13] M. Piliougine, L.E. Garcia-Marrero, K. Lappalainen, and G. Spagnuolo, "Influence of the temperature on the intrinsic parameters of thin-film photovoltaic modules," Renewable Energy, **240**, 122068 (2025). https://doi.org/10.1016/j.renene.2024.122068

[14] P. Dalapati, N.B. Manik, and A.N. Basu, "Influence of temperature on tunneling-enhanced recombination in Si based p-i-n photodiodes," Journal of Semiconductors, **35**(8), 082001 (2013). https://doi.org/10.1088/1674-4926/35/8/082001

[15] S.A. Mirsagatov. R.R. Kabulov, and M.A. Makhmudov, "Injection photodiode based on an n-CdS/p-CdTe heterostructure," Semiconductors, **47**, 825–830 (2013). https://doi.org/10.1134/S106378261306016X

[16] V. Qaradaghi, I. Mejia, and M. Quevedo-Lopez, "Fabrication and Analysis of Thin Film CdTe/CdS-Based Avalanche Photodiodes," IEEE Electron Device Letters, **38**(4), 489 – 492 (2017). https://doi.org/10.1109/led.2017.2670523

[17] S.N. Usmonov, S.A. Mirsagatov, and A.Y. Leyderman, "Study of the current-voltage characteristic of the n-CdS/p-CdTe heterostructure depending on temperature," Semiconductors, **44**, 313-317 (2010). https://doi.org/10.1134/S1063782610030073

[18] Y. Zheng, X. Zhang, X. Yang, Y. Tai, J. Zhang, and B. Li, "Design and Fabrication of CdTe//Si Four-Terminal Mechanical Stacked Solar Cell," IEEE Journal of Photovoltaics, **14**(2), 260-264 (2024). https://doi.org/10.1109/jphotov.2023.3338862

[19] A.E. Rakhshani, "Heterojunction properties of electrodeposited CdTe/CdS solar cells," J. Appl. Phys. **90**(8), 4265-4271 (2001). https://doi.org/10.1063/1.1397279

[20] L. Ma, W. Liu, H. Cai, F. Zhang, and X. Wu, "Catalyst- and template-free low-temperature in situ growth of n-type CdS nanowire on p-type CdTe film and p-n heterojunction properties," Sci Rep. **13**(6), 38858 (2016). https://doi.org/10.1038/srep38858

[21] F.A. Giyasova, "Development of Multilayer Photosensitive Structures Based on GaAs and Si for Optoelectronic Devices," D.Sci. thesis, Institute of Semiconductor Physics and Microelectronics, Uzbekistan (2024).

[22] F.A. Giyasova, and M.A. Yuldoshev, "Investigation of temporal characteristics of photosensitive heterostructures based on gallium arsenide and silicon," Chalcogenide Letters, **22**(2), 123–129 (2025). https://doi.org/10.15251/CL.2025.222.123

[23] Sh.B. Utamuradova, F.A. Giyasova, K.N. Bakhronov, M.A. Yuldoshev, M.R. Bekchanova, and B. Ismatov, "Current Transfer Mechanism in A Thin-Based Heterosystem Based on A^2B^6 Compounds," East Eur. J. Phys. (3), 325 (2025). https://doi.org/10.26565/2312-4334-2025-3-31

[24] S.M. Sze, Y. Li, and K.K. Ng, *Physics of Semiconductor Devices*, 4th Edition, (Wiley, 2021).

[25] S.R. Bera, and S. Saha, "Fabrication of CdTe/Si heterojunction solar cell," Applied Nanoscience, **6**(7), 1037-1042 (2016). https://doi.org/10.1007/s13204-015-0516-5

[26] F.Kh. Khasanov, I.B. Sapaev, B.S. Mirzaev, Q.A. Shakarov, U.T. Davlatov, and N.N. Abdusattorov, "Si-CdTe-CdS Structures of Electronic Processes," AIP Conf. Proc. **2432**, 050017-1–050017-5 (2022). https://doi.org/10.1063/5.0089974

[27] J.Sh. Abdullayev, I.B. Sapaev, N.Sh. Esanmuradova, S.R. Kadirov, and Sh.M. Kuliyev, "Mathematical Analysis of the Features of Radial p-n Junction: Influence of Temperature and Concentration," East Eur. J. Phys. (2), 220 (2025). https://doi.org/10.26565/2312-4334-2025-2-24

[28] Sh.N. Usmonov, Sh.A. Mirsagatov, and A.Yu. Leyderman, "Study of the current-voltage characteristic of the nCdS/pCdTe heterostructure depending on temperature," Semiconductors, **44**(3), 313-317 (2010). https://doi.org/10.1134/S1063782610030073

[29] M.A. Yuldoshev, Z.T. Azamatov, A.B. Bakhromov, and M.R. Bekchanova, East Eur. J. Phys. (4), 250 (2024), https://doi.org/10.26565/2312-4334-2024-4-25

[30] T. Jüstel, *General Chemistry (Part Inorganic Chemistry) Lecture*, April 2024. http://dx.doi.org/10.13140/RG.2.2.36270.93763

[31] N.F. Zikrillayev, M.K. Khakkulov, M.H. Aripova, B.B. Ibragimova, and N.E. Iskandarov, "Electrophysical Properties of Cadmium and Sulfur-doped Silicon with Electronic Conductivity," International Journal of Advanced Research in Science, Engineering and Technology, **6**(12), 12073-12076 (2019).

[32] I.H. Smaili, and G.B. Hmida, "A Review of Minority Carrier Recombination Lifetime Measurements," International Journal for Research in Applied Science & Engineering Technology (IJRASET), **11**(V), 1351-1361 (2023). https://doi.org/10.22214/ijraset.2023.51725

[33] M. Koussour, S. Bekovb, J. Rayimbaev, A. Syzdykova, S. Muminovd, and I. Ibragimov, "Observational constraints on a generalized equation of state model," Physics of the Dark Universe, **47**, 101799 (2025). https://doi.org/10.1016/j.dark.2024.101799

[34] M. Zha, E. Gombia, F. Bissoli, A. Zappettini, and L. Zanotti, "Growth and Deep Level Characterisation of Undoped High Resistivity CdTe Crystals," Phys. Status Solidi B, **229**, 15 (2002). https://doi.org/10.1002/1521-3951(200201)229:1<15::AID-PSSB15>3.0.CO;2-6

[35] Kh.Yu. Rakhimov, H.T. Yusupov, Sh.R. Nurmatov, A. Chaves, and G.R. Berdiyorov, "Wave-packet rectification in graphene with alternating circular electrostatic potential barriers," J. Appl. Phys. **137**, 144302 (2025). https://doi.org/10.1063/5.0250401

[36] I.M. Dharmadasa, and A.A. Ojo, "Unravelling complex nature of CdS/CdTe based thin film solar cells," Journal of Materials Science: Materials in Electronics, **28**(8), 16598-16617 (2017). https://doi.org/10.1007/s10854-017-7615-x

[37] Y.B. Acharya, "Effect of temperature dependence of band gap and device constant on *I-V* characteristics of junction diode," Solid-State Electronics, **45**(7), 1115-1119 (2001). https://doi.org/10.1016/S0038-1101(01)00139-3

[38] Sh.B. Utamuradova, F.A. Giyasova, M.S. Paizullakhanov, S.Yu. Gerasimenko, M.A. Yuldoshev, S.R. Boydedayev, and M.R. Bekchanova, "Investigation of the functional capability of modified silicon-based photodiodes structure," Chalcogenide Letters, **22**(8), 753–764 (2025). https://doi.org/10.15251/CL.2025.228.753

[39] Z. Wang, Z. Cheng, A.E. Delahoy, and K.K. Chin, "A Study of Light-Sensitive Ideality Factor and Voltage-Dependent Carrier Collection of CdTe Solar Cells in Forward Bias," IEEE Journal of Photovoltaics, **3**(2), 843-851 (2013). https://doi.org/10.1109/jphotov.2013.2247095

ДОСЛІДЖЕННЯ ВПЛИВУ ТЕМПЕРАТУРИ НА ПЕРЕХОДИ ГЕТЕРОСИСТЕМИ CdS/Si/CdTe

Ф.А. Гіясова[1], Х.Н. Бахронов[2], М.А. Юлдошев[3], І.Б. Сапаєв[4], Р.Г. Ікрамов[5], Ф.А. Гіясов[1], М.Р. Бекчанова[6], М.М. Кахаров[5], Х.О. Абдуллаєв[5]

[1]Міжнародний університет Кімьо в Ташкенті, Узбекистан
[2]Ташкентський університет інформаційних технологій імені Мухаммада аль-Хорезмі, Узбекистан
[3]Міжнародний університет Туран, Наманган, Узбекистан
[4]Ташкентський інститут інженерів іригації та механізації сільського господарства Національний дослідницький університет, Узбекистан
[5]Наманганський державний технічний університет, Узбекистан
[6]Університет громадської безпеки Республіки Узбекистан

У дослідженні представлені результати дослідження температурної залежності вольт-амперних характеристик гетероструктур CdS/Si/CdTe, виготовлених методом термічного випаровування. Встановлено, що зі збільшенням температури спостерігається експоненціальне збільшення струму, що пояснюється термоактивованою природою провідності та зменшенням потенційного бар'єру на міжфазних межах. В області низьких температур структура демонструє діодоподібну поведінку, тоді як при вищих прикладених напругах (20–40 В) домінує інжекційний механізм транспорту. Енергія активації 0,61 еВ підтверджує, що теплове вивільнення носіїв заряду з локалізованих станів керує транспортом заряду. Отримані результати свідчать про стабільність висоти бар'єру та механізму провідності в досліджуваному діапазоні температур, а також про необхідність врахування теплових ефектів при проектуванні фотоелектричних та оптоелектронних пристроїв на основі структур CdS/Si/CdTe.

Ключові слова: *температура; гетеросистема; шар; носій; рухливість; механізм; струм; напруга; структура*